Retinal imaging : following of structure and cellular activity using static and dynamic Full-Field Optical Coherence Tomography

Kassandra Groux

THÈSE DE DOCTORAT

DE L'UNIVERSITÉ PSL

Préparée à ESPCI Paris - PSL

PSL★
UNIVERSITÉ PARIS

Imagerie de la rétine: suivi de structure et de l'activité cellulaire par OCT Plein Champ statique et dynamique

Retinal imaging: following of structure and cellular activity using static and dynamic Full-Field Optical

Coherence Tomography

Soutenue par
Kassandra GROUX
Le 24 novembre 2021

École doctorale n°564
Physique en Ile de France

Spécialité
Physique - Optique

Composition du jury :

|		
Sandrine LEVEQUE-FORT DR, Université Paris-Saclay		*Présidente*
Arnaud DUBOIS Professeur, Institut d'Optique		*Rapporteur*
Cédric BOUZIGUES MCF, Ecole Polytechnique		*Rapporteur*
Serge PICAUD DR, Institut de la Vision		*Examinateur*
Cathie VENTALON CR, ENS		*Examinatrice*
Mathias FINK Professeur, ESPCI Paris - PSL		*Directeur de thèse*
Katharine GRIEVE DR, CHNO des 15-20		*Directrice de thèse*
Claude BOCCARA Professeur, ESPCI Paris - PSL		*Encadrant de thèse*

ESPCI ★ PARIS | PSL★

A ma tante Béatrice (1964-2021)

How everything began...
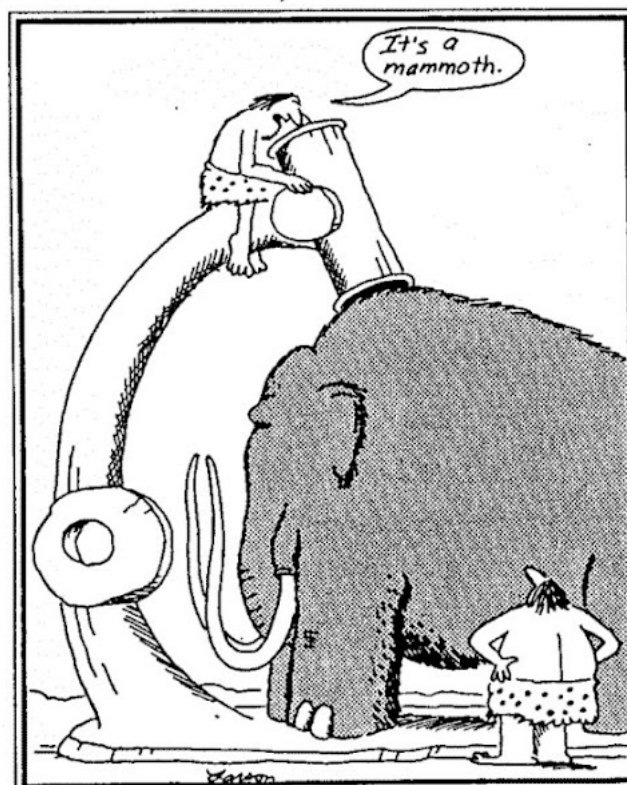
Early microscope

Acknowledgements

First, I would like to thank my thesis directors without whom this thesis would not exist. Thank you **Mathias** for being my director during these three years and for all your advice and fruitful discussion on Physics. I know we did not see each other a lot during these three years, but every meeting was full of ideas and perspectives that really helped me in my experiments and preparation of my defense. **Claude** thank you for all our discussions on optics and biology. I will always remember that you are the only one in the lab excited to talk about biology in the lab with me. Thank you for all your questions that helped me better understand what I was doing. Thank you for always encouraging me to present MY work and my abilities and be confident about it. Don't worry, if there is a need to build a new FFOCT, I will always be there. Also, it is because of you that I did a thesis because you gave me your love for research. **Kate**, I don't know where to begin... I think you are the most amazing director/advisor a PhD student can dream of. You were always here for discussion, help and advice. You were always there to unblock the situations. You are the foundation of the Paris Eye Imaging group and help us work together and understand each others, especially with the biologists. Thank you for all you communication skills for the conferences, especially for the oral presentations. Thank you for your constant amazement about my results and their connection to the *in vivo* cases. You were my mentor and my model during this thesis.

A big thank you to the **FFOCT team (Slava, Pedro, Léo** (not really a FFOCT team member but you were with us in the conferences)**, Paul, Jules, Yao, Ulysse, Tual, Salvatore)** for our discussion but especially for the amazing conferences we did together. Thank you **Jules** for your support and advice at the beginning of my thesis. I will never thank you enough for your expertise in computers. You are welcome for my expertise in Optics and biology (I cover your back for all the dead samples you left behind)... Thank you also for the conferences we did together. Thank you for the amazing lies about our hikes in Canada and United States, the landscapes were great but my knees really suffered because of you (and no, 8km with no elevation gain is not the same as 18km with a 800m elevation gain...).

Thank you to all the members of my **office R32**: **Matthieu, Vincent, Claire, Caroline, Loubnan, Maximilian, Clément, Zofia, Eve, Léo**. Special thank to the best coworkers **Margaux & Romain**: I will never forget our laughter moments and our elephant origamis. Thank you **Romain** for your support in the last months of my thesis and for all the plants you grow in the office.

I also thank all **Langevin Institute** for your welcome and help during these three years, especially **Louis, Clothilde, François, Noet, William, Jeanne, Alexandre, Chloë, Joris, Maxime**. Special thank to **Julie**, **Antoine** and **Cécile** for being my friends during this thesis, I hope we will see each other soon!

I could not forget to mention the **Paris Eye Imaging group** and its (hundreds of) members! Thank you **Marie, Anna, Leyna, Nate, Léa, Serge, Michel** for your advice and help! I learned lots of things thanks to the Tuesday seminars!

I would like to thank some members of the **Vision Institute** who provided lots of samples and advice: **Sacha Reichman, Olivier Goureau, Valérie Forster, Manon**

Contents

Abbreviations

- 1D, 2D, 3D: 1, 2, 3 dimensions

- AMD: Age-related Macular Degeneration

- D-FFOCT: Dynamic Full-Field OCT

- FD: Fourier Domain

- FFOCT: Full-Field OCT

- HSV: Hue Saturation Value

- NA: Numerical Aperture

- OCT: Optical Coherence Tomography

- RGB: Red Green Blue

- RPE: Retinal Pigment Epithelium

- SD: Spectral Domain

- SNR: Signal to Noise Ratio

- SS: Swept Source

- TD: Time Domain

- u.a.: arbitrary unit

- US: Ultrasound

Introduction

The eye is an easily accessible sample of the human body as it is transparent. Over the last decades, multiple techniques have been implemented to study the human eye in different ways.

The easiest way is to study *ex vivo* eyes, extracted from different species such as human, pig, monkey, mouse, etc. To study fresh tissue, the Institut de la Vision can image human tissue donated by the Surgery School or purchased from eye banks, or animal tissue from animal models or waste tissue from other experiments. To study fixed tissue, eyes can be purchased with specific pathologies from eye banks in the US, or fixed tissue can be imaged from their own animal models for example.

An other possibility is to use *in vitro* samples, meaning cell cultures. The first cell culture method was developed in the 19th century by Wilhelm Roux [1]. Cell culture has evolved over the centuries and is now inherent to biology. Nowadays, it is possible to grow cells in 2D to study certain types of cells such as a specific layer of the retina (e.g. Retinal Pigment Epithelium). However, 2D cell cultures do not exactly reflect what is observable *in vivo* [2, 3], especially for the understanding of specific structures such as tumors. Tumors grow in 3D because cells do not receive signals for the stopping of proliferation. This is why 3D cell cultures called spheroids were invented to mimic tumor behaviours [4]. Biologists still needed *in vitro* samples which would be able to mimic a complete organ, with similar function as well as structural similarity [5]. In order to grow this kind of sample, cells must differentiate to create a 3D structure similar to an organ, which is called organoid. For this purpose, the ideal would be to use stem cells (meaning embryonic cells), which can then differentiate. However, ethical problems lead Takahashi et al. to find an alternative: reprogramming cells to induce them in pluripotent stem cells [6, 7]. Pluripotent stem cells are more specific than embryonic stem cells, meaning they can only differentiate in a certain category of organs. Different protocols have been developped over the years to generate this type of cells [8, 9]. The use of pluripotent stem cells is an easy [10] and very promising technique for biologists to generate *in vitro* samples [11, 12], because of the numerous applications such as disease modeling and drug screening. These kind of samples can now be grown to generate retinal organoids in the Institut de la Vision [13, 14].

The last possibility is to image the sample *in vivo*. The transparency of the cornea and lens provide imaging access to the retina. However, its imaging is not straightforward as the retina is also a transparent organ. For this purpose, multiple non invasive imaging techniques have been developed, here are some examples. The first technique was conventional colour fundus photography, but it only reveals blood flow. We had to wait the 1980s to obtain higher resolution and higher contrast with Scanning Laser Ophthalmoscope [15] which allows to visualise the retinal layers hanks to optical sectioning ability. We can also think of Optical Coherence Tomography [16, 17], a scanning technique imaging cross-sections of the retina to visualise the different layers with a better resolution. In 1994, Liang et al. [18] imported the Adaptive Optics technology from Astronomy to eye imaging to correct aberrations of the eye caused by anterior segment (lens, cornea

and tear film), in order to record individual cells with Adaptive Optics Flood-illumination Ophthalmoscope [19]. In 2002, Roorda et al. improved the Scanning Laser Ophthalmoscope which suffers from optical aberrations coming from the cornea and lens for retinal imaging. They developed an Adaptive Optics Scanning Laser Ophthalmoscope [20] which correct the optical aberration to get a higher resolution when imaging individual cells of retinal layers. More recently, a French startup company developed an Adaptive Optics Flood-illumination Retinal Camera [21], allowing to detect and monitor individual photoreceptors, with their first commercial instrument on the market at the beginning of the 2010s.

Usually, *ex vivo* and *in vitro* samples are studied with microscopy techniques. In order to detect specific structures, organelles or proteins, the samples are fixed and labelled in immunohistochemistry, which is an invasive technique. For biological imaging, it was important to find a technique which would be able to characterised samples in a non-invasive way, in order to follow biological behaviours. Optical Coherence Tomography was initially designed for 3D *in vivo* imaging. At the end of the 1990s, an *en face* version was developed by Claude Boccara's team: the Full-Field Optical Coherence Tomography. This technique is suitable either for microscopy imaging (*ex vivo* and *in vitro* samples) or *in vivo* eye imaging.

This manuscript is divided in five chapters. The first chapter presents the interest of studying the human eye. First, the different parts of the human eye are described to understand how it works and how the structures interact. Then, the role of the Retinal Pigment Epithelium, the last layer of the retina which is studied in the fourth chapter, is reported in details. Some retinal diseases are presented, involving either degenerative diseases or environment problems. Finally, I describe the cell cultures samples used in this thesis to mimic the eye.

The second chapter introduces the 3D imaging of biological samples through different techniques. The implementation of OCT is then presented to explain how it was first designed. The three forms of OCT designs are showed and described, with their characteristics. I introduce the *en face* version of OCT: Full-Field OCT. The evolution of the design is discussed with the imaging modalities and characteristics. I finally present the principle of Dynamic Full-Field OCT which is the recording of intra-cellular motion. This chapter introduces then includes the published article Scholler et al., 2019 [22].

The third chapter describes the results we obtained on retinal organoids with my colleague Jules Scholler, PhD student in Institut Langevin during the first two years of my PhD. I present the improvements we made for the acquisitions. The stabilisation of time lapse acquisitions to retrieve the same plane through hours and the computation of images in HSV colorspace for the interpretation of dynamic FFOCT images are described in the first two sections. I finally report the development of proof of concept of dynamic imaging. This chapter introduces then includes the published article Scholler, Groux et al., 2020 [23].

The fourth chapter deals with the use of dynamic FFOCT as a technique to detect cell stress on cell cultures. This chapter introduces then includes the article available on arXiv and currently under peer review Groux et al., 2021 [24]. I first describe the realisation of stress on cell cultures by scratch assays and their study thanks to my SAVE (Scratch Assay Velocity Evolution) Profiler that I developed in Matlab. Then, I present my last progresses in the understanding and validation of the dynamic profile using drugs and immunohistochemistry. To create more repeatable and precise stress on the cell cultures, I developed a new setup with a laser to cut the cell layer. Finally, as real-time imaging

was implemented for the organoids, I present the imaging of microvilli of Retinal Pigment Epithelium in real-time.

The last chapter presents the imaging of *in vivo* retina, a work in collaboration with Pedro Mecê, a post-doctoral student during my PhD at Institut Langevin. I described the different improvements that have been made on the setup with the aim of one day achieving dynamic imaging in vivo. We obtained stabilised acquisitions with a SD-OCT to get rid of movements due to physiological process. We corrected the curvature of the coherence gate of FFOCT to match retinal curvature. We also improved the signal with an adaptive lens placed in front of the patient eye. Finally, I show why the use of dynamic imaging *in vivo* would be a great progress for retinal diseases.

Additional articles on which I was a contributing author, which present the improvements for *in vivo* retinal imaging, are available in the appendix. I also describe my method for a step-by-step design of an FFOCT setup.

Chapter 1

The eye: a window on the whole body

1.1 Structure of the anterior segment

The anterior segment is the front part of the eye, which focuses light onto the retina [25,26]. It is composed of the cornea, the aqueous humour and the lens as shown in Fig.1.1 a.
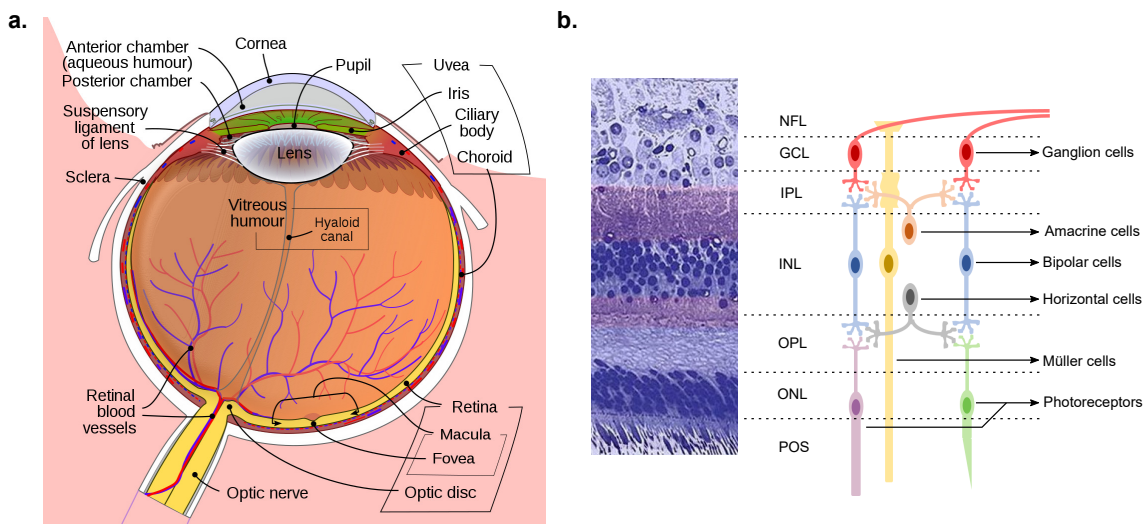
Figure 1.1: **Schematics of the eye and the retina. a.** Schematic of the whole eye. **b.** Schematic of the retinal layers on the right and histology of the retina on the left. NFL: Nerve Fiber Layer. GCL: Ganglion Cell Layer. IPL: Inner Plexiform Layer. INL: Inner Nuclear Layer. OPL: Outer Plexiform Layer. ONL: Outer Nuclear Layer. POS: Photoreceptor Outer Segment.

Cornea The cornea is the first part of the eye, directly in contact with the external environment. It is composed of five different layers, and its principal function is to be transparent to let the light go through to reach the retina. The first layer is the epithelium (composed of several layers of epithelial cells of varying size) which protect the eye from the external environment. The Bowman's layer separates the epithelium from the stroma. The stroma is a very transparent layer, containing keratocytes. Finally the Descemet's membrane separates the stroma from the endothelium (monolayer of cells), which maintains the interface with the aqueous humour in the eye. The cornea presents a curvature, more precisely two different curvatures on each side, participating to the focalisation of light on the retina.

Aqueous humour The Aqueous humour is a viscous substance separating the cornea from the lens. It is mainly composed of water, similar to plasma. It helps to maintain the shape of the eye by maintaining the ocular pressure. It also nourishes the cornea and the lens.

Lens The function of the lens is to focus the light onto the retina. The lens can change its shape to modify the focal length of the eye, in order to focus at different distances, known as accommodation. By changing the size of the pupil, the iris allows the right portion of the light to illuminate the retina through the lens. The lens is involved in cataracts and presbyopia.

1.2 Structure of the vitreous humour, middle chamber of the eye

The vitreous humour constitutes 80% of the whole eye [25, 26]. It is transparent to let the light propagate through it. It helps to maintain the spherical shape of the eye and, by applying pressure on it, to keep the retina in place. With age, the vitreous humour can change, creating some floating elements which create shadows on the retina. Two problems can occur with age blurring the vision: a detachment of the vitreous humour, freeing the pressure on the retina which can lead to the detachment of the retina too, and a haemorrhage tainting the vitreous humour and reducing vision.

1.3 Structure of the posterior eye: the retina

The retina is called the screen of the eye, as it collects the light, which is focused by the anterior segment of the eye. [26–28]

Neural retina The neural retina corresponds to the first layers of the retina, from the nerve fibre layer to the photoreceptor outer segments (Fig.1.1 b.). Just under the nerve fibres are the ganglion cell layer, which are neurons transmitting principally image-formation information to the rest of the retina. Then, there is the inner plexiform layer which make the connection between the ganglion cells and the inner nuclear layer with dendrites, composed of Müller cells, bipolar cells and some Amacrine cells. These cells are connected to the photoreceptor layer by the outer plexiform layer. The photoreceptors are composed of an inner segment (containing the nucleus) and the outer segment. There are two types of photoreceptors: rods and cones. The outer segments are connected to the Retinal Pigment Epithelium.

Retinal Pigment Epithelium The Retinal Pigment Epithelium (RPE) is a monolayer of hexagonal cells separating, on one side, the retina, the light sensitive part of the eye, connected to the RPE by the photoreceptor outer segments (OS), and the blood supply composed of the Bruch's membrane and the choroid, on the other side (Fig.1.2) [29, 30]. The RPE cells contain a basal nucleus, lots of organelles (e.g. endoplasmic reticulum, lysosomes or mitochondria, mainly located in the base of the cell) and melanin granules, which are ovular with a size of 2-3 μm and vertically oriented.

The basal surface of the RPE is connected to the Bruch's membrane. This surface includes invaginations which allows to maximise the surface area for the absorption of nutrients coming from the blood supply.

On the other side of the RPE cells, the apical surface is connected to the retina, more precisely to OS by microvilli [31]. There are two types of microvilli, whose roles are completely different:

- long and thin microvilli, measuring between 5 and 7 μm, maximising the apical plasma membrane, used for the trans-epithelial transport.

- specialised microvilli which grab the OS, also known as photoreceptor sheaths: the rod sheaths, with a cylindrical shape to cover the tip of the OS, and the cone sheaths, with a structure more complex extending further in the inter-photoreceptor matrix to reach the cone OS.
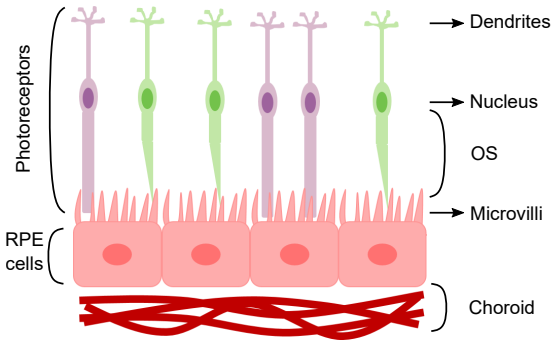
Figure 1.2: Schematic of the RPE layer connections. RPE: Retinal Pigment Epithelium, OS: Outer Segments.

The lateral surface is composed of tight metabolic junctions to create an outer blood-retinal barrier to protect the retina.

Behind the retina: the choroid The choroid contains the vasculature providing nutrients and oxygen supply to the retina and evacuating the waste created by the retina.

1.4 Role of the RPE

The RPE plays different important roles to maintain the integrity of the retina [29, 32].

Light and free radicals protection As the light enters the eye, it is focused on the macula by the lens. This focalisation creates a huge amount of photo-oxidative energy on the retina, creating oxidative damage.On the other side, the RPE is exposed to an overflow of oxygen, coming from the blood supply. For this purpose, the RPE sets up three lines of defense:

- Macular pigment: filtering oxidative wavelength (blue light) and attenuating the intensity of light coming on the RPE

- Melanin: acting like a neutral density filter to attenuate the light power received on the RPE

- Enzymic and non-enzymic antioxidants: neutralising reactive oxygen species

Phagocytosis The concentration of OS is much higher than the concentration of RPE cells: on one RPE cell, almost 45 OS are linked to this unique cell, knowing that the turnover rate for rods is about ten days. This turnover rate is regulated by phagocytosis, which is a degradation mechanism. This phenomenon creates end-products which will be expulsed or recycled in the choroidal capillaries, in the morning (diurnal process induced by light).

Trans-epithelial transport The trans-epithelial transport is happening in two different ways:

- from retina to blood supply: this way allows RPE to relieve all damaging products for the retina.

- from blood supply to retina: this way allows to bring all the material useful for the functioning of the retina.

Transport and storage of retinoid Retinoid is transported from blood. Its main function is to help maintaining the visual cycle (also called visual transduction). The retinoid is then transported through interphotoreceptor matrix binding protein to reach the photoreceptors.

Secretion of growth factors RPE cells secrete lots of different growth factors, e.g. Vascular Endothelial Growth Factor (VEGF) or Fibroblast Growth Factor (FGF). VEGF and FGF are two growth factors mainly known for their role in pathologies, but their roles are essential for normal retina, even if unclear for now. VEGF helps in the vascularisation of the retina. FGF helps in the regulation of apoptosis of cells. These two examples of function are needed in maintaining the global structure of the retina.

1.5   Diseases of the retina and optic neuropathies

AMD Age-related Macular Degeneration (AMD) is characterised by the loss of central vision, while the peripheral vision is still normal [33]. Two types of AMD exist: the dry form and the wet form. For dry AMD, the macula thickness decreases and drusen appear. The dry form represents 80% of people with AMD and there is no treatment yet, but some vitamins and minerals are under study for slowing drusen appearance. Wet AMD corresponds to the growth of abnormal blood vessels under the retina, which cause scars on the macula. This form is really serious as patients lose vision faster than with dry AMD. Wet AMD is treated with anti-VEGF (Vascular Endothelial Growth Factor) drugs to limit the new blood vessels.

Retinal detachment As its name indicates, this disease corresponds to a detachment of the retina (all layers) from the back of the eye [34]. When the retina is detached, it can not work and the vision becomes blurry, it is a serious problem that has to be checked immediately in order to not lose sight.

Epiretinal membrane Epiretinal membrane is the appearance of a semi-translucent thin layer of fibrous tissue on the internal limiting membrane [35]. Most of the patients are asymptomatic but the epiretinal membrane can induce problems of vision (blurred for example). It is a common surgery target.

Macular hole A macular hole is when a tear or a hole is forming in the macula, beginning with a blurry central vision which then can lead to a dark or blind spot in central vision [36]. Peripheral vision is not affected. The main cause is age of the vitreous which pulls away but sometimes detaches the macula also. The treatment is surgical with a vitrectomy.

Macular edema   Macular edema is caused by leaking of fluids in the retina creating an edema under the macula [37]. The symptoms are blurred vision and washed colors. There are many eye diseases and conditions causing macular edema. That is why the treatment is usually to treat the underlying cause of the edema.

Retinoblastoma   Retinoblastoma is a cancer of the eye which first occurs in the retina [38]. It is characterised by a non-regulated growth of the nerve fiber layer, which eventually creates a tumor. This creates a reflection of the light by the retina: the dark pupil appears white. The majority of the patients with retinoblastoma are children, and is usually an inherited disease. The treatments are usual cancer treatments: chemotherapy, radiation therapy and laser surgery, to recover loss of vision and avoid cancer spreading.

Retinitis pigmentosa   Retinitis Pigmentosa is characterised by changes in retina properties: the response to light is different, making the vision difficult for patients [39]. This disease is a genetic condition, which can be caused by over 100 different genes making it difficult to treat. It is characterised by a degeneration of the photoreceptors and the RPE. In lots of cases, there is a hyper-pigmentation of the peripheral retina (corresponding to cell death) and the blood vessels become thinner.

Diabetic retinopathy   Diabetic retinopathy is a disease resulting from diabetes. The high blood sugar causes the damaging of blood vessels of the retina [40]. There are two types of diabetic retinopathy depending on the stage of the disease. The early stage is called non-proliferative diabetic retinopathy, whose main symptom is a blurred vision. Leaking of blood vessels can occur creating macular edema, or some blood vessels will close due to exudates stopping the vascularization of the macula. The advanced stage is called proliferative diabetic retinopathy, which is a more severe stage leading to blindness by loss of central and peripheral visions. In this case there is a neovascularization (non-regulated growth of new very fragile blood vessels in the retina), which creates scars and leaks in the retina, leading to a detached retina. Treatments are focused on blood sugar regulation (especially for non-proliferative case), and regular anti-VEGF injections in the eye for the more severe cases and laser surgery for leaking.

Usher syndrome   The Usher syndrome is a genetic conditions which affects vision and hearing [41]. This genetic condition occurs as Retinitis Pigmentosa for the vision (degeneration). There are no treatments neither for Usher syndrome nor Retinitis Pigmentosa.

Glaucoma   Glaucoma is a pathology affecting the optic nerve due to high pressure in the eye, caused by an excess of aqueous humor [42]. This pathology leads to blindness. In the eye, the aqueous humor is continuously produced and the drained out by the drainage angle. However, sometimes the drainage angle does not work correctly, increasing the amount of aqueous humor in the eye and so the pressure. This excessive pressure damages the optic nerve fibres, creating blind spots in vision, progressively leading to blindness. There are two types of glaucoma. The most common one is primary open-angle glaucoma, caused by an incomplete drainage. This form is painless and progressive. The angle-closure glaucoma is characterised by a blocking of the drainage angle by the iris. In this case, there is a quick eye pressure increase which leads to blindness if not treated right away. It is called an acute attack, with different symptoms: pain, blurry vision in one go, nausea,etc.). The only way to control glaucoma is to control eye pressure with eye drops, lowering the pressure and slowing down the evolution of the pathology. Surgery can also be considered in some cases.

Optic neuritis   Optic neuritis is a pathology in which the optic nerve is swollen [43], leading to blurry vision and alteration of colours. It also causes pain in the back socket of the eye, especially when the eye is moving. Optic neuritis patients are not always under medication. For some of them, corticosteroids are used to improve vision and manage symptoms. Some forms of optic neuritis can be associated to multiple sclerosis.

1.6   Recreating retinal samples with cell cultures

Lots of the retinal diseases listed above are not entirely understood and treatable. It is a crucial need to be able to study the retina and its diseases in an easy and repeatable way. It is also important to perform drug screening to find treatments which can one day be implemented *in vivo*. This is possible with cell cultures, which can be kept in culture over weeks, contrary to retinal explants.

2D cell cultures can recreate a specific layer of the retina such as RPE or photoreceptor outer segments. The easiest way to produce these RPE cell cultures is to use primary cells. To do so, eyes are dissected to extract retinal explants and separate the RPE cells, which are then purified in a suspension. Finally, the cells are plated on a support (Petri dish, glass coverslip or membranes) and allowed to grow in an incubator.

3D cell cultures, also known as organoids, allow biologists to recreate a complete retina with the different layers, organised in a sphere. These organoids and 2D RPE cell cultures can be produced from reprogrammed pluripotent stem cells. This technique was first demonstrated by our collaborators from the Institut de la Vision. When a human embryo is growing, the first step in the development corresponds to stem cells. Then, the stem cells differentiate in several types of pluripotent stem cells, which will create the different organs. Technically, skin cells come from the same pluripotent stem cells as the eye, the nerves and the brain. This allows biologists to collect fibroblast cells from skin and reprogrammed them in pluripotent stem cells [13, 14, 44, 45]. Thanks to a special culture medium, these pluripotent stem cells can be differentiated in retinal cells. At the beginning, the organoid is an "embryo" of retina: the cells are not differentiated yet in the different layers. By growing over the days, the organoid generates the retinal layers with the precursors of precursors of photoreceptors inside the sphere. By manipulating genes, retinal diseases can be recreated in the organoids [46], such as Retinitis Pigmentosa.

Drug screening is easily repeatable on these samples, as multiple samples ca, be created at the same time to test different conditions.

Chapter 2

3D imaging of biological samples: from structure to intracellular motion

This chapter is an introduction to OCT-based techniques and their evolution through the years to get a usefull technique for eye imaging, whether *in vivo*, *ex vivo* or *in vitro*.

The article presented in this chapter was a collaboration between several members of the Institut Langevin and the Institut de la Vision. I designed and built the optomechanical setups for Dynamic Full-Field OCT experiments. Jules Scholler (PhD student during the first two years of my PhD) designed and coded the interface which pilots the microscope for acquisitions. We performed the imaging experiments together, in collaboration with biologists from the Institut de la Vision. We each performed data analysis which contributed to the final results.

2.1 From microscopy to OCT

Since the creation of microscopy, there is a crucial need to be able to image biological samples in 3D-volumes [47]. On one side, the use of usual microscopes makes it necessary to go through different processes with the biological sample [48]. The classical way to explore a sample in 3D with this technique is histopathology. Etymologically, histopathology is the study of tissues microscopically to determine pathological conditions. Histopathology consists in excision of the sample, fixation, embedding, microtoming and finally staining of it. This is an invasive and exogenous method which does not allow to study a living sample. The resolution is determined by the microscope numerical aperture and wavelength. Then, confocal microscopy helped in the 3D imaging of biological samples, as it is possible to image in depth without slicing the sample [49]. But confocal microscopy is still an invasive technique which requires clearing (to go deep inside the sample: through a few hundreds μm) and generally exogenous labels, as confocal microscopy is a fluorescence microscopy technique [50]. On the other side, ultrasound (US) imaging is used *in vivo* as it is non invasive [51]. US imaging sends a sound wave in the sample and record the signal coming back: the wave is reflected differently from the different structures constituting the sample. US can image through a few centimetres in depth with a resolution around 10 to 100 μm.

There was a crucial need to come up with a new technique merging the pros of each two previous techniques introduced. This technique is Optical Coherence Tomography (OCT). It allies the non invasive 3D imaging of US and the resolution of microscopy, as shown in Fig. 2.1.
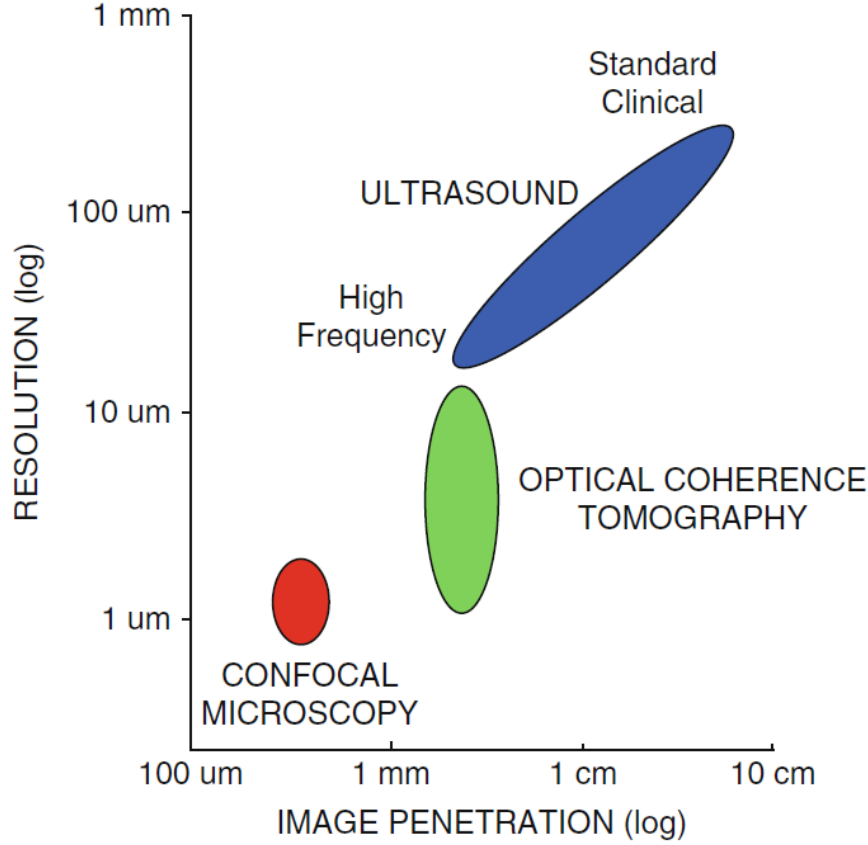
Figure 2.1: **Resolution and penetration of imaging techniques.** Adapted from Drexler and Fujimoto [52].

2.2 OCT technique: inspired by light microscopy and ultrasound

2.2.1 What is OCT?

OCT is a light-based technique: a light wave is sent through the sample and the backscattered light (from the different structures of the sample) is recorded, by looking at the magnitude and the echo time delay of this recorded signal [52]. OCT allies high-resolution (between 1 and 15 μm depending on the configuration of the system), cross-sectional (such as US) and 3D volumetric (transverse scanning) imaging. OCT reveals the structure of a biological tissue at a microscopic level, *in situ* and *in real time*. As biological samples are composed of scattering media, the light and the backscattered light are attenuated along their path through the biological tissue, giving almost 2 mm imaging depth. OCT is integrable into many different medical devices. The use of OCT was first demonstrated by Fercher et al. in 1988 [53], and then with *ex vivo* samples by Huang et al. in 1991 [54]. The first *in*
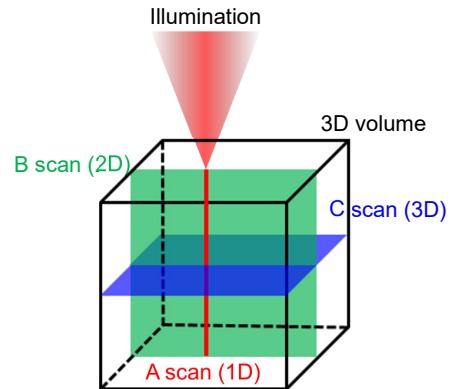
Figure 2.2: Different modalities of scanning in OCT

vivo retinal images were obtained in 1993 by two teams [16, 17], independently.

OCT is based on low coherence interferometry (Michelson interferometry). The light is sent on a beam-splitter, dividing the beam in two. One part goes in the refrence arm and is reflected by a mirror, the other part goes in the sample arm and is reflected by the multiple microstructures of the sample. These two parts are then recombined by the beam-splitter and then focused on a detector. Borrowing from the terminology of US, different images are obtained (Fig. 2.2): A scans, corresponding to a line in depth (1D image), B scans, corresponding to scanning the sample laterally with A scans creating a 2D image, and finally C scans which is an *en face* cross-section. By scanning the whole sample with B scans or C scans, 3D volumes can be recreated.

2.2.2   OCT systems

Two types of OCT systems exist: Time Domain OCT (TDOCT) and Fourier Domain OCT (FDOCT) [52]. TDOCT (Fig. 2.3 **a.**) is based on the temporal study of the signal: the reference arm has to be adjusted to scan the sample in depth (A scan), the scanning mirrors in the sample arm help then to acquire B scans ans C scans. This scanning implies that the signals recorded by the photodetector correspond to different points of the sample and are recorded separately. FDOCT is based on the frequential study of the signal, meaning different frequencies are recorded, corresponding to different depths of the sample. This category is divided into two sub-categories: Swept Source FDOCT (SS-FDOCT or SSOCT) and Spectral Domain FDOCT (SD-FDOCT or SDOCT). SSOCT (Fig. 2.3 **b.**) uses a Swept Source Laser, allowing to tune the delivered wavelength. Each wavelength will focus at a different depth of the sample. These wavelengths will be recorded successively on the photodetector, creating an A scan. This allows to have a fixed reference, as the sample is scanned in depth by the wavelengths. The scanning mirrors of the sample arm create B scans and C scans. SDOCT (Fig. 2.3 **c.**) is composed of a broad-band laser. The laser sends a broad-band beam on the sample: the different wavelengths will focus at different depths at the same time on the sample. To discriminate the different signals (coming from different layers), a grating is used to separate the wavelengths which focus on a linear detector. There is no longer any need to scan either the reference arm or the wavelengths of the light source to obtain an A scan. B scans and C scans are created with the scanning mirrors as previously shown. This technique is faster than TDOCT and SSOCT because A scans are obtained in one shot, although penetration depth is reduced in comparison to SSOCT as sampling is limited by the number of pixels in the spectrometric detection. OCT systems have been improved over the years, with an improvement of the resolution by the choice of the light source and an improvement of the imaging speed with the evolution of the electronics (detectors and scanning mirrors).

2.2.3   OCT characteristics

OCT can be characterised by its transverse resolution and its axial resolution. The transverse resolution depends on the characteristics of the objective lens placed in the sample arm. The axial resolution is controlled by the coherence length of the light source.

$$\Delta x = \frac{4\lambda}{\pi}\frac{f}{d} \propto \frac{2\lambda}{\pi NA} \tag{2.1a}$$

$$\Delta z = 2\frac{ln2}{\pi}\frac{\lambda^2}{\Delta\lambda} \tag{2.1b}$$

where f is the focal length of the objective lens and d is the diameter of the incident beam on the objective lens (eq. 2.1a), and $\Delta\lambda$ is the bandwidth of the light source (eq. 2.1b).
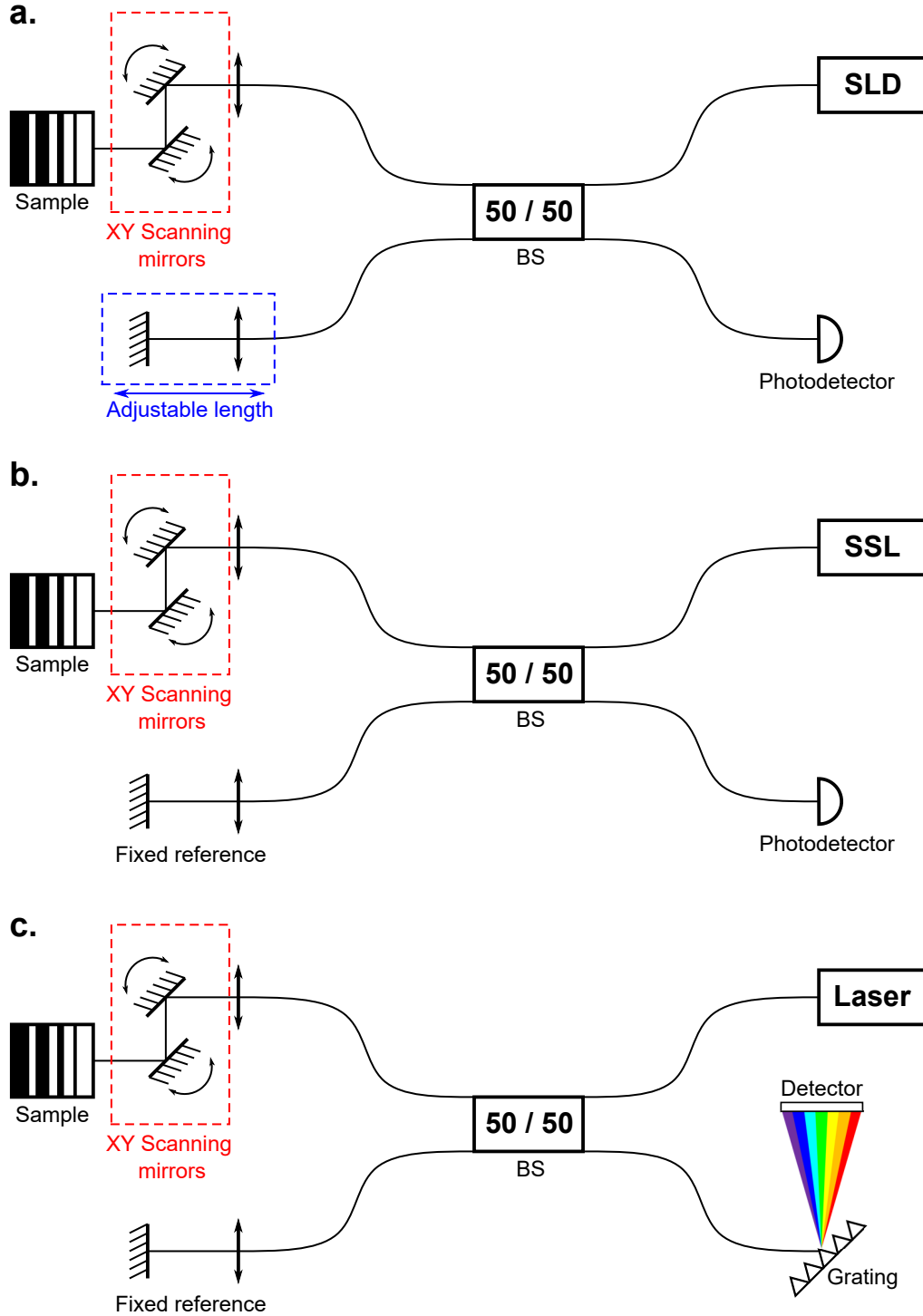
Figure 2.3: **Different OCT systems. a.** Time Domain OCT. BS: Beam-splitter. SLD: Super Luminescent Diode (broad-band light source). Scanning mirrors of the sample arm allows to scan the sample in 2D (B scan), while the length of the reference arm can be adjusted to focus at different depths of the sample (Z-scanning). **b.** & **c.** Fourier Domain OCT. **b.** Swept Source FDOCT. SSL: Swept Source Laser (tunable wavelength), which replace the Z-scanning of TDOCT, allowing a fixed reference. **c.** Spectral Domain FDOCT. Broad-band laser in order to have different wavelengths focusing at different depths in the sample at the same time. The different wavelengths are then separated with a grating focusing on a linear detector (A scan in one shot).

$l_c = \frac{\lambda^2}{\Delta\lambda}$ represents the coherence length of the light source. The depth of field is also an important parameter, which corresponds to the thickness of the imaged layer:

$$b = \frac{\pi\Delta x^2}{\lambda} \tag{2.2}$$

b is also called the confocal parameter.

OCT is also a compromise depending on the lenses used in the sample and reference arms. If the lens has a low NA, the system has a low transverse resolution but a high depth of field, $b > l_c$. On the contrary, if it has a high NA, the system has a high transverse resolution but a low depth of field, $b < l_c$.

The intensity recorded on the detector is :

$$I_0 \sim |E_r|^2 + |E_s|^2 + 2.E_r.E_s.cos(2k\Delta l) \tag{2.3}$$

where Δl is the path length difference between the two arms.

2.3   Full-Field OCT: *en face* version of OCT

Full-Field OCT (FFOCT) had been introduced in 1998 by the team of Claude Boccara [55]. The interest was to create an alternative of OCT to be able to image *en face in vivo* with high-speed instruments. OCT, as a scanning technique, obtains low resolution (10 to 30 μm) in the Y direction while XZ images (B scans) are characterised by high resolution. FFOCT is a parallel version of OCT, allowing to acquire images at a given depth without the need of scanning. This version is also called Optical Coherence Microscopy (OCM). This is possible thanks to a 2D camera and air or immersed objectives in each arm. The immersion medium helps the possibility of imaging deep in the sample (over several hundreds of μm) (greater than confocal microscopy), but also to get rid of unwanted reflections that can be obtained at interfaces.

In this paper, the system had a lateral resolution of 2 μm (which is dependent on the optics and the camera pixel size), and an axial sectioning ability of 8 μm, corresponding to $\frac{l_c}{2n}$ with l_c the coherence length of the light source and n the refractive index of the medium. The total-field-of-view was 500 μm x 500 μm with a detection shot-noise limited. To obtain images, the reference mirror is placed at a zero-path-difference with the sample. To record the coherent light backscattered only coming from the focal plane, a lock-in detection scheme was used. This technique is called 4 phases imaging. A phase shift of alternatively 0, $\frac{\pi}{2}$, π and $\frac{3\pi}{2}$ is applied between the two arms to finally record a signal $\propto Acos(\frac{2\pi\delta}{\lambda})$ and $Asin(\frac{2\pi\delta}{\lambda})$, where A is the amplitude of the coherent backscattered light and δ the average optical path difference between the two arms. A faster technique is 2 phase imaging (phase shift of 0 and π), but the recorded signal is $\propto Acos(\frac{2\pi\delta}{\lambda})$ only, making impossible to distinguish phase from amplitude, despite the fact that the absolute value of the signal can give an estimate of A.
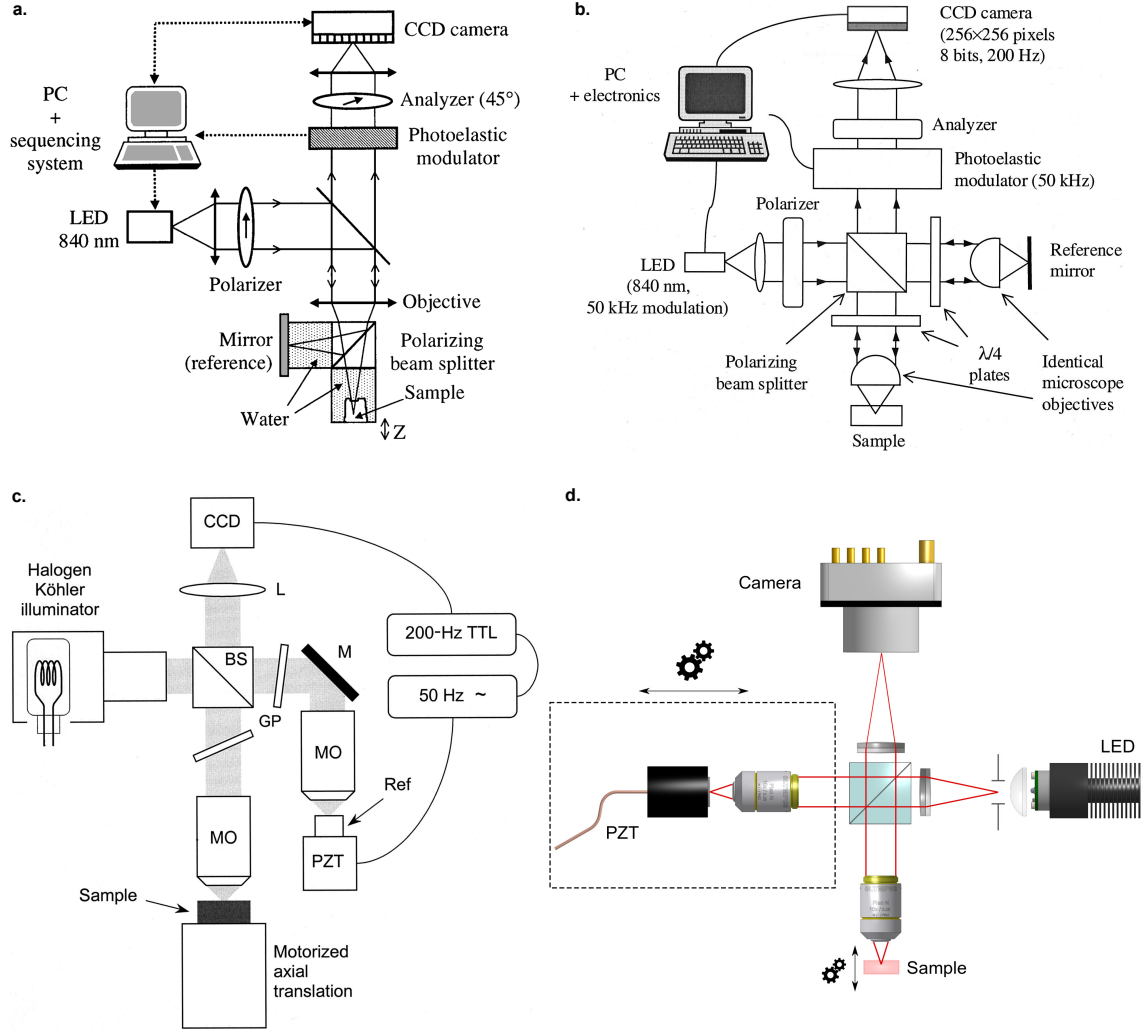
Figure 2.4: **Evolution of the FFOCT systems from 1998 to today. a.** 1998 [55].
b. 2002 [56]. **c.** 2004 [57]. **d.** today

In 2002, a new configuration of FFOCT, based on a Linnik interferometer, was introduced by Dubois et al. [56]. A Linnik interferometer is a version of a Michelson interferometer where identical microscope objectives are introduced in each arm (reference and sample arms). The axial resolution is given by eq. 2.4a. It had been shown that the axial resolution (for quite large coherence length of the source) is dependent on the NA of the objectives (eq. 2.4). For a low NA (eq. 2.4b), the axial resolution is proportional to the coherence length of the light source, while for a high NA (eq. 2.4c), it depends on the depth of field of the objectives. The FFOCT system is also equipped with an incoherent light source (a LED). On one side the short coherence length allows to enhance background rejection during the imaging of scattering media by reducing the width of the interferogram. On the other side, spatial incoherence reduces the speckle formation in images. The transverse resolution is governed by the numerical aperture and the wavelength of the illumination source (eq. 2.5).

$$\Delta z = \frac{1}{\sqrt{\left(\frac{n\pi}{2ln2l_c}\right)^2 + \left(\frac{NA^2}{n\lambda}\right)^2}} \tag{2.4a}$$

$$\Delta z = \frac{l_c}{2n\sqrt{(2)}} \tag{2.4b}$$

$$\Delta z = \frac{0,44\lambda}{n(1 - cos(\theta_{max}))} \sim \frac{0,44\lambda}{n(1 - cos(arcsin(\frac{NA}{n})))} \tag{2.4c}$$

$$\Delta r = 0,61 \times \frac{\lambda}{NA} \tag{2.5}$$

In 2004, the FFOCT setup was slightly modified to obtain ultra-high resolution images [57]. The LED was replaced by a Halogen illumination with a larger spectral bandwidth which allows to obtain a higher axial resolution. The polarization optics were replaced by normal optics and the camera was interfaced with the piezo-electric translation of the reference arm.
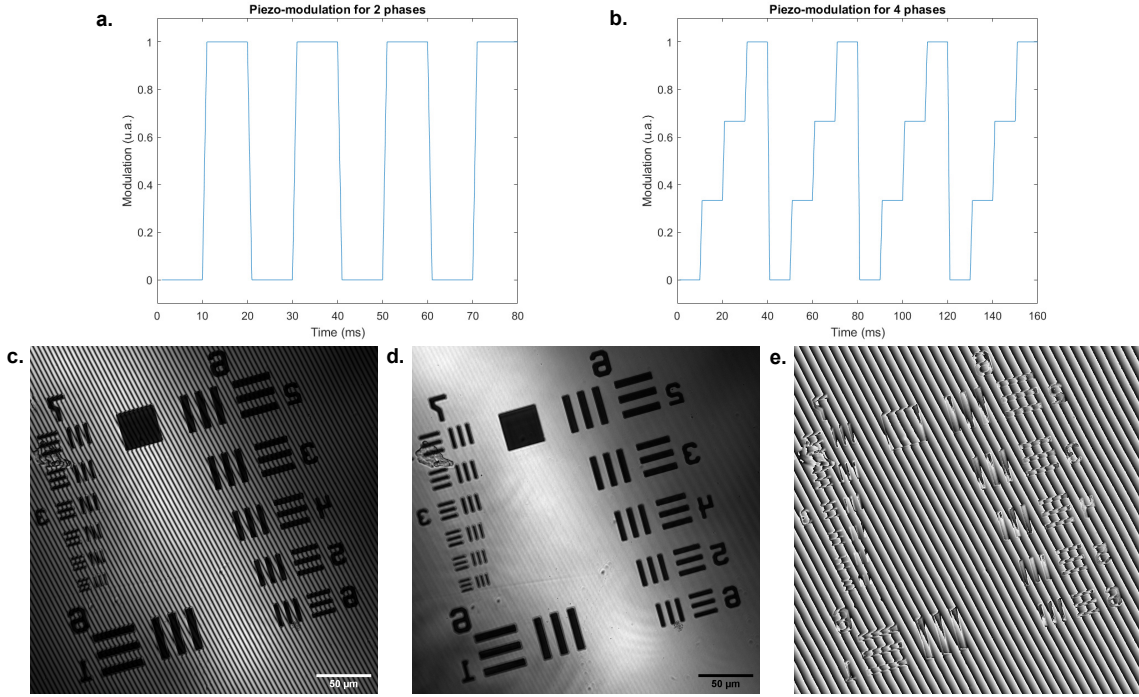
Figure 2.5: **2 phase and 4 phase imaging on a USAF resolution target. a.** Signal sent to the piezoelectric translation (reference arm) for the 2 phase imaging. **b.** Signal sent for the 4 phase imaging. **c.** Image obtained with the 2 phases imaging: amplitude and phase of the signal are mixed. **d.** and **e.** Amplitude and phase images (respectively) obtained with 4 phase imaging: the unmixing is possible.

FFOCT is an interferometric technique, which means the signal of interest (coherent signal) is the light having the same optical path length in each arm. To get rid of the incoherent signal, we perform 2 phase or 4 phase imaging as mentioned above. By modulating the reference mirror as shown in Fig.2.5 a. and b., we can plot FFOCT images. In 2 phase imaging, we record two images with a difference of π in the modulation. By substracting these two images and dividing it by 2 (eq. 2.6a), we obtain a FFOCT image where amplitude and phase are mixed Fig.2.5 c. In 4 phase imaging, four images, with a phase shift of

$\frac{\pi}{2}$ between two images, are recorded. After calculation, we can plot amplitude (eq. 2.6b) and phase (eq. 2.6c) separately in Fig.2.5 d. and e.

$$A\cos(\Delta\phi) = \frac{I_1 - I_2}{2} \tag{2.6a}$$

$$A = \frac{1}{2}\sqrt{(I_1 - I_3)^2 + (I_2 - I_4)^2} \tag{2.6b}$$

$$\Delta\phi = \arctan(\frac{I_2 - I_4}{I_1 - I_3}) \tag{2.6c}$$

Alternatives to the conventional FFOCT have been developed over the years such as polarization-sensitive FFOCT [58], single-objective FFOCT [59], or Fourier-Domain FFOCT for *in vivo* eye imaging [60, 61].

Moreover, FFOCT is a suitable technique for multiple applications on biological tissues [62–66].

2.4   Dynamic Full-Field OCT: from structure to intracellular motion

FFOCT, as every OCT-based technique, reveals the structure of the sample imaged. More recently, a novel type of contrast has been discovered using FFOCT that reveals more details inside the sample in Apelian et al., 2016 [67]. This contrast is based on the time variations which happen in a living biological sample. These variations are produced by the movements of organelles present in the cells. These variations are very weak: they come from organelles which are of approximately the micrometer size. Typically, the light coming back from these variations in the FFOCT setup are around 1 photon over a million of photons approximately. Because of this, the camera needs to be able to record such weak signal. That is why we use a custom Adimec camera, which has a Full Well Capacity of 2 million electrons, allowing to record the dynamic signal. The camera is used near its saturation to be able to record the signal photons.
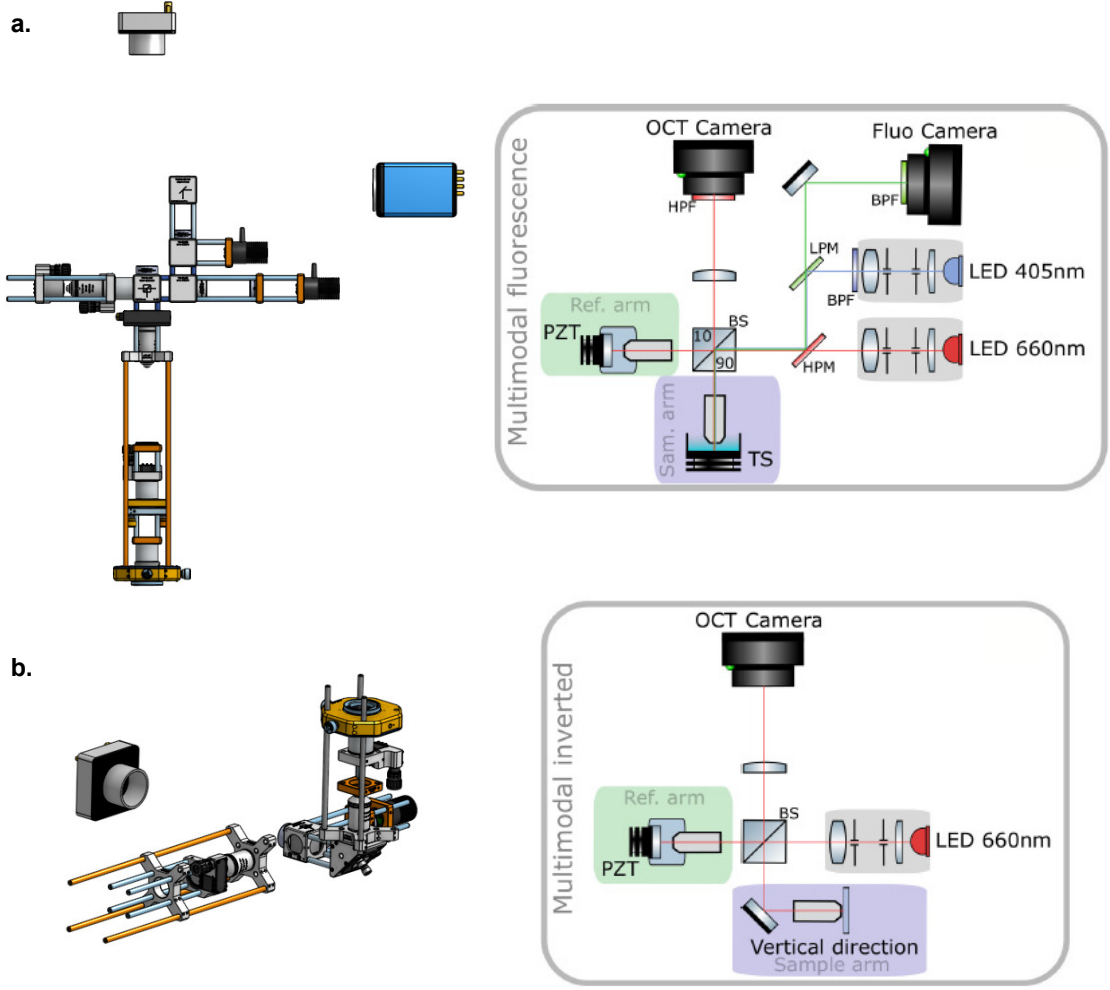
Figure 2.6: **Setups for D-FFOCT imaging. a.** Setup for cell cultures (water-immersion microscope objectives): 3D rendering (left) and schematic (right, from Scholler et al., 2019 [22]). **b.** "Inverted" setup for *ex vivo* samples (oil-immersion microscope objectives): 3D rendering (left) and schematic (right, from Scholler et al., 2019 [22]).

To record these variations, several hundreds of images are recorded at 100Hz without the use of the piezoelectric translation. Different signal profiles come from the different parts of the image. The study of the evolution of these profiles enables the creation of a D-FFOCT image. To obtain a rapid profile of a D-FFOCT image, we perform a Standard Deviation on substacks which are then averaged to give a grayscale D-FFOCT image. If we want to obtain a colored image, meaning a 3D image, we need to make more calculations in order to put some information in each of the three channels. In this case, after acquiring these images, a Fourier Transform analysis is used to determine the different frequencies composing the time variations of the sample. The final image is computed in the RGB colorspace: the blue channel will code for the low frequencies from 0.1 to 0.5 Hz, the green channel from 0.5 to 5 Hz, and finally the red channel for frequencies above 5 Hz [68,69].

As the dynamic signal is really weak, it is important to have a stable sample in order to not blur the dynamic signal with vibrations of the sample. For this purpose, I proposed two different setups which are designed for different types of samples [22]. For cell culture samples (2D and 3D cell cultures) which need to be kept in culture media, water-immersion microscope objectives are used (Fig.2.6 a.). The objectives are directly immersed in the Petri dish where the sample is kept in CO_2 independent culture medium. For *ex vivo*

samples, I created an "inverted" setup with oil-immersion microscope objectives, where the sample arm is pointing up to let the sample settle on a coverslip for the imaging (Fig.2.6 b.). The sample arm is composed of the objective pointing up, where a coverslip in a 30mm cage plate is left. The connexion between the two is made with silicon oil. The sample is just dropped on the coverslip to let it settle.

These setups and the applications performed with them are described in more details in the article below [22].

2.5   Article: "Probing dynamic processes in the eye at multiple spatial and temporal scales with multimodal FFOCT"

Probing dynamic processes in the eye at multiple spatial and temporal scales with multimodal full field OCT

JULES SCHOLLER,[1] VIACHESLAV MAZLIN,[1] OLIVIER THOUVENIN,[1] KASSANDRA GROUX,[1,2] PENG XIAO,[3] JOSÉ-ALAIN SAHEL,[4,5,6] MATHIAS FINK,[1] CLAUDE BOCCARA,[1,2] AND KATE GRIEVE[4,5,*]

[1]*Institut Langevin, ESPCI Paris, CNRS, PSL University, 1 rue Jussieu, 75005 Paris, France*
[2]*LLTech SAS, 29 Rue du Faubourg Saint Jacques, Paris, 75014, France*
[3]*Zhongshan Ophthalmic center, Sun Yat-sen University, Guangzhou, China*
[4]*Vision Institute/CIC 1423, UPMC-Sorbonne Universities, UMR_S 968/INSERM, U968/CNRS, UMR_7210, 17 Rue Moreau, Paris, 75012, France*
[5]*Quinze-Vingts National Eye Hospital, 28 Rue de Charenton, Paris, 75012, France*
[6]*Department of Ophthalmology, University of Pittsburgh School of Medicine, Pittsburgh, PA 15213, USA*
[*]*kategrieve@gmail.com*

Abstract: We describe recent technological progress in multimodal en face full-field optical coherence tomography that has allowed detection of slow and fast dynamic processes in the eye. We show that by combining static, dynamic and fluorescence contrasts we can achieve label-free high-resolution imaging of the retina and anterior eye with temporal resolution from milliseconds to several hours, allowing us to probe biological activity at subcellular scales inside 3D bulk tissue. Our setups combine high lateral resolution over a large field of view with acquisition at several hundreds of frames per second which make it a promising tool for clinical applications and biomedical studies. Its contactless and non-destructive nature is shown to be effective for both following in vitro sample evolution over long periods of time and for imaging of the human eye in vivo.

1. Introduction

Optical coherence tomography (OCT) is used in the biomedical field to image microstructures in tissue using mostly the endogenous backscattering contrast [1, 2]. Full-field optical coherence tomography (FFOCT) is an *en face*, high transverse resolution version of OCT [3, 4]. Using incoherent light sources, two-dimensional detectors and a time-domain phase stepping scheme, FFOCT acquires en face oriented virtual sections of the sample at a given depth and has been used for biology [5], and medicine [6]. Recently, new multimodal techniques, based either on OCT or FFOCT, have enabled the study not only of the static 3D morphology of a sample but also of the dynamics of its scatterers [7, 8] by measuring phase-sensitive temporal fluctuations of the backscattered light. In ex-vivo fresh unfixed tissues, these dynamic techniques reveal subcellular structures that are very weak backscatterers and provide additional contrast based on their intracellular motility [9, 10]. FFOCT multimodal techniques can also detect collective subcellular motion of scatterers resulting from either static deformations or propagating elastic waves for mapping elastic properties or flow of cells in capillaries [11, 12]. Complementary contrast from dynamic and static properties coupled in a multimodal setup with high resolution FFOCT thus enables noninvasive visualization of biological tissue, microstructural, morphological and dynamic properties at the cellular level without the use of exogenous markers. Nevertheless, in order to achieve identification of specific molecular structures, OCT images often need to be compared with fluorescence images or stained histology slides to understand and identify the

27

observed microstructures. Indeed, fluorescence microscopy reveals molecular contrast using dyes or genetically encoded proteins that can be attached to a specific structure of interest and/or monitor changes of the biochemical properties of the tissue. Structured illumination microscopy (SIM) [13–15], a full-field version of confocal microscopy, can perform micrometer scale optical sections in a tissue and has been coupled to static and dynamic FFOCT (D-FFOCT) [16, 17] to allow simultaneous coincident multimodal fluorescence and FFOCT acquisitions.

OCT and FFOCT are often used in tissue to overcome the difficulties linked to scattering induced by small scale refractive index discontinuities, but large-scale discontinuities are also present and induce aberrations that could affect the resolution [18]. Recently, we have demonstrated that low order geometrical aberrations do not affect the point spread function (PSF) but mostly reduce the signal to noise ratio (SNR) when using interferometry with a spatially incoherent source [18, 19]. This allows us to achieve resolution of cone photoreceptors in vivo in the human retina without adaptive optics [19].

In vivo imaging, and detection of in vitro subcellular dynamics, would not have been possible using FFOCT without recent technological advances in detector technology that we will evaluate for static and dynamic FFOCT cases. Although we have developed different multimodal FFOCT-based biomedical imaging applications in oncology [20], embryology, cardiology and ophthalmology [21–23], we will restrict the field of the present paper to new results obtained in ophthalmology. We will discuss the technical issues of sample immobilization for in vitro and ex vivo imaging, along with processing methods that were applied for the first time in FFOCT leading to the first dynamic 3D reconstruction with sub-micron resolution of a macaque retinal explant. An axial sub-micron plane locking procedure is presented to image the same sample plane over several hours in a time-lapse fashion, and applied to image slow wound healing on a macaque cornea. Quantitative methods derived from computer vision were adapted to produce a cell migration map with micrometer resolution. We also introduce a combined posterior/anterior eye imaging setup which in addition to traditional FFOCT imaging offers the possibility to measure the blood flow in the anterior eye that compares favorably to existing techniques [24–26]. Finally, an approach that combines fluorescence labeling for live cells with static and dynamic FFOCT is presented.

2. Methods

Although the principle of OCT is mature and well established, it is still an active area of research where improvements mainly rely on hardware performance. In the case of FFOCT, the camera performance is critical to achieve sufficient single shot sensitivity for imaging 3D biological samples with low reflectivity such as cornea and retina in depth. Recently, a new sensor with an improved full well capacity (FWC) combined with faster electronics allowed faster acquisition with better SNR. The gain in speed is of critical importance when it comes to imaging moving samples, whereas the improvement in SNR is particularly important to image weakly reflective samples in-depth. With the recent development of D-FFOCT, the need for a high FWC camera is even greater as the dynamic fluctuations probed are weaker than the static signals, due to the small size of the moving scatterers. Also the setup stability needs to be studied to ensure that the measured dynamics are in the sample and are not caused by artifactual mechanical vibrations.

2.1. Signal to noise ratio in FFOCT

Two FFOCT modalities were used throughout this work - static images were acquired using a two phase scheme and dynamic images are processed using a stack of direct images - and in both cases the camera is used close to saturation in order to use the whole FWC. For a two phase acquisition, two frames are recorded with a π-shift phase difference. The intensity recorded on a camera pixel is the coherent sum of the reference and sample beams (which contains coherent

and incoherent terms) and can be written:

$$I_{\Phi=0} = \eta\frac{I_0}{4}(R + R_{incoh} + \alpha + 2\sqrt{R\alpha}cos(\Delta\phi)) \tag{1}$$

$$I_{\Phi=\pi} = \eta\frac{I_0}{4}(R + R_{incoh} + \alpha - 2\sqrt{R\alpha}cos(\Delta\phi)) \tag{2}$$

where $I_{\Phi=0}$ is the intensity recorded without phase shift, $I_{\Phi=\pi}$ is the intensity recorded for a π phase shift, η is the camera quantum efficiency, I_0 is the power LED output (we considered a 50/50 beam-splitter), α is the reference mirror reflectivity (i.e. the power reflection coefficient), R is the sample reflectivity (i.e. the power reflection coefficient), $\Delta\phi$ is the phase difference between the reference and sample back-scattered signals, $I_{incoh} = R_{incoh}I_0/4$ is the incoherent light back-scattered by the sample on the camera, mainly due to multiple scattering and specular reflection on the sample surface. The static image is formed by subtracting $I_{\Phi=\pi}$ from $I_{\Phi=0}$ and taking the modulus:

$$I_{2-phase} = \eta I_0\sqrt{R\alpha}|cos(\Delta\phi)| \tag{3}$$

For a 2-phase scheme it is not possible to un-mix amplitude and phase. To get rid of the cosine term we consider that the phase is uniformly distributed (both in time and space) in biological samples and we can average $I_{2-phase}$ with respect to the phase distribution:

$$< I_{FFOCT} > = \eta I_0\sqrt{R\alpha}\frac{1}{2\pi}\int_0^{2\pi}|cos(\Delta\phi)|d\Delta\phi = \frac{2\eta I_0\sqrt{R\alpha}}{\pi} \tag{4}$$

Returning to the recorded intensity I_Φ, the terms related to sample arm reflectivity are negligible compared to the incoherent and reference terms so the intensity corresponding to pixel saturation I_{sat} can be written:

$$I_{sat} \approx \frac{\eta I_0}{4}(\alpha + R_{incoh}) \tag{5}$$

Combining Eq. 4 and Eq. 5 we obtain:

$$< I_{FFOCT} >= \frac{8I_{sat}\sqrt{R\alpha}}{\pi(\alpha + R_{incoh})} \tag{6}$$

If we consider an ideal case when the experiment is shot noise limited, the noise is proportional to $\sqrt{I_{sat}}$, which gives the following signal to noise ratio:

$$SNR_{2-phase} \sim \frac{8\sqrt{R\alpha I_{sat}}}{\pi(\alpha + R_{incoh})} \propto \sqrt{I_{sat}} \tag{7}$$

The SNR is proportional to $\sqrt{I_{sat}}$ and is therefore proportional to the maximal number of photoelectrons that a pixel can generate before saturation, which is the definition of the FWC. Thus the SNR is proportional to the FWC for a 2-phase FFOCT image. D-FFOCT images are computed by taking the temporal standard deviation of the signal, see Section 2.4. We consider that both the local reflectivity and phase can fluctuate. The noise term remains the same, as we also work close to saturation during dynamic acquisitions. The measured intensity can then be written:

$$I_{dynamic} = SD\left(\frac{\eta I_0}{2}\sqrt{R(t)\alpha}cos(\Delta\phi(t))\right) \tag{8}$$

$$= \frac{2I_{sat}}{\alpha + R_{incoh}}SD\left(\sqrt{R(t)\alpha}cos(\Delta\phi(t))\right) \tag{9}$$

29

Where SD is the standard deviation operator. The dynamic SNR can therefore be written:

$$SNR_{dynamic} \sim \frac{2\sqrt{I_{sat}}}{\alpha + R_{incoh}} SD\left(\sqrt{R(t)}\alpha cos(\Delta\phi(t))\right) \propto \sqrt{I_{sat}} \qquad (10)$$

Eq. 10 shows that the camera FWC also limits the SNR in D-FFOCT experiments. One can argue that averaging several FFOCT images could be a workaround for 2-phase images. Considering the case of a weakly reflective sample (e.g. cornea and retina) and a moving sample (e.g. the eye) then one needs to have sufficient signal to perform registration before averaging, therefore SNR on single frames is of great importance and thus all experiments are conducted with the camera working close to saturation.

2.2. Improving signal to noise ratio and speed

The most widely used camera for FFOCT (MV-D1024E-160-CL-12, PhotonFocus, Switzerland) has a 2×10^5 electrons FWC with a maximum framerate of 150 $frame.s^{-1}$ at 1024×1024 pixels. With $\alpha = 0.08$ (as we typically use 4% to 18% reflectivity mirrors) it leads to a 70 dB sensitivity for a 2-phase image reconstruction with 75 processed $images.s^{-1}$. Averaging 100 images with this camera takes just over 1 second and leads to a 90 dB sensitivity. A major recent change in our setups has been the introduction of a new camera, specifically designed for FFOCT requirements (Quartz 2A750, ADIMEC, Netherlands) that has a maximum framerate of 720 $frame.s^{-1}$ at 1440×1440 pixels and a 2×10^6 FWC. With the new camera characteristics, it is possible to achieve 83 dB sensitivity for a 2-phase image reconstruction. Acquiring and averaging 100 images takes under 0.2 second and leads to 103 dB sensitivity. This result brings the SNR of FFOCT and the speed per voxel in *en-face* views up to the typical range of conventional OCT systems, but with a better transverse resolution given by the NA of the objective. Aside from SNR improvement, the second major advantage of this new camera is its acquisition speed. Speed is an important issue for detection of in vitro subcellular dynamics, and crucial to in vivo eye examination. Indeed, in contrast to scanning OCT setups, FFOCT requires the acquisition of a full megapixel image in a single shot, and the signal can be lost if a lateral displacement occurs between two successive images. This typically imposes a minimum acquisition speed higher than 200 $frames.s^{-1}$ as eye motions are mainly below 100 Hz [27, 28], a condition that is easily met by the new camera which offers 720 $frames.s^{-1}$.

2.3. Improving sample stability

Previously described in vitro imaging setups [10, 16] were mounted vertically with the sample placed under the objective and imaged from above, see Fig. 1(a). This setup consists of a Linnik interferometer with an excitation source (M405L3, Thorlabs) for fluorescence imaging and an FFOCT source (M660L3, Thorlabs). Illumination paths are combined and separated using dichroic filters. Both sample and reference arms are mounted on translation stages (X-NA08A25, Zaber Technologies). In addition, the reference mirror is mounted on a piezoelectric translation stage (STr-25, Piezomechanik) for phase-shifting. In this configuration, in order to image fresh ex-vivo samples in immersion, we had to fix them in place using a 3D printed mounting system with transparent membrane covering and gently restraining the sample in order to prevent any movement during imaging. To facilitate imaging of cell cultures that are directly adhered to the base of a dish, and to use gravity to assist immobilization for other tissue samples, we have built a new system in an inverted configuration where the sample is directly placed on a coverslip and imaged from beneath with high-numerical-aperture oil-immersed objectives, see Fig. 1(b). This setup is mounted with the same parts as the previous one, except that it does not feature fluorescence measurement capabilities and is mounted horizontally, with the sample arm mounted vertically. The main advantage is that the sample is held motionless by gravity and is naturally as flattened as possible (thus providing a flat imaging plane) against the coverslip

30

surface without applying compression. Despite these efforts to immobilize the sample, axial drift on the micrometer scale over long periods of time can occur in either configuration. In order to compensate for the axial drift we introduced an automated plane locking procedure based on static FFOCT image correlation around the current position, see Fig. 1(d). FFOCT images are acquired over an axial extent of 10 μm, taking 0.5 μm steps with the sample translation stage, and are then cross-correlated with the target image. The sample is then axially translated to the position corresponding to the maximum of the cross-correlation, which was typically between 0.5-0.8. After each plane correction procedure, a new FFOCT image is taken as target for the next correction in order to account for evolution in the sample position. This procedure was performed every 10 minutes. We observed that for long acquisitions of several hours, the time between autofocus procedures could be increased as we reached a quasi-equilibrium state. Using this procedure we are able to image the same plane in biological samples over a day. The in vivo imaging was performed according to procedures already described in [23] which essentially acquire images in a plane chosen by visual inspection of the live image, and did not include active plane locking.
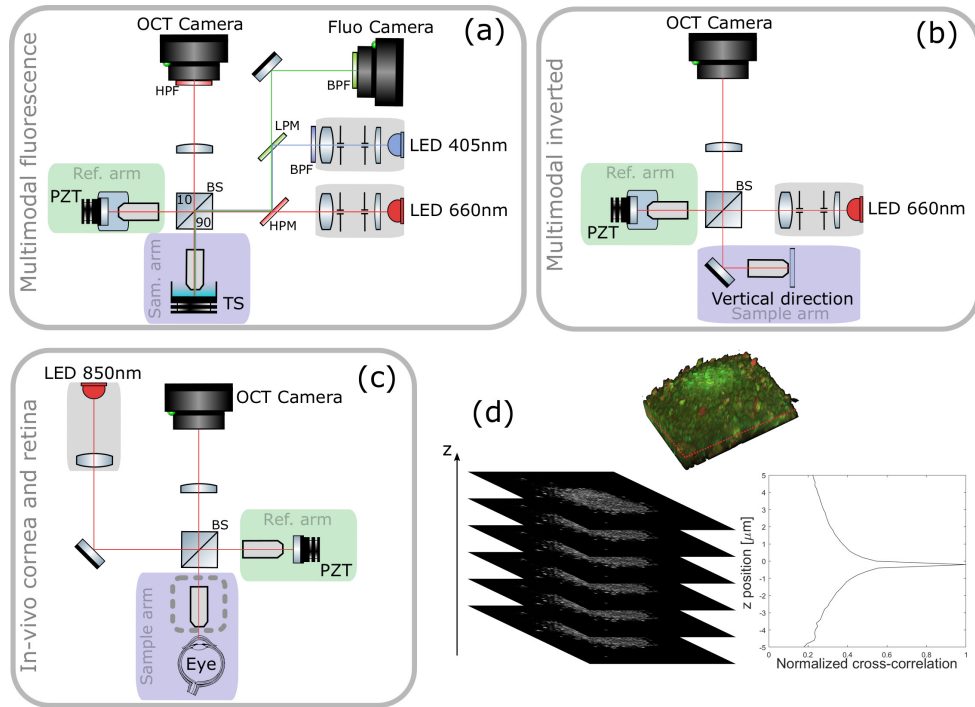
Fig. 1. PZT: piezoelectric translation - TS: translation stage - LPM: low pass dichroic filter - HPM: high pass dichroic filter - (a) Multimodal static and dynamic FFOCT combined with fluorescence *side view*. The camera used for FFOCT in all setups is an ADIMEC Quartz 2A750. The camera used for fluorescence is a PCO Edge 5.5. Microscope objectives are Nikon NIR APO 40x 0.8 NA. (b) Multimodal static and dynamic FFOCT inverted system *top view*. Microscope objectives are Olympus UPlanSApo 30x 1.05 NA. (c) In vivo FFOCT setup for anterior eye imaging (with Olympus 10x 0.3 NA objectives in place) and retinal imaging *top view* (with sample objective removed, at the location indicated by the dashed line box), which is capable of imaging both anterior and posterior eye, in both static mode to image morphology or time-lapse mode to image blood flow. (d) Locking plane procedure. FFOCT images are acquired over an axial extension of 10 *μm* with 0.5 *μm* steps and are then cross-correlated with the target image. The sample is then axially translated to the position corresponding to the maximum of the cross-correlation. This example is illustrated with retinal cells.

Table 1. Setup characteristics.

Setup	Transverse resolution [μm]	Axial resolution [μm]	Field of view [$\mu m \times \mu m$]
Fig. 1(a)	0.5	1.7	320×320
Fig. 1(b)	0.4	1	390×390
Fig. 1(c)	1.7	7.7	1260×1260

32

2.4.　Image computation

FFOCT images presented here are constructed using the 2-phase stepping algorithm. FFOCT images, as well as OCT images, exhibit speckle that is due to the random positions of the back scatterers. In this situation a 2-phase stepping algorithm is enough to recover the FFOCT signal, and moreover 2-phase acquisitions are faster. The method to compute the D-FFOCT images (Fig. 2) is explained in [10] for both grayscale and colored dynamic images. Briefly, grayscale images are constructed from a (N_x, N_y, N_t) tensor, where (N_x, N_y) is the camera sensor dimension and N_t is the number of frames recorded, by using a standard deviation sliding window on the time dimension and then averaged to obtain an image. Colored images are computed in the Fourier domain. The temporal variation of each pixel is Fourier transformed and then integrated between $[0, 0.5]\ Hz$ to form the blue channel, between $[0.5, 5]\ Hz$ to for the green channel and integrated over $5Hz$ for the red channel. The arbitrary selection of which frequencies to assign to which color bands aims to subjectively optimize the visualization in RGB, meaning that color scales are non quantitative. Note that the maximal detectable frequency of the phase fluctuations depends on the acquisition speed and is typically $50\ Hz$ for biological samples (corresponding to the Shannon sampling theorem for an acquisition framerate of $100\ frames.s^{-1}$).

2.5.　Computing and displaying temporal variations in time-lapse sequences

Due to its non-invasive nature, FFOCT can be used to acquire time-lapse sequences at a fixed plane and position over long periods to assess slow dynamics on in-vitro samples, or over short periods in-vivo to assess fast dynamics such as blood flow. This data can be displayed in movie format to visualize movement (Visualization 1, Visualization 2), or can be processed to quantify the movement speed and directionality of target features (Figs 3, 4). There are two main methods to extract quantitative information on motion in image sequences. The first method is solving the optical flow equations. Optical flow is the pattern of apparent motion of objects, surfaces, and edges in a visual scene. The second type of method is to use block-matching algorithms where the underlying supposition behind motion estimation is that the patterns corresponding to objects and background in a frame of video sequence move within the frame to form corresponding objects on the subsequent frame. The former technique is a differential method where a partial differential equation is solved with typical constraints whereas the latter looks to maximize the correlation between blocks of given size between each frame. We tested block-matching methods with phase correlation and normal correlation, as well as differential methods with different regularizers. The one that gave the best result for our corneal wound healing data-set was the Horn–Schunck method [29] which solves the optical flow equations by optimizing a functional with a regularization term expressing the expected smoothness of the flow field. This algorithm is particularly suitable to extract motion on diffeomorphisms which are differentiable maps (i.e. smooth, without crossing displacement fields). Block-matching methods, in addition to being slow for high-resolution images, were failing due to the apparent homogeneity of the intracellular signals requiring blocks of great size, decreasing the accuracy and leading to very long computations. On the contrary, Horn-Shunck regularization considers the image as a whole and provides a regularizing term that controls the expected velocity map smoothness. The optical flow problem consists of solving the following equation:

$$I_x u + I_y v + I_t = 0 \tag{11}$$

where I_x, I_y and I_t are the spatiotemporal image brightness derivatives, and u and v are the horizontal and vertical optical flow, respectively. This is an equation in two unknowns that cannot be solved as such. This is known as the aperture problem. To find the optical flow another set of

33

equations is needed and Horn-Shunck regularization introduces the following functional:

$$\mathcal{L} = \iint \left(I_x u + I_y v + I_t\right)^2 dxdy + \alpha \iint \left\{\left(\frac{\partial u}{\partial x}\right)^2 + \left(\frac{\partial u}{\partial y}\right)^2 + \left(\frac{\partial v}{\partial x}\right)^2 + \left(\frac{\partial v}{\partial y}\right)^2\right\} dxdy \quad (12)$$

where $\frac{\partial v}{\partial x}$ and $\frac{\partial v}{\partial y}$ are the spatial derivatives of the optical velocity v, and the regularizer α scales the global smoothness term. The idea is to minimize the optical flow problem by penalizing flow distortions, where the amount of penalization is controlled by the constant α. This constant gives weight to the right integral term which corresponds to the optical flow Laplacian summed over the whole image, thus containing information on the total flow unsmoothness. The functional is then easily optimized because of its convex nature:

$$[u, v]^T = argmin_{u,v}(\mathcal{L}) \quad (13)$$

For the wound healing migration problem we optimized α by looking at the L_2 error between the velocities computed by the algorithm and 200 manually tracked voxels, see Fig. 3(c). The optimal α was found to be 100.

2.6. Blood flow measurement with FFOCT

For our in vivo blood flow dataset, automated methods based on optical flow failed to extract a velocity map due to the speckle pattern of the images inside vessels. Motion no longer corresponded to a diffeomorphism field, especially locally, leading to a complete divergence of the previous algorithm even with smaller α. Nonetheless we succeeded in extracting a velocity profile inside a vessel using a kymograph plot, i.e. plotting the vessel curvilinear abscissa against time. On such a plot, each event (i.e. a passing particle, such as a blood cell) produces a line, and the slope of this line corresponds to the speed. Using a custom segmentation algorithm, we automatically fit these lines and extracted the speed for each event at a given vessel cross-position. We averaged the speed over the 4 to 18 detected events at each position, and calculated the standard error at each position to evaluate the error in the average speed calculation. Ultimately, the profile can be smoothed and fit to a Poiseuille flow, typically observed in capillaries [30] to extract the maximal velocity v_{max} defined by:

$$v(r) = v_{max}\left(1 - \frac{r^2}{R_{cap}^2}\right) \quad (14)$$

where r is the axial distance to the center of the capillary and R_{cap} is the capillary radius. This fit allows averaging over more than 400 tracked events and reduces the error on the maximal blood flow velocity from $\pm 50 \; \mu m.s^{-1}$ in a single position down to $\pm 15 \; \mu m.s^{-1}$.

2.7. Samples and subjects

All animal manipulation was approved by the Quinze Vingts National Ophthalmology Hospital and regional review board (CPP Ile-de-France V), and was performed in accordance with the ARVO Statement for the Use of Animals in Ophthalmic and Vision Research. Macaque and porcine ocular globes were obtained from a partner research facility and transported to the Vision Institute in CO_2-free neurobasal medium (Thermo Fisher Scientific, Waltham, MA, USA) inside a device that maintained oxygenation, for transport to the laboratory for dissection. We imaged a 2 mm^2 piece of peripheral macaque retina, prepared as described in [10]. Briefly, an incision was made in the sclera to remove the anterior segment. The retina was gently removed from the choroid, with separation occurring at the RPE, and flattened into petals by making

34

four incisions (nasal, temporal, superior, inferior). Pieces approximately 3 mm from the fovea toward the median raphe were selected for imaging. We also imaged a porcine retinal pigment epithelium cell culture, prepared as described in [31]. Briefly, porcine eyes were cleaned from muscle, and incubated during 4 minutes in Pursept-AXpress (Merz Hygiene GmbH, Frankfurt, Germany) for disinfection. The anterior portion was cut along the limbus to remove the cornea, lens and retina. A solution containing 0.25% trypsin-EDTA (Life Technologies, Carlsbad, CA, USA) was introduced for 1 hour at $37°C$ in the eyecup. RPE cells were then gently detached from the Bruch's membrane and resuspended in Dulbecco's Modified Eagle medium (DMEM, Life Technologies) supplemented with 20% Fetal Bovine Serum (FBS, Life Technologies) and 10 $mg.ml^{-1}$ gentamycin (Life Technologies). Cells were allowed to grow in an incubator with a controlled atmosphere at 5% CO_2 and $37°C$. Samples were placed in transwells, and immersed in CO_2-free neurobasal and HEPES (Thermo Fisher Scientific, Waltham, MA, USA) medium for imaging. Fluorescent labeling in RPE cultures used a polyanionic green fluorescent (excitation/emission 495 nm/ 515 nm) calcein dye (LIVE/DEAD® Viability/Cytotoxicity Kit, Thermo Fischer Scientific, France) which is well retained within live cells. For in vitro setups, typical power incident on the sample surface is approximately 0.1mW, though this varies from sample to sample as the power level is adapted to work close to saturation of the camera for each experiment.

Using the new combined anterior/posterior setup (Fig. 1(c)) similar to those described in [19,23], in vivo imaging was performed on a healthy volunteer who expressed his informed consent, and the experimental procedures adhered to the tenets of the Declaration of Helsinki. For in vivo imaging, thorough calculations of light safety according to the appropriate standards are available in [23]. Weighted retinal irradiance of our setup is 49 $mW.cm^{-2}$, corresponding to 7% of the maximum permissible exposure (MPE), and corneal irradiance is 2.6 $W.cm^{-2}$, corresponding to 65% of the MPE, which is further reduced by operating the light source in pulsed mode.

3. Results

3.1. Subcellular contrast enhancement and dynamics detection in retinal explants and cell cultures

FFOCT and D-FFOCT are useful to reveal contrast inside transparent tissue such as retina. We imaged a fresh retinal explant from macaque with the inverted setup shown Fig.1(b). We acquired 100 μm deep FFOCT and D-FFOCT stacks with 1 μm step leading to stacks of 101 en-face images. Fig. 2 shows a 3D volume, en face slices and a reconstructed cross sectional view from this acquisition. Fig. 2(a-e) show the contrast enhancement in D-FFOCT on cellular features in layers such as the inner and outer nuclear and photoreceptor layers. Fig. 2(g) demonstrates the complementarity of static and dynamic FFOCT modes, for example to understand the disposition of nerve fibers and inner plexiform structures (visible in static mode) in relation to ganglion cells (visible in dynamic mode). In comparison to the stack acquisition performed in past setups [10], the improved immobilisation of the sample in the new inverted multimodal setup facilitated automated acquisition of 3D stacks with reliable micrometer steps so that volumetric and cross-sectional representations (Fig. 2(a, b)) may be constructed to improve understanding of retinal cellular organization. The automated plane locking procedure to correct for axial drift means that we are able to repeatedly acquire 3D stacks beginning at the exact same plane, making 3D time-lapse imaging possible and ensuring perfect coincidence of multimodal FFOCT/D-FFOCT stacks. In addition to volumetric imaging through bulk tissue, D-FFOCT can also be used to image 2D cell cultures to monitor culture behavior over time. An en face image of a 2D retinal pigment epithelium cell (RPE) culture (Fig. 2(f)) shows high contrast on cell nuclei and cytoplasm and enables identification of multinucleated cells or cytoplasmic variations from cell to cell. As a result of the improvements in sample stability and time-lapse acquisition offered

by the inverted setup, time-lapse imaging over periods of hours, in conjunction with the fast dynamic signal which creates the D-FFOCT contrast in a single acquisition, can now be reliably performed. This allows us to identify dynamic behavior at various time scales in these in vitro conditions over time. We can therefore follow in vitro cellular decline in situ in explanted tissues, or in vitro cellular development in a growing culture. These capabilities allow understanding of retinal organization and monitoring of cell viability in disease modeling applications or quality control of cultured tissue for graft.
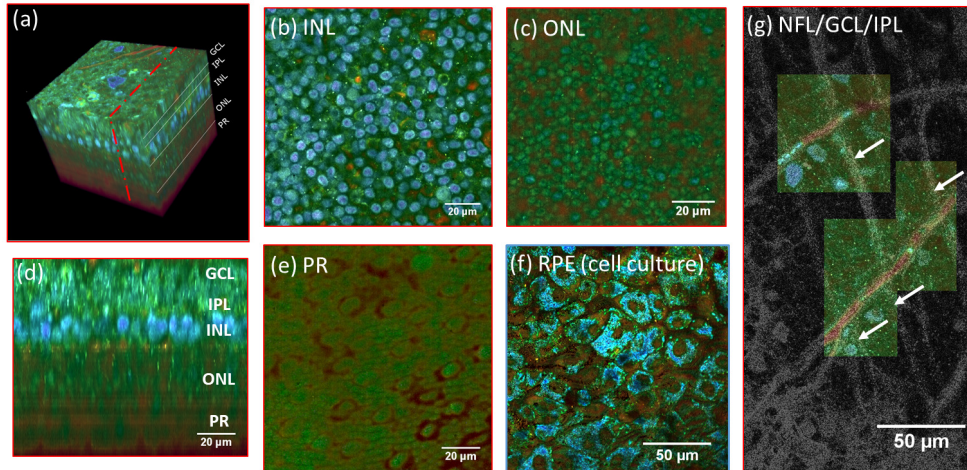

Fig. 2. (a) 3D reconstruction of a D-FFOCT image stack in explanted macaque retina over a 120 by 120 μm field of view. Note that FFOCT signal is damped with increasing penetration depth, so that upper retinal layers are more clearly visible than lower ones. (b, c, e) En-face images of the (b) inner nuclear layer, (c) outer nuclear layer and (e) photoreceptor layer presenting a similar appearance to two-photon fluorescence imaging [32] and (d) reconstructed cross-section at the location represented by the red dotted line in (a). The cross-section in (d) was linearly interpolated to obtain a unitary pixel size ratio. (f) D-FFOCT image of a porcine retinal pigment epithelium cell culture [31]. (g) Overlay of colored D-FFOCT and FFOCT at the interface between the layers of the nerve fibers (white arrows point to nerve bundles that are very bright in static and invisible in dynamic mode), ganglion cells (blue and green cells, visible in dynamic mode) and inner plexiform (fibrous network, bottom left, visible in static mode). Samples were maintained in vitro in culture medium at room temperature during imaging.

3.2. Slow dynamics: corneal wound healing imaging

To demonstrate the potential benefits of time-lapse D-FFOCT we imaged a corneal wound. A macaque cornea was maintained in graft storage conditions, i.e. at room temperature in graft transport medium (CorneaJet, Eurobio, France), during imaging. Epithelium was scraped in a small region of the corneal surface using tweezers, creating a wound in the epithelial layer. The acquired time-lapse sequence in the epithelial layer showed that in addition to revealing epithelial cells and their arrangement, we were also able to detect the slow corneal healing with the migration of cells to fill the wound. We acquired 112 dynamic images in a time-lapse fashion on a wounded macaque cornea with the method and setup introduced in [7], but with the inverse configuration, as described in Section 2.3 above. The acquisition duration was 112 minutes, corresponding to 1 minute between each dynamic image (see Visualization 1). We optimized the grayscale range of the dynamic image by applying a non-local mean filter to remove

the noise while preserving the edges and then averaged 8 images leading to a stack composed of 14 grayscale images. We computed 13 optical flow maps (between each of the 14 frames) and summed them to compute the motion map, see Fig. 3(b). The velocities measured range between $10 - 25$ $\mu m.h^{-1}$ from near the wound center to periphery respectively. In the literature, epithelial cell migration speed in vivo in wound healing is around 50 $\mu m.h^{-1}$ and lower when the wound is starting to close [33]. Our figures are therefore of a similar order of magnitude, although lower, possibly as we were imaging ex-vivo samples at $25°C$ instead of in vivo cornea at $37°C$ and imaged close to an almost closed wound. Indeed, our measured migration rates are closer to those reported for similar in vitro reepithelialization cell migration studies in rabbit ($10 - 16$ $\mu m.h^{-1}$ [34]). Our algorithm was validated by comparing with manual tracking of 200 voxels in cells on successive images. Using the previous errors computation presented in Section 2.5 with $\alpha = 100$ we obtained an accuracy of 2.9 ± 0.6 $\mu m.h^{-1}$.
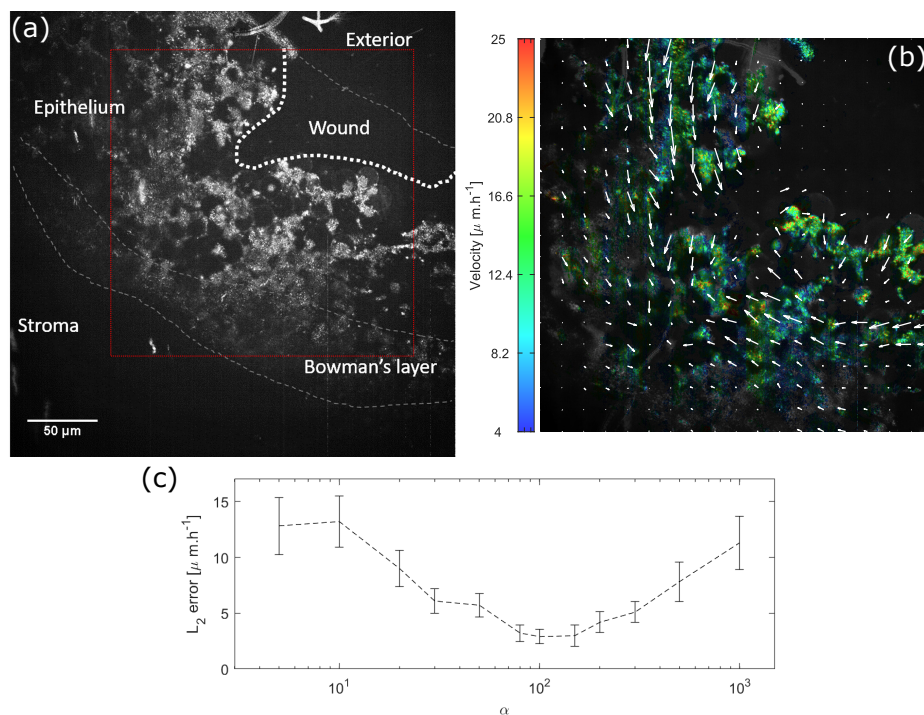
Fig. 3. (a) Dynamic grayscale image of a wounded macaque cornea - the red box shows where the computation is done, see Visualization 1 (b) Same dynamic image superimposed with colors coding for the cell migration velocity averaged over the 112 minute acquisition. Each arrow represents the mean motion in a pixel - (c) Velocity errors for different Horn-Shunk smoothness terms α. The curve represents the mean error we found by comparing the optical flow computation with 200 manually tracked voxels. Error-bars represent the error standard deviation. The optimal α was found to be 100.

3.3. Fast dynamics: blood flow in vivo anterior eye

The fast acquisition speed allows FFOCT to obtain images in vivo and estimate velocities of physiological processes. Fig. 4 and Visualization 2 depict FFOCT images of conjunctival blood flow in the in vivo human eye. Images were obtained using a fast acquisition at 275 $frames.s^{-1}$ [23] followed by template-matching with an ImageJ plugin to remove lateral

misalignment [35, 36]. Flow was quantified using the method described in Section 2.6. The measured flow profile was fitted to a Poiseuille flow profile with good accuracy ($R^2 > 0.95$) and showed a maximal velocity of $600 \pm 15 \mu m.s^{-1}$ (Fig. 4(c)), where both speed and diameter are in agreement with previous experimental findings in the literature, which used slit-lamp microscopy, coupled with a CCD camera [24, 37]. The accuracy of our technique seems to outperform the accuracy we can estimate from other existing techniques to measure blood flow in the eye by about one order of magnitude [24–26].
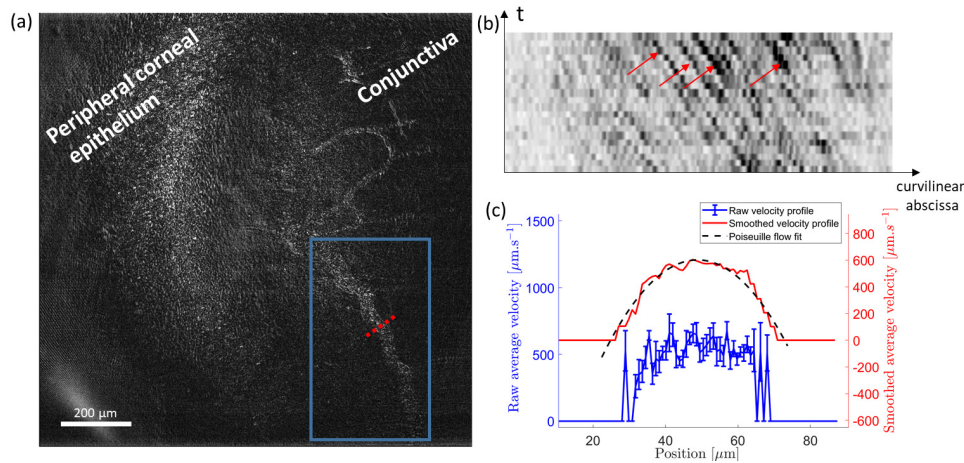

Fig. 4. (a) Single FFOCT-frame of conjunctival blood flow near the limbal region of the in vivo anterior human eye. See Visualization 2 for a movie of blood flow in the drawn box. (b) Kymograph plot (space-time domain) inside the blood vessel at $x = 10 \ \mu m$. Grayscale is inverted so that the black particles indicated by the red arrows are red blood cells flowing into the vessel. The slope corresponds to the particle speed. (c) Raw velocity profile inside the blood vessel (blue) computed along the dotted line in (a) with the method explained in Section 2.6. The standard error is calculated at each position and ranges around 50 $\mu m.s^{-1}$ at the center of the profile and 200 $\mu m.s^{-1}$ on the sides. The smoothed profile (red) with the fit to a Poiseuille flow profile (black dashed line) are superimposed and voluntarily shifted up for increased visibility.

3.4. Towards label free non invasive specific imaging

Multimodal setups that combine fluorescence microscopy and OCT have been developed [38, 39] in order to combine the targeted contrast of fluorescent dyes and antibodies with the structural contrast of OCT. Recently, a multimodal setup (Fig. 1(a)) was proposed to combine static and dynamic FFOCT with fluorescence microscopy [40]. This setup can be used to confirm the FFOCT identity of specific cell types or behaviours via comparison with the fluorescent signal. Simultaneous coincident imaging on a single multimodal setup is vital in order to correctly identify the cells at the pixel to pixel scale and so remove any uncertainty that can occur when imaging one sample on multiple microscopes. To illustrate this validation approach, we labelled living retinal pigment epithelium (RPE) cells in a sparse culture, using calcein dye. The polyanionic dye calcein is well retained within live cells, producing an intense uniform green fluorescence in live cells. We jointly acquired FFOCT, D-FFOCT and fluorescence images of the labeled cells, in order to compare the different modalities within the same plane at precisely the same time. Static FFOCT provided the baseline information about cell presence. The refractive index mismatch between the culture medium and the cells induces light backscattering from cells

measured by FFOCT. Dynamic FFOCT highlights areas where there is motion of back-scatterers (e.g. mitochondria), indicating that the cell metabolism was somewhat active. Fluorescence images showed which cells were alive when we carried out the labelling procedure. The results are shown in Fig. 5 by merging each channel by pairs: (a) merges static FFOCT and dynamic FFOCT, highlighting the active cells over all the cells; (b) merges the static and fluorescently labeled live cells, validating successful labeling as only a subset of cells are fluorescent; (c) merges dynamic FFOCT and fluorescently labeled live cells allowing the comparison between live, dead and dying cell dynamics. As shown in Fig. 5(a-c), we thereby observed 3 different configurations: i) Active cells exhibiting fluorescence indicating that these cells were alive (green in b, c); ii) Inactive cells without fluorescence indicating that these cells were dead (red arrows in Fig. 5(b,c)); iii) Highly active cells without fluorescence suggesting that the cell was dying (white arrows on Fig. 5(a-c)).
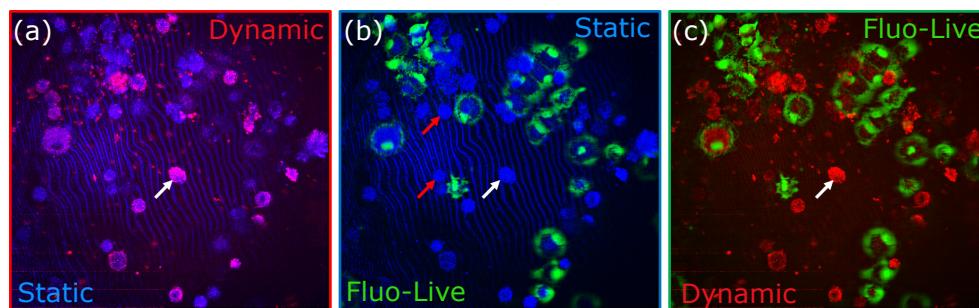

Fig. 5. Multimodal binary merging. Static FFOCT is represented in blue, dynamic FFOCT in red and living labeled cells in green, imaged with the fluorescence setup presented Fig. 1(a). White arrows show active cells without fluorescence suggesting that apoptosis was occuring. Red arrows show inactive cells without fluorescence indicating that these cells were dead.

4. Discussion

Through these examples of multimodal static and dynamic FFOCT images, we have demonstrated the imaging of multiple spatial scales of morphology and temporal scales of dynamic processes in the eye with multimodal FFOCT. However in order for the technique to be adopted by the microscopy and medical communities as true label-free microscopy, validation is required in relation to existing techniques. In addition, further technical improvements could be made with regards to improving efficiency of data management to enable real-time dynamic imaging and improve real-time in vivo image display.

4.1. Towards label free dynamic FFOCT

Using the validation approach of fluorescent labeling in tandem with static and dynamic FFOCT to identify the dynamic signature for specific cell behaviors or types should allow us to achieve reliable true label-free imaging in 3D tissue samples with FFOCT alone. The proof of concept presented in Section 3.4 was a first step toward label free imaging as we only used the dynamic image which is the result of a strong dimension reduction. Indeed, in order to construct an image, we map the dynamic signal over one or three dimensions depending on the desired output (i.e. grayscale or color image). The next step is to consider the full signal in order to train machine learning algorithms to find the optimal signal representation that could distinguish cells based on different criteria, e.g. live, dead and undergoing apoptosis. We hope that by studying the dynamic distribution inside cells it will be possible to extract more information such as cell cycle, cell type, etc. making D-FFOCT a powerful tool for cell biology.

4.2. Towards real time dynamic FFOCT

Currently each dynamic image is computed in approximately 10 seconds on a GPU (NVidia Titan Xp). Most of this time is dedicated to memory management. In the original D-FFOCT configuration [7], images were computed using the CPU so the frame grabber was configured to save data directly on the computer Random Access Memory (RAM). The difficulty for real-time applications is the data transfer bottleneck. Indeed, a GPU can process data only as fast as the data can be transferred to it. In traditional system memory models, each device has access only to its own memory so that a frame grabber acquires to its own set of system buffers. Meanwhile, the GPU has a completely separate set of system buffers, so any transfer between the two must be performed by the CPU, which take times if the amount of data is important. Our current framework waits for the image to be completely copied to the RAM and then transfers it to the GPU which limits the maximal system speed. The average load of the GPU during the overall procedure is less than 5%. In the near future we plan to take advantage of the latest advance in GPU computing and establish a direct link between the frame grabber and the GPU memory. Taking the Titan Xp as reference and being limited only by the computation, we expect to be able to achieve real-time dynamic images. We hope that real-time dynamic movies could highlight new biological behavior at the cellular and subcellular level. In addition, the faster processing will improve our real-time in vivo image display.

5. Conclusion

We have demonstrated detection of slow and fast dynamic processes in the eye thanks to recent technological progress in multimodal full-field optical coherence tomography. Combined static, dynamic and fluorescence contrasts are moving towards the goal of achieving label-free high-resolution imaging of anterior eye and retina with temporal resolution from milliseconds to several hours. Its contactless and non-destructive nature makes FFOCT a useful technique both for following in vitro sample evolution over long periods of time and for imaging of the human eye in vivo.

Disclosures

CB: LLTech SAS (I), K. Groux: LLTech SAS (E), others: none.

References

1. D. Huang, E. Swanson, C. Lin, J. Schuman, W. Stinson, W. Chang, M. Hee, T. Flotte, K. Gregory, C. Puliafito *et al.*, "Optical coherence tomography," Science **254**, 1178–1181 (1991).
2. W. Drexler and J. G. Fujimoto, eds., *Optical Coherence Tomography: Technology and Applications* (Springer, 2015), 2nd ed.
3. E. Beaurepaire, A. C. Boccara, M. Lebec, L. Blanchot, and H. Saint-Jalmes, "Full-field optical coherence microscopy," Opt. Lett. **23**, 244–246 (1998).
4. A. Dubois, K. Grieve, G. Moneron, R. Lecaque, L. Vabre, and C. Boccara, "Ultrahigh-resolution full-field optical coherence tomography," Appl. Opt. **43**, 2874–2883 (2004).
5. J. Ben Arous, J. Binding, J.-F. Léger, M. Casado, P. Topilko, S. Gigan, A. C. Boccara, and L. Bourdieu, "Single myelin fiber imaging in living rodents without labeling by deep optical coherence microscopy," Journal of Biomedical Optics **16**, 116012 (2011).

6. M. Jain, N. Shukla, M. Manzoor, S. Nadolny, and S. Mukherjee, "Modified full-field optical coherence tomography: A novel tool for rapid histology of tissues," J. Pathol. Informatics **2**, 28 (2011).

7. C. Apelian, F. Harms, O. Thouvenin, and A. C. Boccara, "Dynamic full field optical coherence tomography: subcellular metabolic contrast revealed in tissues by interferometric signals temporal analysis," Biomed. Opt. Express **7**, 1511–1524 (2016).

8. J. Lee, W. Wu, J. Y. Jiang, B. Zhu, and D. A. Boas, "Dynamic light scattering optical coherence tomography," Opt. Express **20**, 22262–22277 (2012).

9. C.-E. Leroux, F. Bertillot, O. Thouvenin, and A.-C. Boccara, "Intracellular dynamics measurements with full field optical coherence tomography suggest hindering effect of actomyosin contractility on organelle transport," Biomed. Opt. Express **7**, 4501–4513 (2016).

10. O. Thouvenin, C. Boccara, M. Fink, J. Sahel, M. Pâques, and K. Grieve, "Cell motility as contrast agent in retinal explant imaging with full-field optical coherence tomography," Investig. Opthalmology & Vis. Sci. **58**, 4605 (2017).

11. A. Nahas, M. Tanter, T.-M. Nguyen, J.-M. Chassot, M. Fink, and A. C. Boccara, "From supersonic shear wave imaging to full-field optical coherence shear wave elastography," J. Biomed. Opt. **18**, 18 (2013).

12. J. Binding, J. B. Arous, J.-F. Léger, S. Gigan, C. Boccara, and L. Bourdieu, "Brain refractive index measured in vivo with high-na defocus-corrected full-field oct and consequences for two-photon microscopy," Opt. Express **19**, 4833–4847 (2011).

13. M. A. A. Neil, R. Juškaitis, and T. Wilson, "Method of obtaining optical sectioning by using structured light in a conventional microscope," Opt. Lett. **22**, 1905–1907 (1997).

14. J. Mertz, *Introduction to Optical Microscopy*, vol. 138 (W. H. Freeman, 2009).

15. M. G. L. Gustafsson, "Nonlinear structured-illumination microscopy: Wide-field fluorescence imaging with theoretically unlimited resolution," Proc. Natl. Acad. Sci. **102**, 13081–13086 (2005).

16. E. Auksorius, Y. Bromberg, R. Motiejūnaitė, A. Pieretti, L. Liu, E. Coron, J. Aranda, A. M. Goldstein, B. E. Bouma, A. Kazlauskas, and G. J. Tearney, "Dual-modality fluorescence and full-field optical coherence microscopy for biomedical imaging applications," Biomed. Opt. Express **3**, 661–666 (2012).

17. O. Thouvenin, M. Fink, and A. C. Boccara, "Dynamic multimodal full-field optical coherence tomography and fluorescence structured illumination microscopy," J. Biomed. Opt. **22**, 226004 (2017).

18. P. Xiao, M. Fink, and A. C. Boccara, "Full-field spatially incoherent illumination interferometry: a spatial resolution almost insensitive to aberrations," Opt. Lett. **41**, 3920–3923 (2016).

19. P. Xiao, V. Mazlin, K. Grieve, J.-A. Sahel, M. Fink, and A. C. Boccara, "In vivo high-resolution human retinal imaging with wavefront-correctionless full-field oct," Optica **5**, 409–412 (2018).

20. K. Grieve, L. Palazzo, E. Dalimier, P. Vielh, and M. Fabre, "A feasibility study of full-field optical coherence tomography for rapid evaluation of EUS-guided microbiopsy specimens," Gastrointest. Endosc. **81**, 342–350 (2015).

21. K. Grieve, M. Paques, A. Dubois, J. Sahel, C. Boccara, and J.-F. Le Gargasson, "Ocular tissue imaging using ultrahigh-resolution, full-field optical coherence tomography," Investig. Ophthalmol. & Vis. Sci. **45**, 4126 (2004).

22. K. Grieve, O. Thouvenin, A. Sengupta, V. M. Borderie, and M. Paques, "Appearance of the retina with full-field optical coherence tomography," Investig. Ophthalmol. & Vis. Sci. **57**, OCT96 (2016).

23. V. Mazlin, P. Xiao, E. Dalimier, K. Grieve, K. Irsch, J.-A. Sahel, M. Fink, and A. C. Boccara, "In vivo high resolution human corneal imaging using full-field optical coherence tomography," Biomed. Opt. Express **9**, 557–568 (2018).

24. M. Shahidi, J. Wanek, B. Gaynes, and T. Wu, "Quantitative assessment of conjunctival microvascular circulation of the human eye," Microvasc. research **79**, 109–113 (2010).

25. A. Wartak, R. Haindl, W. Trasischker, B. Baumann, M. Pircher, and C. K. Hitzenberger, "Active-passive path-length encoded (apple) doppler oct," Biomed. optics express **7**, 5233–5251 (2016).

26. C. J. Pedersen, D. Huang, M. A. Shure, and A. M. Rollins, "Measurement of absolute flow velocity vector using dual-angle, delay-encoded doppler optical coherence tomography," Opt. letters **32**, 506–508 (2007).

27. C. K. Sheehy, Q. Yang, D. W. Arathorn, P. Tiruveedhula, J. F. de Boer, and A. Roorda, "High-speed, image-based eye tracking with a scanning laser ophthalmoscope," Biomed. Opt. Express **3**, 2611–2622 (2012).

28. K. V. Vienola, B. Braaf, C. K. Sheehy, Q. Yang, P. Tiruveedhula, D. W. Arathorn, J. F. de Boer, and A. Roorda, "Real-time eye motion compensation for oct imaging with tracking slo," Biomed. Opt. Express **3**, 2950–2963 (2012).

29. B. K. Horn and B. G. Schunck, "Determining optical flow," Artif. Intell. **17**, 185–203 (1981).

30. B. R. Munson, D. F. Young, T. H. Okiishi, and W. W. Huebsch, *Fundamentals of Fluid Mechanics*, vol. 69 (John Wiley & Sons, Inc, 2006).

31. E. Arnault, C. Barrau, C. Nanteau, P. Gondouin, K. Bigot, F. Viénot, E. Gutman, V. Fontaine, T. Villette, D. Cohen-Tannoudji, J.-A. Sahel, and S. Picaud, "Phototoxic action spectrum on a retinal pigment epithelium model of age-related macular degeneration exposed to sunlight normalized conditions," PLOS ONE **8**, 1–12 (2013).

32. R. Sharma, D. R. Williams, G. Palczewska, K. Palczewski, and J. J. Hunter, "Two-photon autofluorescence imaging reveals cellular structures throughout the retina of the living primate eye," Investig. Ophthalmol. & Vis. Sci. **57**, 632 (2016).

33. B. D. Ashby, Q. Garrett, and M. Dp, "Corneal Injuries and Wound Healing – Review of Processes and Therapies," Austin J. Clin. Ophthalmol. p. 25 (2014).

34. M. Gonzalez-Andrades, L. Alonso-Pastor, J. Mauris, A. Cruzat, C. H. Dohlman, and P. Argüeso, "Establishment of a novel in vitro model of stratified epithelial wound healing with barrier function," Sci. Reports **6** (2016).

35. J. Schindelin, C. T. Rueden, M. C. Hiner, and K. W. Eliceiri, "The imagej ecosystem: An open platform for biomedical

image analysis," Mol. Reproduction Dev. **82**, 518–529 (2015).

36. Q. Tseng, E. Duchemin-Pelletier, A. Deshiere, M. Balland, H. Guillou, O. Filhol, and M. Théry, "Spatial organization of the extracellular matrix regulates cell–cell junction positioning," Proc. Natl. Acad. Sci. **109**, 1506–1511 (2012).

37. L. Wang, J. Yuan, H. Jiang, W. Yan, H. R. Cintrón-Colón, V. L. Perez, D. C. DeBuc, W. J. Feuer, and J. Wang, "Vessel sampling and blood flow velocity distribution with vessel diameter for characterizing the human bulbar conjunctival microvasculature," Eye & contact lens **42**, 135 (2016).

38. F. Harms, E. Dalimier, P. Vermeulen, A. Fragola, and A. C. Boccara, "Multimodal full-field optical coherence tomography on biological tissue: toward all optical digital pathology," Proc.SPIE **8216**, 821609 (2012).

39. H. Makhlouf, K. Perronet, G. Dupuis, S. Lévêque-Fort, and A. Dubois, "Simultaneous optically sectioned fluorescence and optical coherence microscopy with full-field illumination," Opt. Lett. **37**, 1613–1615 (2012).

40. O. Thouvenin, C. Apelian, A. Nahas, M. Fink, and C. Boccara, "Full-field optical coherence tomography as a diagnosis tool: Recent progress with multimodal imaging," Appl. Sci. **7**, 236 (2017).

Chapter 3

Robust 3D & time imaging: retinal organoids

In this chapter, I describe the progresses made on the robustness and understanding of D-FFOCT imaging with the application on retinal organoids.

The article presented in this chapter was a collaboration between several members of the Institut Langevin and the Institut de la Vision. This work was an equal contribution with Jules Scholler. I designed and built the optomechanical setups for Dynamic Full-Field OCT experiments. Jules Scholler designed and coded the interface which pilots the microscope for acquisitions, and introduced me to their use and writting. We performed the imaging experiments together, in collaboration with biologists from the Institut de la Vision. We each performed data analysis which contributed to the final results.

3.1   D-FFOCT: robust multiple imaging modalities

D-FFOCT is a tomographic technique, enabling the imaging of samples in 3D thanks to optical sectioning. It is possible to record virtual plane sections at different depths in the sample with an axial resolution determined by the microscope objectives for high NA objectives. The signal recorded is the back-scattering of the light by the different planes of the sample: it creates an attenuation of the weak D-FFOCT signal in depth. We evaluated the depth of imaging in D-FFOCT at approximately $200\mu m$ for quite transparent samples (e.g. retinal organoids, *ex vivo* retina), and almost $80\mu m$ for non transparent samples (e.g. *ex vivo* organs such as liver). For the 3D acquisitions, Zaber motors, with a sub-micrometric displacement precision, are used to iterate the recording of planes with a precise distance between them.

As a non-invasive technique, D-FFOCT acquisitions can be performed over hours in the same plane, without damaging the sample. During these time-lapse acquisitions, the sample is likely to drift a little bit due to many factors. One possibility is that the sample is not symmetric or does not have the same density all over its volume. This can cause the sample to drift by sinking or floating a little bit for example. An other possibility is because of the imaging medium. As we use culture medium, which is made with water, for biological sample for imaging over hours, some evaporation may occur, creating also a drift on the sample. To get ride of these drifts which may change the plane of imaging during the acquisition, we have developed a stabilisation software. This software uses the autocorrelation on FFOCT images in order to retrieve the right plane. For this purpose, the first FFOCT image is used for the reference in the stabilisation software. Then, every 10 acquisitions in a time-lapse recording mode, the autocorrelation is performed between the FFOCT reference and the current FFOCT image. If the autocorrelation factor is high, the acquisition continues, if not, an FFOCT stack is performed with a step of $1\mu m$ until

the better plane is found to continue the acquisition.

3.2 Image computation: improving robustness along acquisitions

In order to improve the robustness of D-FFOCT imaging over different acquisitions, we added changes in the way the images are computed.

By getting a more consistent image computation, the analysis of D-FFOCT images over each acquisition, but also over different acquisitions, would be more coherent. That is why we decided to change the computation of the images in order to integrate different physical parameters in each channel of a coloured image. RGB colorspace has interwoven channels, which is not convenient to implement different physical parameters in each channel. So we had to find an other colorspace with independent channels. This colorspace is the HSV colorspace, which code for colour (Hue), saturation (Saturation) and intensity (Value). For this purpose, a stack of 512 images is analysed with a power spectrum analysis. By these calculations, we can get for each voxel the mean frequency of fluctuations and the frequency bandwidth. The mean frequency is coded in the Hue channel: for a low frequency, the colour will be blue, while for a high frequency it will be red. For a medium frequency, the colour will be green. The distribution of colours is Gaussian fitted to smooth it. The saturation is represented by the inverse of the frequency bandwidth. If the bandwidth is large, it means several frequencies appear in a voxel variations, in this case the saturation will be low, meaning the colour will appear grey. On the contrary, if the bandwidth is small, the saturation will be high to create a vivid colour. Finally, the value is computed as for a grayscale image: we perform a standard deviation on substacks of 50 images with a sliding window (shifted of 16 images), which are then averaged. The three channels are then recombined to create the D-FFOCT image.

The question is: why did we choose a standard deviation calculated on substacks of 50 images shifted of 16 images which are then averaged? We performed different calculations on D26 retinal organoid, on the area represented by the red line in Fig.3.1 a. To identify the best calculation, we compared calculation time, SNR, contrast and aspect of the image. The calculation times shown here are calculated on a CPU while the calculations during experiments are done on a GPU (faster), but the evolution is consistent.

Usually, the standard deviation is calculated on substacks shifted of the same number of images as the substack. As we acquire 512 images, the possibilities of length are powers of 2 (from 8 to 256). In Fig.3.1 b. is plotted the signal for the different standard deviation lengths. The calculation time decreases with the number of images used in each calculation of standard deviation (Fig.3.1 c.), while the SNR is increasing (Fig.3.1 d.). The contrast is quite similar for the different standard deviation lengths, while the maximum difference in signal (which is represented by the maximum in the signal minus the minimum in the signal) is better between 32 and 128 images used for the calculations (Fig.3.1 e. and f.), which will be called the signal contrast further on. In Fig.3.1 g. are represented the different Value images: the aspect of the 128 image looks granular, the best aspect is finally for the 32 image or the 64 image. The signal contrast can be increased by using a standard deviation shifted of a different number of images than the substack.
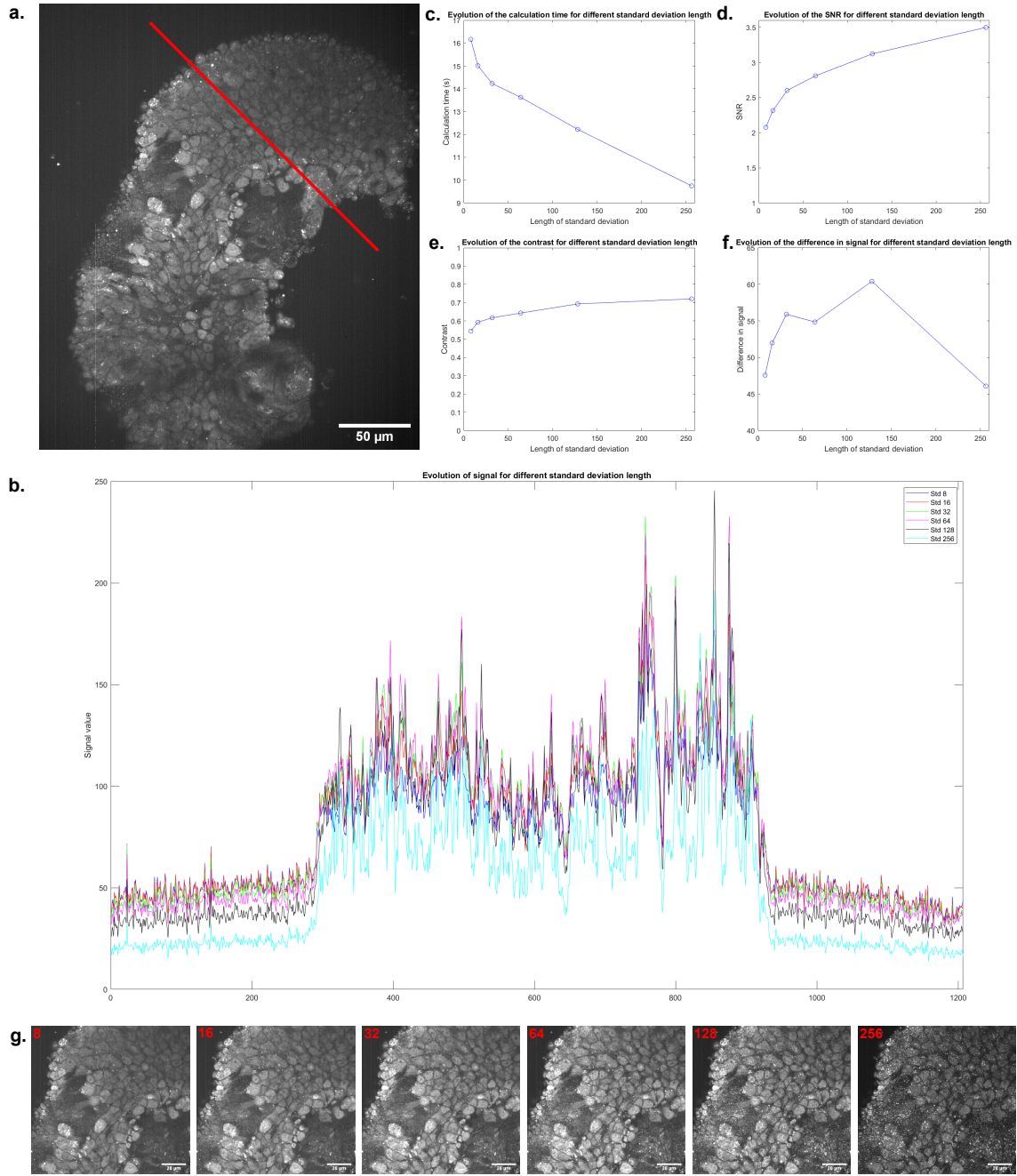
Figure 3.1: **Evaluation of the Value image for different simple standard deviation lengths.** Value images were computed for different simple standard deviation lengths (8, 16, 32, 64, 128 and 256), meaning the shift between two calculations was of the same number of images as in the calculation. **a.** Value image of a D26 retinal organoid for a standard deviation length of 8 images. The red line represents the area where the calculations of performance were done. (scale-bar: $50\mu m$) **b.** Plot of the profile of the signal for the different standard deviation lengths. **c.** Calculation time for the different standard deviation lengths. **d.** SNR for the different standard deviation lengths. **e.** Contrast for the different standard deviation lengths. **f.** Maximum difference in the signal ($max(signal) - min(signal)$) for the different standard deviation lengths. **g.** Zoom on the Value images for the different standard deviation lengths (written in red) (scale-bar: $20\mu m$).

To evaluate the best numbers for this, we studied substacks' lengths of 25, 50, 100, 150,

200 and 250, with shifts powers of 2 between 16 and 128. To avoid loss of information, the shift length must be smaller than the substack length. We plotted the calculation time for the remaining possibilities in Fig.3.2: we fixed a limit of 30 seconds of time calculation (not on GPU). By looking at the aspect of the different images, for a shift of 64 images and over, the image looks granular. Also, the signal contrast is better for substacks between 25 and 150 images (Fig.3.2 c.). The final four possibilities obtained are: 25, 50 and 100 images in the substack with a shift of 16 or 32 images. The SNR, shown in Fig.3.2 b., is smaller for a substack of 25 images. We finally chose a substack of 50 images with a shift of 16 because of the final aspect showing more details and uniformity in the signal (Fig.3.2 d.)
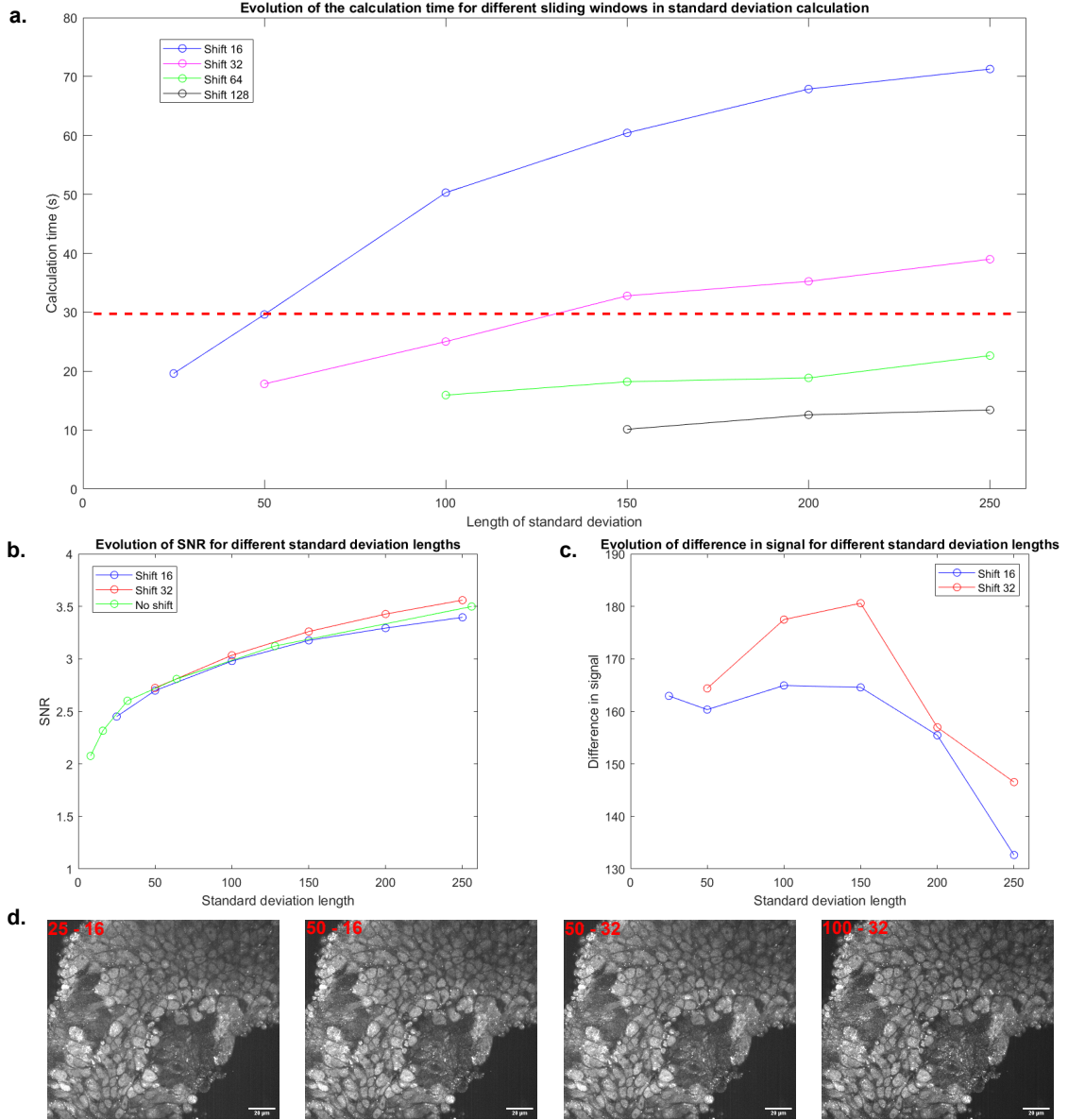
Figure 3.2: **Evaluation of the Value image for different shifted standard deviation lengths.** Value images of a D26 retinal organoid were computed for different standard deviation lengths (25, 50, 100, 150, 200 and 250), with a shift between two calculations was of 16, 32, 64 or 128. **a.** Calculation time for the different standard deviation lengths and shifts. **b.** SNR for different standard deviation lengths with shift of 16, 32 or the standard deviation length. **c.** Maximum difference in the signal. **d.** Value images for 25, 50 and 100 standard deviation lengths with 16 and 32 shifts.

3.3 Proof of concept: dynamic profile as a new contrast

A new imaging contrast can be useful for many biologists if it allows them to distinguish behaviours, cell types etc., but also if the technique brings something new and easier in the sample preparation.

As D-FFOCT is a brand new technique, it is important to compare the pros and cons of the sample preparation to the usual techniques used in biology. First of all, D-FFOCT is a completely non-invasive label-free imaging technique: a sample can be imaged in depth without any cutting and the contrast does not require any labels. The usual techniques used for imaging 3D samples [70] in biology are histology and immunochemistry. These techniques use fixation and exogenous labelling of the samples, even cutting for histology, meaning we need to sacrifice the samples. Phase contrast imaging is a non-invasive technique but there is no optical sectioning, the samples can not be scanned in 3D. OCT allows optical sectioning but there is no cellular resolution as D-FFOCT. Some techniques give sub-cellular information such as Fluorescence Lifetime Imaging Microscopy and Hyspectral Imaging, but these techniques label proteins and not phenotypes.

In order to show the use of this new contrast, we needed to compare D-FFOCT signal to gold standard in biology: fluorescence. In 2017, Thouvenin et al. introduced a multimodal FFOCT, coupled with wide-field fluorescence [71, 72]. The setup was tested on living biological samples labelled with fluorescent molecules: the results showed that D-FFOCT shows some biological processes.

In Scholler et al., 2019 [22], we showed that, by comparing D-FFOCT images to FFOCT images and fluorescence images, we can differentiate living cells from dying cells and dead cells. Indeed, dead cells (red arrow) were only visible in FFOCT images (blue channel), while dying (white dotted arrow) and living cells were both visible in D-FFOCT (red channel) and FFOCT images, but only living cells were visible in fluorescence images (green channel) as shown in Fig.3.3 a. Moreover, just above the white dotted arrow, a cell is visible in fluorescence, which seems to have exploded. This is a dead cell which was previously alive (labelled): by exploding, the only remaining signal visible is the fluorescence. The cell is visible neither in D-FFOCT images nor in FFOCT images, meaning that the waste of a dead cell is not visible in FFOCT.

In Scholler, Groux et al., 2020 [23], we went further by showing that dying cells exhibit a particular dynamic profile: an over-activation of subcellular organelle movements appearing bright and red in D-FFOCT images as shown in Fig.3.3 b. second row. Some cell types were also distinguishable only by their dynamic profile (see Fig.3.3 b. first row and c.), especially with the labelling of precursors of photoreceptors in a special CRX reporter iPSC retinal organoid line exclusively labelling photoreceptors in red (mCherry). We were able to overlay fluorescence and D-FFOCT images, showing a match between the fluorescent photoreceptors and cells appearing blue-green in D-FFOCT. D-FFOCT enables the differentiation of cell types by their dynamic profile alone, creating a new totally label-free contrast, useful in biology.
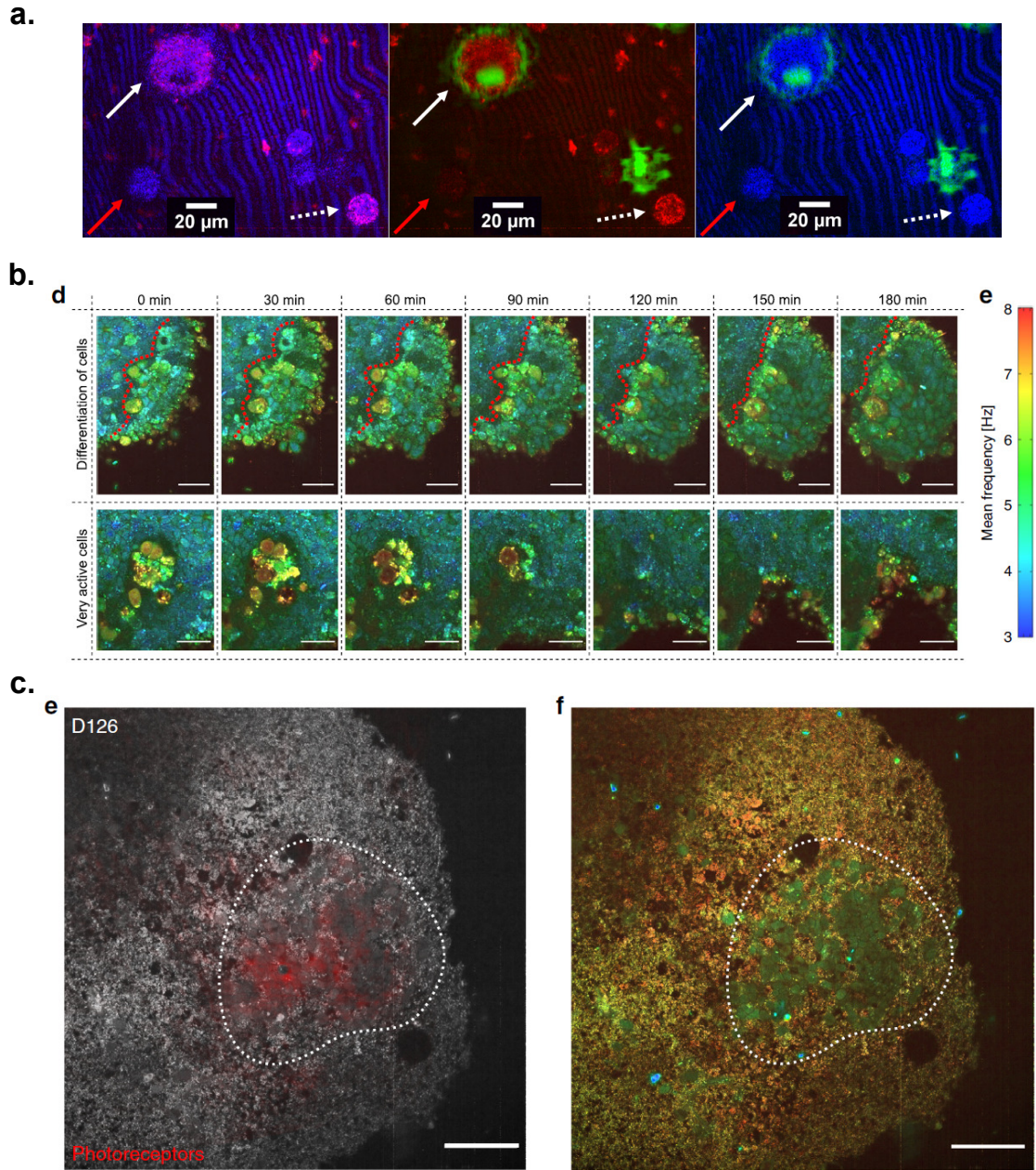
Figure 3.3: **Probing D-FFOCT signal. a.** "Multimodal binary merging. Static FFOCT is represented in blue, dynamic FFOCT in red and living labeled cells in green, imaged with our fluorescence setup." White arrow shows a living cell. Red arrow shows a dead cell. White dotted arrow shows a dying cell. Adapted from Scholler et al., 2019 [22]. **b.** "(d) High magnification images of two different areas of the organoid during a 3h time-lapse acquisition: magnified images in the top row show the change in dynamic profile that could reflect a differentiation process (the boundary between the two types of cells is represented by a red dotted line); images in the bottom row show a very active zone composed of cells exhibiting fast and high dynamics, possibly undergoing apoptosis, in the centre of the organoid. (e) Colour bar of the D-FFOCT images for the 3D and time-lapse acquisitions with a consistent colormap for (d). Scale-bar: $20\mu m$." Adapted from Fig.2 Scholler, Groux et al., 2020 [23] **c.** "D126 retinal organoid derived from a fluorescent cone rod homeobox (CRX) reporter iPSC line exclusively labelling photoreceptors in red (mCherry). (e) Overlaid image on which the photoreceptor fluorescence matches the blue-green cells of (f), the DFFOCT image. These areas are highlighted by a white dotted line. These precursors of photoreceptors have their own particular dynamic signature, which allows them to be distinguished from the surrounding cells by D-FFOCT alone. Scale-bar: $50\mu m$." Adapted from Fig.3 Scholler, Groux et al., 2020 [23].

3.4 Article: "Dynamic Full-Field Optical Coherence Tomography: 3D live-imaging of retinal organoids"

LETTER

Open Access

Dynamic full-field optical coherence tomography: 3D live-imaging of retinal organoids

Jules Scholler [1], Kassandra Groux[1], Olivier Goureau[2], José-Alain Sahel[2,3,4,5], Mathias Fink [1], Sacha Reichman [2], Claude Boccara[1] and Kate Grieve[2,3]

Abstract
Optical coherence tomography offers astounding opportunities to image the complex structure of living tissue but lacks functional information. We present dynamic full-field optical coherence tomography as a technique to noninvasively image living human induced pluripotent stem cell-derived retinal organoids. Coloured images with an endogenous contrast linked to organelle motility are generated, with submicrometre spatial resolution and millisecond temporal resolution, creating a way to identify specific cell types in living tissue via their function.

The comprehension of the human body and its mechanisms at the subcellular scale is still an open area of research. During the seventeenth century, the first examinations of life under the microscope were conducted directly on humans, animals and bacteria[1]. Then, at the end of the nineteenth century, cell culture studies began to replace in vivo studies, as this allows the creation of in vitro models beneficial for the comprehension of biological phenomena in different environments[2,3]. Because of the two-dimensional nature of early cultures, the possibilities of understanding tissues and organs as a whole were limited. Recently, three-dimensional (3D) cultures have been developed from stem cells to generate organoids that mimic a variety of tissues and serve as models of human development[4] and disease studies[5–7]. Organoids could also serve as sources of human tissues for transplantation and as platforms for drug screening[8–10]. These self-organizing structures develop cellular compositions and architectures similar to in vivo tissues, thereby replicating biologically relevant intercellular phenomena in vitro[11,12].

For each biological trend, optical imaging devices have been developed and optimized to image tissues, cell cultures and, recently, organoids, which are one of the most fundamental tools in biology, clinical pathology and medical diagnosis[13]. There are many challenges in imaging 3D structures: due to their relatively transparent nature, it is difficult to obtain contrast on specific structures without staining. Moreover, 3D samples require optical sectioning to discriminate the layer in focus from out-of-focus layers. In this study, we present dynamic full-field optical coherence tomography (D-FFOCT) as a technique to image retinal organoids derived from human induced pluripotent stem cells (hiPSCs)[14], which are a major breakthrough in the study of the retina and retinal diseases[15–17]. These hiPSC-derived retinal organoids are routinely imaged with various techniques (see Supplementary Table 1). However, each of the existing methods presents major drawbacks, such as the need for fixation or mechanical sectioning, rendering the study of dynamic phenomena impossible; the need for labelling, requiring cumbersome and costly preparation; or a lack of functional contrast, indicating only cell presence and not cell health or behaviour[18–20]. Optical coherence tomography (OCT) is commonly used in biology and medicine to obtain 3D images of microstructures in tissue. OCT contrast arises from the local endogenous optical backscattering level[21]. The main drawback of traditional OCT

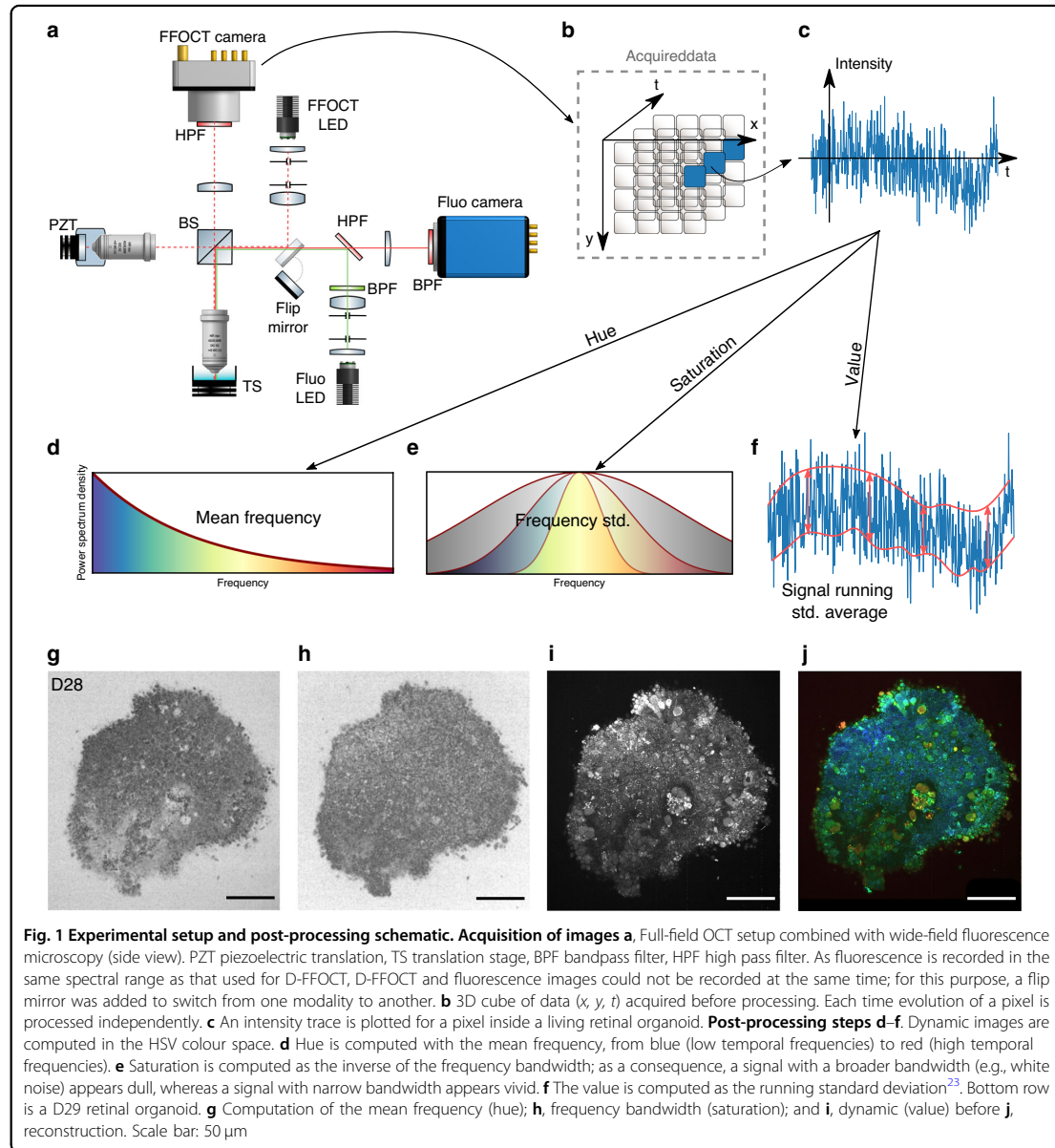Correspondence: Kate Grieve (kategrieve@gmail.com)
[1]Institut Langevin, ESPCI Paris, PSL University, CNRS, 10 rue Vauquelin, Paris, France
[2]Institut de la Vision, Sorbonne Université, INSERM, CNRS, F-75012 Paris, France
Full list of author information is available at the end of the article.
These authors contributed equally: Jules Scholler, Kassandra Groux

Fig. 1 Experimental setup and post-processing schematic. Acquisition of images a, Full-field OCT setup combined with wide-field fluorescence microscopy (side view). PZT piezoelectric translation, TS translation stage, BPF bandpass filter, HPF high pass filter. As fluorescence is recorded in the same spectral range as that used for D-FFOCT, D-FFOCT and fluorescence images could not be recorded at the same time; for this purpose, a flip mirror was added to switch from one modality to another. **b** 3D cube of data (*x*, *y*, *t*) acquired before processing. Each time evolution of a pixel is processed independently. **c** An intensity trace is plotted for a pixel inside a living retinal organoid. **Post-processing steps d–f**. Dynamic images are computed in the HSV colour space. **d** Hue is computed with the mean frequency, from blue (low temporal frequencies) to red (high temporal frequencies). **e** Saturation is computed as the inverse of the frequency bandwidth; as a consequence, a signal with a broader bandwidth (e.g., white noise) appears dull, whereas a signal with narrow bandwidth appears vivid[23]. **f** The value is computed as the running standard deviation[23]. Bottom row is a D29 retinal organoid. **g** Computation of the mean frequency (hue); **h**, frequency bandwidth (saturation); and **i**, dynamic (value) before **j**, reconstruction. Scale bar: 50 µm

is the trade-off between imaging depth and resolution. To increase the lateral resolution, the numerical aperture of the system must be increased. As a consequence, the depth of field decreases, and only a small layer of the sample can be imaged. Current OCT systems therefore have a lateral resolution on the order of 10 µm, which is insufficient to resolve cell structures laterally. Using an incoherent light source and a camera, time domain full-field OCT (FFOCT) is an en face variant of OCT with a higher spatial and temporal resolution than OCT in the en face plane[22]. As FFOCT acquires an entire en face plane rather than a line in the depth dimension, the numerical aperture can be arbitrarily increased without any imaging depth trade-off. Using the FFOCT experimental setup shown in Fig. 1(a) and detailed in the Methods section, a novel contrast mechanism has recently

been exploited by measuring temporal fluctuations of back-scattered light in a technique called dynamic FFOCT (D-FFOCT)[23]. By revealing sub-cellular structures that have very weak back-scattering, these dynamic measurements provide contrast based on local intra-cellular motility[24,25] with sub-micrometre resolution, and can achieve millisecond temporal resolution to study fast phenomena.

In FFOCT, light coming back from the sample slice of interest interferes with light coming back from the reference mirror and is projected onto the camera (Fig. 1 (a)). To compute a D-FFOCT image, a movie (typically 512 frames) of the interferogram pattern is recorded and processed (see Methods) to extract local fluctuations and render them coloured (Fig. 1(b–j)). Using the hue-saturation-value (HSV) colour space, image brightness is linked to fluctuation amplitude, whereas colour is linked to fluctuation speed, from blue (slow) to red (fast) through green (in between). By translating the sample in the axial direction to acquire a stack of planes, see Supplementary Vid. 1, a 3D volume can be reconstructed (see Methods). Alternatively, a series of dynamic images may be acquired in the same plane to follow the evolution of activity over several hours in a time-lapse fashion with a temporal resolution of up to 20 ms (see "Methods").

A 3D reconstruction of a 28-day-old (D28) retinal organoid is depicted in Fig. 2(a), corresponding to an optic vesicle stage during retinogenesis[9,10,15,16], along with a sub-volume in Fig. 2(b), highlighting the layered internal retinal progenitor cell organization. A cross-section is shown in Fig. 2(c), in which the elongated shape of cells is seen. A time-lapse video at 50 μm depth was acquired on the same organoid to study its temporal evolution over three hours (see Fig. 2(d) and Supplementary Video 2 for the full recording). In these acquisitions, different dynamic profiles of cells can be observed: surface cells exhibit faster dynamics than those inside the sample volume. This could be explained by the fact that at the surface of the organoid, the cells are in contact with the external environment, making them more vulnerable to change and often leading to their death. In Fig. 2(d), cells in the centre of the organoid exhibit fast and intense activity until their disappearance, possibly indicating that they are undergoing apoptosis. Evolution of cell dynamics near a clear boundary between two distinct types of cells is also visible. On one side of the boundary, cells exhibit faster and stronger dynamics, suggesting a differentiation process towards specific retinal lineages[15], and on the other side, small rounded progenitor cells have slower activity. These two cell types are therefore distinguishable by their dynamic profile alone. Generated D-FFOCT images present a consistent colormap in which each frequency is continuously represented by the same colours; therefore, similar results are obtained for different retinal

organoids at the same developmental stage. Supplementary Video 3 shows a time-lapse movie of the D28 retinal organoid shown in Fig. 2(a–c) alongside a D29 retinal organoid. The same clear boundary between distinct types of cells is present for both. By processing the data contemporaneously on the GPU using a modified version of Holovibes software[26], an enhanced temporal resolution of 20 ms was achieved, which represents a 500-fold improvement without the need to store the raw data (up to $4\,Go.s^{-1}$). The price paid for this improvement is the use of an alternative version of the dynamic computation, which is noise-sensitive and non-quantitative (see "Methods"). Figure 2(f–h) shows high temporal resolution (20 ms) images of a D147 retinal organoid. The typical rosette organization of retinal cells, previously described[14,15], is visible in the centre, i.e., photoreceptors (seen from the side) in the inner part of the rosette centre with emerging outer segments (indicated by white lines on Fig. 2(h)), and other surrounding retinal cells are evident. Photoreceptor nuclei exhibit different dynamic profiles (Fig. 2(g))—either compact and uniform, inflated, or absent—which may correspond to the nuclear G0/G1, dying and M states, respectively. The gain in temporal resolution allows the study of fast biological processes such as organelles moving inside the cytoplasm (see Supplementary Video 4). A series of retinal organoids imaged by D-FFOCT at consecutive steps of development showed the gradual differentiation of retinal cell progenitors into neural cells and photoreceptors (Supplementary Fig. 2), as validated by comparison with a similar organoid series imaged with immunofluorescence on a confocal microscope[14].

To further validate the D-FFOCT signal origin via direct comparison between D-FFOCT and specific fluorescence labelling in the same organoids, a multimodal setup was developed that combines D-FFOCT and fluorescence channels to allow a pixel-to-pixel overlay of D-FFOCT and fluorescence images. A D29 retinal organoid was labelled with a dye targeting the nuclei of dead cells (see "Methods"). D-FFOCT images overlaid with fluorescence wide-field images are shown Fig. 3(a–d). Two fluorescent red spots are clearly visible (Fig. 3(a)) and correspond to very weak dynamic signals in the D-FFOCT image, confirming that dead cells exhibit low activity and that the contrast revealed by D-FFOCT is metabolic. These two areas are magnified in Fig. 3(c, d), and dark zones are encircled by a white dotted line. A retinal organoid was imaged with the combined D-FFOCT-fluorescence system at D126, via which a large number of differentiating photoreceptors can be detected in rosette-like configurations (Fig. 3(e, f)). A red fluorescent zone corresponding to photoreceptors is visible in Fig. 3(e), whereas in the D-FFOCT image (Fig. 3(f)), the different activity level in photoreceptors compared to surrounding cells is
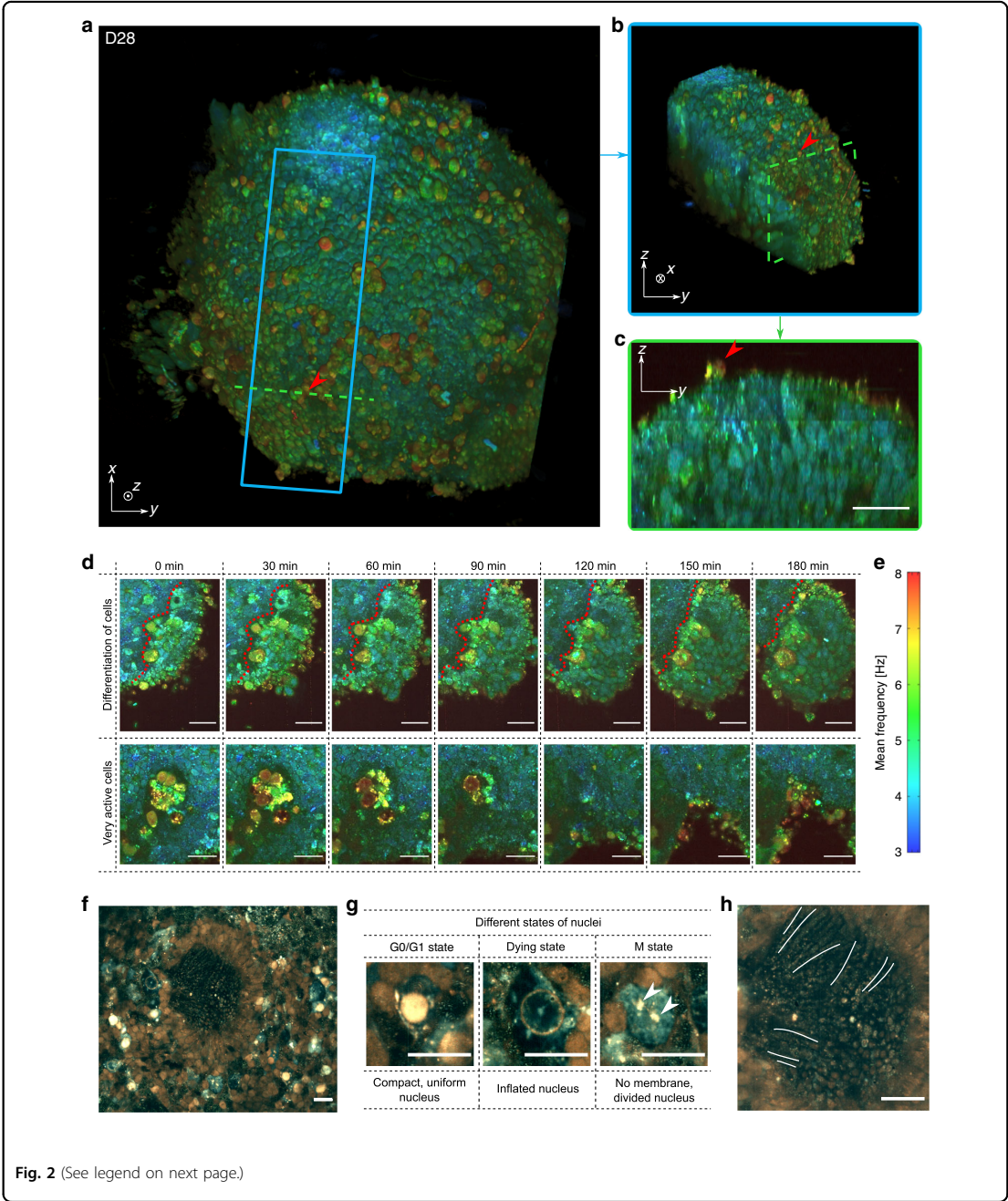
Fig. 2 (See legend on next page.)

sufficient to provide distinction of the cell type through the dynamic signal alone, across a region that is coincident with the fluorescently labelled zone. Underlying biological processes responsible for the dynamic contrast,

which has been shown to be linked to cell metabolism[23], could include movement of organelles. Preliminary experiments suggest mitochondrial contribution, but other potential contributors, such as Golgi bodies,

(see figure on previous page)
Fig. 2 Imaging hiPSC-derived retinal organoids with D-FFOCT. a 3D reconstruction of the spherical D28 retinal organoid, composed of cells ~5 μm in diameter. Red arrows highlight surface cells exhibiting fast dynamics. **b** Image represents a sub-volume of **a** (blue square). **c** Image represents a cross-section in (**a**) (green dashed line) in which one can see the organization of the layers inside the retinal organoid. **d** High-magnification images of two different areas of the organoid during a 3h time-lapse acquisition: magnified images in the top row show the change in dynamic profile that could reflect a differentiation process (the boundary between the two types of cells is represented by a red dotted line); images in the bottom row show a very active zone composed of cells exhibiting fast and high dynamics, possibly undergoing apoptosis, in the centre of the organoid. **e** Colour bar of the D-FFOCT images for the 3D and time-lapse acquisitions with a consistent colormap for (**a–d**). High-temporal-resolution imaging performed on a D147 retinal organoid. **f** Part of the retinal organoid revealing fusiform structures corresponding to emerging photoreceptor outer segments in the centre of the rosette. **g** Magnified view of nuclei in three different states around the rosette: (i) a nucleus in a normal state with a compact, uniform shape and is very bright (i.e., exhibiting a high activity); (ii) an seemingly dying, inflated nucleus, exhibiting almost no activity; and (iii) a nucleus undergoing division with no defined nuclear membrane in the cytoplasm, and two distinct parts (white arrows) of the content of a nucleus (suggesting mitosis of the nucleus with chromosomes already divided, with the same subcellular activity level as the "normal" nucleus). **h** Magnified image of the photoreceptor outer segment-like structures imaged side-on; three of them are marked with a white line. Scale bar: 20 μm

lysosomes, vesicles, and pigments, have not yet been discarded.

With D-FFOCT, once installed in the culture lab under controlled environmental conditions, we anticipate being able to follow retinal organoid developmental processes that have been documented by traditional methods[14,19], such as the quantification of cells exhibiting the same dynamic profile at multiple time points. In addition, we should also gain additional biological insights owing to the non-invasive nature of our imaging method, as it provides access to the time course of continuous processes such as progenitor cell proliferation and migration, cell type differentiation including evolution of the boundary between neural and non-neural retinal cells (Fig. 2(d)) and evolution of the organoid into layered retina. Interestingly, combining D-FFOCT and a 3D organoid-based model of retinal dystrophies due to patient-specific iPSCs offers the opportunity to understand fundamental subcellular processes leading to diseases in a way that was not previously possible.

Dynamic FFOCT imaging creates a new label-free non-invasive contrast for imaging retinal organoids. As this technique does not damage the samples, it complements and could potentially replace the imaging modalities traditionally used. D-FFOCT allows imaging of different layers at multiple depths while preserving the sample integrity, i.e., using neither exogenous labelling nor destructive methods, and is therefore suitable to follow the evolution of the same organoid at different stages of its development. The high dimensionality of the probed signals (512 interferograms per pixel) is useful for developing statistical approaches such as automated classification and clustering, and we are working towards the identification of cells via their D-FFOCT contrast alone using machine learning algorithms, with the ultimate goal of removing the need for markers entirely. The only missing part, for now, is the lack of ground truth validation data (e.g., segmented cells with labels that could be generated by fluorescence or by annotating experts), which will be a milestone in the further development of this technique.

Methods
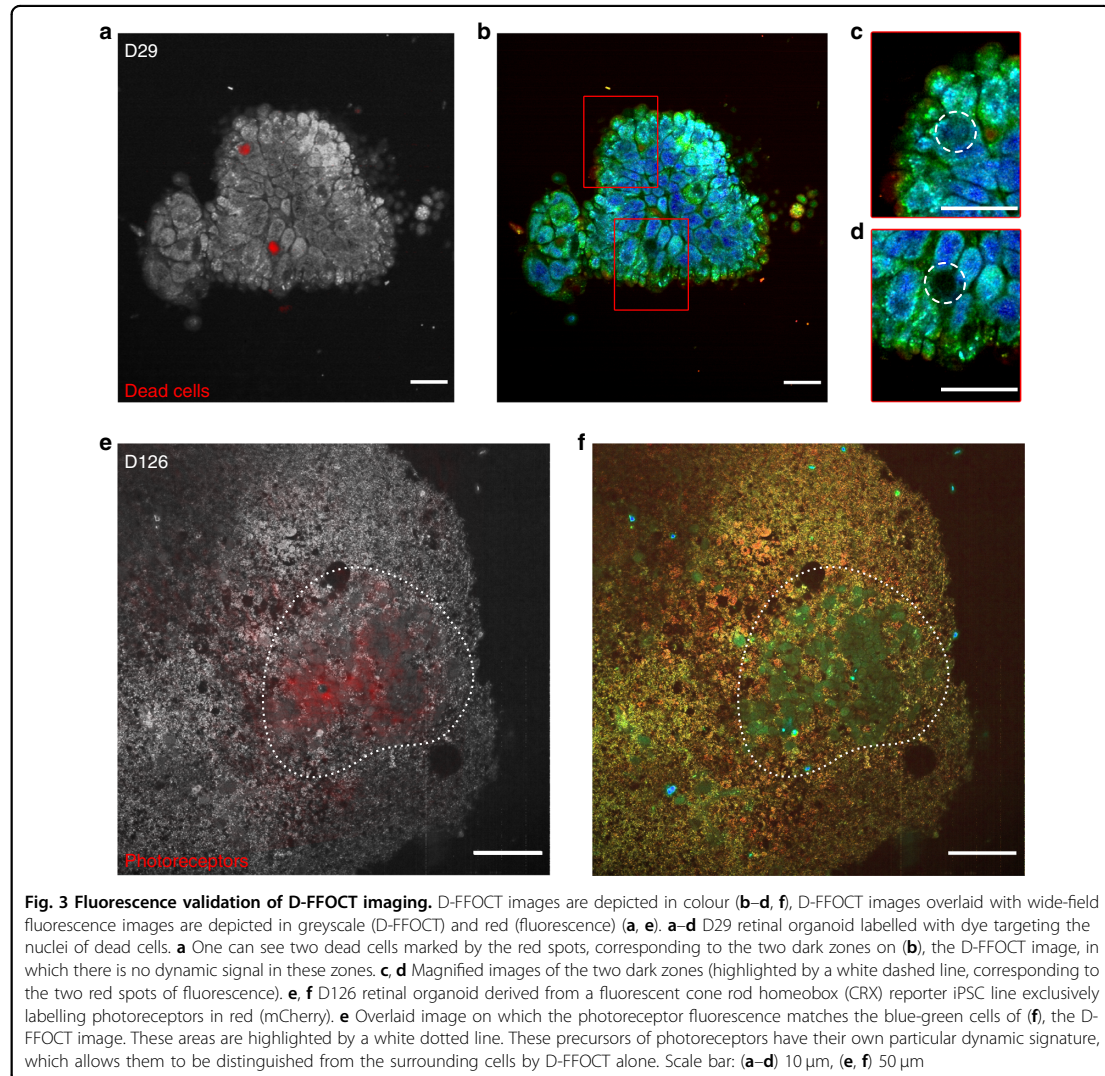
Human iPSC maintenance and retinal differentiation

Two established human iPSC lines, hiPSC line-5f[17] and fluorescent reporter AAVS1::CrxP H2BmCherry hiPSC line[27], both derived from retinal Müller glial cells, were cultured as previously described[14]. Briefly, hiPSC lines were cultured on truncated recombinant human vitronectin-coated dishes with Essential 8TM medium (Thermo Fisher Scientific, Les Ulis, France). For retinal differentiation, adherent hiPSCs were expanded to 70–80%, and FGF-free (fibroblast growth factor) medium was added to the cultures for 2 days, followed by a neural induction period allowing retinal structures to appear. Identified retinal organoids were manually isolated and cultured as floating structures for several weeks to follow retinal cell differentiation as previously described[14,28].

Sample preparation for D-FFOCT imaging

Retinal organoids were placed in CO_2-independent medium (Gibco^{TM}, Thermo Fisher Scientific) in a Petri dish and kept close to 37 °C during imaging. Samples were mounted on a 3-axis translation stage under the sample arm objective and imaged directly after mounting. After imaging, each organoid was either cultured again for further D-FFOCT imaging or fixed using a solution of paraformaldehyde (PFA) for 15 min at 4 °C followed by three rinses and stored in a sucrose solution for further traditional imaging. For dead cell labelling (LIVE/DEAD Viability/Cytotoxicity Kit for Mammalian Cells, Thermo Fisher Scientific), organoids were incubated with 10 μM EthD-1 at 37 °C for 20 min before imaging and were mounted immediately after incubation and imaged within 10 min.

Immunostaining and imaging of retinal sections

For cryosectioning, retinal organoids were fixed for 15 min in 4% PFA at 4 °C and washed in phosphate-buffered saline (PBS). Structures were incubated at 4 °C in PBS/30% sucrose (Sigma Aldrich, Saint-Quentin-Fallavier, France) solution for at least 2 h and embedded in a

Fig. 3 Fluorescence validation of D-FFOCT imaging. D-FFOCT images are depicted in colour (**b**–**d**, **f**), D-FFOCT images overlaid with wide-field fluorescence images are depicted in greyscale (D-FFOCT) and red (fluorescence) (**a**, **e**). **a**–**d** D29 retinal organoid labelled with dye targeting the nuclei of dead cells. **a** One can see two dead cells marked by the red spots, corresponding to the two dark zones on (**b**), the D-FFOCT image, in which there is no dynamic signal in these zones. **c**, **d** Magnified images of the two dark zones (highlighted by a white dashed line, corresponding to the two red spots of fluorescence). **e**, **f** D126 retinal organoid derived from a fluorescent cone rod homeobox (CRX) reporter iPSC line exclusively labelling photoreceptors in red (mCherry). **e** Overlaid image on which the photoreceptor fluorescence matches the blue-green cells of (**f**), the D-FFOCT image. These areas are highlighted by a white dotted line. These precursors of photoreceptors have their own particular dynamic signature, which allows them to be distinguished from the surrounding cells by D-FFOCT alone. Scale bar: (**a**–**d**) 10 µm, (**e**, **f**) 50 µm

solution of PBS, 7.5% gelatine (Sigma Aldrich, Saint-Quentin-Fallavier, France), and 10% sucrose and frozen in isopentane at −50 °C. Ten-micrometre-thick cryosections were collected in two perpendicular planes. Sections were washed with PBS, nonspecific binding sites were blocked for 1 h at room temperature with a PBS solution containing 0.2% gelatine and 0.1% Triton X100 (blocking buffer) and then overnight at 4 °C with the primary antibodies VSX2 (goat, 1:2000, Santa Cruz Biotechnology, Clinisciences, Nanterre, France), CRX (mouse, 1:5000, Abnova, Clinisciences) and RHODOPSIN (mouse, 1:500, Merck, Guyancourt, France) diluted in blocking buffer. Slides were washed three times in PBS with 0.1% Tween

and then incubated for 1 h at room temperature with appropriate secondary antibodies conjugated with either Alexa Fluor 488 or 594 (Jackson ImmunoResearch Lab., Interchim, Montluçon, France) diluted at 1:600 in blocking buffer with 4′,6-diamidino-2-phenylindole diluted at 1:1000 to counterstain nuclei. Fluorescent staining signals were captured with an Olympus FV1000 confocal microscope.

Experimental setup

Time-domain FFOCT[22,29] is a variant of scanning OCT[21] in which two-dimensional en face images are captured using a CMOS camera. Three-dimensional

images can be acquired and reconstructed by scanning in the depth dimension with high precision motors. This configuration, together with the use of a broad-band LED source, allows for higher axial and en face resolution than conventional OCT and can perform micrometre resolution 3D imaging noninvasively in both fresh and fixed ex vivo tissue samples. For the D-FFOCT imaging of retinal organoids, a laboratory setup was designed with a 0.5 μm lateral resolution using high-magnification water-immersion objectives (Nikon NIR APO 40x 0.8 NA), for a field of view of ~320 × 320 μm². Because of the high numerical aperture, an axial resolution of 1.7 μm was also obtained by the microscope objectives in this particular configuration in which the coherence length of the source is larger than the depth of focus. The light source used for the FFOCT system was an LED with a central wavelength of 660 nm (M660L3, Thorlabs, Newton, NJ, USA). The choice of the light source for an FFOCT system is one of the most important parameters. First, it needs to be spatially incoherent to avoid cross-talk artefacts due to multiple scattering. The optical power must be high enough to image close to camera saturation to maximize the signal-to-noise ratio. The central wavelength was chosen to be as close as possible to near-infrared to maximize the penetration depth while remaining in the visible spectrum (as fluorescence measurements were done in the visible spectrum and some optical components were coated only for the visible spectrum). Finally, the LED coherence length (computed as the width at half maxima of the axial fringe pattern) was 13.28 μm in water, which allowed a robust 3D alignment between the coherence plane and the focal plane, therefore allowing a homogeneous contrast over the whole field of view. The FFOCT signal was recorded on a custom camera (Quartz 2A750, Adimec). For validation purposes, this FFOCT setup was combined with a fluorescence microscope using an LED source centred at 565 nm (M565L3, Thorlabs, Newton, NJ, USA) for excitation and filtered with a bandpass filter centred on 562 nm with a bandwidth of 40 nm (Semrock FF01-562/40-25). The emitted fluorescence was filtered with another bandpass filter centred on 624 nm (Semrock FF01-624/40-25) and then imaged using a sCMOS camera (PCO Edge 5.5). The excitation and fluorescence wavelengths were separated by a dichroic mirror at 593 nm (Semrock FF593-Di03-25).

Data acquisition and processing

Producing each dynamic image slice required the acquisition of many (typically 512) direct images without modulating the piezo position. As opposed to static FFOCT acquisition, the measured fluctuations in D-FFOCT arise from subcellular motion. In this study, the frame rate was set to 100 Hz, which was a good trade-off between acquisition speed and signal-to-noise ratio (see

the following section). For a given acquisition, we typically obtain a (1440,1440,512) tensor in which 1440 × 1440 is the number of sensor pixels and 512 is the number of recorded frames. After acquiring data, the first step is to correct for the camera frame-to-frame instability by normalizing each frame to compensate for exposure time variations. Previously, we showed colour images that were constructed by integrating signals in the Fourier domain for three frequency ranges[30]. Here, we propose a new scheme wherein colour images are computed in the HSV colour space in which, contrary to the red-green-blue (RGB) colour space, it is possible to assign a physical property to each of the three channels for quantitative visual interpretation. The idea is then to attribute a colour for each pixel depending on the characteristic time period or frequency of the dynamic signal. Each individual pixel can be thought of as a sum of subcellular random walks with a typical covariance function depending on the motion type (e.g., diffusive, hyperdiffusive). To distinguish between several dynamic profiles, we performed power spectrum analysis. Note that a correlation analysis could also be performed and gives similar results but requires more computing time. We started by computing the power spectrum density (PSD) using Welch's method for each pixel and then used an L1 normalization on each PSD as if it were a probability distribution. Then, the hue channel, was computed as the mean frequency (which is simply the dot product between the normalized PSD and the frequency array). The values were then inverted and rescaled between 0 and 0.66 to go from blue (low frequencies) to red (high frequencies). We observed that two successive acquisitions could lead to different perceptual colour maps. We found that the lowest frequencies were slightly unstable (either due to sensor or mechanical instabilities as described in[31]). We removed this artefact by removing 3% of the lowest frequencies in the PSD. Then, the value (which corresponds to the perceived pixel intensity) was computed as the average of the temporal standard deviation with a window size of 50 samples. We saturated 0.1% of the highest value pixels to improve the contrast. For 3D stacks, the saturation threshold value was kept constant throughout the stack to obtain a consistent colour map. Finally, saturation was computed as the inverse of the normalized PSD bandwidth. As a consequence, the saturation channel carries the frequency bandwidth information. In practice, it is computed as the standard deviation of the frequencies (i.e., it corresponds to the frequency histogram width) as:

$$S = P.f^2 - (P.f)^2 \qquad (1)$$

where P is the normalized PSD array, f is the frequency array and "." is the dot product. The saturation map is then inverted and rescaled between 0 and 0.8 to obtain a

visually pleasing output. The broader the spectrum, the lower the saturation. White noise has a broader bandwidth and will therefore appear greyish instead of coloured. Finally, the dynamic image is transformed in the RGB colour space for display purposes. A (1440, 1440, 512) stack is processed in less than 10 s by the GPU (Nvidia Titan V) using MATLAB (MathWorks) and our custom software[32], hence limiting temporal resolution by processing the data after each acquisition. To improve temporal resolution, we also used a modified version of a previous method[26], which computes real-time dynamic images on the GPU. In this case, the algorithm used to generate dynamic images is no longer quantitative and is subject to more noise. The 3D cube of data is first Fourier transformed; the Fourier transform magnitude of each temporal signal is then integrated into three bands to reconstruct an RGB image in which the band corresponding to lower frequencies is coded in the blue channel, the band corresponding to medium frequencies is coded in the green channel and the band corresponding to high frequencies is coded in the red channel. The processing power of the GPU allowed us to process a new cube of data every 2 frames, leading to a D-FFOCT frame rate of 50 Hz in practice and a temporal resolution of 20 ms. For 3D volumes, the temporal resolution depends on the number of planes per volume. In practice, the final plane is delayed by several minutes compared with the first acquired plane. However, as the biological changes being evaluated are on time scales slower than minutes, this lag was not an issue (see Supplementary Video 2). For 3D stacks, each plane is registered during post-processing using a feature-based method (rigid registration using SIFT features and RANdom SAmple Consensus algorithms to find correct matches) to compensate for the sample lateral drift. Stacks are then interpolated in the depth dimension using bicubic interpolation to obtain a square voxel edge size of 220 nm. For 3D display purposes, a nonlocal mean filter[33] can be applied to remove granularity.

Choosing the frame rate for D-FFOCT

The choice of 100 Hz for the camera frame rate is the result of the optimization between the acquisition speed and the signal-to-noise ratio. For a given number of frames, the signal-to-noise ratio increases in D-FFOCT when the frame rate decreases because scattering structures have more time to move and a greater volume can be explored, therefore leading to higher phase shifts and higher intensity fluctuations on the camera. For 512 frames, the signal-to-noise ratio starts decreasing when going faster than 100 Hz, so this value was chosen to maximize both the acquisition speed and signal-to-noise ratio.

Correcting for sample drift

Due to thermal effects, we observed a slow mechanical drift (on the order of $5\,\mu m.h^{-1}$), which could prevent us from measuring dynamic images in the same plane over several hours (axial resolution is 1.7 μm). To compensate for this drift, we developed a correlation-based method called the plane locking procedure[25]. This procedure was utilized when the cross-correlation between the current image and the target image was below a threshold (typically between 0.2 and 0.4). In this case, FFOCT images were acquired over an axial extent of 10 μm, with 0.5 μm steps using the sample translation stage and were then cross-correlated with the target image. The sample was then axially translated to the position corresponding to the maximum of the cross-correlation, which was typically between 0.5 and 0.8. After each plane correction procedure, a new FFOCT image was chosen as the target for the next correction to account for evolution in the sample position.

Combining FFOCT and fluorescence microscope channels

The FFOCT and fluorescence cameras do not share the same sensor size and resolution, so to construct overlays, FFOCT images were registered onto fluorescence images using a projective transformation. The projective transformation was calibrated using a deformation target (R1DS1N, Thorlabs, Newton, NJ, USA) before experiments. The final overlays were constructed in RGB colour space, the value channel corresponding to dynamic amplitude was inserted into every channel (R, G, and B), and a fluorescence image was added only to the R channel. In this way, the dynamic image appeared in greyscale with the fluorescence superimposed in red.

Author details
[1]Institut Langevin, ESPCI Paris, PSL University, CNRS, 10 rue Vauquelin, Paris, France. [2]Institut de la Vision, Sorbonne Université, INSERM, CNRS, F-75012 Paris, France. [3]Quinze-Vingts National Eye Hospital, 28 Rue de Charenton, Paris 75012, France. [4]Fondation Ophtalmologique Rothschild, F-75019 Paris, France. [5]Department of Ophthalmology, The University of Pittsburgh School of Medicine, Pittsburgh, PA 15213, United States

Author contributions
J.S. wrote the software for experiments and data processing. J.S. and K.Gro. performed the experiments and analysed the results. J.S., K.Gro., C.B. and K.Gri. devised and designed the experiments driven by inputs from S.R. and O.G. O.G. and S.R. provided the samples. All authors discussed the results and contributed to the manuscript.

Data availability
The study data are available from the corresponding author upon request.

Code availability
The control and acquisition software is available at https://github.com/JulesScholler/FFOCT.

Conflict of interest
The authors declare that they have no conflict of interest.

References
1. Hajdu, S. I. The first use of the microscope in medicine. *Ann. Clin. Lab. Sci.* **32**, 309–310 (2002).
2. Mazzarello, P. A unifying concept: the history of cell theory. *Nat. Cell Biol.* **1**, E13–E15 (1999).
3. Jedrzejczak-Silicka, M. History of cell culture in New Insights into Cell Culture Technology. ed. Sivakumar Joghi Thatha Gowder, IntechOpen, (2017).
4. Hynds, R. E. & Giangreco, A. Concise review: the relevance of human stem cell-derived organoid models for epithelial translational medicine. *Stem Cells* **31**, 417–422 (2013).
5. Lancaster, M. A. & Knoblich, J. A. Organogenesis in a dish: modeling development and disease using organoid technologies. *Science* **345**, 1247125 (2014).
6. Clevers, H. Modeling development and disease with organoids. *Cell* **165**, 1586–1597 (2016).
7. Hartogh, S. C. D. & Passier, R. Concise review: fluorescent reporters in human pluripotent stem cells: contributions to cardiac differentiation and their applications in cardiac disease and toxicity. *Stem Cells* **34**, 13–26 (2016).
8. Fatehullah, A., Tan, S. H. & Barker, N. Organoids as an in vitro model of human development and disease. *Nat. Cell Biol.* **18**, 246–254 (2016).
9. Gagliardi, G., M'Barek, K. B. & Goureau, O. Photoreceptor cell replacement in macular degeneration and retinitis pigmentosa: a pluripotent stem cell-based approach. *Prog. Retinal Eye Res.* **71**, 1–25 (2019).
10. Llonch, S., Carido, M. & Ader, M. Organoid technology for retinal repair. *Developmental Biol.* **433**, 132–143 (2018).
11. Rossi, G., Manfrin, A. & Lutolf, M. P. Progress and potential in organoid research. *Nat. Rev. Genet.* **19**, 671–687 (2018).
12. Lancaster, M. A. & Huch, M. Disease modelling in human organoids. *Dis. Models Mechanisms* **12**, dmm039347 (2019).
13. Yuste, R. Fluorescence microscopy today. *Nat. Methods* **2**, 902–904 (2005).
14. Reichman, S. et al. Generation of storable retinal organoids and retinal pigmented epithelium from adherent human iPS Cells in Xeno-free and feeder-free conditions. *Stem Cells* **35**, 1176–1188 (2017).
15. Reichman, S. et al. From confluent human iPS cells to self-forming neural retina and retinal pigmented epithelium. *Proc. Natl Acad. Sci. USA* **111**, 8518–8523 (2014).
16. Zhong, X. F. et al. Generation of three-dimensional retinal tissue with functional photoreceptors from human iPSCs. *Nat. Commun.* **5**, 4047 (2014).
17. Slembrouck-Brec, A. et al. Reprogramming of adult retinal müller glial cells into human-induced pluripotent stem cells as an efficient source of retinal cells. *Stem Cells Int.* **2019**, 7858796 (2019).
18. Browne, A. W. et al. Structural and functional characterization of human stem-cell-derived retinal organoids by live imaging. *Investigative Ophthalmol. Vis. Sci.* **58**, 3311–3318 (2017).
19. Capowski, E. E. et al. Reproducibility and staging of 3D human retinal organoids across multiple pluripotent stem cell lines. *Development* **146**, dev171686 (2019).
20. Cora, V. et al. A cleared view on retinal organoids. *Cells* **8**, 391 (2019).
21. Huang, D. et al. Optical coherence tomography. *Science* **254**, 1178–1181 (1991).
22. Dubois, A. et al. Ultrahigh-resolution full-field optical coherence tomography. *Appl. Opt.* **43**, 2874–2883 (2004).
23. Apelian, C. et al. Dynamic full field optical coherence tomography: subcellular metabolic contrast revealed in tissues by interferometric signals temporal analysis. *Biomed. Opt. Express* **7**, 1511–1524 (2016).
24. Thouvenin, O. et al. Cell motility as contrast agent in retinal explant imaging with full-field optical coherence tomography. *Investigative Ophthalmol. Vis. Sci.* **58**, 4605–4615 (2017).
25. Scholler, J. et al. Probing dynamic processes in the eye at multiple spatial and temporal scales with multimodal full field OCT. *Biomed. Opt. Express* **10**, 731–746 (2019).
26. Atlan, M. Holovibes: hologram rendering made easy. at http://holovibes.com. (2014)
27. Gagliardi, G. et al. Characterization and transplantation of CD73-positive photoreceptors isolated from human iPSC-Derived retinal organoids. *Stem Cell Rep.* **11**, 665–680 (2018).
28. Slembrouck-Brec, A. et al. Defined xeno-free and feeder-free culture conditions for the generation of human iPSC-derived retinal cell models. *J. Vis. Exp.* **139**, e57795 (2018).
29. Beaurepaire, E. et al. Full-field optical coherence microscopy. *Opt. Lett.* **23**, 244–246 (1998).
30. Apelian, C., Gastaud, C. & Boccara, A. C. Extracting relevant information for cancer diagnosis from dynamic full field OCT through image processing and learning. Proceedings of SPIE 10053, Optical Coherence Tomography and Coherence Domain Optical Methods in Biomedicine XXI. San Francisco, California, United States: SPIE, 2017.
31. Scholler, J. Motion artifact removal and signal enhancement to achieve in vivo dynamic full field OCT. *Opt. Express* **27**, 19562–19572 (2019).
32. Scholler, J. Jules Scholler/FFOCT: FFOCT_v0.1. (2019). at https://zenodo.org/record/3137246#.Xuxc8fk6veQ.
33. Buades, A., Coll, B. & Morel, J. M. A non-local algorithm for image denoising. Proceedings of 2005 IEEE Computer Society Conference on Computer Vision and Pattern Recognition (CVPR'05). San Diego, CA, USA: IEEE (2005).

Integrated supplementary information for

Dynamic full-field optical coherence tomography: 3D live-imaging of retinal organoids

Jules Scholler[1,†], Kassandra Groux[1,†], Olivier Goureau[2], José-Alain Sahel[2,3,4,5], Mathias Fink[1], Sacha Reichman[2], Claude Boccara[1] and Kate Grieve[2,3,*]

[1]Institut Langevin, ESPCI Paris, PSL University, CNRS, 10 rue Vauquelin, Paris, France
[2]Institut de la Vision, Sorbonne Université, INSERM, CNRS, F-75012, Paris, France
[3]Quinze-Vingts National Eye Hospital, 28 Rue de Charenton, Paris, 75012, France
[4]Fondation Ophtalmologique Rothschild, F-75019 Paris, France
[5]Department of Ophthalmology, The University of Pittsburgh School of Medicine, Pittsburgh, PA 15213, United States

[†]These authors contributed equally to this work
[*]kategrieve@gmail.com

		Imaging techniques			
		FFOCT/D-FFOCT	OCT	Conventional microscopy	Confocal, multiphoton or light sheet microscopy
Resolution (µm)	Lateral	0.5	10	0.5	0.5
	Axial	1.4	1	-	1.9
	Depth penetration	1000 / 150	1000	-	150 - 1000 (clearing)
Aquisition	3D	✓	✓	-	✓
	Live imaging	✓	✓	✓	✓
	Time	s / min	s	s	min - h
Sample preparation	Preparation time	s	s	h - d	h - d
	Clearing	-	-	-	×
	Fixation	-	-	×	×
	Labeling	-	-	×	×
	Sectioning	-	-	×	×
Biological insights	Dynamic profile	✓	-	-	-
	Tissue development	✓	-	-	-
	Cell motility	✓	-	-	-
	Tissue organisation	✓	✓	✓	✓
	Specific protein distribution	-	-	✓	✓

– (not required/possible); ✓ (possible); ✗ (required); s (second); min (minute); h (hour); d (day)

Table 1: Comparison of the different techniques that can be used to image hiPSC-derived retinal organoids. Lateral resolution computed for the same microscope objective (Nikon NIR APO 40x 0.8 NA) is diffraction-limited for all methods aside from OCT, wherein the need for a large depth of field limits the lateral resolution to 10 μm. Axial resolution in (D-)FFOCT is determined by the depth of field of the objective rather than the coherence length in the current configuration as high NA objectives are used (i.e., as the depth of field is smaller than the coherence length, the axial resolution is limited by the numerical aperture). Confocal, multiphoton, and light sheet immunohistochemistry methods achieve the same axial resolution at shallow depths as (D-)FFOCT but usually require invasive tissue clearing procedures to maintain the resolution at greater depths. The lower penetration depth of D-FFOCT than that of FFOCT comes from the low reflectivity of the moving organelles [31] that produce the dynamic signals. No method can currently penetrate the full organoid depth with submicrometre resolution without sectioning. However, imaging of the entire organoid is not always necessary because with an imaging depth of 150 μm, part of the organoid that is representative of the entire structure can be successfully imaged even in the largest organoids, thanks to their spherical organization. Should 3D imaging of entire organoids prove worthwhile, aberration correction methods could be utilized with FFOCT to reach greater penetration depths, combined with organoid rotation and additional postprocessing. Immunohistochemistry methods rely either on staining, which adds specific colour contrast and in which the sample is mechanically sliced to provide sectioning (immunohistology), or with targeted dyes, wherein various techniques (confocal illumination/detection, light-sheet illumination, etc.) provide optical sectioning. Relying on

1

exogenous contrasts for imaging at specific time points greatly limits the structures or events that can be seen in samples and ultimately leads to the destruction of the sample, as these techniques all require sectioning, clearing or fixation steps that preclude live imaging and, therefore, monitoring of the development of the same sample over a long period of time. D-FFOCT is not only a unique technique that combines high spatial and temporal resolution but also a non-destructive approach that provides the possibility of following the development of the same organoids over time throughout development. This process could be automated by integrating the D-FFOCT setup directly inside a cell culture incubator under a CO_2 atmosphere. D-FFOCT can therefore offer new biological insights such as cellular motility, tissue development and organization and dynamic profile evolution and comparison.
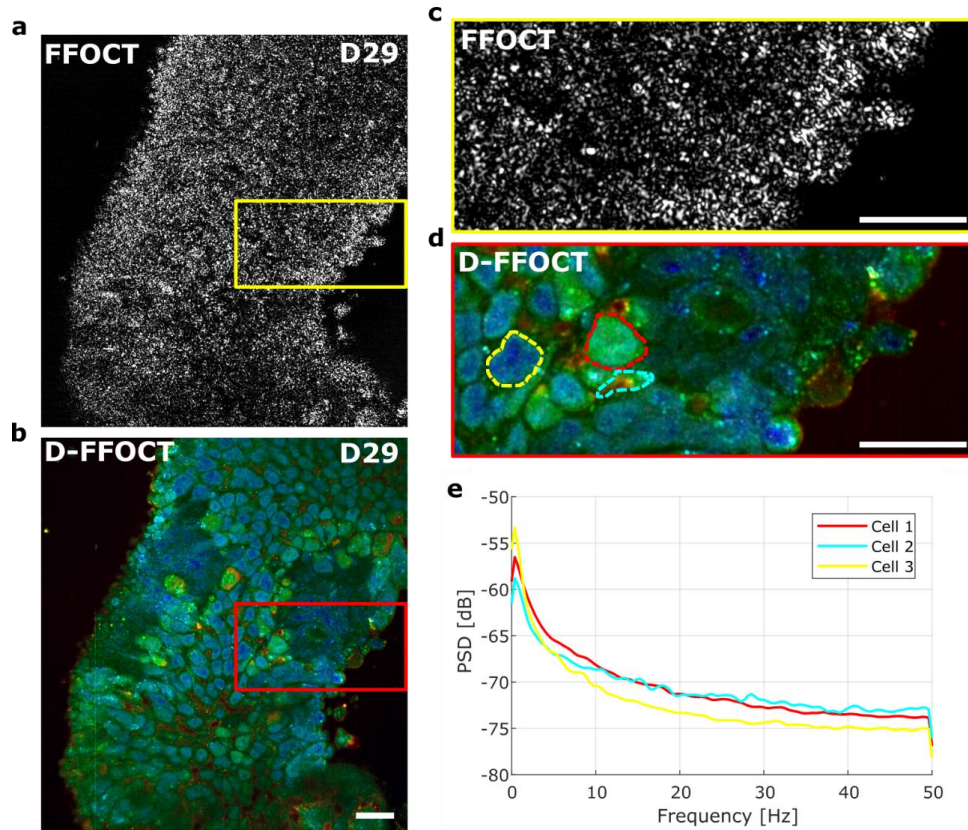
Figure 1: Comparison between FFOCT and D-FFOCT images on a D29 organoid. (a) FFOCT image of a D29 retinal organoid with (b) the corresponding D-FFOCT image. The FFOCT image was acquired using a 2-phase bucket scheme using a piezoelectric actuator to move the reference mirror [25] and extract the interferometric signal. 256 FFOCT amplitude images (corresponding to a total of 512 acquired images with 256 images for each phase) were averaged to obtain the final output. The D-FFOCT image was acquired with 512 direct images (without using piezoelectric modulation) and exhibits much higher contrast on cells. (c) Magnification of the FFOCT image (a) with the corresponding magnification of the D-FFOCT image (d). The mean power spectrum density was computed using Welch's method on the 3 cells drawn with the dashed line in (d) on graph (e). Scale-bar: 20 μm.

2
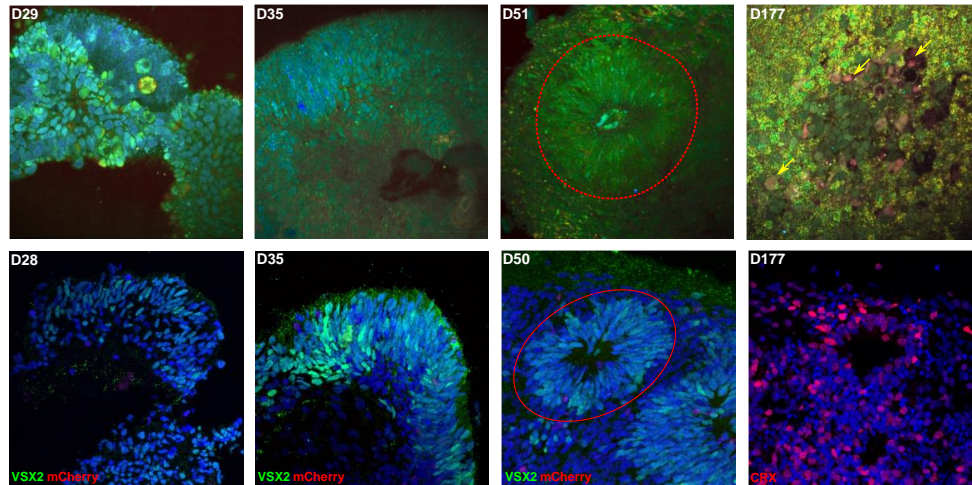
Figure 2: D-FFOCT imaging (top) and immunohistochemistry images acquired with confocal microscopy (bottom) of distinct retinal organoids at four equivalent stages of development. On D29 and D35, organoids are mainly composed of multipotent retinal progenitor cells expressing the Visual System Homeobox 2 (VSX2) transcription factor (green). At D51, rosette formation observed by D-FFOCT was confirmed by immunohistochemistry with differentiation of progenitor cells (red dotted lines). Photoreceptors can be identified in immunohistochemistry by CRX expression in rosette structures at D177 and are seen in DFFOCT as blue-green cells in the rosette centre (white arrows). In addition, the D-FFOCT image shows putative inner retinal neurons (identified due to their position around the edge of the rosette [15]) in red (yellow arrows). Nuclei are counterstained with DAPI (blue). The field of view of D-FFOCT images has been reduced to correspond to the field of view of the confocal images. Scale bar: 50 μm.
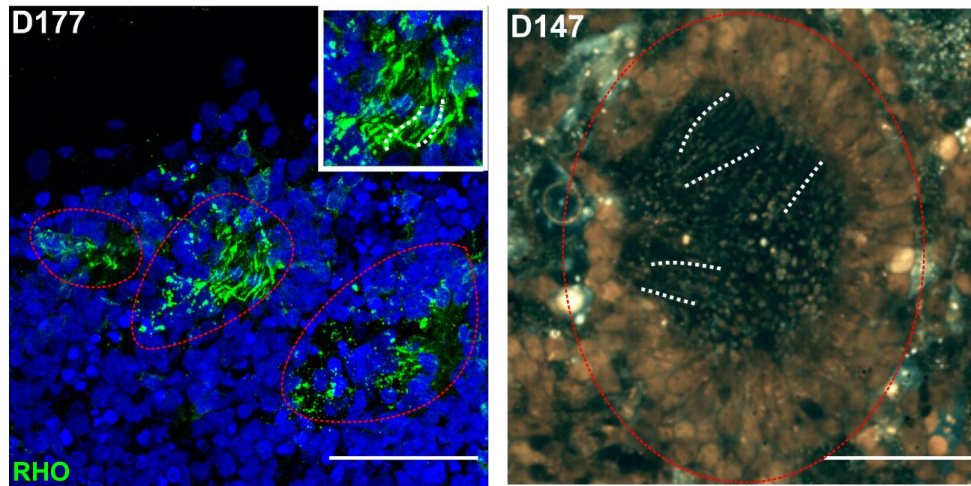
Figure 3: Immunohistochemistry image (left) acquired with a confocal microscope of a D177 retinal organoid wherein photoreceptor outer segments containing rhodopsin (green fluorescent label) are visible inside rosettes (red dotted lines). The magnified image in the top right corner highlights photoreceptor outer segments (green filaments, annotated with white dotted lines). Nuclei are counterstained with DAPI (blue). D-FFOCT image (right) of a similar retinal organoid at D147 showing a rosette (red dotted line) containing photoreceptor outer segments (white dotted lines), similar to those in the immunohistochemistry image. Rosette sizes can vary greatly and happen to be smaller in the organoid on the left than in the organoid on the right. The D-FFOCT field of view has been cropped to match the immunohistochemistry image; see Supplementary Vid. 4 for the whole field of view. Scale bar: 50 μm.

3

Supplementary files information

Video 1:

Depth stack of the D28 hiPSC-derived retinal organoid shown in Fig. 2(a-c). Planes from top 0 μm to approximate center of the organoid 101 μm, in 1 μm steps are shown revealing the internal structure of the organoid.

Video 2:

Time-lapse video with 1 min temporal resolution of the evolution of the D28 hiPSC-derived retinal organoid shown in Fig. 2(d). Video shows the evolution of the whole organoid over three hours of imaging, with three magnifications corresponding to the zones depicted in Fig. 2(d).

Video 3:

Time-lapse video with 1 min temporal resolution of the evolution of the D29 hiPSC-derived retinal organoid shown in Supplementary Fig. 2. Video shows the evolution of the whole organoid over three hours of imaging.

Video 4:

Time-lapse of the D29 hiPSC-derived retinal organoid and of the D28 hiPSC-derived retinal organoid. Both organoids exhibit the same consistent colormap and structures demonstrating that D-FFOCT can reliably images different samples at different times consistently.

Video 5:

Time-lapse video with 1 min temporal resolution of the evolution of a D42 hiPSC-derived retinal organoid. Video shows the evolution of the whole organoid over three hours of imaging, especially the behaviour in a rosette.

Video 6:

Time-lapse video with 5 seconds temporal resolution of the evolution of a D147 hiPSC-derived retinal organoid with zoomed areas. Zoomed areas have a temporal resolution of 1 second and highlight the sensitivity of D-FFOCT to dynamic phenomena. The colors are computed like the images of Fig. 2(f-h).

4

Chapter 4

Detection of cell stress with D-FFOCT

In this chapter, I got further in the explanation of the dynamic signal and the use of of D-FFOCT for the study of degenerative diseases on RPE cell cultures, in a collaborative work with Sacha Reichman and Anna Verschueren at the Institut de la Vision.

I designed and performed the D-FFOCT setups and experiments, and I wrote the codes to analyse the results. Anna Verschueren, post-doctoral student, designed and performed immunohistochemistry experiments for dynamic signal validation.

4.1   Scratch assays: towards disease modeling

The retina is touched by numerous degenerative diseases. Some of these diseases begin in the RPE cell layer.

In order to model a degeneration disease, we wanted to create a stress in the RPE cell layer. By creating a hole in the cell layer, we can study the behaviour of the cells following this induced stress. We decided to perform scratch assays to create this stress, with a scalpel blade on RPE cell cultures. Moreover, by creating a physical stress, we can differentiate the cells whether they are far from the wound or close to it: "normal" cells and "stressed" cells respectively. The idea was to create a program that would be able to evaluate this behaviour in acquisitions of several hours. Two parameters of the wound are usually evaluated: the width and the area of the wound. By calculating the evolution of the width of the wound, we can determine the speed of closing. The evolution of the area helps calculate the wound closure which determine the percentage of closure of the wound over time.
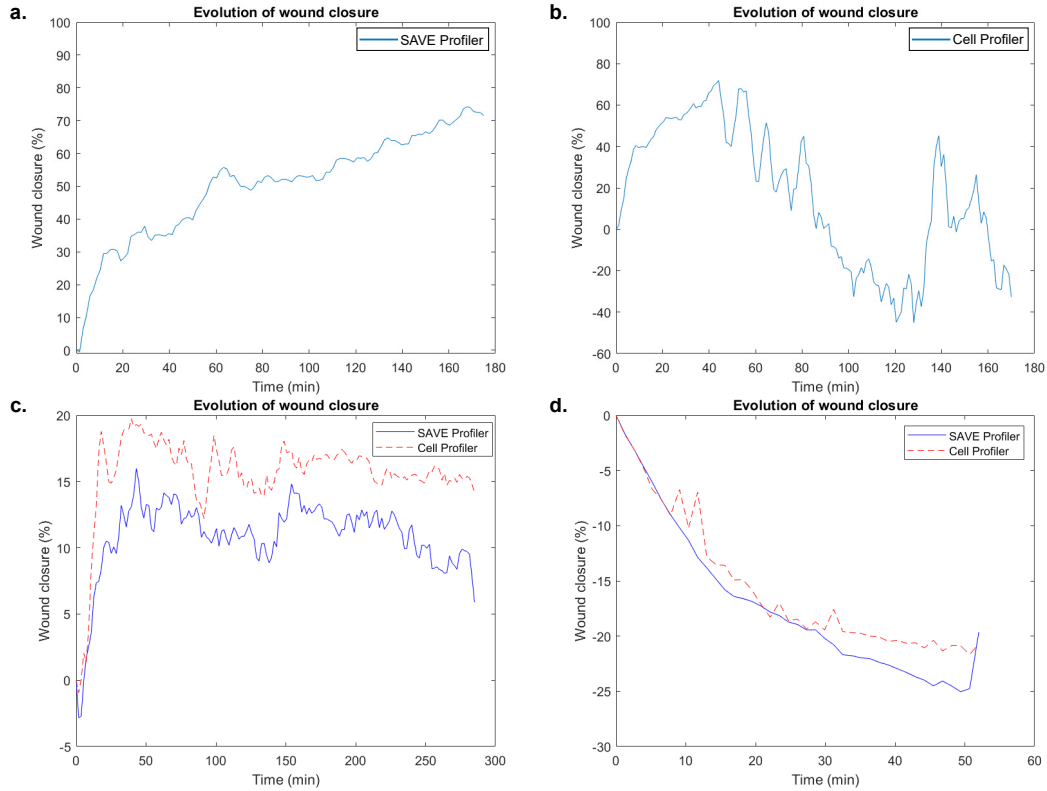
Figure 4.1: **Comparison of wound closure results with our SAVE Profiler and Cell Profiler on hiRPE scratch assays. a. & b.** Results on a closing scratch assay for SAVE Profiler and Cell Profiler respectively. **c.** Results on a failing to close scratch assay. **d.** Results on an expanding scratch assay.

I developed a software in Matlab to analyse the results of scratch assays, called SAVE Profiler (Scratch Assay Velocity Evolution). This software is a semi-automated segmentation and analysis Matlab code for scratch assays. The stack of grayscale images is first binarized to differentiate the wound (0) from the cells (1). As the intensity level can variate from an acquisition to another, the software first shows the user a default level, which can be accepted or changed by the user. Moreover, some variations in intensity can also be observed through an acquisition: two different levels can be chosen for the first and the last image. The threshold is then smoothed linearly from the first to the last image. Then, the direction of the scratch on the images is retrieved by the user. The images are automatically rotated to get the scratch on a vertical direction on the images. The user is finally asked to draw the contour of the wound on the first image (for a closing or failing to close evolution) or the last image (for an expanding evolution), which will serve as margins to avoid noise coming from cell interstices. Finally, the software calculates the different parameters described above to evaluate the evolution of the scratch assay.

The validation of the evaluation of speed by our SAVE Profiler was done with the Optical Flow calculations in Matlab, using the Horn-Schunck method [22]. We obtained very similar results, validating our SAVE Profiler for the speed calculation.
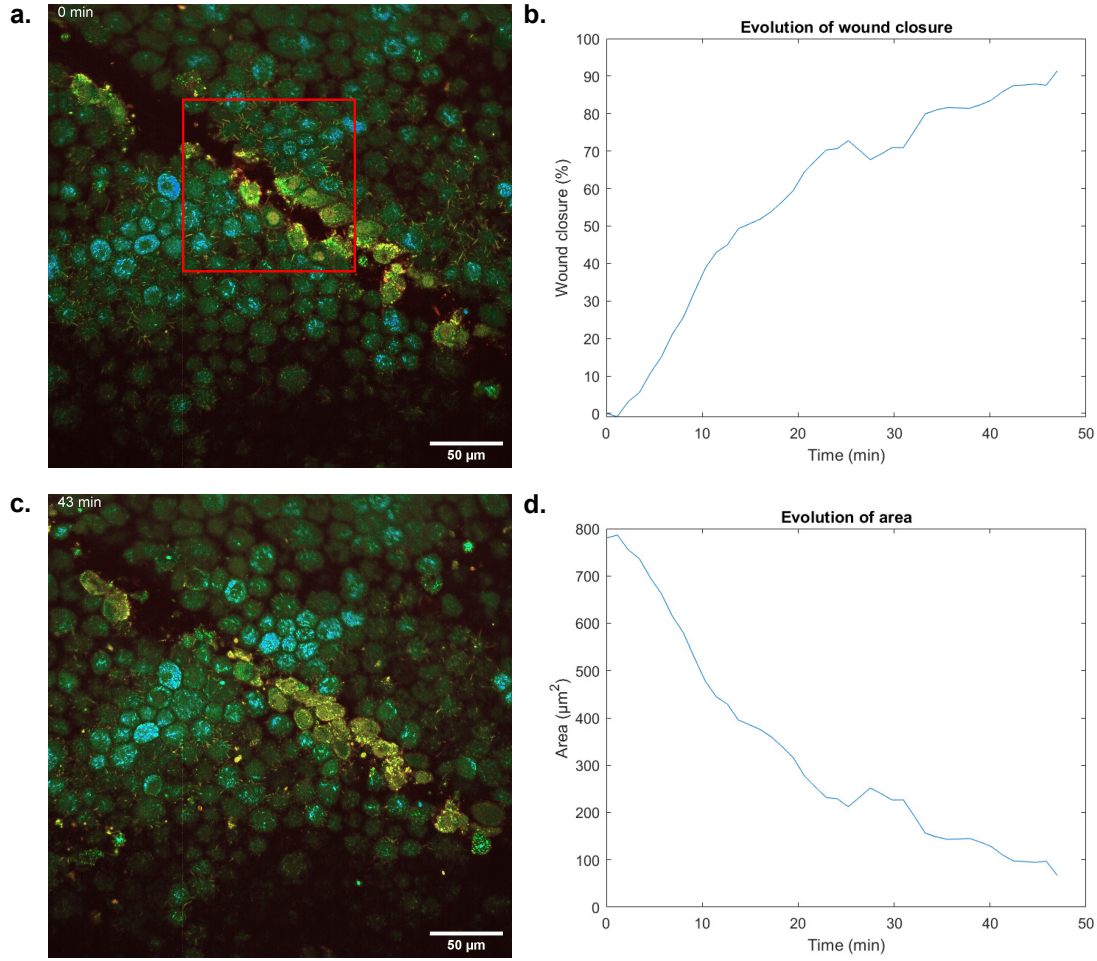
Figure 4.2: **Results with a semi-automated segmentation. a. & c.** First and last images of an acquisition of a closing ppRPE at the beginning and end of the acquisition. The red square shows the area where the calculations are done. **b.** Wound closure results. **d.** Evolution of the area.

To validate the wound closure calculations, we used the Cell Profiler software [73]. The Cell Profiler automatically segment the images and calculates the proportion of the area effectively occupied by cells. However, the process of calculations is slow and not as efficient as our semi-automated segmentation, as shown in Fig.4.1. The Cell Profiler does not manage the fluctuations of intensity inside the cell layer obtained in D-FFOCT images: it adds "wound" inside the "cells".The final results of wound closure were acceptable for failing to close (Fig.4.1 c.) and expanding (Fig.4.1 d.) scratch assays but not for closing scratch assays (Fig.4.1 a. & b.).

In order to compare the segmentation part of our SAVE Profiler, we tried manual segmentation on a closing ppRPE (acquisition of 40 minutes, shown in Fig.4.2) and performed the rest of the SAVE Profiler. In Fig.4.3 a. and c. are shown the manual segmentation results at the beginning and the end of the acquisition. The wound closure and evolution of area are shown in Fig.4.3 b. and d. The results are similar to those of our SAVE Profiler shown in Fig.4.2 b. and d. The manual segmentation took half an hour against 30 seconds for the segmentation in our SAVE Profiler.
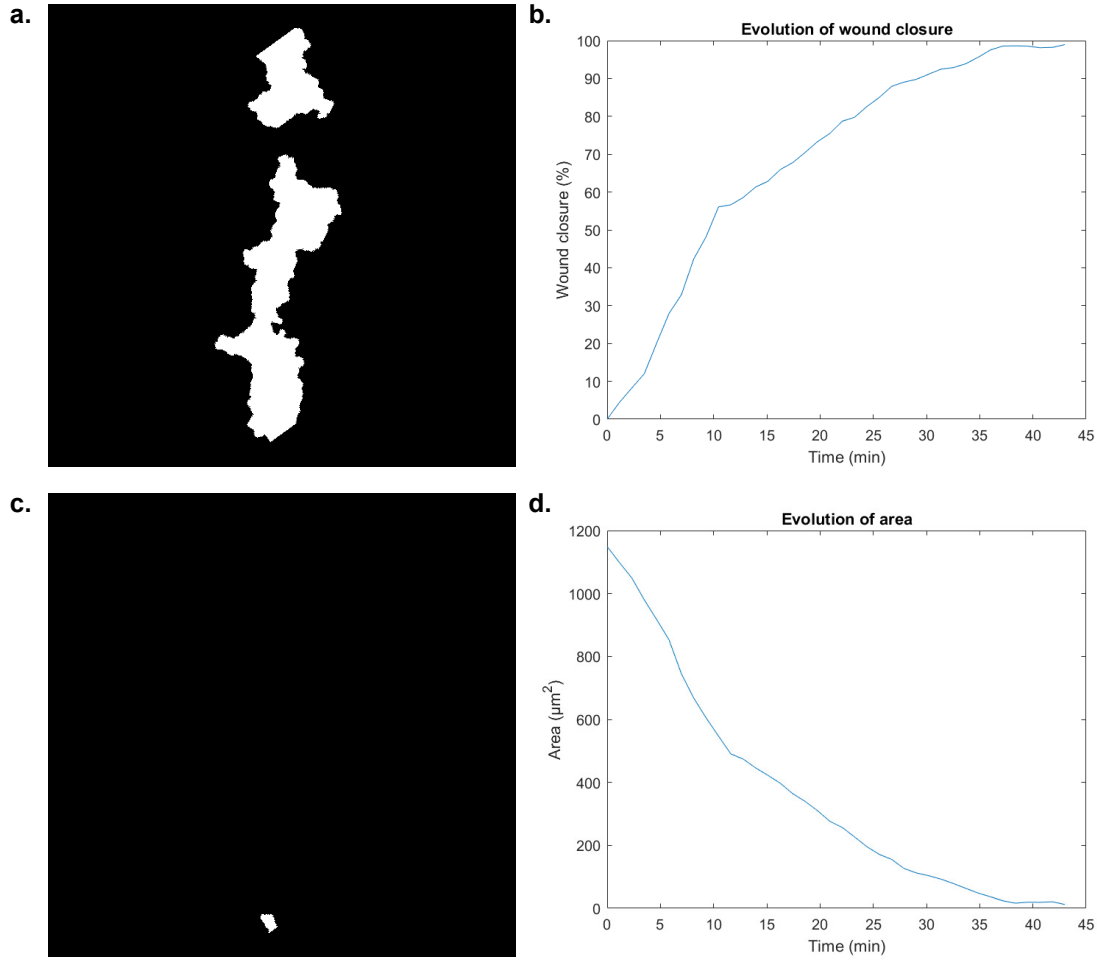
Figure 4.3: **Results with a manual segmentation. a. & c.** Manual segmentation on a closing ppRPE at the beginning and end of the acquisition. **b.** Wound closure results. **d.** Evolution of the area.

This software would allow studies of degenerative diseases modeling by analysing D-FFOCT images for further understanding of the diseases and testing of drugs.

4.2 Dynamic profile: further understanding of the contrast

The usefulness of D-FFOCT has been proven multiple times since the first presentation in 2016 by Apelian et al. [67]. The coding of D-FFOCT signal in RGB was then demonstrated, showing a new contrast that can discriminate areas in a sample by the frequency of the subcellular movements [68, 69]. The team then showed at multiple occasions that D-FFOCT signal can discriminate cell type or behaviour, with a fluorescence validation [22, 23, 71]. But no one yet has explained the origin of D-FFOCT signal: which parts of the cell were responsible for the dynamic profile observable with D-FFOCT.

D-FFOCT images reveal a specific contrast enabling the visualisation of intrinsic sub-cellular movements, which we call dynamic profile. When we look at a cell, it is composed of multiple organelles which are moving to contribute to the survival of the cell by the transport of nutrients, proteins, etc. Our first thought was to use inhibitors of different organelles on a cell culture to evaluate if it takes part in the dynamic profile of a cell. We knew that two main organelles are moving in cells: mitochondria and vesicles, produced by the Golgi apparatus. With the help of biologists from the Vision Institute, I obtained two drugs: Brefeldin A, whose role is to disassembly the Golgi apparatus, and

66

CCCP which impact mitochondria by uncoupling their oxidative phosphorylation (protein synthesis). Usually these drugs are used on fibroblast cell cultures, as these cells are very flat and have a huge surface to see any changes in organelles activities in fluorescence imaging. Unfortunately, fibroblasts are very bad candidates for D-FFOCT imaging: as a very flat cell, it creates the same artefacts that can be observable with a mirror which are fringes created by the interferometer. We decided to try with Retinal Pigment Epithelium (RPE) cell cultures which are less flat. Specific protocols for use of these drugs in RPE cell cultures were not available in the literature. We therefore administered similar drug quantities to those used in the fibroblast protocols. Results were however inconclusive, showing no changes after the drugs were added. At this stage, due to the experimental complexity of applying potentially toxic drugs in the optics laboratory environment, we therefore decided to explore alternative ways to validate DFFOCT signals.

The easiest way is to compare our technique to the gold standard in biology: fluorescence imaging. As a full field technique, D-FFOCT can be combined with wide field fluoresence [22,23,71,72]. This has allowed us to image in both fluoresence and D-FFOCT modalities with pixel by pixel correspondence for accurate validation of D-FFOCT in isolated cells or zones of a 3D sample. However, wide field fluorescence lacks optical sectioning, meaning that fluorophores distributed throughout a 3D sample cannot be distinguished. Therefore, imaging organelles of the size of few micrometers is not possible with our multimodal system. To overcome thisproblem, we decided to use two different techniques and compare the images after the experiments: D-FFOCT and confocal fluorescence microscopy (labelling with immunohistochemistry) as shown in Groux et al., 2021 [24]. We faced the problem of sample-holder: D-FFOCT requires culture membranes while confocal microscopy requires coverslip for the fixation and manipulation. Two sets of samples were prepared in parallel: one set on Poly-Carbonate membranes for D-FFOCT and one set on coverslip for fluorescence imaging. This means we only compared similar samples. We need to have two distinguish state for a cell in order to see the variations in organelles' behaviour. Inducing stress is the most simple possibility. Scratch assays allow to stress only a few cells of the culture and they are easily identifiable. The scratch assays were performed with a scalpel blade on the cell layer. Observing the stressed area with D-FFOCT, we observed that the cells close to the wound exhibit a different dynamic profile, meaning the phenotype in these cells was impacted by the stress. The phenotype is governed by the organelles present in the cells. In order to identify the origin of the changes in phenotype, we tested multiple organelles in immunohistochemistry in two types of cells: stressed cells close to the wound, and normal cells far from the wound.

Different organelles and phenotypes were tested:

- mitochondria, using two different labels: mCoxIV and ATP synthase

- nuclei using DAPI

- actin filaments using phalloidine

- lysosomes using two labels: LAMP1 and CATSD

- golgi apparatus using TGN46

- dying cells labelled with propidium iodide

These experiments allowed us to identify and validate the dynamic profile. Actin filaments are part of the cytoskeleton, the microvilli and the filipods. Cytoskeleton is a static part of the cell: it appears dark on D-FFOCT images. On the other hand, microvilli and filipods are active actin filaments: microvilli try to make connection with the photoreceptors outer segments, while filipods make the link between the cells. That

is why they are visible in D-FFOCT and exhibit a fast and intense dynamic profile. Golgi apparatus exhibit the same signal for stressed cells and normal cells in immunochemistry images. We concluded that Golgi apparatus contribute evenly to the dynamic profile of cells. We identified two organelles contributing to the signal of stressed cells. First, lysosomes appears in dying cells in immunochemistry. Those cells in D-FFOCT had a very active signal (red and intense). As shown in Groux et al., 2021 [24], mitochondria are the organelles which exhibit the more changes if we compare stressed cells and normal cells. Their organisation is modified in stressed cells and dying cells [74–76]. Indeed, in normal cells, the mitochondria are organised in a network in the cells, appearing as linked filaments in immunochemistry images. On the contrary, in stressed or dying cells, the mitochondria progressively change their organisation from a network to separated mitochondria, looking like dots in immunochemistry images. Given that, these modifications impact the dynamic profile of cells in D-FFOCT images: the dynamic profile becomes more intense and goes from a range of blue-green to yellow and then red (i.e. faster dynamics). We therefore concluded that mitochondria are the main contributor of the D-FFOCT signal.

4.3   Towards more repeatable scratch assays: laser cutting

In order to improve the repeatability and precision of the scratch assays, I decided to build a setup combined with a laser to use it as a cutting tool (Fig.4.4). For this purpose, I need to construct a system where the laser beam can be directed easily on the sample to create precise cuts in the cells. A custom-made laser, centered at 805 nm (kindly given by the student labs of the ESPCI), was associated to 2D galvo mirrors from Thorlabs (GVS102), which are conjugated with the back focal plane of the objectives in order to scan the sample with the laser beam (controlled with a shutter SH05 from Thorlabs). I also salvaged an old commercial FFOCT system from LLTech [77] which allowed me to get the microscope objectives of this system to create my new setup. The microscope objectives are made for water-immersion (UMPLFLN10XW, Olympus), with a smaller NA than the microscope objectives of my other systems. With this microscope objectives, I get a transverse resolution of $1.3 \mu m$ (see Appendix A for more details on the specifications of the microscope objectives and on the construction of a FFOCT system). For the FFOCT part of this system, I used a M625L3 LED from Thorlabs, the microscope objectives mentioned above, a BS013 beamsplitter (50:50 coated for 400nm - 700nm) from Thorlabs and a AC254-400-A lens from Thorlabs to focus the image on the Adimec camera. As the microscope objectives have a low NA, the axial resolution of the FFOCT system is ruled by the coherence length of the light source. In this case, I obtained an axial resolution of $7.6 \mu m$. The galvo mirrors were interfaced in Matlab, with the imaging interface, in order to control their movements and speed.

Once the system was built, I faced a few problems. First, as the laser was custom-made and used in student labs, the beam was far from perfect: it was diverging a lot which leads to loss of power and a too big spot on the sample. To solve this, I tried to collimate the beam with a low magnification microscope objective, but the beam was still too big. A second problem was the microscope objectives used for my system. As the axial resolution is ruled by the coherence length in this case, I obtain a quite large axial resolution for the imaging of a cell layer. This created difficulties to align the system, making it practically impossible without damaging the sample. I decided to try other microscope objectives I had in the experimental room: air objectives with a numerical aperture of 0.7 (UCPLFLN20X, Olympus). I obtained a transverse resolution of $0.54 \mu m$ and an axial resolution of $1 \mu m$. However, I faced a new problem: these objectives do not need an immersion medium and have a very low working distance (0.8mm, meaning I need a very small layer of culture media on the sample if I want to image it). The diameter of

those objectives is of 29mm while the diameter of the membrane where the cell are grown (Corning 3412) is of 24mm, which do not allow to reach the working distance.
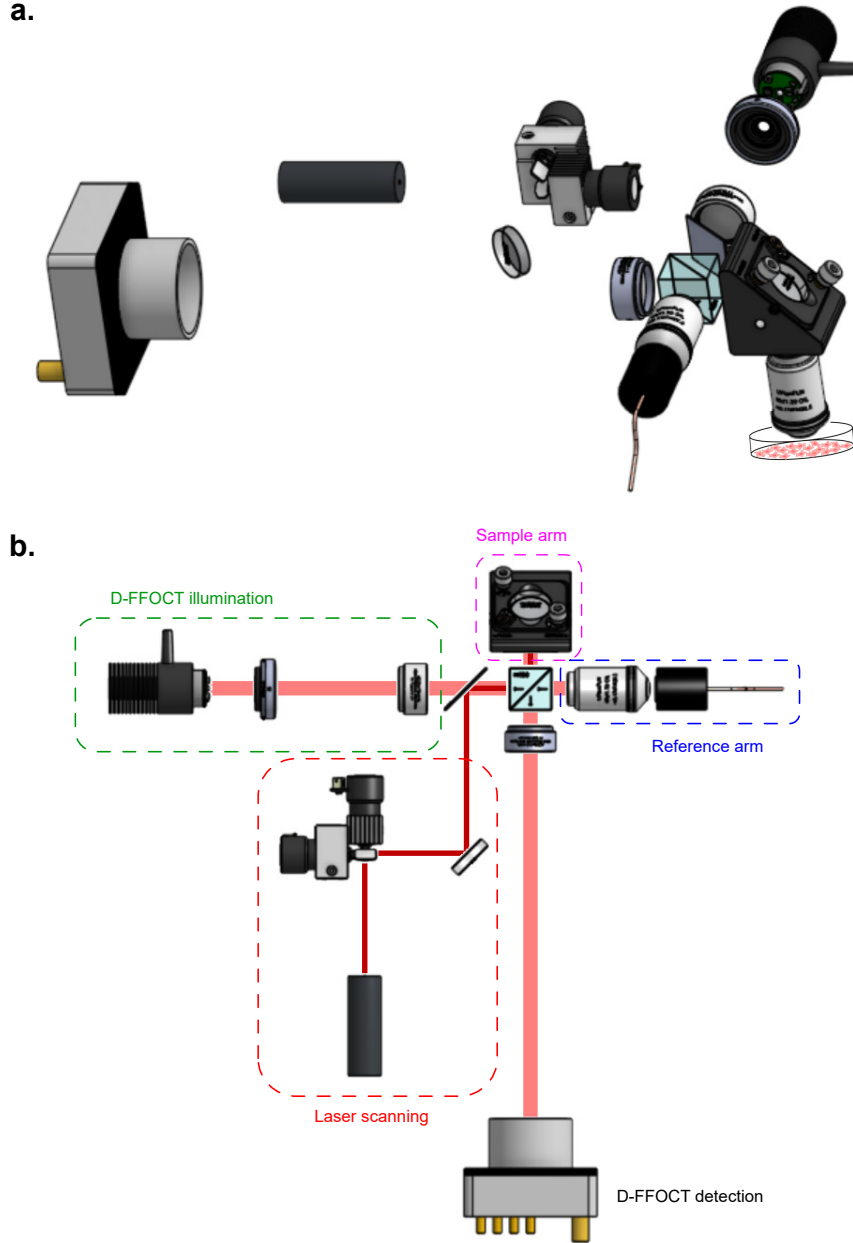

Figure 4.4: **Schematic of the laser-cutting D-FFOCT setup. a.** Side view of the setup. **b.** Top view of the setup with identification of the different parts.

My perspectives are to improve the elements of our system: a new laser with much more power and a smaller beam diameter, but also other microscope objectives, similar to those of my setup for imaging cell cultures.

4.4 Imaging of microvilli in real-time

In chapter 2, I showed the application of D-FFOCT to retinal organoids imaging. In this perspective, we tested a new modality for the imaging of the organoids: the imaging in real-time. This was possible thanks to a software developed in our lab by Michael

Atlan called Holovibes [78]. This software is originally designed for the computation of holographic images in real-time. Michael Atlan's team kindly modified the software for the computation of D-FFOCT images in real-time. As it requires heavy computation, we had to make a compromise on the rendering of the images. The speed of rendering needs a compensation: the images are obtained in grayscale and not in color with the value channel of HSV computation, representing the intensity fluctuations in the stack of raw images. For this purpose, the images were acquired at $150Hz$ continuously. For fast rendering, Holovibes uses 128 images to create D-FFOCT images. The first image is computed, then the software waits the next 16 new images and used the 112 previous images to create a new D-FFOCT image allowing real-time imaging. On retinal organoids, we were able to observe organelles moving inside cells and also to differentiate nuclei by their state in the mitosis cycle.

With these promising results, I decided to test real-time imaging on *in vitro* RPE cell cultures. As shown in chapter 1, RPE cells present microvilli on their apical surface. Microvilli are very active parts of RPE cells because they grab photoreceptors outer segments in the retina. While imaging them with "regular" D-FFOCT, I observed that they were exhibiting a bright and red dynamic profile, consistent with their known activity. Microvilli have been previously imaged with phase contrast imaging, immunohistochemistry and electronic microscopy [25, 30, 31, 79]. These techniques allow to image the structure of the microvilli but do not permit to observe their movements. I tested the D-FFOCT imaging in real-time on the top of a primary porcine RPE cell culture and observed that microvilli. Some images were averaged to obtain a better contrast but the movements of microvilli were clearly visible. To our knowledge, this is the first time in literature that microvilli are imaged in real-time. The perspectives are to study the activity of the microvilli by adding macrophages or photoreceptor outer segments on the culture. We expect to observe the phagocytosis of microvilli by the macrophages, which is their function in the retina to clean the retina from the waste. For the photoreceptor outer segments, we expect to image the grabbing of outer segments by a part of the microvilli, which helps maintaining the integrity of the retina *in vivo*.

4.5 Article: "Detecting cell stress on RPE cell cultures with Dynamic Full-Field OCT"

Non invasive live imaging of a novel RPE stress model with Dynamic Full-Field OCT

Kassandra Groux[1,2], Anna Verschueren[2,3], Céline Nanteau[3], Marilou Clémençon[3], Mathias Fink[1], José-Alain Sahel[2,3,4,5], Claude Boccara[1], Michel Paques[2], Sacha Reichman[3] and Kate Grieve[2,3*]

[1]Institut Langevin, ESPCI Paris - PSL, CNRS, 10 rue Vauquelin, Paris, 75005, France
[2]Paris Eye Imaging Group, Quinze-Vingts National Eye Hospital, INSERM-DGOS, CIC 1423, 28 rue de Charenton, Paris, 75012, France
[3]Institut de la Vision, Sorbonne Université, INSERM, CNRS, 17 rue Moreau, Paris, F-75012, France
[4]Department of Ophthalmology, Fondation Ophtalmologique Adolphe de Rotschild, F-75019 Paris, France
[5]Department of Ophthalmology, The University of Pittsburgh School of Medicine, Pittsburgh, PA 15213, United States of America
*kategrieve@gmail.com (Supplementary available on request)

Abstract

Retinal degenerative diseases lead to the blindness of millions of people around the world. In case of age-related macular degeneration (AMD), the atrophy of retinal pigment epithelium (RPE) precedes neural dystrophy. But as crucial as understanding both healthy and pathological RPE cell physiology is for those diseases, no current technique allows subcellular *in vivo* or *in vitro* live observation of this critical cell layer. To fill this gap, we propose dynamic full-field OCT (D-FFOCT) as a candidate for live observation of *in vitro* RPE phenotype. In this way, we monitored primary porcine and human stem cell-derived RPE cells in stress model conditions by performing scratch assays. In this study, we quantified wound healing parameters on the stressed RPE, and observed different cell phenotypes, displayed by the D-FFOCT signal. In order to decipher the subcellular contributions to these dynamic profiles, we performed immunohistochemistry to identify which organelles generate the signal and found mitochondria to be the main contributor to D-FFOCT contrast. Altogether, D-FFOCT appears to be an innovative method to follow degenerative disease evolution and could be an appreciated method in the future for live patient diagnostics and to direct treatment choice.

Article

Introduction

The retinal pigment epithelium (RPE) is the most external layer of the retina, placed between the photoreceptors which collect the light and the blood supply from the choroid [1]. The RPE layer is affected in degenerative diseases such as age related macular degeneration (AMD) [2–4]. AMD is one of the leading causes of blindness in developed countries, affecting 170 million people worldwide [Klein et al 2011] [5]. In late form dry AMD, called geographic atrophy (GA), it may lead to expanding atrophic foci of the RPE. Little is known about the mechanisms underlying the propagation of RPE atrophy. Animal models were used to model AMD. However, the environmental conditions are less controllable than for a cell-based model, such as RPE cells [6], used to test drug therapies or the involvement of proteins in AMD. By following the behavior of RPE in culture in response to damage, we take a step towards mimicking formation of geographic atrophy (GA) lesions in AMD. Future developments will use multi-layered cell-based models, including other layers of the retina or the choroid to match *in vivo* conditions.

Dynamic Full-Field OCT (D-FFOCT) has recently been presented as a non-invasive live imaging technique suitable for the study of 2D and 3D cell cultures [7, 8]. Intracellular organelle movement is known to generate the D-FFOCT signal, but the precise identity of the organelles has not yet been deciphered. RPE cells have also been imaged with electron microscopy [9], but this technique does not allow live-cell imaging, preventing the imaging of organelle dynamics. Live-cell imaging is possible with several imaging techniques, but certain requirements have to be met. It is important to keep the cell cultures healthy to image them over long periods of time, meaning avoiding photo-toxicity. Imaging methods such as fluorescence imaging techniques, multiphoton microscopy, or widefield systems, have been applied to live-cell imaging [10]. However, many of these techniques require the use of invasive fluorophores, preventing continued use of the sample after the imaging. Others, such as widefield systems, usually have a low lateral resolution and do not have optical sectioning for 3D imaging. The use of spinning-disc confocal microscopy for RPE live-cell imaging has been demonstrated [11, 12], but shows significant problems with autofluorescence background in images and the impossibility to reuse the samples after the imaging due again to the use of invasive fluorophores.

In this article, we propose the use of D-FFOCT to perform non invasive live imaging of RPE cell cultures. We validate a novel RPE stress model, provide a new tool to quantify RPE wound healing parameters, and identify the organelles responsible for the D-FFOCT signal.

1

Results

RPE stress model and quantification methods   Primary porcine RPE cell cultures (ppRPE) (n=5), which have the advantage of being highly pigmented as human mature RPE cells, and human induced pluripotent stem cell derived RPE (hiRPE) at an early development stage (unpigmented) [13, 14] (n=9) were grown on poly-carbonate (PC) membranes. The setup used for D-FFOCT imaging is shown in Fig.1 A. We followed the evolution of the RPE cell cultures over periods from 1 to 6 hours (3 hours on average) of D-FFOCT live imaging after inducing stress. Stress was created by performing a scratch assay on the cell layer with a scalpel blade, allowing us to generate a focal and easily reproducible stress damage to the epithelium as shown in Fig.1 B (see Materials and methods). Fig.1 C shows a D-FFOCT image of an intact ppRPE sample with the corresponding colorbar, where the three channels H, S and V of image processing (see Materials and methods) are represented in the lower left corner. Sets of parallel cultures were imaged at fixed timepoints with immunohistochemistry (an histology technique using bio-engineered antibodies coupled with fluorescent probes to stain specific proteins and cellular structures within tissues), in order to identify the organelles generating the D-FFOCT signal.

Depending on the origin of the cells (ppRPE or hiRPE) and the width of the scratch, cell behaviours differed. Two main features are usually used to quantify wound healing: the speed of closure, i.e. the evolution of the width of the scratch, and the wound closure, measuring the evolution of the area of the scratch [15]. Semi-automatic segmentation based software, named Scratch Assay Velocity Evolution (SAVE) Profiler, (see Materials and Methods), was developed to segment the wound and calculate the width and area of the scratch in order to quantify wound closure. Our SAVE Profiler method outperformed the reference methods using optical flow calculations [16] and the Cell Profiler using the Wound Healing example [17].

RPE behaviour observed after stress   In this RPE stress model, we separated three cases: scratches inferior to $25\mu m$ wide (Fig.1), scratches between 25 and $100\mu m$ (Fig.2, and scratches superior to $100\mu m$ (Fig. supplementary 1).

Figure 1 shows wound closure on both ppRPE (1 D to J) and hiRPE (1 H to K) cell cultures for scratches smaller than $25\mu m$. In a ppRPE sample, after 47 min, the wound was completely closed (Fig.1 D) (see the whole acquisition in Movie S2). Calculations of scratch assay evolution were made over a small area (white dotted square on Fig.1 D) to reduce calculation time. Fig.1 F plots the wound closure, which represents the evolution of the wound area, as calculated with the SAVE profiler. A quasi complete closing was achieved, with the wound closure reaching over 90% during the acquisition. Fig.1 E represents the evolution of the mean scratch width (blue points). This evolution could be fitted with a double exponential $f(x) = a \times exp(b \times x) + c \times exp(d \times x)$. The characteristic time of closing obtained with this fit was approximately 18 minutes. The closest distance of closing of around $1\mu m$ was reached after 23 minutes, corresponding to the average interstice between cells which is not affected by the scratch. Average wound closing speed for this ppRPE sample was thus calculated to be $15.7\mu m/h$. Fig.1 G presents an optical flow calculation over the same area. The velocity of movements throughout the acquisition is shown, with two fronts of motion in opposite directions revealed by the arrows. By averaging the velocities (i.e. the absolute values without taking the direction into account) plotted in Fig.1 G, the medium speed of one front can be calculated as $8.25\mu m/h$. As there are two opposite moving fronts, the total velocity of closing is the multiplication of the average speed of one front by 2, giving a total speed of $16.5\mu m/h$. This result is consistent with the results obtained with our custom-written SAVE profiler software. The same analysis was performed on hiRPE cell cultures (Fig.1 H to K) (see the whole acquisition in Movie S3). Fig.1 H shows the cell layer, almost closed, 103 minutes after the first image was acquired. The white dotted square on Fig.1 H represents the area over which calculations were performed. The wound does not completely close (Fig.1 H), reaching an average wound closure of 70% (Fig.1 J). As for the ppRPE scratch assay, the mean scratch width was plotted in Fig.1 I, where it could also be plotted with a double exponential. In this case, the characteristic time of closing was around 55 minutes, and an average limit of $2.5\mu m$ was reached after approximately 60 minutes. The average speed of closing was therefore $6.5\mu m/h$. The results of the optical flow method are shown in Fig.1 K, clearly showing two borders which progress in two different directions, but the upper border is more active than the lower (see the aspect of arrows in Fig.1 K). The average speed calculated on the optical flow representation was $4.05\mu m/h$, or multiplying this result by 2 to be cohesive with two different borders, we obtain $8.1\mu m/h$, consistent with the results of the SAVE profiler. The SAVE Profiler was validated on the Wound Healing example of Cell Profiler. Cell Profiler showed less effective segmentation (Fig.1 M for the ppRPE sample and O for the hiRPE sample) as it does not uniquely target the wound. The Cell profiler results of wound closure (in Fig.1 L and N) are therefore not consistent with our observations. Moreover, SAVE profiler was twice as fast as Cell Profiler.

As the scratch assays were performed manually with a scalpel blade, the initial width of the wound could vary. In wounds sized between $25\mu m$ and $100\mu m$, the wound failed to close. Fig.2 presents failure of wound closure on wounds of greater than $25\mu m$ width in ppRPE and hiRPE. In ppRPE ((Fig.2 A) (see the whole acquisition in Movie S4), the first and the last images of the acquisition are 665 minutes apart. Calculations were performed over the area in the white dotted square. The evolution of the scratch width (Fig.2 B) and the

wound closure (Fig.2 C) show that the cell layer first tends towards closure for the first 50 minutes, followed by a period of retraction. Fig.2 D presents the results of the optic flow calculations: the arrows show an initial movement towards wound closure, but the inside of the wound remains stationary, in contrast to wounds under 25 μm size in Fig.1. hiRPE generally showed similar behaviour (Fig.2 E-H) (see the whole acquisition in Movie S5). Two cells appear with a higher velocity: these cells were dying and detached from the border of the wound. Cell Profiler was more effective on non-closing than on closing wounds and gave consistent results with those calculated with SAVE Profiler (see Fig.supplementary 2).

In summary, small wounds (under $25\mu m$) lead to a repair of the damaged cell layer, while large wounds (between 25 and 100 μm) tend to create a movement towards closure followed by a retraction. For wounds larger than $100\mu m$, we observed a direct expansion of the cell layer with no evidence of attempt at closure as shown in Fig.supplementary 1. Comparing repair processes for the two types of RPE cells, ppRPE tend to close faster, with a mean speed between 15 and 18 μm/h, while hiRPE close with a speed between 3 and 8 μm/h. Moreover, ppRPE tend to reach a wound closure of almost 100%, while for hiRPE this is not always the case. The statistics of the scratch assays performed are compiled in supplementary Tab.supplementary 2.

Validation of D-FFOCT signal with immunohistochemistry In D-FFOCT images, the dynamic profile of the cells around the border of the scratch evolve throughout the acquisition. In order to understand which organelles were involved in these phenomena, ppRPE and hiRPE scratch assays and wound healing observed over a period of several hours with D-FFOCT were paralleled by a set of identical cultures fixed at different timepoints for immunohistochemistry validation, via fluorescent labeling of different organelles. Actin filaments (labelled using a high-affinity F-actin probe conjugated to fluorescent dye, Fig.3 A) contribute to the cytoskeleton of the cell in varied cell structures in RPE: the cell cortex (first column of Fig.3 A), the microvilli (second column of Fig.3 A) and the fillipods (last column of Fig.3 A). The cytoskeleton includes the cortex sustaining the plasmic membrane, which is static, while the microvilli and the fillipods are both very active. As the cortex is static, it appears black on D-FFOCT images, while microvilli and fillipods were very active: moving rapidly and constantly (high intensity and red) in D-FFOCT. Individual microvilli were easily visible at the surface of RPE cells on D-FFOCT images compared to immunohistochemistry images, and could be imaged in 3D by performing a stack acquisition in depth. Their movement could be followed through live image sequences using a custom GPU-computing software (Holovibes `http://holovibes.com/` [18] (see Movie S7)), for the first time to our knowledge. After a closed scratch assay, an accumulation of actin is visible in immunohistochemistry (Fig.4 D). It is composed of the border cells of the wound which seem to disintegrate after the closing, as observable in the corresponding D-FFOCT image. This is coherent with the literature [19].

Pigment particles (ovular, 2 - 3 μm x 0.5 - 1 μm) absorb light, making them visible in conventional microscopy and phase contrast microscopy (here we used Normanski interference contrast and superimposed the fluorescent phalloidin image corresponding in green as reference image). They were individually resolved throughout the D-FFOCT images in Fig.3 B. As primary cultures, ppRPE were highly pigmented, while hiRPE contained little pigment. Pigment was active but very slow moving, giving a bright blue dynamic profile in D-FFOCT. The ovular shapes measured around 3 μm x 1 μm, corresponding to the literature [9]. The difference in pigment signal between ppRPE and hiRPE is highly visible (Fig.3 B). This assumption was confirmed by phase contrast microscopy of the samples, showing a large difference in melanin concentration.

The dynamic profile was different for cells far from the wound and for cells close to the wound (Fig.3 E). The main parameter that changes in the dynamic profile was the colour, meaning the frequency of sub-cellular movements.

Golgi apparatus (cyan label) showed a uniform distribution and activity across all cells, regardless of cell damage or wounding in Fig.3 C. Golgi therefore contributed evenly to the D-FFOCT signal throughout the sample. Lysosomes (magenta label in Fig.3 C and D, using two different antigenes for confirmation), vesicles that contain hydrolytic enzyme and act as the waste disposal system of the cell, were visible in a small proportion of cells which detached from the culture and became mobile. Their high activity and mobility during late apoptosis caused them to have a bright red dynamic profile in D-FFOCT, and they tended to migrate toward the wound during closure. In cells neighboring the wound, mitochondria (yellow label in Fig.3 C and green label in Fig.3 D, using two different antigenes for confirmation) change aspect in the cells circled in yellow on stressed cell images. Therefore, we can affirm that mitochondria are involved in D-FFOCT signal. To go further in this observation, we compared immunohistochemistry imaging of mitochondria to D-FFOCT images at four different timepoints (0 hour, 1 hour, 2 hours and 3 hours) on both normal cells and stressed cells in Fig.4 A. While the mitochondria organisation in immunohistochemistry and their dynamic profile in D-FFOCT were identical over time for normal cells, we observed that mitochondria change form from a filament network to isolated round spheroids in stressed cells (two right columns), which is coherent with the literature [20–22]. These changes were visible in D-FFOCT thanks to their form, their high activity revealed by their colour changing from green to red, and their enhanced brightness. As the resolution of D-FFOCT is $0.5\mu m$, healthy individual mitochondria (diameter $0.4\mu m$) were not resolved but gave a general background signal, while the bright dots in stressed cells suggest that they are damaged mitochondria which formed larger spheres that could

3

be individually distinguished. [21, 22] Dying cells are distinguishable in D-FFOCT. Cells undergoing apoptosis or necrosis were labelled with propidium iodide (magenta label) in Fig.4 B. These cells (circled in yellow) show a condensed nucleus and a change in mitochondria organisation (green label), thus undergo apoptosis. In D-FFOCT, these cells appear with a faster subcellular activity (red dynamic profile) and a condensed nucleus with also a higher activity. The size of nuclei were measured and compared in both imaging techniques and the results were consistent (diameter under $7\mu m$ for condensed nuclei). However D-FFOCT signal is not related to dead cells: those few cells which died (showing a high concentration of lysosomes in magenta label) following apoptosis and remained mobile in the cultures are dark in D-FFOCT due to absence of organelle activity (Fig.4 C), but the structure is visible in static FFOCT, recorded in parallel, which reveals static structural rather than functional information.

Our results are confirmed by those shown in electron microscopy [9], where the RPE cytoplasm is mainly filled with mitochondria (usually arranged in a network for unstressed cells) and pigment granules (of similar size to those measured here with D-FFOCT). Electron microscopy of microvilli is also consistent with what we observed with D-FFOCT, but is not capable of showing the movements that were visible with D-FFOCT.

Discussion

D-FFOCT is able to non invasively show mitochondrial dynamics, microvilli and fillipods, and pigment distribution in RPE cells via live imaging in real time. Comparison of wound healing parameters quantified using optical flow [16], semi-automatic segmentation methods (SAVE Profiler) and Cell Profiler software [17], showed that our custom-developed SAVE Profiler succesfully combines results from both optical flow and Cell Profiler in a shorter calculation time. Wound healing parameters such as speed agreed with the literature [23]. In our experiments (between 1 hour and 6 hours), we only saw migration of cells especially for small wounds, which is coherent with Hergott et al., 1993 [23], while large wounds tend to involve proliferation. Moreover, we saw that the integrity of the membrane was important for the closing of the wound as shown in Geiger et al., 2001 [19]. Jacinto et al., 2001 [24] and Farooqui et al., 2005 [25] which show that several rows of cells participate in the closing of the wound. This phenomenon was observable on closing wounds in D-FFOCT. Filipods seem to also be involved in the closing of the wound, which is confirmed by Jacinto et al., 2001 [24]. The different methods presented to calculate the evolution of scratch assays present consistent results on the speed of either closing or expansion. Differences were observed depending on the origin and maturation stage of the sample, in accordance with the literature [15]. The experiments were performed multiple times (n=5 ppRPE; n=9 hiRPE) giving the same results each time on speed and wound closure. In small ($<25\mu m$) scratches, wounds closed at $16\mu m/h$ for ppRPE and $5\mu m/h$ for hiRPE on average. After wound closure, the actin remained thickened around the wound, some damaged mitochondria remained encompassed by other cells, and cells along the wound border remained raised above the rest of the culture surface. In wounds with large scratches ($>25\mu m$), a different behaviour was observed: an initial attempt at wound closure (cell sheet moving inwards) was overcome by a retractive movement away from the wound, with sliding of the whole cell sheet. This behaviour displays some similar characteristics to those seen *in vivo* over long (several months to years) time periods on patients with GA lesions forming [26]. The dynamic profile of cells was also consistent throughout the acquisitions: cells on the border of the wound show a faster (i.e. colour tending to yellow/red) and higher (i.e. brighter) signal than cells far from the wound. These observations on D-FFOCT images were consistent with the results obtained in immunohistochemistry, showing that mitochondria have a different behaviour in the damaged cells, and appears to be the organelles undergoing the most drastic phenotype change. In order to get closer to human *in vivo* RPE cells, we tried to study hiRPE at a mature development stage (pigmented, 90 days of growing). Unfortunately, we were not able to determine if the cell movements were due to the scratch assay or breaks in the cell layer caused by lack of membrane adhesion. This problem was also observed by Abu Khamidakh et al., 2018 [15]. Future developments of this study would be to automatize the realization of scratch assays with a new setup combining a laser to cut the cell layer with better repeatability. We could also test the addition of molecules to change the speed of closure [27]. We showed that D-FFOCT combined with custom-developed calculation software allow imaging and study of degeneration in RPE cell cultures, which may contribute to the comprehension and the following of *in vivo* degenerative retinal diseases (such as AMD) evolution, and could be an appreciated method for live patient diagnostics and direct treatment choice in the future. As a marker of mitochondrial dynamics and fragmentation and thus of their activity [22], D-FFOCT may also be used in the understanding of optic nerve disease, where mitochondria are implicated. Parallels of wound healing or wound retraction in the RPE layer are found with *in vivo* adaptive optics imaging of AMD patients over year long periods [28].
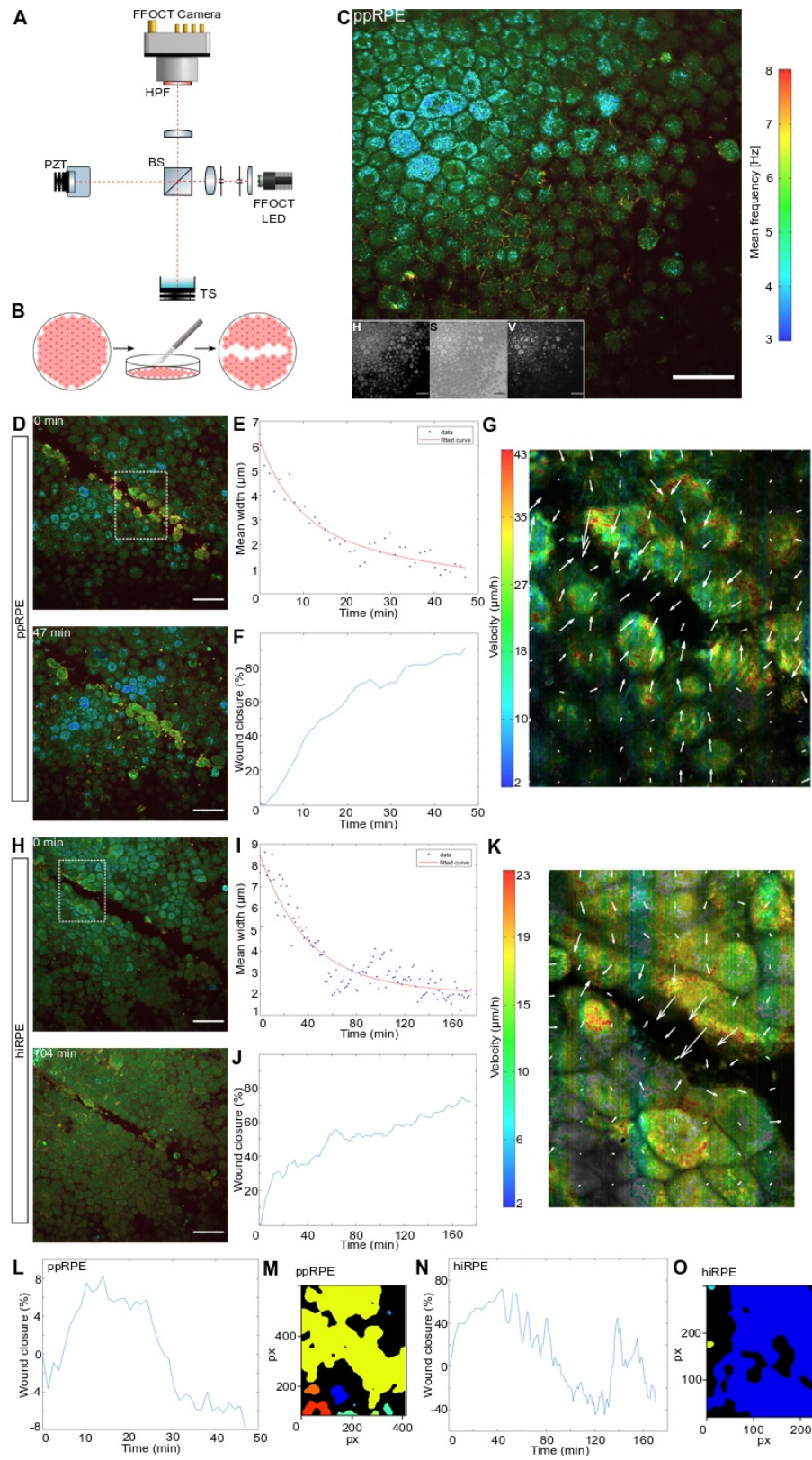
4

Figure 1

Figure 1: **D-FFOCT imaging & scratch techniques (A to C) and results of closing ($<25\mu m$) scratch assays (D to O). (scale-bar: 50 μm) A** Drawing of our custom-built Full-Field OCT system. BS: Beam-Splitter; HPF: High-Pass Filter; PZT: Piezo-electric Translation; TS: Translation stage (for the sample). **B** Schematic of the RPE cell layer before and after the scratch assay (from left to right). **C** Recombined three channels of HSV computation and the three different channels in lower left. The colorbar represents the frequency variations of the sample (Hue channel). **D to G** Results of the analysis of a closing scratch assay on a primary porcine RPE cell culture (ppRPE). **D** Beginning and end (i.e. closing) of the imaging of the scratch assay. The dotted white square corresponds to the area used for calculations. **E & F** Plots of the evolution of scratch width and wound closure over the acquisition, calculated with SAVE Profiler. **G** Optical flow calculations showing velocity and motion direction. **H to K** Results of the analysis of a closing scratch assay on a hiRPE cell culture. **H** Beginning and end (i.e. closing) of the imaging of the scratch assay. **I & J** Plots of the evolution of scratch width and wound closure over the acquisition, calculated with SAVE Profiler. **K** Optical flow calculations. **L & N** Wound closure calculated on the closing ppRPE and hiRPE scratch assays with Cell Profiler. **M & N** Segmentations of the final images of the acquisitions with Cell Profiler, showing the superior performance of SAVE Profiler.
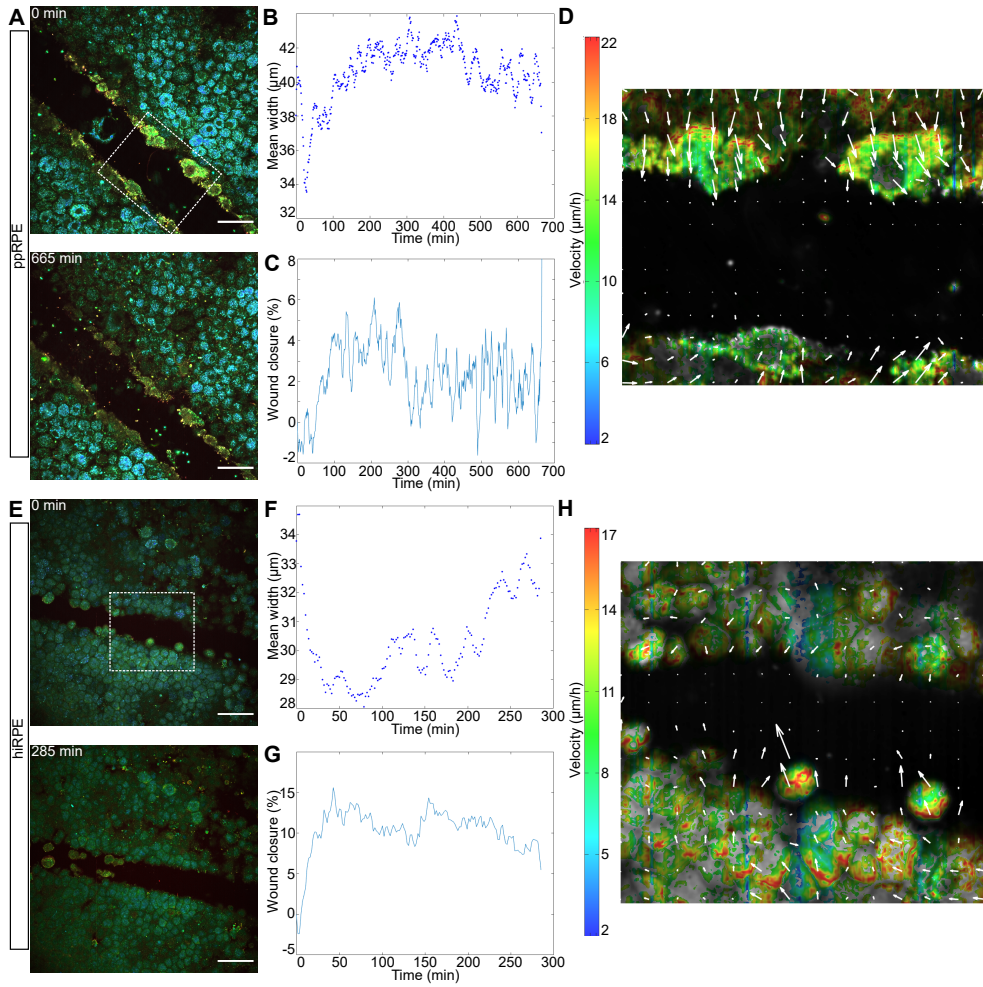
Figure 2: **Results on scratch assays ($>25\mu m$) on ppRPE and hiRPE cell cultures, failing to close entirely. A** Beginning and end of the imaging of a scratch assay on ppRPE cell culture. **B & C** Evolution of scratch width and wound closure calculated with our program and **D** optical flow calculations. **E** Beginning and end of the imaging of a scratch assay on hiRPE cell culture. **F & G** Evolution of the scratch width and wound closure, calculated with the SAVE profiler and **H** optical flow calculations. (Scale-bar: 50 μm)

6
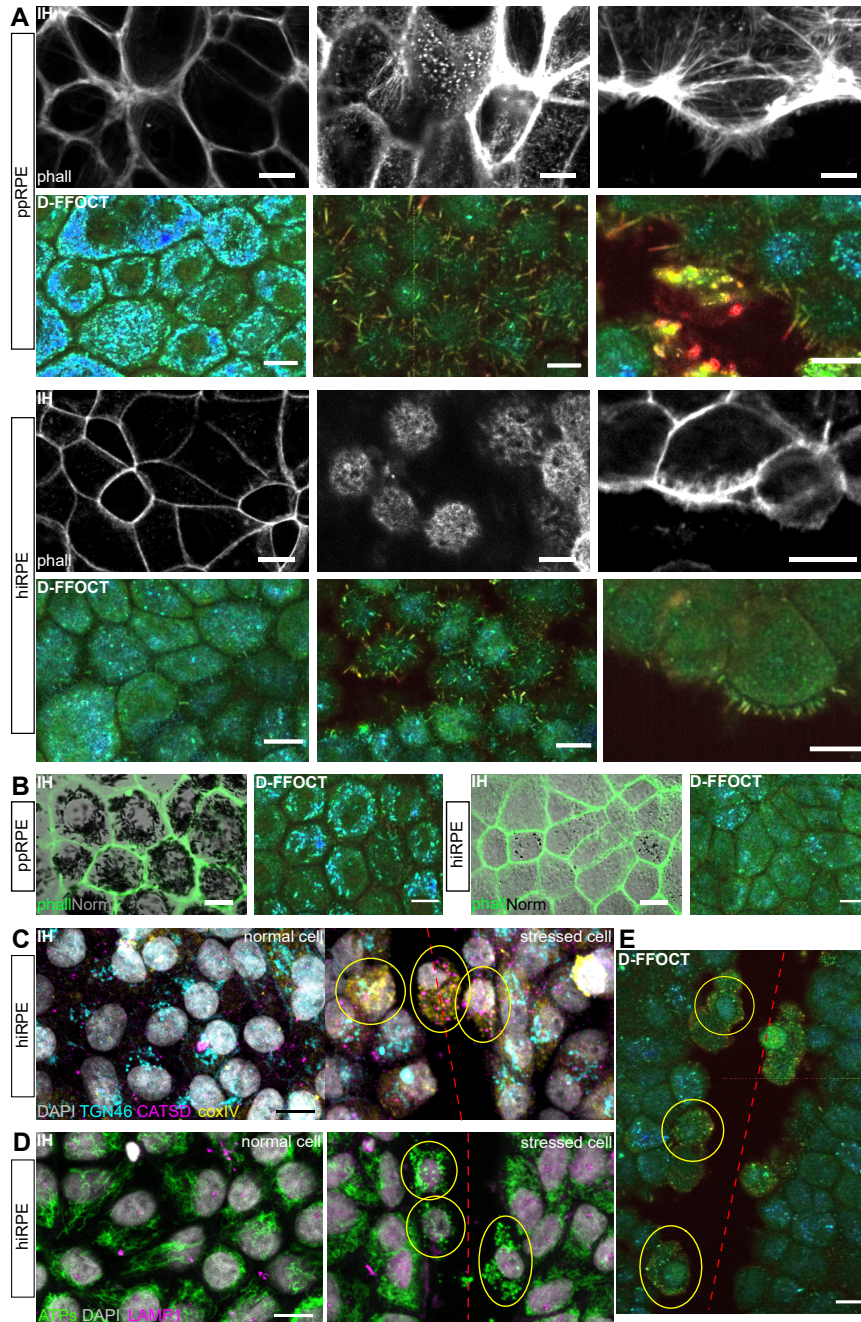
Figure 3: **Immunohistochemistry validation of organelles.** Nuclei were labelled with DAPI. Red dashed lines show the scratch direction. **A** Actin filaments (phalloidine in IH) validation on ppRPE and hiRPE. The left column shows the cell cortex (static) appearing dark in D-FFOCT. The center column presents microvilli. Their visualisation is easier in D-FFOCT: they appear as red cillias on top of RPE cells. The right column shows filipods on the side of the cells close to the wound, appearing in red in D-FFOCT such as microvilli. **B** Comparison of pigment granules on both ppRPE (highly pigmented) and hiRPE (few pigments). Actin filaments (cytoskeleton) are labelled with phalloidine in IH, while pigments were imaged with phase contrast imaging. **C** Golgi apparatus (TGN46 in cyan), lysosomes (CATSD in magenta) and mitochondria (coxIV in yellow) IH comparison between normal cell and stressed cell (circled in yellow). **D** Mitochondria (ATPs) and lysosome (LAMP1) validation in IH between normal cell and stressed cell (circled in yellow). **E** Related D-FFOCT image for **C - D** showing both normal cells and stressed cells (circled in yellow). IH: immunohistochemistry. (Scale-bar: $10\mu m$)

7
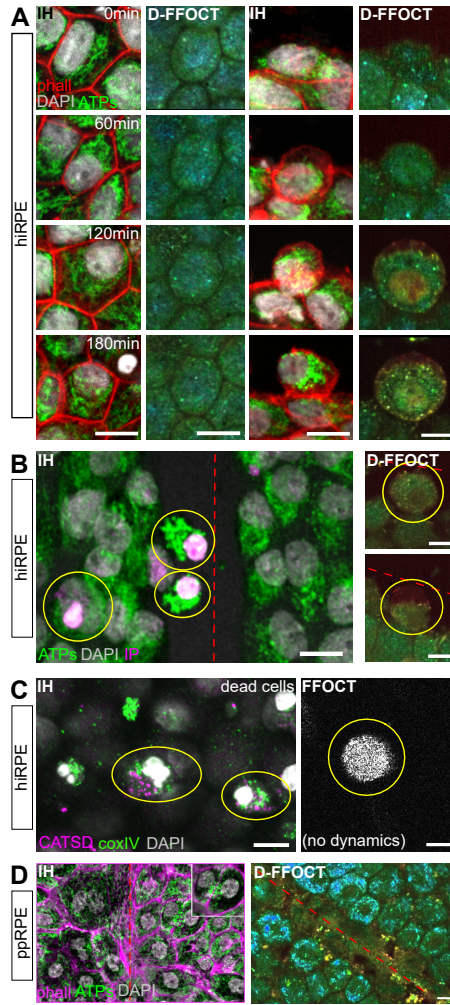
Figure 4: **Cell phenotypes.** Nuclei were labelled with DAPI. Red dashed lines show the scratch direction. **A** Mitochondria phenotype evolution over 3 hours. The two left columns show the evolution of a normal cell, with a constant phenotype. The two right columns present the evolution of a stressed cell, with changes in mitochondria aspect (IH) and in dynamic profile (D-FFOCT). **B** Dying cells (circled in yellow) 2 hours after the scratch, labelled with propidium iodide (IP in magenta), showing a condensed nuclei. Mitochondria are labelled with ATPs (green). Corresponding cells in D-FFOCT on the right. **C** Dead cells (circled in yellow) floating over the cell culture. Lysosomes labelled with CATSD (magenta), mitochondria with coxIV (green) in IH. Corresponding cells do not exhibit any dynamic signal and are only visible in static (structural not functional) FFOCT. **D** Imaging of a closed scratch assay on a ppRPE sample. Actin filaments labelled with phalloidine (magenta) and mitochondria with ATPs (green) in IH. Corresponding D-FFOCT imaging. IH: immunohistochemistry. (Scale-bar: $10\mu m$)

8

Materials and methods

Dynamic Full-Field OCT: Experimental setups and image processing

Optical Coherence Tomography (OCT) is an imaging technique which allows non invasive scanning of a sample in depth, invented in 1991 [29]. Time-domain Full-Field OCT (FFOCT) [30–32] is an interferometric imaging technique which is an *en face* variant of OCT. This configuration, based on a Linnik interferometer i.e. an OCT setup with microscope objectives in the reference and sample arms, allows the recording of 2D images on a CMOS camera in a single shot. By scanning the sample in depth, 3D volumes of the structure of the sample can be acquired (see Movie S1). For our study, we used a laboratory-designed time-domain FFOCT, see Fig.1 A. This setup is composed of a water-immersion microscope objective in each arm (Nikon NIR APO 40x 0.8 NA), giving a lateral resolution of $0.5\mu m$ for a total field-of-view of $320\times320\mu m^2$. The axial resolution of $1.7\mu m$ is also determined by the microscope objectives, due to their high numerical aperture. The camera used is an Adimec camera (Quartz 2A750, Adimec), custom-built for our purpose. The illumination is performed by an LED, centered at $660nm$ (M660L3, Thorlabs), which is separated into reference and sample arms by a beamsplitter (BS028, Thorlabs). The reference arm is composed of a silicon mirror (to approach a reflectivity match with the biological samples), affixed to a piezo-electric translation stage. The piezo-electric translation stage in the reference arm is used to generate a phase shift. A pair of π-phase shifted images are recorded and subtracted to extract the coherent part of the interference signal between the imaged sample plane and the reference mirror.

Recently, we showed that a new type of contrast could be extracted from images acquired with FFOCT [33]. By acquiring several hundred images without using the piezo-electric translation of the reference arm, and calculating the standard deviation over the image stacks, we are able to extract the intrinsic motion of the biological sample. The intrinsic motion is created by the movements of the organelles inside the cells constituting the biological sample [34]. These dynamics are referred to as the "dynamic profile" throughout this article. The image computation of the dynamic profile is based on a power spectrum analysis, as shown in Scholler et al [8]. For this purpose, 512 images are recorded at 100Hz on our FFOCT setup. The power spectrum analysis is then performed on each voxel of the stack of images. The study of the time variations over each voxel helps to highlight the intra-cellular motion recorded. These variations are coded in the Hue-Saturation-Value colorspace, which is an orthogonal colorspace, providing us three different channels to compute different physical parameters.

The mean frequency of the recorded intra-cellular motion codes for the Hue channel, which represents the colour in the image. The colour ranges from blue, representing low frequencies, to red, coding for high frequencies. The saturation channel is coded by the inverse of the frequency bandwidth of each voxel. For a broad bandwidth, meaning there is a large range of frequencies, the saturation will be low, creating a greyish appearance. On the contrary, for a sharp bandwidth, where a specific frequency is emphasised, the saturation will be high, creating a vivid colour. Finally, the value, which codes for the intensity in the image, is calculated as the standard deviation over a moving window of 50 images, which are then averaged, to give the final intensity highlighting the intra-cellular motion. Finally, the three channels are combined to create a coloured image, representing the dynamic profile of the imaged sample, see Fig.1 C.

RPE cell cultures

RPE is a cell monolayer composed of hexagonal cells with a basal nucleus, containing a variety of organelles. On the basal surface, the RPE is linked to the choroidal vasculature, while on the apical surface, RPE cells have microvilli which grab the photoreceptor outer segments to maintain the integrity of the retina [35]. Different methods have been developed to grow RPE [36]. We described here the methods used for both ppRPE and hiRPE samples.

Porcine eyes were bought at a local slaughterhouse (Guy Harang, Houdan, France) in agreement with the local regulatory department and the slaughterhouse veterinarians (agreement FR75105131). This procedure adheres to the European initiative for restricting animal experimentation as not a single animal was killed for our experimentation. Eyes were taken from animals sacrificed daily for human consumption. Eyes were cleaned from muscle, and incubated for 4 minutes in Pursept-AXpress (Merz Hygiene GmbH, Frankfurt, Germany) for disinfection. The anterior portion was cut along the limbus to remove the cornea, lens and retina. A solution containing 0.25% trypsin-EDTA (Life Technologies, Carlsbad, CA, USA) was introduced for 1 hour at 37°C in the eyecup. RPE cells were then gently detached from the Bruch's membrane and resuspended in Dulbecco's Modified Eagle medium (DMEM, Life Technologies) supplemented with 20% Fetal Bovine Serum (FBS, Life Technologies) and 10 μg/ml gentamycin (Life Technologies). Purified cells from one eye were pooled and plated in 2 Transwell inserts (reference: 3412 Corning). Cells were allowed to grow in an incubator with a controlled atmosphere at 5% CO_2 and 37°C. The culture medium was renewed 24 hours after the first seeding.

HiRPE were generated using established protocol using AHF1pi2 hiPSC clone as described in Reichman et al., 2017 [13]. Thawed hiRPE cells at passage 1 (hiRPEp1) were seeded on Geltrex (ThermoFisher) precoted

9

flask at 50.000 cells/cm^2 and expanded in the ProN2 medium composed of DMEM/F12, 1% MEM nonessential amino acids, 1% CTS N2 supplement, 10 units per ml Penicillin, and 10 mg/ml Streptomycin; and the medium was changed every 2-3 days. At confluence, hiRPEp2 cells were dissociated using trypsin and replated at 100.000 cells/cm^2 on Gletrex precoted 6 well plate (reference: 3412 Corning) for D-FFOCT experiments and in p24 on Gletrex precoted glass inserts for immunostaining. All experiments were done with confluent hiRPEp3. Cells were allowed to grow in an incubator with a controlled atmosphere at 5% CO$_2$ and 37°C.

Choice of sample holder for D-FFOCT imaging and scratch assays

In order to model *in vitro* degeneration on a RPE cell culture, scratch assays were performed manually with a scalpel blade through the cell layer on the sample holder. The wounds performed ranged from 20μm wide to over 300μm.

Different materials were tested as sample holder for the cells (see Tab.supplementary 1 in Supplementary materials). The material needs to have three main characteristics: i) the cells should grow easily on it, ii) it should have a refractive index close to that of water, in order to avoid fringe artefacts caused by our interferometric technique, and iii) it should be resistant to scratches made by the scalpel blade. Most commonly, cells are grown in Petri dishes made of polystyrene, where they easily and rapidly grow. However, the refractive index of polystyrene is 1.59, far from the refractive index of water, creating fringe artefacts on the D-FFOCT images. Polytetrafluoroethylene (PTFE) membranes with a refractive index of 1.31 do not create artefacts, but PTFE is very fragile and cells do not grow easily on it. The best compromise was found to be polycarbonate (PC) membranes. These membranes have a refractive index of 1.58 but, as they are porous, the water can enter the membrane and artificially reduce the effective refractive index. Moreover, this material is quite resistant to scratches and cells grow more easily on it than on PTFE.

Immunochemistry preparation and imaging

To allow both immunohistochemistry and observation of cells using confocal microscopy, parallel sets of hiRPE and ppRPE cells were cultured on glass inserts (as polycarbonate membranes do not permit confocal imaging of the epithelium). To obtain samples similar to D-FFOCT observations, scratch assays were performed on hiRPE and ppRPE cells, followed by tissue fixation using paraformaldheyde 4% at various timepoints: 0 min (fixation just after performing the scratch), 60 min, 120 min, 180 min and 24 h. Propidium iodide staining was performed using a pre-fixation incubation of the samples for one hour at 37∘C before cell fixation. Immunostaining was performed using the following solution: PBSGT, 1 x PBS containing 0.2% gelatin: 24350262, Prolabo, and 0.5% Triton X-100 T8787, Sigma Aldrich. A first incubation of the tissues with PBSGT alone for 2h (at room temperature, with shaking at 70 rpm) allowed blockage of non-specific binding and permeabilization. The cultures were then incubated with the primary and secondary antibodies, in the same PBSGT added with corresponding antibodies, at 4 ∘C overnight for the primary antibody and the secondary antibody.

Different organelles were labelled using the following primary antibodies:

- Mitochondria: ATP synthase Subunit Beta Mouse Monoclonal Antibody (A21351 Life technologies) 1/500 and mCoxIV (mouse monoclonal [20E8] ab14744 Abcam) 1/250

- Nuclei: Hoescht 1/1000

- Actin filaments: phalloidin 1/40 (10634053 Fisher Scientific)

- Lysosomes: LAMP1 (ab24170 Abcam) 1/500 and CATSD (sc6486 Santa Cruz) 1/150

- Golgi apparatus: TGN46 (rabbit polyclonal ab50595 Abcam) 1/250

- Dying cells: propidium iodide (P4170, Sigma Aldrich) 1/1000

Fluorescent Secondary antibodies were produced in donkey, against rabbit, goat, and mice and coupled with Alexa 488 and 594 (1/500, Sigma aldrich).

After immunostaining, samples were then mounted in Vectashield (H1000, Vector Laboratories). All images were acquired with a confocal microscope, with an oil immersion objective (classical imaging) using either confocal fluorescent imaging or Normansky phase contrast imaging. Images were observed and processed with FIJI [37].

Optical flow

Optical flow is a method to study the motion between frames of a video. It relies on changes in the brightness pattern throughout an acquisition, and is used in navigation control and robotics, or Artificial Intelligence for example. Here, we first take the intensity channel of the images of an acquisition and apply a median filter

to remove noise (e.g. line noise from the camera). We average 8 by 8 frames to improve the intensity and reduce the time of calculation. Then, we apply the Optical Flow from Matlab [7], using the Horn-Schunck method [16]. The Horn-Schunck method is based on the derivatives of the brightness of the frames, assuming there is a certain smoothness in the flow between the images. The optical flow gives magnitude, orientation, and the velocity components on x and y axes.

For the representation of the velocity and the angle of the optical flow, we choose a limit of 2μm/h as a minimum velocity. The angle is plotted by summing all the different angles calculated through the optical flow process. Velocity is plotted from the magnitude using the quiver function from Matlab, which gives a representation of the velocity with arrows.

The SAVE Profiler: Custom-developed software to segment and analyze wound closure

In order to evaluate the movement of the cells following the scratch, we wished to study the speed and the percentage of closure of the wound by directly measuring the size of the wound over a time-stack of images. For this purpose, custom software was developed in Matlab, which we name the Scratch Assay Velocity Evolution (SAVE) profiler.

The first step is to segment the scratch to create a binary image of the scratch and the cells. In order to obtain the best binary image (i.e. which considers the cell interstices, which are not associated with the scratch, as part of the cells), we applied a multiple threshold to the image and retained only the first level, which separated the scratch from the rest of the image. We performed this multiple thresholding on the first and the last images of the stack, as the intensity level in the images can change during an acquisition. As we thus obtain two different threshold levels, we smooth the threshold linearly throughout the stack of images.

The second step is to facilitate the calculation over the scratch. The user is asked to draw a line along the scratch, helping to evaluate the direction of the scratch. The images are then rotated to have the scratch placed vertically on the images.

We then remove any remaining pixels which do not belong to the scratch by drawing an approximate contour of the wound, which is applied to all of the images. If the scratch is closing, the contouring is done on the first image (as it is on this image that the scratch is the largest). For an expanding scratch, the contouring is done on the last image. The images are also resized to crop the edges of the images before rotation.

The stack of images is finally ready for calculation. First, we calculate wound closure [38], which evaluates the evolution of the area of the scratch over the acquisition period. The area is calculated on each frame by counting the pixels contained within the region of the scratch. The formula of the wound closure is: $\frac{area(t=0)-area(t)}{area(t=0)} \times 100$, giving a percentage of closure or expansion.

Secondly, we calculate wound size evolution. The width of the scratch is calculated by counting the pixels in each row of the image (as the scratch is oriented vertically, the width corresponds to an horizontal line, i.e. a row). Then, for each frame, we calculate the maximum and the minimum widths, but also the mean width and the 50th percentile (i.e. the median). The mean width and the median width were plotted over time and fitted with a bi-exponential function, determining the characteristic time and the speed of closing. The limit of closing was fixed at around 1-2 μm, which is the average interstice between cells far from the wound.

We validated our custom developed SAVE profiler software against an existing software. Cell Profiler is a cell image analysis software developed in 2005 [17]. We used the Wound Healing example available on the website `https://cellprofiler.org`. By analysing images of a healing wound over time, this software calculates the area occupied by the cells on each image. Thus, we were able to calculate the wound closure (formula explained above) in order to compare with the results obtained with our SAVE profiler. We observed that Cell profiler was efficient on non closing wounds (i.e. failure of closing and expansion) and gives similar results. However, the segmentation performed by Cell profiler on closing wounds was incomplete (as shown in Fig.1 M and O) as it takes into account the differences of intensity in the images, misrepresenting the results of wound closure. Moreover, calculation time using Cell Profiler is considerably extended for long acquisitions (e.g. twice as long for more than 150 images), compared to our SAVE profiler.

D-FFOCT and immunochemistry comparison

D-FFOCT has already been shown as a way to distinguish different states of a cell. In [7], it was shown that, while comparing FFOCT and D-FFOCT images of cell cultures, we can differentiate living cells from dying or dead cells, as these cells show a different dynamic profile. In [8], we showed that dead cells can be identified from D-FFOCT images alone. Also, different cell types (RPE, photoreceptors, inner retinal neurons) were shown to be distinguishable with D-FFOCT alone.

In this article, we wished to identify the specific organelles responsible for D-FFOCT signal generation, and hence compared to immunohistochemistry.

11

Acknowledgements

References

[1] Olaf Strauss. The retinal pigment epithelium by Olaf Strauss – Webvision. In *Webvision – The Organization of the Retina and Visual System*. Webvision edition, 2013. Library Catalog: webvision.med.utah.edu.

[2] Mike Boulton and Pierrette Dayhaw-Barker. The role of the retinal pigment epithelium: Topographical variation and ageing changes. *Eye*, 15(3):384–389, May 2001.

[3] Dorothea Besch, Herbert Jägle, Hendrik P. N. Scholl, Mathias W. Seeliger, and Eberhart Zrenner. Inherited multifocal RPE-diseases: mechanisms for local dysfunction in global retinoid cycle gene defects. *Vision Research*, 43(28):3095–3108, December 2003.

[4] J.R. Sparrow, D. Hicks, and C.P. Hamel. The Retinal Pigment Epithelium in Health and Disease. *Current molecular medicine*, 10(9):802–823, December 2010.

[5] Ronald Klein, Chiu-Fang Chou, Barbara E. K. Klein, Xinzhi Zhang, Stacy M. Meuer, and Jinan B. Saaddine. Prevalence of age-related macular degeneration in the US population. *Archives of Ophthalmology (Chicago, Ill.: 1960)*, 129(1):75–80, January 2011.

[6] David L. Forest, Lincoln V. Johnson, and Dennis O. Clegg. Cellular models and therapies for age-related macular degeneration. *Disease Models & Mechanisms*, 8(5):421–427, May 2015.

[7] Jules Scholler, Viacheslav Mazlin, Olivier Thouvenin, Kassandra Groux, Peng Xiao, José-Alain Sahel, Mathias Fink, Claude Boccara, and Kate Grieve. Probing dynamic processes in the eye at multiple spatial and temporal scales with multimodal full field OCT. *Biomedical Optics Express*, 10(2):731–746, February 2019.

[8] Jules Scholler, Kassandra Groux, Olivier Goureau, José-Alain Sahel, Mathias Fink, Sacha Reichman, Claude Boccara, and Kate Grieve. Dynamic full-field optical coherence tomography: 3D live-imaging of retinal organoids. *Light: Science & Applications*, 9(1):140, August 2020. Number: 1 Publisher: Nature Publishing Group.

[9] U. F. O. Themes. Cell Biology of the Retinal Pigment Epithelium, March 2017. https://entokey.com/cell-biology-of-the-retinal-pigment-epithelium/.

[10] Ellen C. Jensen. Overview of Live-Cell Imaging: Requirements and Methods Used. *The Anatomical Record*, 296(1):1–8, 2013.

[11] Kimberly A. Toops, Li Xuan Tan, and Aparna Lakkaraju. A detailed three-step protocol for live imaging of intracellular traffic in polarized primary porcine RPE monolayers. *Experimental eye research*, 124:74–85, July 2014.

[12] Gurugirijha Rathnasamy, Li Xuan Tan, and Aparna Lakkaraju. Live-cell imaging of mitochondrial dynamics in the retinal pigment epithelium. *Investigative Ophthalmology & Visual Science*, 59(9):4028–4028, July 2018. Publisher: The Association for Research in Vision and Ophthalmology.

[13] Sacha Reichman, Amelie Slembrouck, Giuliana Gagliardi, Antoine Chaffiol, Angelique Terray, Celine Nanteau, Anais Potey, Morgane Belle, Oriane Rabesandratana, Jens Duebel, Gael Orieux, Emeline F. Nandrot, Jose-Alain Sahel, and Olivier Goureau. Generation of Storable Retinal Organoids and Retinal Pigmented Epithelium from Adherent Human iPS Cells in Xeno-Free and Feeder-Free Conditions. *Stem Cells*, 35(5):1176–1188, 2017.

[14] Sacha Reichman, Angélique Terray, Amélie Slembrouck, Céline Nanteau, Gaël Orieux, Walter Habeler, Emeline F. Nandrot, José-Alain Sahel, Christelle Monville, and Olivier Goureau. From confluent human iPS cells to self-forming neural retina and retinal pigmented epithelium. *Proceedings of the National Academy of Sciences*, 111(23):8518–8523, June 2014.

[15] Amna E. Abu Khamidakh, Alejandra Rodriguez-Martinez, Kai Kaarniranta, Anne Kallioniemi, Heli Skottman, Jari Hyttinen, and Kati Juuti-Uusitalo. Wound healing of human embryonic stem cell-derived retinal pigment epithelial cells is affected by maturation stage. *BioMedical Engineering OnLine*, 17(1):102, July 2018.

[16] J.L. Barron, D.J. Fleet, S.S. Beauchemin, and T.A. Burkitt. Performance of optical flow techniques. In *Proceedings 1992 IEEE Computer Society Conference on Computer Vision and Pattern Recognition*, pages 236–242, June 1992. ISSN: 1063-6919.

[17] Michael R. Lamprecht, David M. Sabatini, and Anne E. Carpenter. CellProfiler™: free, versatile software for automated biological image analysis. *BioTechniques*, 42(1):71–75, January 2007. Publisher: Future Science.

[18] Michael Atlan. Holovibes: hologram rendering made easy, 2014. http://holovibes.com/.

[19] Benjamin Geiger, Alexander Bershadsky, Roumen Pankov, and Kenneth M. Yamada. Transmembrane crosstalk between the extracellular matrix and the cytoskeleton. *Nature Reviews Molecular Cell Biology*, 2(11):793–805, November 2001. Number: 11 Publisher: Nature Publishing Group.

[20] Damien Arnoult. Mitochondrial fragmentation in apoptosis. *Trends in Cell Biology*, 17(1):6–12, January 2007.

[21] T. Ahmad, K. Aggarwal, B. Pattnaik, S. Mukherjee, T. Sethi, B. K. Tiwari, M. Kumar, A. Micheal, U. Mabalirajan, B. Ghosh, S. Sinha Roy, and A. Agrawal. Computational classification of mitochondrial shapes reflects stress and redox state. *Cell Death & Disease*, 4(1):e461–e461, January 2013. Number: 1 Publisher: Nature Publishing Group.

[22] Yoshihiro Miyazono, Shingo Hirashima, Naotada Ishihara, Jingo Kusukawa, Kei-ichiro Nakamura, and Keisuke Ohta. Uncoupled mitochondria quickly shorten along their long axis to form indented spheroids, instead of rings, in a fission-independent manner. *Scientific Reports*, 8(1):350, January 2018. Number: 1 Publisher: Nature Publishing Group.

[23] G. J. Hergott, H. Nagai, and V. I. Kalnins. Inhibition of retinal pigment epithelial cell migration and proliferation with monoclonal antibodies against the beta 1 integrin subunit during wound healing in organ culture. *Investigative Ophthalmology & Visual Science*, 34(9):2761–2768, August 1993. Publisher: The Association for Research in Vision and Ophthalmology.

[24] A. Jacinto, A. Martinez-Arias, and P. Martin. Mechanisms of epithelial fusion and repair. *Nature Cell Biology*, 3(5):E117–123, May 2001.

[25] Rizwan Farooqui and Gabriel Fenteany. Multiple rows of cells behind an epithelial wound edge extend cryptic lamellipodia to collectively drive cell-sheet movement. *Journal of Cell Science*, 118(1):51–63, January 2005.

[26] Michel Paques, Serge Meimon, Florence Rossant, David Rosenbaum, Sarah Mrejen, Florian Sennlaub, and Kate Grieve. Adaptive optics ophthalmoscopy: Application to age-related macular degeneration and vascular diseases. *Progress in Retinal and Eye Research*, 66:1–16, September 2018.

[27] Roxanne H. Croze, William J. Thi, and Dennis O. Clegg. ROCK Inhibition Promotes Attachment, Proliferation, and Wound Closure in Human Embryonic Stem Cell–Derived Retinal Pigmented Epithelium. *Translational Vision Science & Technology*, 5(6):7–7, November 2016. Publisher: The Association for Research in Vision and Ophthalmology.

[28] Kiyoko Gocho, Valérie Sarda, Sabrina Falah, José-Alain Sahel, Florian Sennlaub, Mustapha Benchaboune, Martine Ullern, and Michel Paques. Adaptive Optics Imaging of Geographic Atrophy. *Investigative Ophthalmology & Visual Science*, 54(5):3673–3680, May 2013. Publisher: The Association for Research in Vision and Ophthalmology.

[29] D. Huang, E. A. Swanson, C. P. Lin, J. S. Schuman, W. G. Stinson, W. Chang, M. R. Hee, T. Flotte, K. Gregory, C. A. Puliafito, and Al Et. Optical coherence tomography. *Science*, 254(5035):1178–1181, November 1991.

13

[30] E. Beaurepaire, A. C. Boccara, M. Lebec, L. Blanchot, and H. Saint-Jalmes. Full-field optical coherence microscopy. *Optics Letters*, 23(4):244–246, February 1998.

[31] Arnaud Dubois, Laurent Vabre, Albert-Claude Boccara, and Emmanuel Beaurepaire. High-resolution full-field optical coherence tomography with a Linnik microscope. *Applied Optics*, 41(4):805–812, February 2002.

[32] Arnaud Dubois, Kate Grieve, Gael Moneron, Romain Lecaque, Laurent Vabre, and Claude Boccara. Ultrahigh-resolution full-field optical coherence tomography. *Applied Optics*, 43(14):2874–2883, May 2004.

[33] Clement Apelian, Fabrice Harms, Olivier Thouvenin, and Claude Boccara. Dynamic full field optical coherence tomography: subcellular metabolic contrast revealed in tissues by interferometric signals temporal analysis. *Biomedical Optics Express*, 7(4):1511, March 2016.

[34] Olivier Thouvenin, Claude Boccara, Mathias Fink, Jose-Alain Sahel, Michel Paques, and Kate Grieve. Cell motility as contrast agent in retinal explant imaging with full-field optical coherence tomography. *Investigative Ophtalmology & Visual Science*, 58(11):4605, September 2017.

[35] Vera L. Bonilha, Mary E. Rayborn, Sanjoy K. Bhattacharya, Xiarong Gu, John S. Crabb, John W. Crabb, and Joe G. Hollyfield. The Retinal Pigment Epithelium apical microvilli and retinal function. *Advances in experimental medicine and biology*, 572:519–524, 2006.

[36] Aaron H Fronk and Elizabeth Vargis. Methods for culturing retinal pigment epithelial cells: a review of current protocols and future recommendations. *Journal of Tissue Engineering*, 7:2041731416650838, January 2016. Publisher: SAGE Publications Ltd STM.

[37] Johannes Schindelin, Ignacio Arganda-Carreras, Erwin Frise, Verena Kaynig, Mark Longair, Tobias Pietzsch, Stephan Preibisch, Curtis Rueden, Stephan Saalfeld, Benjamin Schmid, Jean-Yves Tinevez, Daniel James White, Volker Hartenstein, Kevin Eliceiri, Pavel Tomancak, and Albert Cardona. Fiji: an open-source platform for biological-image analysis. *Nature Methods*, 9(7):676–682, July 2012. Number: 7 Publisher: Nature Publishing Group.

[38] Ayman Grada, Marta Otero-Vinas, Francisco Prieto-Castrillo, Zaidal Obagi, and Vincent Falanga. Research Techniques Made Simple: Analysis of Collective Cell Migration Using the Wound Healing Assay. *Journal of Investigative Dermatology*, 137(2):e11–e16, February 2017.

14

Supplementary information
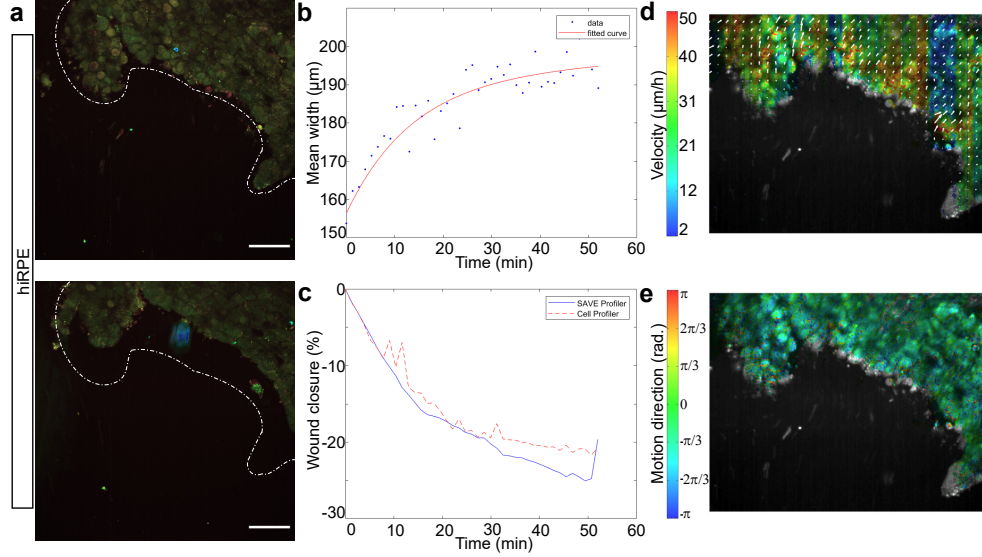
Supplementary Figure 1: **Results on expanding scratch assay on hiRPE cell culture. a** Beginning and end of the imaging of an expanding scratch assay on hiRPE cell culture. The white dotted line represents the border of the wound at the beginning of the acquisition. **b** Evolution of scratch width over the acquisition, calculated with our program. **c** Wound closure calculated with both SAVE Profiler and the Cell Profiler software. **d & e** Results of the optic flow calculations showing both the velocity and the direction separately. (Scalebar: 50 μm)

1
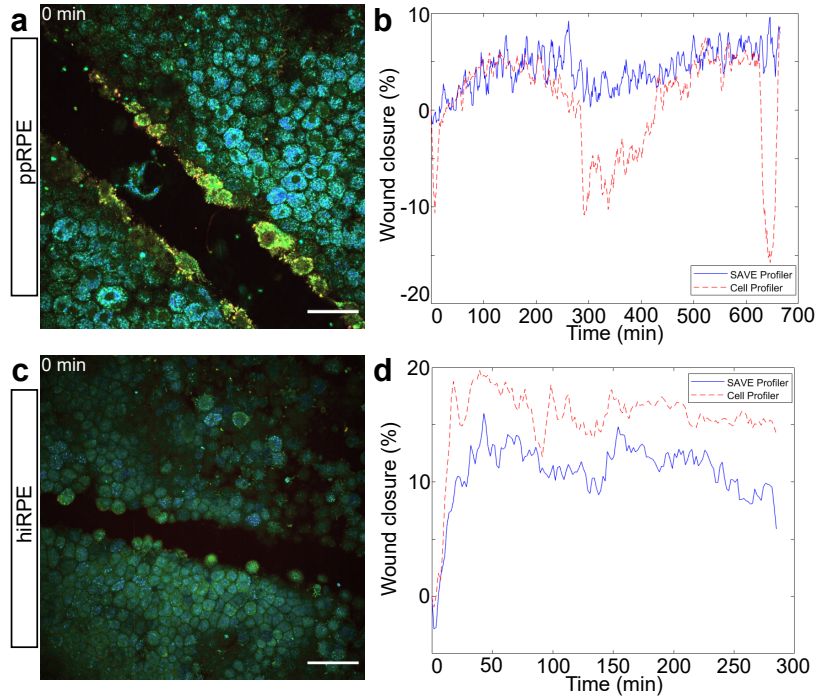
Supplementary Figure 2: **Results of Cell Profiler compared to SAVE Profiler on the samples that failed to close of Fig.2 a** Beginning of the imaging of a scratch assay failing to close on ppRPE cell culture. **b** Wound closure calculated with both SAVE Profiler and the Cell Profiler software on the ppRPE sample. **c** Beginning of the imaging of a scratch assay failing to close on hiRPE cell culture. **d** Wound closure calculated with both SAVE Profiler and the Cell Profiler software on the hiRPE sample. Note the overestimation of wound closure from Cell Profiler. (Scalebar: 50 μm)

Supplementary Table 1: Features of the different sample holders

Features / Sample holder	Petri dish: polystyrene	PTFE membranes	PC membranes
Refractive index	1.59	1.31	1.58
Porosity	✗	✓	✓
Adhesion of cells	✓✓	✗	✓
No fringe artefacts	✗	✓✓	✓
Scratch resistance	✓✓	✗	✓

Supplementary Table 2: Statistics of the scratch assays.

	Total number of hiRPE samples	Total number of ppRPE samples
$\leq 25\mu m$ (Closing)	4	2
$25\mu m \leq . < 100\mu m$ (Failing to close)	4	3
$> 100\mu m$ (Expanding)	1	0

2 Supplementary Movie 1 : stacks ppRPE and hiRPE Depth stacks in both ppRPE and hiRPE cell cultures.
3 Differences in the dynamic profile are clearly visible, depending on the maturation stage and origin of the
4 samples. hiRPE (less mature than ppRPE) appear with less pigments, showing a quite homogeneous green
5 dynamic profile inside the cells, while ppRPE appear with blue granules. We can also observe that at the apical
6 surface of the RPE cells (top), microvilli are more present (number, length) and dynamic (i.e. appearing red)
7 on ppRPE than hiRPE.

2

Supplementary Movie 2 : closing ppRPE Closing scratch assay of ppRPE presented in Fig.1.

Supplementary Movie 3 : closing hiRPE Closing scratch assay of hiRPE presented in Fig.1.

Supplementary Movie 4 : closing failure ppRPE Expanding scratch assay of ppRPE, where the cell layer first tends towards wound closure but then finally retracts.

Supplementary Movie 5 : closing failure hiRPE Expanding scratch assay of hiRPE, where the cell layer first tends towards wound closure but then finally retracts.

Supplementary Movie 6 : expanding hiRPE Expanding scratch assay of hiRPE presented in Supplementary Figure 1.

Supplementary Movie 7 : microvilli in real-time, recorded on ppRPE with Holovibes software [1]. Each image is separated from the next by $5ms$. The movements of microvilli are clearly visible.

References

[1] Michael Atlan. Holovibes: hologram rendering made easy, 2014. http://holovibes.com/.

3

Chapter 5

Towards dynamic *in vivo* retinal imaging with FFOCT

A few years ago, a new application of FFOCT was developed [65]. As a promising *en face* imaging technique, without need of contact with the sample, FFOCT for *in vivo* eye imaging was implemented in two different ways: for corneal imaging [80] and for retinal imaging [81]. Corneal imaging FFOCT consists in two microscope objectives with low NA, while retinal imaging FFOCT gets rid of the microscope objective in the object arm as the eye plays this role to focus light on the retina.

In this chapter, I show results obtained on *in vivo* retina, which was a work in collaboration with Pedro Mecê, post-doctoral student in Institut Langevin during my thesis.

5.1 Robust FFOCT for retinal imaging

The eye is submitted to numerous sources of movements from physiological processes: breathing, heartbeat, fixational eye movements including saccades, drift and tremor. The first two movements are sinusoidal movements at low frequencies. Breathing is $0.2Hz$, while heartbeat creates pics at 1, 2 and $3Hz$ [82,83]. However, the eye movements are more difficult to register and predict: there are different from a person to another, different over time [84]. Even if the aberrations created by the fixational movements [84] and FFOCT is almost insensitive to some aberrations [85, 86], the movements of the eye induce loss of coherence between eye and reference mirror. There is a need of a specific following of the eye to keep the layer of interest in the coherence gate of the imaging setup. For this purpose, we developed an axial stabilization based on a SD-OCT. The retina is axially tracked with the SD-OCT, which helps to keep the layer of interest in the coherence gate by adjusting the length of the reference arm to match optical paths as shown in Mecê et al., 2020 [87] (see Appendix C.1). It also helps to perfectly position the eye of the patient in front of the setup by recording the position of the retina in real-time. This combination with SD-OCT has also been implemented for corneal imaging [88].

5.2 Correction of retinal curvature

The eye is a spherical organ, with different curvatures for anterior eye (cornea) and posterior eye (retina). Cornea presents two different curvatures for the endothelial layers and sub-basal nerve plexus [89]. Recently, Mazlin et al. [90] have implemented a new FFOCT technique called curved-field OCT to match the curvatures of the cornea. By introducing different lenses in the reference arm with curvatures equivalent to those of the cornea,

the reference plane can be curved to then obtain wide-field images of a unique layer by matching the coherence gate to the cornea.
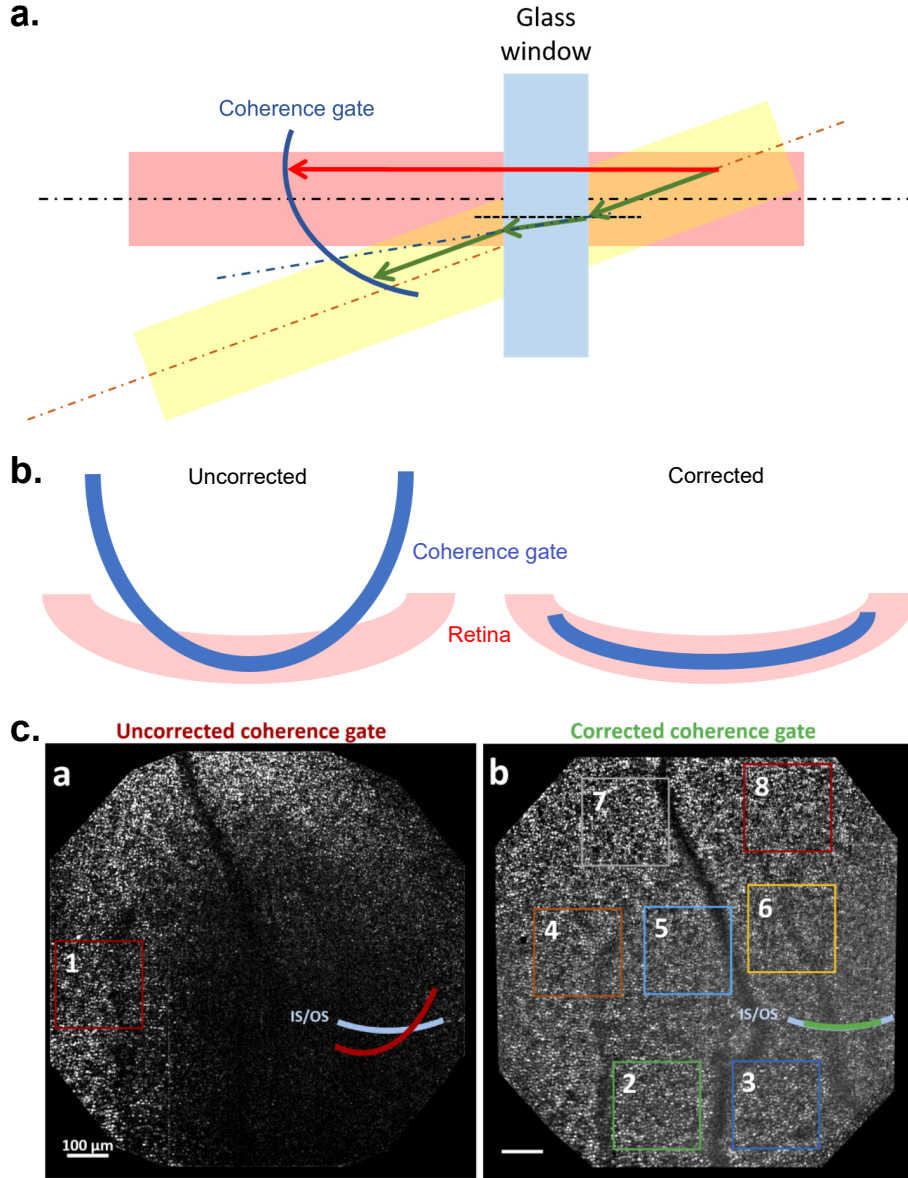
Figure 5.1: **Coherence gate curvature. a.** Schematic explaining the curved coherence gate after introducing a glass window. Two beams are represented: a horizontal beam (red) and a deviated beam (yellow). The arrows show the same optical path length for the two different beams: the red arrow for the red beam and the green arrow for the yellow beam. This shows the creation of a curvature in the coherence gate. **b.** Schematic showing the retina and coherence gate curvatures for uncorrected and corrected systems. **c.** "a,b, Respectively, acquired FFOCT images from the IS/OS junction before and after correcting for the coherence gate curvature." Adapted from Fig.4 from Mecê et al., 2020 [91].

Unlike cornea, retina has the same curvature for the whole layers as it covers the back of the eye. When imaging, we need to match the curved layer of interest in the retina and the plane of the reference mirror: there is a mismatch which do not allow to obtain a wide-field image but instead creates an annular effect. In the case of retinal imaging, the symmetry of the Linnik interferometer is broken because the microscope objective of the reference arm is not exactly identical to the eye [81,87]. This introduces a curved coherence

gate (Fig.5.1 b. and c.). We needed to artificially transform the curved coherence gate by flattening it in order to match the curvature of the retina. For this purpose, we introduced a 20mm thick N-BK7 glass window in the sample arm to flatten the sample layer (Fig.5.1 a.). This window allows a match between the retina and the reference mirror [91] (see Appendix C.2) as shown in Fig.5.1 b. and c. However, this window introduces dispersion due to its thickness. Other materials exist which compensate dispersion too, but they are expensive.

5.3   Improving signal: adaptive lens to reduce aberrations
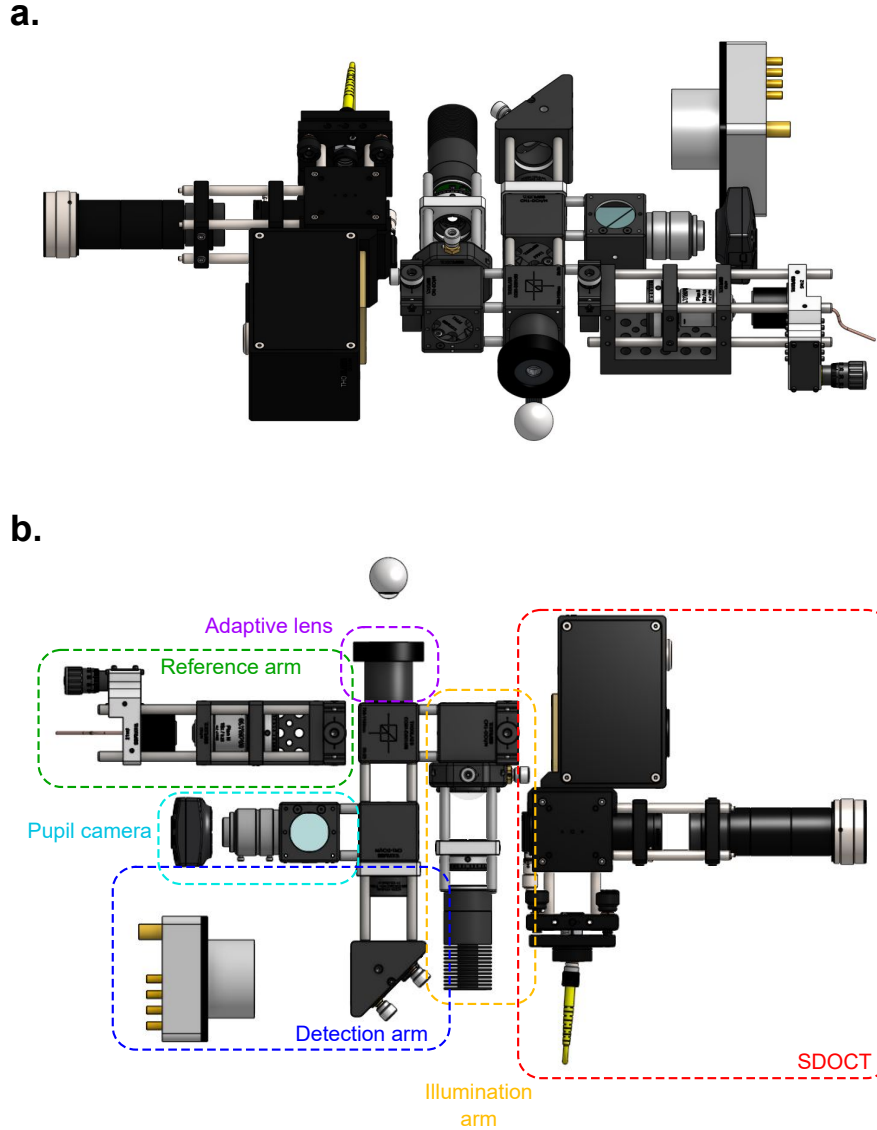
Figure 5.2: **Schematic of the FFOCT setup for *in vivo* retinal imaging. a.** View of the setup from the patient size. **b.** Top view of the setup.

The function of the retina is to transmit the light, not to reflect it back: this is why the backscattered signal is really weak. It is important to collect as much signal as we can: can we improve the level of signal collected? The main cause of loss of signal we can play with is the aberrations of the eye. Usually, to correct this loss, complex adaptive optics are used (multiple mirrors on several meters of optical path) making the setup difficult to align and

use. Here, we proposed to use an adaptive lens in front of the eye, as shown in Fig.5.2, to improve the SNR of the SD-OCT signal by reducing first order eye aberrations [92]. We obtained more signal and contrast on the FFOCT images and improve the occurrence of usable images. We also get an easier tracking of eye movements and an easier positioning to have a wide-field image.

5.4 Towards dynamic *in vivo*

We recently showed that D-FFOCT is a useful imaging technique for *in vitro* samples. 2D and 3D cell cultures exhibit high D-FFOCT signals with a wide range of dynamic profiles. We observed retinal organoids [23] and RPE cell cultures [24] showing multiple dynamic profiles depending on the type of the cell or their state. D-FFOCT allows to detect cell stress at every developmental stage of an *in vitro* sample, showing promising results for *in vivo* eye diseases.

Thanks to our setup adapted for *ex vivo* samples, we were able to image *ex vivo* retina for different species (mouse, macaque, human) (see Fig.5.3). We can distinguish each layer of the imaged retina only by their dynamic profiles [93], comforting us in the fact that D-FFOCT will be a great tool to detect diseases at early stage *in vivo*.

The next step is to implement D-FFOCT *in vivo*, but there are still some limitations which need to be overcome. A first limitation is the aberrations of the eye, caused by the lens and the cornea. However, it has been shown that FFOCT is less sensitive to aberrations than other optical techniques [85, 86]. This allows us to avoid the integration of complex adaptive optics to FFOCT setup. Due to the physiological movements of the eye, the acquisition time is an important parameter to obtain enough FFOCT images. Mazlin et al. [94] recently showed that, while acquiring FFOCT images of *in vivo* cornea at 0.1ms and 1ms acquisition times, the number of "good" images was totally different. Actually, for 0.1ms, the phase shift in images is limited to $\pm\frac{\pi}{2}$, while for 1ms 80% of the images present a phase shift $> \frac{\pi}{2}$. This is a big problem for D-FFOCT images as the sample should stay static during the acquisition which is around 10ms for our *in vitro* and *ex vivo* setups. Some post-processing corrections can be implemented thanks to Singular Value Decomposition [95], but it is not efficient if the image is in another plane of the sample. Two options are worth considering: the implementation of a faster and more precise motor for the reference arm in order to stabilise acquisitions in one layer, or improve the speed of acquisitions to get multiple volumes in one acquisition.

Currently, we are still considering which design and options would be the best to be able, one day, to acquire D-FFOCT images *in vivo*.
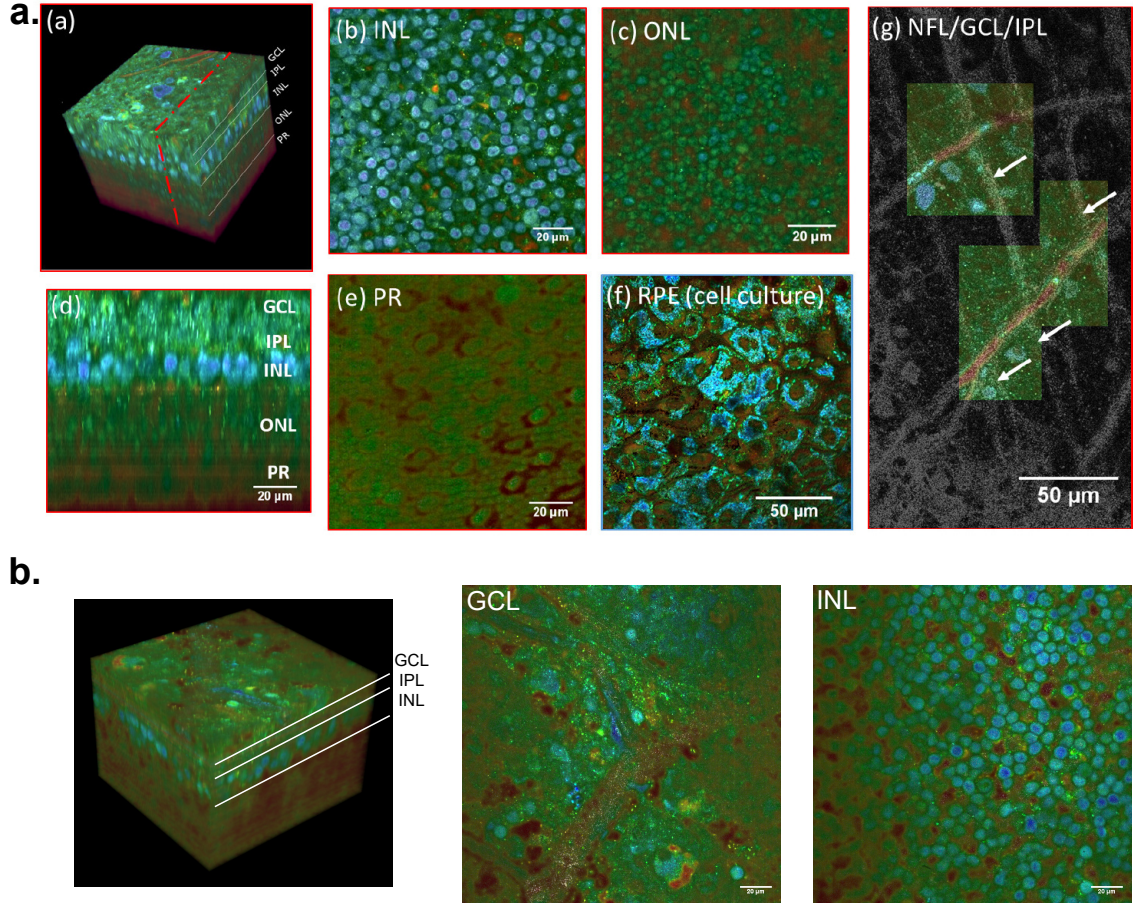
Figure 5.3: **D-FFOCT images of *ex vivo* retinas. a.** D-FFOCT images of *ex vivo* macaque retina. "(a) 3D reconstruction of a D-FFOCT image stack in explanted macaque retina over a 120 by 120 μm field of view. Note that FFOCT signal is damped with increasing penetration depth, so that upper retinal layers are more clearly visible than lower ones. (b, c, e) En-face images of the (b) inner nuclear layer, (c) outer nuclear layer and (e) photoreceptor layer presenting a similar appearance to two-photon fluorescence imaging and (d) reconstructed cross-section at the location represented by the red dotted line in (a). The cross-section in (d) was linearly interpolated to obtain a unitary pixel size ratio. (f) D-FFOCT image of a porcine retinal pigment epithelium cell culture. (g) Overlay of colored D-FFOCT and FFOCT at the interface between the layers of the nerve fibers (white arrows point to nerve bundles that are very bright in static and invisible in dynamic mode), ganglion cells (blue and green cells, visible in dynamic mode) and inner plexiform (fibrous network, bottom left, visible in static mode). Samples were maintained in vitro in culture medium at room temperature during imaging." Adapted from Scholler et al., 2019 [22]. **b.** D-FFOCT images of *ex vivo* human retina. From left to right: 3D reconstruction of a D-FFOCT image stack in explanted human retina, *en face* image of ganglion cell layer and *en face* image of inner nuclear layer.

5.5   Articles: "Adaptive-glasses time-domain FFOCT for wide-field high-resolution retinal imaging with increased SNR"

Optics Letters

Adaptive-glasses time-domain FFOCT for wide-field high-resolution retinal imaging with increased SNR

JULES SCHOLLER,[1,2] KASSANDRA GROUX,[1,2] KATE GRIEVE,[2] CLAUDE BOCCARA,[1,2] AND PEDRO MECÊ[1,2,*]

[1]*Institut Langevin, ESPCI Paris, CNRS, PSL University, 1 Rue Jussieu, 75005 Paris, France*
[2]*Paris Eye Imaging Group, Quinze Vingts National Ophthalmology Hospital, Paris, France*
Corresponding author: pedro.mece@espci.fr

The highest three-dimensional (3D) resolution possible in *in vivo* retinal imaging is achieved by combining optical coherence tomography (OCT) and adaptive optics. However, this combination brings important limitations, such as small field-of-view and complex, cumbersome systems, preventing so far the translation of this technology from the research lab to clinics. In this Letter, we mitigate these limitations by combining our compact time-domain full-field OCT (FFOCT) with a multi-actuator adaptive lens positioned just in front of the eye, in a technique we call the adaptive-glasses wavefront sensorless approach. Through this approach, we demonstrate that ocular aberrations can be corrected, increasing the FFOCT signal-to-noise ratio (SNR) and enabling imaging of different retinal layers with a 3D cellular resolution over a 5° × 5° field-of-view, without apparent anisoplanatism. © 2020 Optical Society of America

https://doi.org/10.1364/OL.403135

Optical coherence tomography (OCT) revolutionized ophthalmology in the 1990s owing to its high axial resolution, which enabled clinicians to distinguish the retinal layers *in vivo* [1]. Although the axial resolution of OCT is sufficient to resolve retinal features at a micrometer scale, the lateral resolution is limited by ocular aberrations [2]. Owing to its capacity to correct for ocular aberrations in real-time, adaptive optics (AO) has become the primary technique to achieve high lateral resolution in the retina [3]. When coupled to OCT, AO has enabled micrometer resolution in all spatial dimensions for *in vivo* retinal imaging [4], contributing to the understanding of retinal function and diseases. Nevertheless, the high lateral resolution achieved with AO comes with a cost of a small field-of-view (FOV), which is limited by the isoplanatic patch of the eye (around 2° × 2°) [5] but also by the trade-off between the spatial sampling of the scan and the acquisition speed, in order to avoid image distortion due to eye motion. Most importantly, AO-OCT systems are complex and cumbersome, requiring long imaging sessions to acquire a large FOV [4]. These limitations have prevented the translation of AO-OCT from the research lab to clinics. Much

recent work has aimed at addressing these limitations, by reducing the AO-OCT system complexity and footprint through the use of conjugated lens-based wavefront sensorless AO [6], or by increasing the FOV to 4° × 4° using multi-conjugate AO [7]. However, the former still presents a small FOV because of the limited isoplanatic patch of the eye and spatial sampling of the scan, and the latter adds complexity as two deformable mirrors are necessary.

In this Letter, we propose a lens-based sensorless AO approach using a multi-actuator adaptive lens (MAL, Dynamic Optics srl, Italy) positioned in front of the examined eye, i.e., without strict pupil conjugation, in a technique we call the adaptive-glasses approach. The proposed optimization scheme does not require any calibration step and is, therefore, straightforward to implement in existing systems without increasing system footprint or optical complexity. We implemented the adaptive-glasses approach in our compact time-domain full-field OCT (henceforth, named FFOCT) system. FFOCT was found to behave differently to conventional imaging systems and Fourier-domain OCT with regards to optical aberrations. The lateral resolution of FFOCT is less affected by symmetric aberrations [8], which dominate in the eye, owing to the use of a spatially incoherent source. This interesting feature was recently highlighted for high-resolution retinal imaging over a FOV of 3.5° × 3.5°, without apparent anisoplanatism [9]. Nevertheless, although symmetrical aberrations may not be adversely affecting the resolution in FFOCT, the presence of aberrations still provokes a loss of signal-to-noise ratio (SNR). Low SNR strongly impacts the robustness of FFOCT imaging, especially at large pupil size, and prevents imaging of retinal layers other than photoreceptors [9,10]. Here, we show that the use of the adaptive-glasses approach to correct for ocular aberrations can considerably increase the SNR and robustness of FFOCT, enabling imaging of different retinal layers with three-dimensional (3D) cellular resolution over a 5° × 5° FOV acquired in a single shot, while retaining a compact system design. To the best of our knowledge, the presented method is the first to ally 3D high-resolution, wide FOV, and small

system footprint, which are essential characteristics for clinical deployment.

The FFOCT system was described in detail elsewhere [10] and has a footprint of 50 cm × 30 cm (See Visualization 1 for a mechanical drawing of the system). Importantly for this study, the FFOCT setup comprises a spectral-domain (SD) OCT channel used to track eye axial motion and drive at 50 Hz loop rate a fast translation stage on which the FFOCT reference arm is mounted, enabling the FFOCT to acquire *en face* images at a given depth in the retina. Since the phase modulation of FFOCT is performed almost randomly by the residual eye axial motion after correction [10], the brightness of FFOCT retinal images varies from one image to another, making the FFOCT signal an unreliable merit function for wavefront correction. We therefore use the brightness of the SD-OCT B-scan as a surrogate for the FFOCT SNR optimization. The FFOCT and SD-OCT channels have central wavelengths of 850 nm (30 nm bandwidth) and 930 nm (60 nm bandwidth), respectively. Since these two wavelengths are close, correcting aberrations using the brightness of SD-OCT as a merit function is also suitable for FFOCT. For both FFOCT and SD-OCT channels, the beam diameter at the pupil is 7.5 mm. The MAL is composed of 18 actuators and can correct up to the fourth Zernike order [6]. It has a transmission of 94% in the near-infrared and a response time of less than 2 ms. The MAL is positioned 2–3 cm in front of the subject's cornea, i.e., without strict pupil conjugation. It has a 10 mm diameter, meaning that it is large enough to avoid vignetting and resolution loss, which would occur with a smaller numerical aperture. Its diameter and position favor anisoplanatic correction through wavefront sensorless optimization similar to a pupil-conjugated scheme [11]. The coherence gate geometry was shaped to fit the retinal curvature, and dispersion was compensated using a 20 mm N-BAK1 optical window in the sample arm [9]. The size of an individual pixel of the FFOCT camera corresponds to 1 μm in the retinal plane. The SD-OCT has an A-scan rate of 36 kHz. We chose to scan over a line of 2° FOV with 256 A-scans, i.e., at 140 Hz, providing a good trade-off between acquisition speed and SNR [10]. B-scans were averaged in the lateral dimension, and used for three purposes: (1) tracking the eye axial motion for correction in real-time, (2) guiding positioning of the FFOCT coherence gate at the layer of interest, and (3) as a merit function for the wavefront optimization. The merit function can be applied for any retinal layer of interest to automatically adjust the MAL shape to favor imaging in that particular layer.

To perform the optimization, we used the DONE algorithm [12], which had three major advantages for the problem we wished to solve. First, it does not require evaluation of the merit function gradient and, hence, mitigates the MAL hysteresis by limiting the number of times that voltages are updated. Second, the DONE algorithm is very stable due to the use of regularization and is, therefore, well suited for noisy experimental data. Finally, as we use the actuator voltages as input degree of freedom, no calibration step is necessary since no modal decomposition is used. The DONE algorithm models the unknown merit function using a random Fourier expansion (RFE) $g(x) = \sum_{k=1}^{D} c_k \cos(\omega_k^T x + b_k)$ fit to the experimental data using a least squares approach. It iteratively finds a minimum of the merit function on a compact set $X \subseteq [V_{\min}, V_{\max}]^d$ representing each actuator voltage (where $d = 18$ is the number of actuators) by updating the RFE at each new measurement,
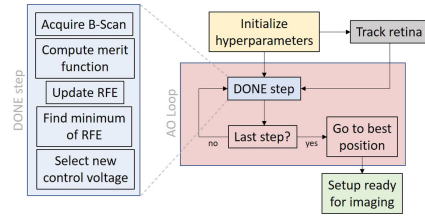
and using this RFE as a surrogate of the merit function for optimization. Hyperparameters were selected by trial and error by imaging a model eye, and then refined for *in vivo* imaging. The number of basis functions D was set to 100. Increasing D leads to a better RFE fit at the cost of more computation time (complexity is $O(D^2)$). To prevent underfitting and overfitting, a regularization parameter λ is used in the least squares fit for finding the RFE coefficients c_k. It also helps with dealing with few measurements. We set λ = 0.01. Finally, the probability density function of frequencies ω for the RFE model is drawn from a Gaussian distribution (variances $\sigma_\zeta^2 = \sigma_\xi^2 = 1$) and influences the exploration of the RFE surrogate and the original function, respectively. The optimization steps are described in Fig. 1.

Retinal imaging was performed on three healthy near-emmetropic subjects (age range 25–30). Research procedures followed the tenets of the Declaration of Helsinki. Informed consent was obtained from subjects after the nature and possible outcomes of the study were explained. The study was authorized by the appropriate ethics review boards [CPP and ANSM (IDRCB number: 2019-A00942-55)]. Each subject was seated in front of the system and stabilized with a chin and forehead rest and asked to fixate a target. To maximize pupil diameter, image acquisition was performed in a dark room. Images were acquired just after wavefront optimization in parallel with real-time correction of axial eye motion. Image sequences were composed of 150 frames acquired at 300 Hz. During image acquisition, the total power entering the eye from the FF-OCT illumination source and the SD-OCT scanning source were respectively 1.3 mW (for the 0.5 s of image acquisition) and 0.25 mW (continuous scanning), which are below the ocular safety limits established by the ISO standards for group 1 devices. Image processing was previously described in details elsewhere [10], and was composed of 2-phase demodulation, image selection, alignment and averaging. We used the ImageJ plugin MosaicJ to stitch together five images into a 12° × 12° FOV. A photoreceptor density map was computed using a fully automated algorithm based on modal spacing as described in [13].

We first tested the adaptive-glasses approach on a 1951 USAF target after adding a microscope objective in the FFOCT sample arm and positioned the MAL at the back plane of the microscope objective. We added a 0.3 D defocus in the sample arm and acquired FF-OCT images before and after correcting aberrations [Fig. 2(a)]. Aberrations induce phase artifacts yielding ringing effects and inversion of contrast. All of these were corrected after using the adaptive-glasses approach. Figure 2(b) shows the power spectral density (PSD) of these
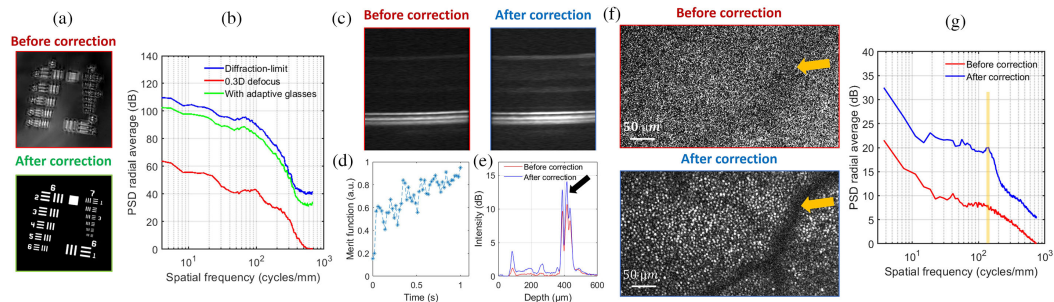

Fig. 1. Retina is tracked during the optimization to compute the merit function on the selected layer. The number of iterations was set to 50, for a total of 1 s optimization duration.

Fig. 2. Validation of the adaptive-glasses approach. (a) USAF target FFOCT image before and after aberration correction and (b) their respective PSD compared to the expected diffraction limit case. (c) SD-OCT retinal cross section before and after aberration correction. (d) Values of the merit function during wavefront optimization using the DONE algorithm. (e) Lateral average of SD-OCT B-scan highlighting the increased signal after aberration correction. Black arrow points to the retinal layer used for wavefront optimization. (f) Single non-averaged FFOCT frames before and after aberration correction at 5° temporal. Image contrast was stretched independently so the shadow of a vessel positioned in a retinal layer above the photoreceptor layers can be visualized (yellow arrows). (g) Their respective PSDs, outlining the gain in terms of SNR.

images compared to the diffraction-limited PSD. Note that all three PSD plots present an almost identical distribution of spatial frequencies, showing the robustness of FF-OCT to symmetric aberrations (here defocus) in terms of resolution, while SNR drops significantly. Using the adaptive-glasses approach, we were able to recover the lost SNR, almost reaching the value we would expect for diffraction-limited imaging.

Figures 2(c)–2(g) show the capacity of the adaptive-glasses approach to correct ocular aberrations and increase the SNR at the same time for the SD-OCT [Figs. 2(c) and 2(e)] and FFOCT [Figs. 2(f) and 2(g)] for *in vivo* retinal imaging. The wavefront optimization [Fig. 2(d)] was realized using the signal of the cone outer segment tips [COST, black arrow in Fig. 2(e)]. Figure 2(f) presents the same retinal zone before and after correcting ocular aberrations with the adaptive glasses approach. A considerable increase in SNR is observed, thus making it possible to resolve the photoreceptor mosaic with a 7.5 mm pupil diameter in a single non-averaged frame. PSDs of these images, highlighting the gain in terms of SNR, are given in Fig. 2(g), where the yellow line indicates the spatial frequency of the photoreceptor mosaic, which is hidden by phase artifacts before aberration correction.

Using the SD-OCT and the axial motion stabilization, we can precisely position the FFOCT coherence gate at the retinal layer of interest. However, a mismatch of the coherence gate and focal plane positions produces low SNR FFOCT images. At the full-aperture, e.g., for a 7 mm pupil diameter, the depth of focus is approximately 10 times thinner than the retina, making focus position an essential step [14]. During each imaging session, SD-OCT B-scans are displayed in real-time, allowing the user to select the retinal layer of interest, where the coherence gate is then automatically positioned. In addition, when activating the wavefront optimization, only the brightness of the selected layer is taken into account, optimizing the focal plane position to the coherence gate position. Owing to this procedure, we were able to image nerve fiber layer (NFL) and photoreceptor inner/outer segment junction (IS/OS) at the same retinal region with ease (Fig. 3). Green arrows indicate the retinal layer selected for the merit function in the SD-OCT B-scan. Note that the MAL defocus amplitude correction is limited, thus limiting brightness when imaging the inner retina, which could be corrected by
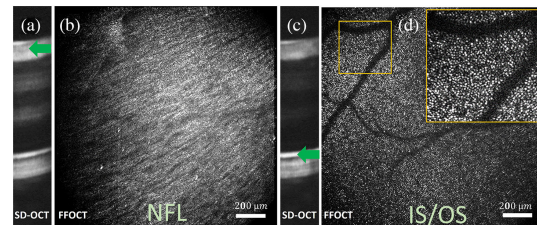

Fig. 3. Wavefront optimization for a given retinal depth. (a) and (b) SD-OCT retinal cross section and FF-OCT *en face* image acquired when optimizing for the retinal NFL (green arrow). (c) and (d) At the same region as (a) and (b) but at a different retinal depth after applying the wavefront optimization at the IS/OS junction.

adding a variable focal length lens [6]. Visualization 2 presents FFOCT images acquired at different depths in the NFL at 8° nasal, highlighting the high axial resolution afforded by FFOCT technique (i.e., 8 µm).

Another benefit of correcting ocular aberrations for FFOCT is increased robustness. Indeed, FFOCT images are generated after a two-phase demodulation step, meaning that they carry an amplitude signal modulated by the phase difference of two consecutive images, i.e., $A \times \cos(\Delta\phi)$ (where A is the amplitude signal, and $\Delta\phi$ is the phase difference of two consecutive images) [10]. Since phase modulation is performed almost randomly by the residual axial eye motion after correction [10], and ocular aberrations dampen the measured amplitude, the majority of acquired images are dominated by noise. Aberration correction restores the amplitude signal, thus increasing the number of high SNR images. Visualization 3 and Visualization 4 present an FFOCT image sequence after correcting ocular aberrations with the adaptive-glasses approach, where the NFL and photoreceptor mosaic, respectively, can be visualized in single frames and monitored over time with a 6 ms resolution.

One important hurdle of AO-OCT for clinical translation is the challenge of allying high-spatial resolution with a wide FOV, which is beneficial for clinical applications. The combination of FFOCT and the adaptive-glasses approach opens a new avenue to wide FOV high-resolution retinal imaging in a
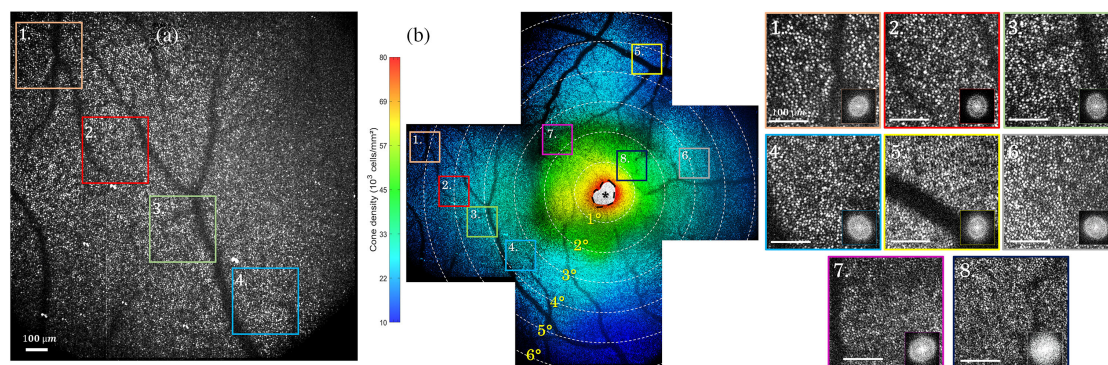
Fig. 4. (a) 5° × 5° FOV FFOCT retinal image, where the photoreceptor can be resolved without any apparent anisoplanatism (see zoomed areas). (b) 12° × 12° FOV image after stitching together five FFOCT images. The color map represents the computed photoreceptor density. Black dashed area indicates where cone density was unreliably measured, automatically detected, and discarded. Zoomed areas of 1° × 1° FOV, chosen to be representative of different eccentricities, and their respective Fourier transforms are also shown.

compact imaging system. Figure 4(a) presents a 5° × 5° FOV image obtained in a single shot (0.5 sec acquisition duration), as close as 2° from the foveal center, where photoreceptors can be resolved over almost the entire FOV (limited only by the retinal curvature). Zoomed areas highlight that no apparent anisoplanatic effect is observed.

The wide FOV obtained in a single shot facilitates important tasks in the clinical environment to diagnose retinal disorders at early stages, such as image montaging and the computation of photoreceptor-based biomarkers. Figure 4(b) shows a 12° × 12° FOV image at the fovea composed of five images acquired at different retinal locations. Photoreceptor density is color coded and was consistent with the literature [15] except within 0.5° of the fovea (black dashed area) where photoreceptors were not resolved but were nevertheless automatically detected and discarded using the method proposed by [14]. The total time necessary to obtain such an image (including subject alignment, image acquisition, and processing) is about 15 min. For comparison, an instrument with a 2° × 2° FOV (i.e., the typical size of the eye's isoplanatic patch) would need to stitch around 60 images to obtain the same image area with an image processing time multiplied by at least a factor of 10.

We proposed the adaptive-glasses approach as a wavefront sensorless AO method favoring small footprint and low optical complexity. We successfully applied this approach to *in vivo* retinal imaging using FFOCT, achieving 3D high-resolution images over a 5° × 5° FOV at 300 Hz in a single shot. To the best of our knowledge, this is the first demonstration of AO successfully coupled to FFOCT for retinal imaging. Although we mainly illustrated the proposed approach for dual-channel SD-OCT and FFOCT retinal imaging, it can be adapted to other imaging modalities and samples. Finally, the combination of the adaptive-glasses approach with FFOCT tackles those challenges that have so far prevented transfer of AO-OCT technology from bench to clinics.

REFERENCES

1. D. Huang, E. A. Swanson, C. P. Lin, J. S. Schuman, W. G. Stinson, W. Chang, M. R. Hee, T. Flotte, and K. Gregory, and C. A. Puliafito, Science **254**, 1178 (1991).
2. J. Jarosz, P. Mecê, J.-M. Conan, C. Petit, M. Paques, and S. Meimon, Biomed. Opt. Express **8**, 2088 (2017).
3. E. Gofas-Salas, P. Mecê, C. Petit, J. Jarosz, L. M. Mugnier, A. M. Bonnefois, K. Grieve, J. Sahel, M. Paques, and S. Meimon, Appl. Opt. **57**, 5635 (2018).
4. R. S. Jonnal, O. P. Kocaoglu, R. J. Zawadzki, Z. Liu, D. T. Miller, and J. S. Werner, Investig. Ophthalmol. Vis. Sci. **57**, OCT51 (2016).
5. P. Bedggood, M. Daaboul, R. Ashman, G. Smith, and A. Metha, J. Biomed. Opt. **13**, 024008 (2008).
6. H. R. G. W. Verstraete, M. Heisler, M. J. Ju, D. Wahl, L. Bliek, J. Kalkman, S. Bonora, Y. Jian, M. Verhaegen, and M. V. Sarunic, Biomed. Opt. Express **8**, 2261 (2017).
7. E. Brunner, M. F. Shirazi, M. Laslandes, W. Drexler, A. Pollreisz, C. K. Hitzenberger, and M. Pircher, Investig. Ophthalmol. Vis. Sci. **61**, 224 (2020).
8. U. Tricoli and R. Carminati, J. Opt. Soc. Am. A **36**, C122 (2019).
9. P. Mecê, K. Groux, J. Scholler, O. Thouvenin, M. Fink, K. Grieve, and C. Boccara, Biomed. Opt. Express **11**, 4928 (2020).
10. P. Mecê, J. Scholler, K. Groux, and C. Boccara, Biomed. Opt. Express **11**, 492 (2020).
11. J. Mertz, H. Paudel, and T. G. Bifano, Appl. Opt. **54**, 3498 (2015).
12. L. Bliek, H. R. G. W. Verstraete, M. Verhaegen, and S. Wahls, IEEE Trans. Neural Netw. Learn. Syst. **29**, 167 (2018).
13. R. F. Cooper, G. K. Aguirre, and J. I. Morgan, Transl. Vis. Sci. Technol. **8**, 26 (2019).
14. P. Mecê, E. Gofas-Salas, M. Paques, K. Grieve, and S. Meimon, Biomed. Opt. Express **11**, 4069 (2020).
15. C. A. Curcio, K. R. Sloan, R. E. Kalina, and A. E. Hendrickson, J. Comp. Neurol. **292**, 497 (1990).

Conclusion and perspectives

In this thesis, I looked at the possibilities offered by FFOCT for retinal imaging, whether it is for the study of degenerative diseases through disease modeling and drug screening, or for the investigation of these diseases directly *in vivo*. The eye is a complex organ that is easily accessible for imaging, exhibiting lots of different diseases which still need to be investigated especially in the retina. I showed that FFOCT is a suitable technique for microscopy (*in vitro* and *ex vivo* samples) and for *in vivo* imaging, offering lots of opportunities to study the eye.

By giving structural information, I demonstrate that FFOCT will be an interesting tool for biology in many ways. This technique is non invasive: it is non contact and do not need any labelling or sample preparation. This allows us to study living samples, which can potentially be imaged over days. I also investigated Dynamic FFOCT by showing that this innovative intrinsic contrast reveals cellular activity, differentiating cells by their type or phenotype. Imaging retinal organoids and RPE cells helped me in the characterisation of D-FFOCT and improvements of 3D and timelapse acquisitions. We were able to stabilise the acquisitions and to create a better representation of the cellular activity thanks to the computation of intrinsic variations on the HSV colorspace, helping in the differentiation of cells. We showed the possibilities offered by real-time imaging with Holovibes [78]. I also implemented a Matlab code allowing to follow scratch assays evolution on RPE cell cultures, from the perspective of doing AMD disease modeling. This conveys me in the fact that D-FFOCT is perfectly suitable for disease modeling in retinal degenerative diseases with *in vitro* samples. I also brought some elements about the understanding of the dynamic signal produced by cells, after years of testing inhibitors. By comparing with immunohistochemistry, it appeared that mitochondria seem to be the main contributor of the signal, while Golgi apparatus contributes evenly to the signal in different cell phenotypes. I demonstrated the stabilisation of acquisitions and maximisation of signal for wide-field images in *in vivo* imaging with FFOCT. All these elements comfort us in the idea that one day we will be able to use dynamic imaging for *in vivo* retina, in order to investigate degenerative diseases previously drug screened *in vitro*.

Many perspectives take shape for the use of D-FFOCT for eye applications.

Following of retinal organoids Recently, in collaboration with the Institut de la Vision, the OREO project (ANR grant) was created for the study of retinal organoids. This project consists in the design of a new setup combining FFOCT and confocal microscope for fluorescence imaging. This setup will be placed in a controlled environment, a L2 laboratory in Institut de la Vision, and user friendly interface to allow the imaging of retinal organoids over days for the following and evolution of degenerative diseases such as Retinitis Pigmentosa.

RPE diseases (IHU REPLICA) AMD is a disease where the RPE layer degenerates and holes appear. To reproduce this disease, we tested scratch assays with a scalpel blade, but this technique is not perfectly repeatable. This is why we proposed the setup combined

with laser in chapter 4. The perspective is to improve the setup by solving the problems raised in chapter 4. Recently, Gilles Tessier team, in Institut de la Vision, proposed a digital holographic microscopy technique combined with a pulsed laser to perform cuts in RPE cell cultures and retinal organoids, and then image the variations. An other approach would be to perform drug screening after scratch assays in order to determine some treatment for degenerative diseases [96–98]. Thanks to the real-time imaging, we can also think of imaging apical processes on RPE cells, such as phagocytosis by disposing photoreceptor outer segments on microvilli [99], or macrophages.

Automatic detection of dynamic signal   We can also think of the application of machine learning to the detection of dynamic signal. Recently, the use of machine learning was demonstrated for the detection and classification of cancer with D-FFOCT [93]. The previous PhD student Jules Scholler also tried machine learning on *ex vivo* retinas for the classification of cells while they belong to different retinal layers. The use of machine learning could be applied to detect changes in dynamic signal in disease modeling and interpret it automatically to ease the use of D-FFOCT for drug screening by biologists for example.

Appendix A

Assembly of a FFOCT system

A.1   Equipement required to construct a FFOCT system

Illumination source   LED (preferentially $\lambda >$600nm for biological applications[1]), with a coherence length at least of the same size of the depth of focus of the microscope objectives (see section B.3).

Optics

- Two identical microscope objectives with a high numerical aperture, the NA will determine the lateral resolution of the system (see A.1).

- Tube lens: will determine the field-of-view of the system, but also its magnification[2].

- Collimator lens: Conjugation lens to send the image of the iris on the focal plane of the microscope objectives (usually achromatic doublet to correct for aberrations).

- Condenser lens: Lens to optimise the viewing angle of the LED.

- Beam-splitter: coated for the LED wavelength.

Camera   With high full well capacity (see section 2.4 for explanation).

Mechanical pieces

- Iris (field iris), to ease the adjustment of the system.

- Translation stage (motorized or not): to scan the sample.

- 2-axis (XY) translation mount for the microscope objective of the sample arm.

- Z-axis translation mount (optional): for the position of the iris.

Electrical components

- Two motors: one for the sample arm (to move the sample in order to scan it in depth), one for the reference arm (to move the entire arm to retrieve the optical path of the sample arm).

- Piezoelectric motor for the reference arm.

---

[1]See section B.2

[2]Corresponds to the size of the camera pixel in the object plane in μm/pixel.

A.2   Assembly

The system is built around the beam-splitter, which allows to create stability. There are four arms around this beam-splitter: the illumination arm, the reference arm, the sample arm and the detection arm.

The illumination arm   It is important to construct correctly the illumination arm of the FFOCT setup as it helps to adjust the rest of the setup. The illumination arm is built in order to create a Köhler illumination with a condenser lens, a field iris[3] and a collimator lens. The condenser lens (usually with a focal length between 30mm and 60mm) is used to optimised the beam of the LED to ensure a full illumination of the iris. Then the collimator lens (focal length of 75mm) sends the image of the iris to infinity. It is important to not optically conjugate the LED pattern with the iris[4]. This is due to the fact that I do not want the pattern of the LED to overlay my images. I usually mount this arm in cage systems to fix it to the beam-splitter for stability.

The reference arm   This part of the setup is a crucial part: it will allow to create FFOCT images. It is composed of a microscope objective, a mirror (which will be the reference plane, usually a silicon mirror), a piezo-electric motor. The silicon mirror has to be glued on the piezo-electric (as much planar as possible). Then the mirror must be placed in the focal plane of the microscope objective. To allow an easier adjustement of this distance, I usually mount the piezo-electric motor on a Z-axis translation mount to finely tune the position. Finally the whole arm is mounted on a one-axis motor which will permit to match optical path between reference arm and sample arm.

The sample arm   This arm will image the sample: it is important to have a stable arm. The different pieces to construct this arm are: a microscope objective, a 2 axis translation mount and a translation stage (XY) combined with a motor to move the sample. The 2 axis translation mount is used to adapt the position of the microscope objective (i.e. the microscope objective is screwed in the 2 axis translation mount) to the reference arm (matching beams from the two microscope objectives). I prefer to mount this arm in a cage system linked to the beam-splitter to improve the stability of the system.

The detection arm   This part of the system allows to create the image: it is composed of a tube lens and a camera. The tube lens sends the image on the camera's detector. With the reference arm, they are the only parts of the system to do not be attached to the beam-splitter.

A.3   Complete and functional system

This part of the assembly consists in assembling the four arms around the beam-splitter and adjust them (Fig. A.1).

Adjustment of the setup   Firstly, the illumination arm is fixed to the beam-splitter (e.g. with cage mounts) and the tube lens. To verify the adjustment of the illumination arm, I place a paper screen at the focal plane of the tube lens and close the iris (not completely). If the illumination arm is correctly mounted, the image of the iris on the

---

[3]An aperture iris is not necessary because the aperture of the system is managed by the microscope objectives.

[4]See Adjustment of the setup.

screen should be clear. Then, the camera can be added at the right distance of the tube lens (focal plane).

Secondly, the reference arm is placed opposite to the illumination arm (on the other side of the beam-splitter). As the position of the camera must be adjusted (last step), the position of the reference mirror compared to the microscope objective can be tuned thanks to the image of the iris on it. The position of the LED can also be verified in this step: the pattern of the LED should not overlay the image of the iris[5]. Finally, the sample arm is fixed to the beam-splitter. As a substitute for the "real" sample, I use a mirror to replace it to ease the adjustment. First, after blocking the beam coming from the reference arm (between the beam-splitter and the microscope objective), the distance between the microscope objective and the sample mirror is tuned thanks to the motor (with the image of the iris as well). Then, the reference arm is released: the images of the

Figure A.1: **Final look of the system.**

iris by the reference mirror and the sample mirror should be overlaid. If it not the case, the superposition can be adjusted using the 2 axis translation mount of the sample arm's microscope objective.

Creation of the interference pattern A software has been developed by Jules Scholler to control the FFOCT setup and to acquire images [100]. To obtain the FFOCT images, interferences (fringes pattern) should be created. In this case, the optical paths coming from the reference arm and the sample arm should match (when the system is completely adjusted). For this purpose, the piezo-electric motor of the reference mirror should be activated to obtain FFOCT images on the camera (see section 2.3). Moreover, the two arms should be close to the matching position to avoid long and laborious adjustment. Then the reference arm is moved[6] (quite slowly to be able to see the interference pattern on the camera) to the right position where the interference fringes are visible with a maximum contrast.

---

[5]Usually it is visible a few millimetres around the focus.
[6]With the motor.
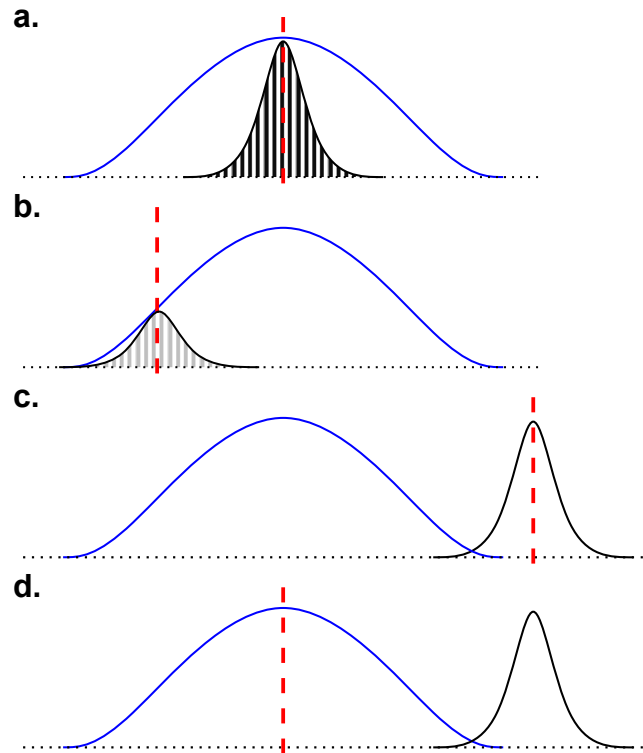
Figure A.2: **Interferences for different alignments of depth of focus and coherence length on a mirror.** The black curve represents the coherence length, the blue one is the depth of focus. The red dashed line shows the imaging plane. **a.** Depth of focus and coherence length perfectly aligned: high contrast fringes and clear image. **b.** Depth of focus and coherence length slightly drifted: low contrast fringes and clear image. **c. & d.** Depth of focus and coherence length completely misaligned: clear image and no fringes & blurry image and fringes not distinguishable (very low contrast).

Congratulations! System is ready Take your favourite sample, image it and enjoy!

A.4 How to choose the correct microscope objectives for your application

Lots of different microscope objectives exist on the market. Here are some key points to choose the best microscope objectives for your application.

Chromatic specifications The microscope objectives should match the wavelength of your application (visible, IR, multiple wavelengths). If you use multiple wavelengths in your application, it is better if the microscope objectives are achromatic (at least) or apochromatic[7].

Numerical aperture and magnification The numerical aperture will determine the lateral resolution of your system: the higher the numerical aperture, the better the lateral resolution. The Magnification will take part in the final proportions of the field-of-view (combined with the tube lens).

---

[7]See section B.1

Immersion   Each microscope objective is adapted to be "immersed" in a specific medium. Three main types exist: air objectives, water-immersion objectives or oil-immersion objectives[8]. Air objectives are ideal for non-contact applications, such as *in vivo* imaging (e.g. eye imaging) or material imaging (e.g. structures). Water-immersion is useful for *in vitro* imaging, such as cell cultures which are grown and stored in culture media. Finally, oil-immersion objectives are usually used with cover glass, which is suitable for *ex vivo* imaging (e.g. organs removed from animals or biopsies from human beings).

Working distance and cover glass thickness   Depending on how deep you want to image in your sample and if you want the microscope objective to touch it or not, the choice of the microscope objective will be crucial. Indeed, the working distance, plus the use of a cover glass, will determine the overall depth of your sample you can image. For example, for a microscope objective with no cover glass, you will be able to image from the surface through the whole working distance until it touches the sample, whereas for a microscope with a cover glass, it will allow you to image from the surface to the working distance minus the cover glass thickness.

Examples of microscope objectives used in our lab   Table A.1 shows the specifications of the different microscope objectives that we use on our different systems in the lab.

Brand	Olympus	Olympus	Olympus
Type	PLAN N	LMPLAN N IR	UM PLAN FL N
Reference	PLN10X	LMPLN10XIR	UMPLFLN10XW
Immersion	Air	Air	Water[9]
NA	0.25	0.3	0.3
Magnification	10	10	10
WD (mm)	10.6	18	3.5
Cover glass (mm)	-	-	-
Application	*In vivo*: retina	*In vivo*: cornea	*In vitro* (W)[10]
Tran. res. (μm)[11]	1.6	1.3	1.3

Brand	Olympus	Nikon
Type	UPLAN SAPO	NIR APO DIC N2
Reference	UPLSAPO30WS	NIR 40X W
Immersion	Silicon oil	Water
NA	1.05	0.8
Magnification	30	40
WD (mm)	0.8	3.5
Cover glass (mm)	0.13 - 0.19	-
Application	*Ex vivo*[12]	*In vitro*[13]
Tran. res. (μm)[11]	0.38	0.50

Table A.1: Specifications and applications for the different microscope objectives present on our systems. WD: working distance; Tran. res.: tranverse resolution.

---

[8]Different types of oil too.
[9]Works also with Silicon oil, as used by LLTech.
[10]Also *ex vivo* with Silicon oil by LLTech.
[11]Calculated for a 660nm wavelength of illumination.
[12]Removed organs such as liver, retina etc.
[13]Cell cultures (2D or 3D).

A.5 Multimodal systems

It is possible to combine a FFOCT setup to other modalities in order to compare results. Three multimodal systems are present in the lab: SD-OCT, fluorescence imaging and laser cut.

SD-OCT for *in vivo* eye imaging   As I explained in Chapter 5, to obtain consistent images during an acquisition of a specific plane of the sample, it is important to have the selected plane inside the depth of focus and coherence gate. For *in vitro* and *ex vivo* samples, the drift is really small and slow making it easily controllable, but for *in vivo* samples, which move with a higher frequency due to the body, we need to track the sample to keep the imaged layer in the depth of focus and coherence gate. For this purpose, a industrial SD-OCT is added in the FFOCT setup to track the eye (cornea or retina depending on the application). The SD-OCT is positioned in the illumination arm of the FFOCT using a dichroic mirror. Then, to avoid the reflection of the SD-OCT illumination on FFOCT images, we introduced filters in the reference arm and detection arm (i.e. camera). We then combine the SD-OCT signal to the motor of the reference arm to manage the length of it to keep the layer of interest in the coherence gate.

Fluorescence imaging   The combination of fluorescence imaging and FFOCT is tricky. To obtain the best fluorescence images, the ideal is to use a confocal microscope, which is a scanning technique using pinholes and single detectors. The difference in the imaging of the sample by these two systems makes it really difficult to combine them, without degrading the specifications of either system. As we imaged pretty thin samples, such as 2D cell cultures and organoids, we could combined a wide-field fluorescence imaging modality to our FFOCT setup. The fluorescence is recorded on a second camera, adapted for fluorescence imaging. The FFOCT and fluorescence beams are separated with dichroic mirrors and fluorescence filters.

Laser cutting for scratch assays   To include a laser path for cutting samples in a FFOCT setup requires a specific design. First, your laser path must allow you to create different patterns of scanning (similar to what is done in confocal microscopy for the sample scanning). This is possible with Galvo mirrors, conjugated with the back focal plane of the microscope objectives to create patterns on the sample. An other point is to keep the rest of the FFOCT setup safe from the laser beam. For this purpose, filters should be carefully chosen and placed in the setup to block the laser beam especially through the reference arm and the detection arm to not damage the reference mirror and the camera. Finally, the laser and the FFOCT illumination LED should have different wavelength to avoid detection problems.

Appendix B

Optics dictionary

B.1   Achromatic & apochromatic optics

Singlet lenses are made of a unique material, polished to create a certain curvature on each side of the lens to give it a specific focal length. The surfaces are spherical, introducing spherical aberration. As the lens is made with a unique material, it may introduce chromatism due to the dipersion of the material. To correct these aberrations, different materials are combined to create doublets and triplets.

Achromatism   An achromatic lens is usually a doublet, i.e. made of two lenses of different materials glued together (or air-spaced). Thanks to the combination of two different materials, the focal distance of the lens is corrected for two different wavelengths (usually it is a blue wavelength and a red wavelength to cover a large range of the spectrum), see Fig. B.1a. It also corrects for the spherical aberration for one wavelength.
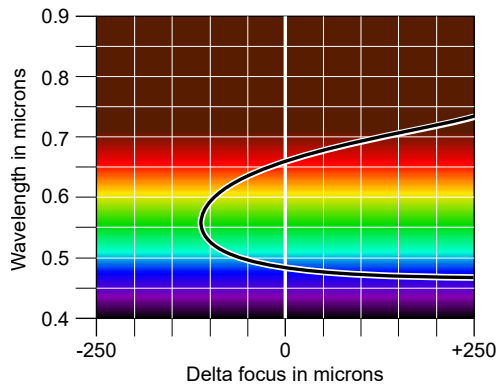
(a) Evolution of the difference between the effective focal distance and the given focal distance in function of the wavelength for an achromatic optic.
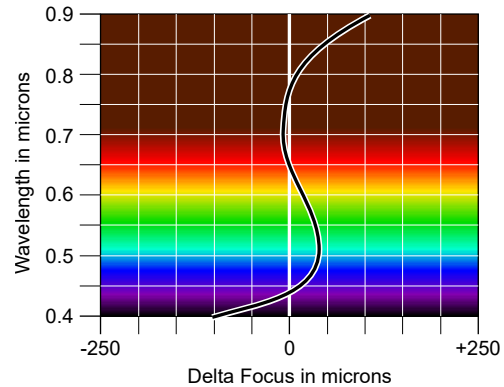
(b) Evolution of the difference between the effective focal distance and the given focal distance in function of the wavelength for an apochromatic optic.

Figure B.1: **Difference between achromatism and apochromatism.** The "0" corresponds to delta focus equates to 0, meaning the effective focal distance is the given focal distance of the optic. ©Wikimedia Commons

Apochromatism   An apochromatic lens is an improved version of the above-mentioned achromatic lens. Since the achromatic lens is only corrected for two wavelengths, the apochromatic lens corrects achromatism for three different wavelengths, giving an almost constant focal distance for a large range of the spectrum see Fig. B.1b. It also improves the correction of the spherical aberration, as it works for two different wavelengths.
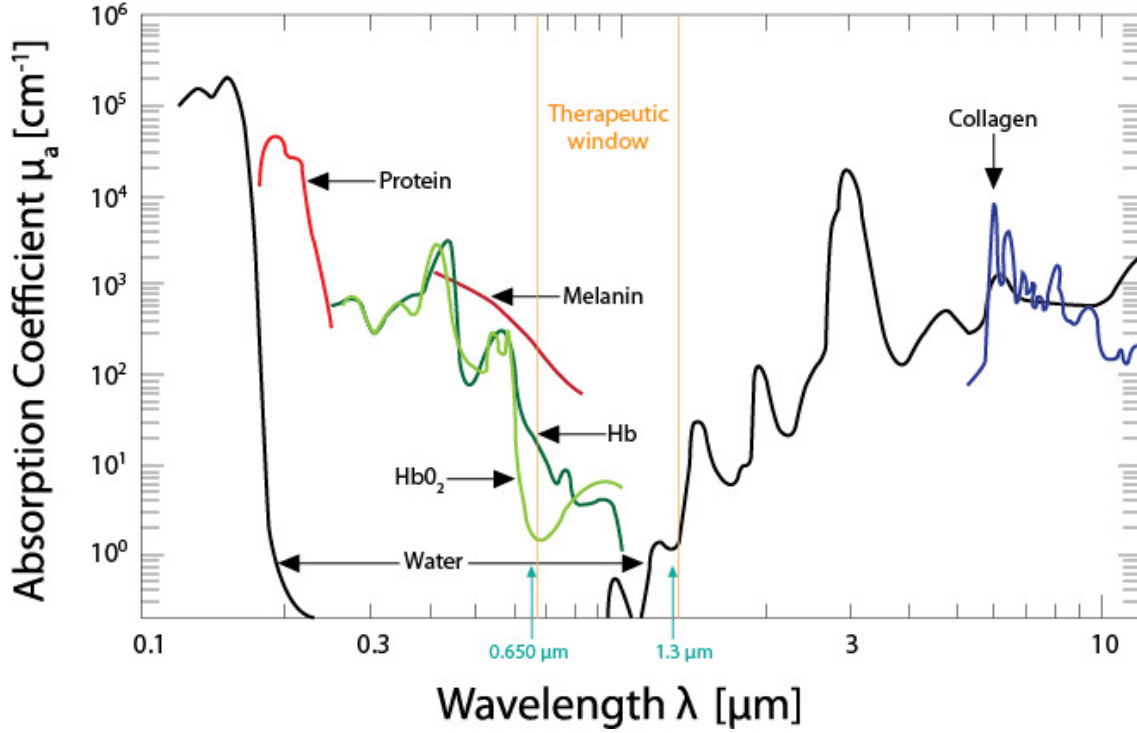
Figure B.2: **Identification of the therapeutic window. Graph representing the absorption coefficients of the main components of biological tissues.** ©Litecure

B.2 Optical therapeutic window

Biological tissues are diffusive materials. Everyone has done the experiment of putting a flashlight behind his/her finger to see that the light passing through it appears red. This is due to the fact that the different parts forming biological tissues have different light absorption spectra.

The main component of biological tissues is water as our body is made of 60%. The absorption of water is low between 200nm and 1.3μm. The blood, composed of two types of haemoglobin (oxyhaemoglobin HbO_2 and deoxyhaemoglobin Hb) is highly absorbent for low wavelengths. The absorption coefficient is under $10cm^{-1}$ for wavelengths above 600μm. Collagen fibres are highly absorbent for high wavelengths (above several μm). The absorption of melanin is high for low wavelengths but is acceptable above 600μm.

Finally, there is a "window" where all the components are less absorbent: between 650μm and 1.3μm. This window is called therapeutic window for which biological tissues are easily to image in depth.

B.3 Coherence length vs. depth of focus

Coherence length The coherence length is dependent on the illumination source and the imaging medium as shown in eq. B.1. It represents the coherence gate of the wave and is important in interferometric techniques: to obtain interferences, the waves which interfere should differ by less than the coherence length.

$$l_c = \frac{\lambda^2}{n\Delta\lambda} \tag{B.1}$$

Depth of focus The depth of focus of a system is the length along the optical axis in which the image still appear clear. This is dependent on the resolution of the system which is not a single point. Using Thales theorem, we can determine the depth of focus for FFOCT (dof) as shown in eq. B.2 and Fig. B.3.
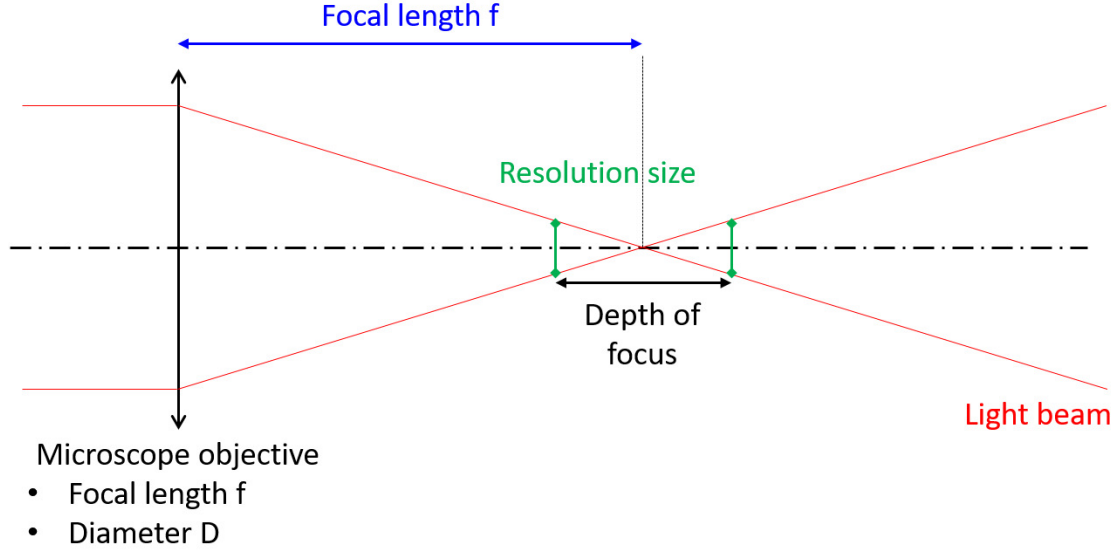
Figure B.3: **Schematic of the depth of focus of a microscope objective.**

$$\frac{dof/2}{f} = \frac{Res.}{D} \tag{B.2}$$

In a FFOCT setup, the microscope objectives use an infinity - focal plane conjugation, meaning $\frac{f}{D} = N$ and $N = \frac{1}{2NA}$, and the resolution is given in eq. 2.5. We finally obtain the formula in eq. B.3.

$$dof \approx 0,61 \times \frac{\lambda}{NA^2} \tag{B.3}$$

Figure B.4: **Depth of focus versus Coherence length.**

Why these two parameters are important for a FFOCT setup?   It is difficult to know exactly where your imaged plane is in the depth of focus, and you have to match it with the coherence length to obtain images. This is why it is easier to match depth of focus inside coherence gate: the coherence gate has to be at least the same length as the depth of focus. In Fig. B.4 a., as the coherence length is inferior to the depth of focus, it is difficult to match the coherence length to the position of the plane of interest, even if it is in the depth of focus. Now, if the depth of focus has the same length as the coherence gate (see Fig. B.4 b.), by making them coincident, the position of the plane of interest will be in the coherence length. Finally, in Fig. B.4 c., when the coherence length is superior to the depth of focus, it is really easy to image the plane of interest: once it is in the depth of focus, it will automatically be in the coherence gate.

Appendix C

First steps to obtain stable and repeatable FFOCT images of *in vivo* retina

These are two other articles on which chapter 5 of this thesis is based on.

C.1   Optical stabilization of axial motion

High-resolution *in-vivo* human retinal imaging using full-field OCT with optical stabilization of axial motion

PEDRO MECÊ,[*] [ID] JULES SCHOLLER, KASSANDRA GROUX, AND CLAUDE BOCCARA

Institut Langevin, ESPCI Paris, CNRS, PSL University, 1 rue Jussieu, 75005 Paris, France
[*]*pedro.mece@espci.fr*

Abstract: Time-domain full-field OCT (FF-OCT) represents an imaging modality capable of recording high-speed *en-face* sections of a sample at a given depth. One of the biggest challenges to transfer this technique to image *in-vivo* human retina is the presence of continuous involuntary head and eye axial motion during image acquisition. In this paper, we demonstrate a solution to this problem by implementing an optical stabilization in an FF-OCT system. This was made possible by combining an FF-OCT system, an SD-OCT system, and a high-speed voice-coil translation stage. B-scans generated by the SD-OCT were used to measure the retina axial position and to drive the position of the high-speed voice coil translation stage, where the FF-OCT reference arm is mounted. Closed-loop optical stabilization reduced the RMS error by a factor of 7, significantly increasing the FF-OCT image acquisition efficiency. By these means, we demonstrate the capacity of the FF-OCT to resolve cone mosaic as close as 1.5^o from the fovea center with high consistency and without using adaptive optics.

1. Introduction

Optical Coherence Tomography (OCT) has become a gold standard for living human retinal imaging in the clinical environment [1,2]. Owing to its unprecedented axial resolution, OCT enables the diagnosis of retinal disorders at the earliest stages and monitoring of the progression of retinal diseases. While physicians are capable of interpreting tomographic retinal cross-sections from OCT, there is nevertheless a demand for *en-face* views. Although OCT can produce *en-face* retinal images from 3-D stacks, it presents a low lateral resolution compared with Adaptive Optics (AO) ophthalmoscopes [3]. By correcting static and dynamic ocular aberrations [4,5], AO can explore the full aperture of the eye's pupil to achieve micrometer lateral resolution. To be able to combine both high axial resolution from OCT, and the high lateral resolution from AO, a great effort was made to develop AO-OCT systems [6,7]. However, the commercialization and the clinical deployment of AO-OCT are still challenging, mainly because of cost, optical complexity, size and heavy image post-processing linked to the use of AO [6].

Another modality of OCT is the time-domain Full-Field OCT (FF-OCT) [8] (henceforth, we refer to this imaging modality simply as FF-OCT). Contrary to conventional OCT, which scans an illumination spot across a tissue surface and records at each spot the depth structure, FF-OCT uses a spatially incoherent light source, high-speed megapixel camera and time-domain phase modulation to acquire *en-face* sections of the sample at a given depth. One attractive point of this technique for retinal imaging, is the fact that FF-OCT presents a low sensitivity to low-order ocular aberrations (*i.e.* defocus and astigmatism), due to the use of the spatially incoherent light source [9,10]. This interesting feature was highlighted in [11], where cone mosaic at 6° from the foveal center of a healthy subject (without prescription eyeglasses) was resolved without using AO. This first image was made possible by the combination of FF-OCT and a Spectral-Domain OCT (SD-OCT). Through the images generated by the SD-OCT both retinal cross-section and

the FF-OCT reference mirror were visible, and a manual match, just before the acquisition, was possible. Nevertheless, this strategy faces significant challenges in providing consistent and reproducible images, mainly due to involuntary axial head and eye motion, which can achieve a median maximum axial speed in the order of 1mm/s [12]. As a consequence, a considerable amount of images has to be acquired to increase the chances of matching the optical path of both arms for a retinal layer of interest.

Hence, to be able to record efficiently and consistently *en-face* sections of the retina *in-vivo*, an axial optical stabilization strategy is necessary. An optical stabilization of axial motion applied in time-domain FF-OCT for retinal imaging was first proposed by Miller *et al.*, combining the FF-OCT with an auxiliary time-domain 1-D OCT and a voice coil translation stage in the reference arm [13]. However, the time-domain 1-D OCT used for axial motion tracking was too slow to work *in-vivo* (20 A-scans per second). Later, Pircher *et al.* [14] combined a transverse scanning OCT system (which directly extracts *en-face* images) with a high-speed Fourier domain 1-D OCT, used to track the cornea apex signal, and a rapid scanning optical delay line montage for real-time optical stabilization. Although the achieved performance was satisfactory, because of the scanning illumination/detection scheme of the proposed OCT, *en-face* images were acquired with a low frame rate, limited FOV and suffered from motion artifacts and distortion due to fixational eye movements [15]. Therefore, continuous involuntary head and eye motion remains one of the biggest challenges in time-domain FF-OCT when imaging the living human retina.

In this paper, we present an FF-OCT retinal imaging system with optical stabilization of axial motion. This system was made possible by combining the FF-OCT system with an SD-OCT. The idea is to use B-scans generated by the SD-OCT to measure the retinal axial position and to drive a high-speed voice-coil translation stage, where the reference arm of the FF-OCT is mounted, correcting for the eye motion. By these means, we demonstrate the capacity of the FF-OCT to resolve cone mosaics as close as 1.5^o from the fovea center with high consistency and efficiency, without using adaptive optics.

2. Methods

2.1. Experimental setup

Figure 1 presents the schematic drawing of the custom-built FF-OCT system coupled with a SD-OCT system. The FF-OCT comprises a light-emitting diode (LED) with λ = 850 nm center wavelength and 30 nm bandwidth (M850L3, Thorlabs), used as a spatially incoherent illumination source, giving a theoretical axial resolution of approximately 8 μm in water. The LED is focused by a condenser 20 mm in front of the eye's pupil. A physical diaphragm is positioned in front of the LED, conjugate to the retina and the FF-OCT reference mirror. The illumination beam is split into the reference and the sample arms by a 50:50 cubic beam splitter (BS). For the reference arm, an Olympus 10X/0.25 NA Plan Achromat objective is used with a silicon mirror placed at the focal plane of the objective. The whole reference arm (microscope objective and silicon mirror) is mounted on a fast voice-coil translation stage (X-DMQ12P-DE52, Zaber Technologies Inc.), allowing for adjustment of the coherence gate depth position with a maximum speed of 10 mm/s. For the sample arm, optical windows were introduced to compensate for dispersion effects (not shown in Fig. 1) and the healthy volunteer's eye was aligned along the optical axis. The FF-OCT light beam arrives with an 8 mm diameter in the eye's pupil. The back-scattered photons from both arms are recombined by the same BS and focused onto a high-speed (up to 720 Hz) CMOS camera (Q-2A750-Hm/CXP-6, Adimec) for FF-OCT imaging.

The use of an SD-OCT system coupled with our custom-built FF-OCT is driven by two motivations: firstly, to measure the retinal axial position through SD-OCT cross-sectional images, which is a crucial step to correct for axial motion; secondly, once the axial motion is stabilized, to display in real-time SD-OCT retinal cross-sections of sufficient quality to guide the positioning of the FF-OCT coherence gate at the retinal layer of interest. To address these
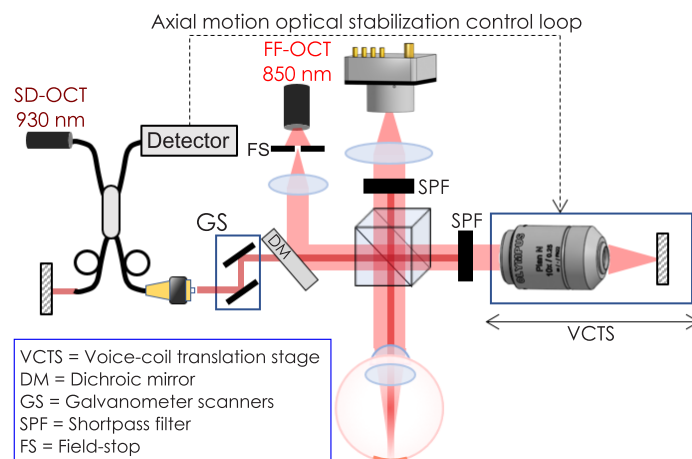
Fig. 1. Schematic drawing of the custom-built FF-OCT system coupled with an SD-OCT for real-time axial motion correction and FF-OCT coherence gate positioning guidance.

motivations, we considered a trade-off between acquisition rate, for fast axial motion tracking, and enough signal-to-noise ratio (SNR), for retinal layer identification, helping the positioning of the FF-OCT coherence gate. The SD-OCT system (Thorlabs Ganymede-II) was coupled through a dichroic mirror positioned between the FF-OCT illumination source and the BS. The SD-OCT galvanometer scanners were 20-cm away and not conjugate to the eye's pupil due to three main factors: mechanical restrictions imposed by the commercial SD-OCT system, to avoid specular reflections in the FF-OCT detector by introducing optical lens in the sample arm [16], and to favor a compact optical design.

The SD-OCT system comprises a broadband superluminescent diode with $\lambda = 930$ nm center wavelength and 60 nm bandwidth, giving a theoretical axial resolution of $4.5\mu m$ in water. It presents an A-scan rate up to 36 kHz with a sensitivity of about 96 dB and 1024 axial pixels, comprising an imaging depth (axial range) of 2.2 mm in water. As the galvanometer scanners and the eye's pupil are not conjugated, the SD-OCT light beam arrives in the eye's pupil with a 4 mm diameter, slightly scanning the pupil plane. Shortpass filters were introduced to block the SD-OCT signal in the reference and detection arms of the FF-OCT.

2.2. Axial motion correction

Initially, we manually match the optical path of the FF-OCT reference mirror with a fixed model eye in the sample arm to determine the initial position of the voice-coil translation stage. This calibration step is necessary only once. B-scans generated by the SD-OCT are used to measure the retinal axial position by the following means: 1) A-scans composing the B-scan are averaged, obtaining an axial profile with increased SNR (named from here after "averaged A-scan"); 2) the averaged A-scan is cross-correlated with a reference A-scan and the relative retinal axial position is measured, 3) parabolic fitting is used to obtain a subpixel estimation of the axial retinal position with sub-micrometer precision. The reference A-scan is the first averaged A-scan generated after activating the axial motion correction. This reference is kept until the axial motion correction procedure is deactivated. After the measurement, a corresponding voltage is sent to the voice-coil translation stage, which moves the whole reference arm of the FF-OCT to compensate for the axial motion, re-matching the reference arm with the retinal layer of interest. A custom-developed real-time calculator, comprising core libraries written in MATLAB, controls the axial motion stabilization closed-loop with a 50 Hz loop rate. Control strategy is a PI (proportional-integral) controller with 0.5 gain and the main steps of the chronogram are: SD-OCT B-scan acquisition

(7 ms), SD-OCT B-scan processing (2 ms), axial eye motion measurement (1 ms) and voice-coil translation stage reaction and positioning (10 ms).

2.3. Image acquisition

To obtain statistics on axial motion, we acquired 13 SD-OCT image sequences (7 to 28 s of duration) from three healthy subjects, for a total of 4700 analyzed A-scans. Simultaneous FF-OCT and SD-OCT image acquisition was performed on a young healthy subject (aged 25) presenting a refractive error of $1.5D \times 0.5D \times 160^o$ (spherical × cylindrical × axis of cylindrical errors). Research procedures followed the tenets of the Declaration of Helsinki. Informed consent was obtained from the subject after the nature and possible outcomes of the study were explained. This study was authorized by the appropriate ethics review boards (CPP and ANSM (IDRCB number: 2019-A00942-55)). Subjects were seated in front of the system and stabilized with a chin and forehead rest and asked to fixate a target placed at an infinite focal conjugate. During the imaging session, subjects were wearing their prescription glasses to increase the signal level of both SD-OCT and FF-OCT [10]. Image acquisition was realized in a dark room, maximizing the pupil dilation. Four sets of data were recorded simultaneously during imaging sessions: FF-OCT images, SD-OCT B-scans, retinal axial position and the position of the voice-coil translation stage (equivalent to the position of the FF-OCT reference mirror). Phase modulation was performed by the residual axial motion after optical stabilization (*i.e.* the residual tracking error). FF-OCT images were acquired at 300 Hz using custom-built software [17]. The FF-OCT camera worked close to saturation to use the whole full well capacity, decreasing relative importance of shot noise [18]. Concerning the SD-OCT, we empirically chose to scan 1° FOV of the retina with 256 A-scans, providing a good trade-off between acquisition speed and SNR. The latter had to be sufficient to distinguish most of the retinal layers, crucial for guiding the positioning of the FF-OCT coherence gate to the retinal layer of interest. During image acquisition, the total power entering the eye from the FF-OCT illumination source and the SD-OCT scanning source were respectively 1.3 mW (during 0.25s) and 0.25 mW (continuous scanning), which are below the ocular safety limits established by the ISO standards for group 1 devices.

2.4. Image processing

As detailed in [18], the intensity recorded on a camera pixel is the coherent sum of the reference and sample beams, containing coherent and incoherent terms, expressed as follows:

$$I_{\phi=\phi_N} = \eta \frac{I_0}{4}(R_{eye} + R_{ref} + R_{incoh} + 2\sqrt{R_{eye}R_{ref}}cos(\Delta\phi_N)) \qquad (1)$$

where $I_{\phi=\phi_N}$ is the intensity recorded at time point N with a ϕ_N phase shift, η is the camera quantum efficiency, I_0 is the LED's power output (we considered a 50/50 beam-splitter), R_{eye} is the eye reflectivity (*i.e.* the power reflection coefficient), R_{ref} is the reference mirror reflectivity (*i.e.* the power reflection coefficient), $I_{incoh} = R_{incoh}\frac{I_0}{4}$ is the incoherent light detected by the camera, mainly induced by multiple scattering and back-scattering from out-of-focus retinal layers, and $\Delta\phi$ is the phase difference between the reference and the sample back-scattered signals.

From the acquired image sequence, each image was normalized by dividing each image by its mean value. Since the phase was randomly modulated by the residual tracking error, and to eliminate the incoherent terms, we adopted a 2-phase demodulation. The 2-phase demodulation consists of subtracting one image $I_{\phi=\phi_N}$ from the next $I_{\phi=\phi_{N+1}}$ and taking the modulus:

$$I_{2-phase} = |I_{\phi_N} - I_{\phi_{N+1}}| = \eta \frac{I_0}{2}\sqrt{R_{eye}R_{ref}}|cos(\Delta\phi_N) - cos(\Delta\phi_{N+1})| \qquad (2)$$

Note that for a 2-phase demodulation strategy it is not possible to un-mix amplitude and phase. Next, images with a very low or absent useful signal, mainly due to an insufficient

phase shift between consecutive images (*i.e.* low value for $|cos(\Delta\phi_N) - cos(\Delta\phi_{N+1})|$), were automatically detected using an intensity-based threshold algorithm, and then excluded from the image sequence. Finally, useful images were registered using a custom-built normalized cross-correlation algorithm, where the image presenting the highest signal level was chosen as the reference.

3. Results

3.1. Performance of the axial motion stabilization

Figures 2(A) and (B) present two examples of retinal axial position as a function of time. The black line corresponds to the measured axial position of the retina and the red line corresponds to the position of the FF-OCT reference mirror. Fast oscillations and slower drifts of the retinal axial motion are clearly visible. Time points during blink occurrences (black areas) were automatically excluded from the study after applying an intensity-based algorithm to SD-OCT images. Figures 2(C) and (D) illustrate again the axial motion as a function of time, but now applied to the acquired averaged A-scans, where the red rectangle indicates the coherence gate thickness of the FF-OCT system, *i.e.* depth positions where interference takes place. The continuous motion drastically reduces the chances of acquiring an FF-OCT image of a layer of interest (here the inner/outer segment junction - IS/OS). From the collected data set of retinal axial position temporal evolution (excluding blink occurrences), we computed a peak-to-valley amplitude of $244.9 \pm 49.2\mu m$, a mean deviation from zero position of $62.5 \pm 29.5\mu m$ and a root-mean-square (RMS) error of $61.5 \pm 14.2\mu m$. In this condition, the expected efficiency to acquire FF-OCT images of a layer of interest (absolute error inferior to half of the axial resolution, here $4\mu m$), supposing a perfect initial manual match between both arms of the FF-OCT, is 7.4 ± 1.8 %.

Figures 2(A) and (B) also show the difference (blue line) between measured retinal position and FF-OCT reference mirror position. Slower drifts were filtered out and fast oscillations were reduced. An absolute residual tracking error of $6.7 \pm 3.1\mu m$ remains mainly because of the inherent time delay of the control loop and the inertia of the voice-coil translation stage. However, the residual error is low enough to considerably increase the chances of acquiring FF-OCT of a retinal layer of interest, as illustrated in Figs. 2(E) and (F). The presented axial motion stabilization method reduced peak-to-valley amplitude to $48 \pm 2\mu m$, mean deviation from zero position to $0.31 \pm 0.13\mu m$, and RMS error to $9.1 \pm 0.68\mu m$. In this condition, the expected efficiency was increased by a factor of 8.5 (62.4 ± 4.1 %). Visualization 1 shows a simulation of the expected B-scan temporal evolution with optical stabilization compared to the position of the FF-OCT coherence gate. Table 1 summarizes the achieved performance with the proposed method to optically stabilize the axial motion.

Table 1. Axial motion statistics with and without the use of the method to optically stabilize retinal axial motion. Statistics took into account 13 image sequences of 7 to 28s duration from three subjects, for a total of 4700 analyzed A-scans. PV stands for peak-to-valley amplitude.

	PV (μm)	Mean deviation (μm)	RMS error (μm)	Efficiency (%)
Without stabilization	244 ± 49.2	62.5 ± 29.5	61.5 ± 14.2	7.4 ± 1.8
With stabilization	48 ± 2	0.31 ± 0.13	9.1 ± 0.68	62.4 ± 4.1

To evaluate the temporal performance of the control loop, we computed its rejection transfer function (or sensitivity function) [19], which describes how different axial motion temporal frequencies are attenuated by the optical stabilization control loop. The rejection transfer function is the ratio between temporal power spectral densities (PSD) of the residual tracking error and of the retinal axial position. Figure 3(A) presents an example of the temporal PSD computed for the retinal position (blue line) and residual tracking error (red line). Note that temporal
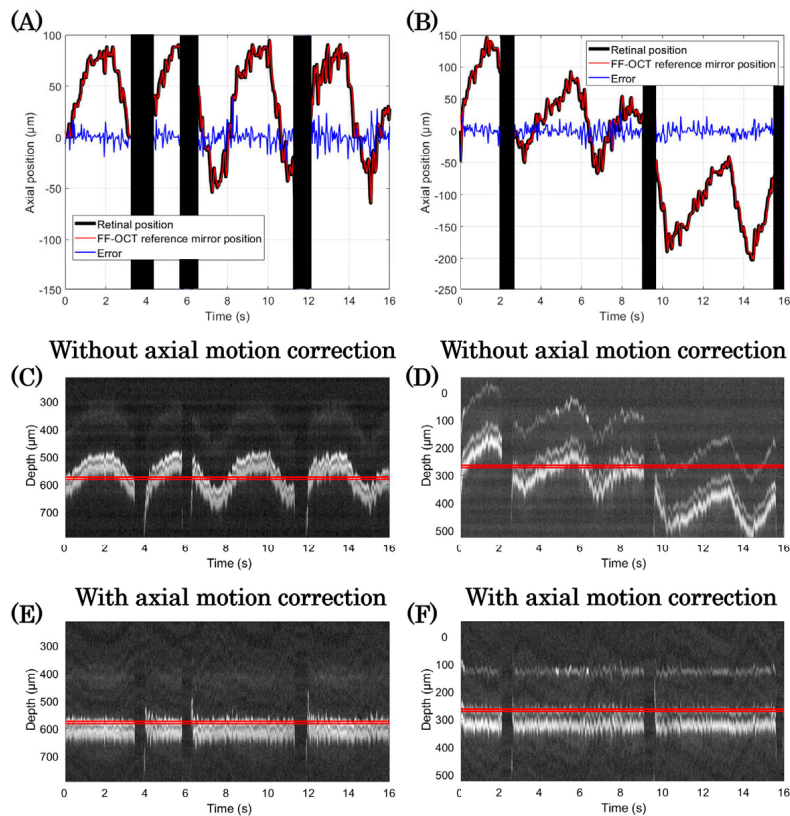
Fig. 2. Performance of the axial eye motion optical stabilization. (A) and (B) are two examples of the axial position temporal evolution. Black line: measured axial position of the retina. Red line: position of the FF-OCT reference mirror. Blue line: Residual tracking error. Black areas represent blink occurrences and were excluded from the study. (C) and (D) averaged A-scan time series without axial motion correction. (E) and (F) presents the same averaged A-scan time series as (C) and (D) but now with expected performance after correcting for axial motion. Red rectangles represent the coherence gate axial position and volume. See Visualization 1 for a simulation of the expected B-scan temporal evolution with optical stabilization compared to the position of the FF-OCT coherence gate. Note that all SD-OCT images are shown in linear scale.

frequencies up to approximately 4 Hz are attenuated. Figure 3(B) shows the rejection transfer function obtained by averaging the temporal PSD for different acquired sequences (black line) and the theoretical temporal PSD (red line), assuming a PI controller with 0.5 gain and two-frame delay [19,20]. The good match between the experimental and theoretical plots demonstrates that no additional delay or jitter was present during the acquisition, meaning that the temporal performance of the loop is as expected. Note that, although a loop rate of 50 Hz is adopted, the loop cut-off frequency, *i.e.* the highest corrected temporal frequency (associated with 0 dB), is approximately 4 Hz [3,19].

3.2. FF-OCT imaging of living human retina with axial motion correction

Visualization 2 shows an FF-OCT image sequence where the optical stabilization is activated during image acquisition. To begin, the voice-coil translation stage was manually positioned close to the IS/OS junction. A low-signal coming from photoreceptors in the bottom of the frame for a few frames duration is sometimes seen. When optical stabilization is activated, the
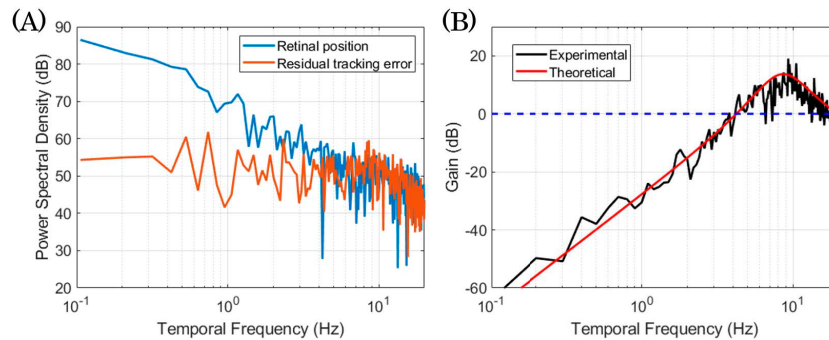
Fig. 3. Temporal performance of the axial motion correction control loop. (A) examples of temporal PSD computed for the retinal axial position (blue line) and the residual tracking error (red line). (B) Experimental (black line) rejection transfer function obtained by averaging temporal PSD for different acquired sequences, and the theoretical temporal PSD (red line). Note that, although a loop rate of 50 Hz is adopted, the loop cut-off frequency, *i.e.* the highest corrected temporal frequency (associated with 0 dB), is approximately 4 Hz.

photoreceptor mosaic becomes visible and the signal consistency significantly improves. After activating the axial motion correction, one can observe a temporal fluctuation of the intensity signal where the cone mosaic is visible. This intensity fluctuation occurs mainly due to two phenomena: mispositioning of the coherence gate, or an random phase modulation (see Sect.3.3), both due to the residual tracking error. Figure 4(A) shows the averaged image obtained during axial motion correction. The lateral retinal motion was corrected by digital registration. Another interesting retinal feature perceived in the image is the central foveal depression, *i.e.* an elevation of the IS/OS junction compared to the cone outer segment tip (COST) in the center of the foveola (see schematic of Fig. 4(A) at the right upper part). Because of the depression, this region of the retina is perceived as a dark circled area surrounding the foveal center. This phenomenon happens because this region is out of the FF-OCT coherence gate, which is about $8 \mu m$ thick. The diameter of the dark circled area is around $180 \mu m$ which corresponds to the typical size of the foveal umbo of a healthy subject [21].

By translating the FF-OCT reference arm laterally (*i.e.* not in depth), perpendicularly to the optical axis, one can generate a tilted coherence gate in the sample arm, producing FF-OCT images with band-type useful FOV. In the case of imaging photoreceptor layers, we expect to obtain two bright bands coming from the IS/OS junction and the COST layer. Tilting the coherence gate allows visualization of the impact of the axial motion correction directly in FF-OCT images. Visualization 3 shows an FF-OCT image sequence with a tilted coherence gate without axial motion correction. It is possible to visualize both photoreceptor bands moving continuously. Band motion is mainly due to axial motion. Lateral retinal motion, caused by fixational eye movements [15], only induces a shift of the retinal zone observed in the band FOV. Visualization 4 shows an FF-OCT image sequence with a tilted coherence gate now with axial motion correction, where band motion is strongly attenuated. In this case, due to the axial motion correction, one can register and average consecutive FF-OCT images to achieve a final image with enhanced quality. Figure 4(B) presents the averaged image generated from Visualization 4. Here, both IS/OS and COST photoreceptor mosaics are visible and could be resolved in a single image.

Figure 4 also shows zoomed areas from (A) and (B) and their respective spatial PSD. The estimated eccentricity (distance from the foveal center) of the zoomed areas are respectively 1°, 1.5^o, 3°, 2° and 2°. All zoomed areas, except for the first one, presented a clear and well defined Yellot's ring, the spectral signature of photoreceptor mosaic image [22]. Although it seems that
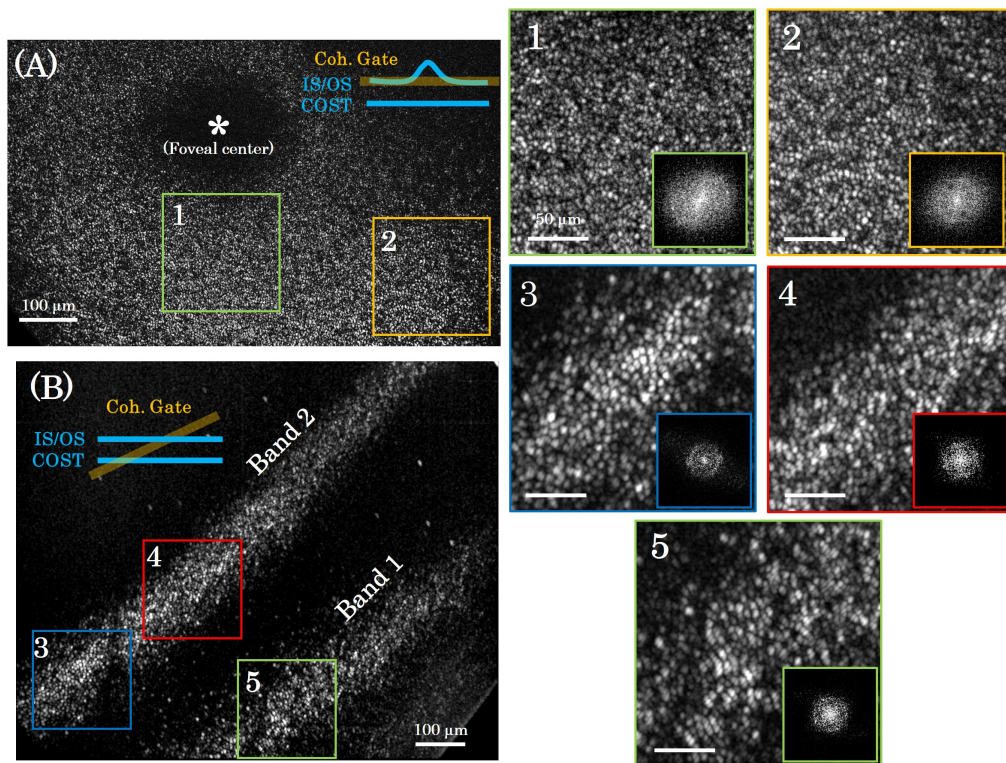
Fig. 4. Images of cone photoreceptor mosaic acquired with the help of the axial motion correction method. (A) Cone mosaic averaged image from Visualization 2, acquired at the IS/OS junction at the fovea center. Eccentricities of zoomed areas 1 and 2 are respectively 1°, 1.5^o. (B) Averaged image from Visualization 4. Both cone mosaic from the IS/OS junction and the COST layer close to the fovea center are visible in a single image. Eccentricities of zoomed areas 3, 4 and 5 are respectively 3°, 2° and 2°. For all zoomed areas the equivalent PSDs were computed.

the subject's pupil diameter was not sufficient to resolve cone mosaic from zoomed area 1, the majority of individual cones are visible. By using modal spacing method proposed by [22], we computed cone densities of 45 000 cones/mm^2, 20 700 cones/mm^2, 29 000 cones/mm^2 and 31 700 cones/mm^2 for zoomed areas 2, 3, 4 and 5 respectively. These values are in accordance with the expected cone density for a healthy subject at the eccentricities observed [23].

3.3.   2-phase demodulation and FF-OCT image averaging

Typically, a 3- or 4-phase modulation/demodulation strategy makes it possible to eliminate incoherent terms and un-mix the amplitude and the phase information [8]. This strategy works fine for static samples, but it fails for *in-vivo* retinal imaging due to the continuous three-dimensional (3D) eye motion, which randomly modulates the phase. Therefore, we adopted a 2-phase modulation/demodulation strategy, where the residual tracking error directly modulates the signal. Although incoherent terms can still be suppressed, it is not possible to separate amplitude and phase, meaning that the FF-OCT signal presents spatial intensity fluctuations. This random fluctuation, along with shot noise, affects the image contrast (see an example for FF-OCT image - N=1 in Fig. 5(A)).
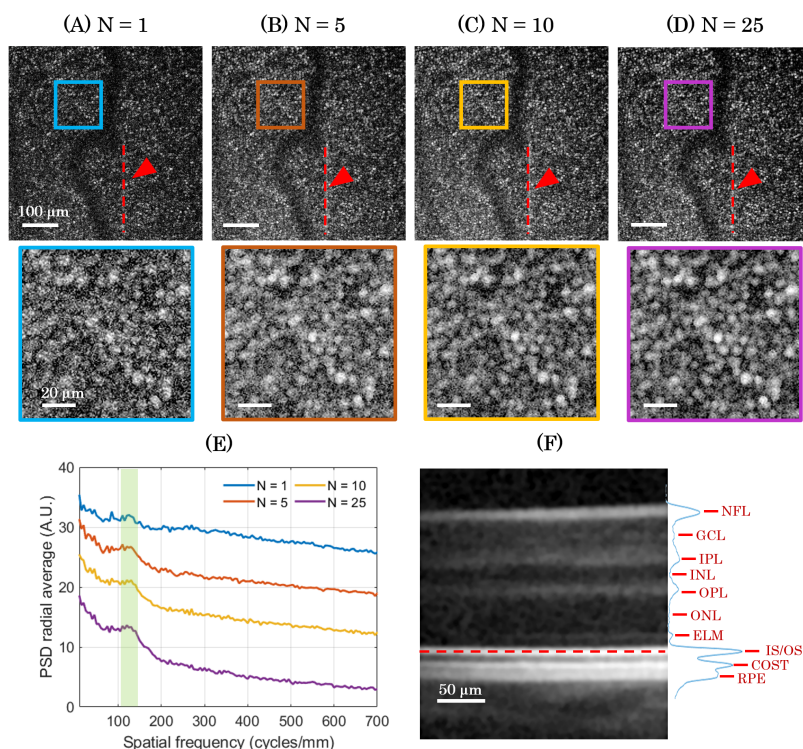
Fig. 5. Averaging registered FF-OCT images improves the clarity of photoreceptors. (A),(B),(C) and (D) show images of photoreceptor mosaic at 4° eccentricity for different amount of averaging (from N = 1, N = 5, N = 10 and N = 25 images). The red dashed line, highlighted by a red arrow, indicates where a simultaneous SD-OCT acquisition took place. The increase of image contrast is more visible in the zoomed areas. (E) Power spectral density radial average from each zoomed area. The green area indicates the photoreceptor mosaic spatial frequency, which is present for all the cases presented. (F) Tomographic retinal cross-section image obtained with the SD-OCT after averaging 10 consecutive B-scans. The red dashed line highlights the location where the FF-OCT images were simultaneously acquired, *i.e.* at the IS/OS junction. All averaged images were extracted from Visualization 5.

Since we adopt a random phase modulation, spatial intensity fluctuations vary from one FF-OCT image to another. Therefore, by averaging consecutive FF-OCT images, both phase and noise average out; the signal becomes proportional only to the amplitude, and its contrast is enhanced. This enhancement is highlighted in Fig. 5 for a different number of averaged images (N), where zoomed areas are also shown. Figure 5(E) introduces the computed PSD for each case. Note that for N=1, although the cone mosaic image does not present a sharp contrast, its PSD already indicates a Yellot's ring (green area highlights the cone mosaic spatial frequency), and cone density can be easily computed. The cone density of the zoomed area, localized at 4° eccentricity, was 18 300 cones/mm^2, which is in accordance with the expected cone density for a healthy subject at the eccentricity observed [23]. Although image averaging helps to visualize and resolve individual photoreceptors, the appearance of the cone mosaic seems different compared to AO-assisted ophthalmoscopes [3]. This might be explained by the fact that the reflection sites of the IS/OS junction and COST layer might not be exactly within the coherence gate [24].

3.4. Simultaneous FF-OCT and SD-OCT imaging of living human retina

Owing to the SD-OCT coupled in our custom-built FF-OCT system, we can access tomographic retinal cross-section images, from the SD-OCT, at the same time as high-resolution *en-face* images from the FF-OCT. Now with the axial motion correction, images from both modalities can be displayed consistently in real-time during the imaging session, helping to position the FF-OCT coherence gate at the retinal layer of interest before image acquisition. Visualization 5 shows one example, where the retinal image sequences from both modalities were recorded simultaneously. We purposely removed the shortpass filter used to block the SD-OCT light source at the FF-OCT camera to help to visualize the SD-OCT acquisition in parallel to the FF-OCT acquisition. The averaged *en-face* image generated by the FF-OCT is shown in Fig. 5(D), where the red dashed line, highlighted by the red arrow, indicates the location where the SD-OCT was acquired simultaneously. The averaged retinal cross-section generated by the SD-OCT is presented in Fig. 5(F). All retinal layers commonly resolved by an SD-OCT were identified and labeled according to [7]. The red dashed line indicates the retinal layer where the FF-OCT image was acquired, *i.e.* the IS/OS junction.

4. Discussion

One of the biggest challenges in applying the FF-OCT technique for living human retinal imaging is the presence of continuous involuntary head and eye axial motion during image acquisition. We showed in Sect. 3.1 that axial motion is mainly composed of slow drifts and fast oscillations. Even though *in-vivo* retinal imaging was possible under this condition [11], long and tedious imaging sessions would be necessary to increase the chances of acquiring enough data (the efficiency would be lower than 7%). Moreover, we saw in Sect. 3.3 that, even if photoreceptors could be visualized and resolved in a single frame (see Fig. 5(A)), image averaging is an important process to eliminate the spatial intensity fluctuation imposed by the random phase modulation of FF-OCT signal.

4.1. Using SD-OCT to guide FF-OCT in-vivo imaging

In this paper, we present a method to overcome this major limitation, based on the combination of an FF-OCT, an SD-OCT and a high-speed voice-coil translation stage. The SD-OCT is used to measure the retinal axial position and to drive the position of the voice-coil translation stage, where the FF-OCT reference arm is mounted. We showed that the proposed method was able to suppress slow drifts and strongly attenuate fast oscillations, increasing the FF-OCT image acquisition efficiency to almost a factor of 10, *i.e* 60% success. This efficiency was highlighted by Visualization 2, Visualization 4 and Visualization 5, where FF-OCT image sequences with axial motion correction were presented.

Another essential role of the SD-OCT is to guide the FF-OCT coherence gate positioning. Indeed, once the axial motion is stabilized, and since the initial position of the FF-OCT coherence gate in the sample arm is known (calibration step described in Sect. 2.2), one can manually position the FF-OCT coherence gate assisted by the SD-OCT retinal cross-sections displayed in real-time. In spite of choices of optical design to favor the FF-OCT system, sometimes to the detriment of the SD-OCT system, and the mechanical restrictions imposed by the SD-OCT commercial system, we showed in Fig. 5 and Visualization 5 that retinal cross-section images, with sufficient contrast to identify all retinal layers, can be generated simultaneously to FF-OCT, a crucial condition to guide FF-OCT image acquisition.

4.2. High cellular resolution in-vivo retinal imaging with FF-OCT

Throughout this paper, we demonstrated the ability of our FF-OCT imaging system to achieve high cellular resolution in the living human retina. There has been increased interest in the

past ten years in associating different retinal imaging modalities to achieve a cellular resolution in all three dimensions, with most groups combining AO-OCT and AO-SLO [25,26]. The main difference of our multimodal imaging system compared to previous works is the potential to achieve cellular resolution in all three dimensions without AO, significantly reducing the system complexity, size and cost. Figure 4 demonstrated the capacity of the FF-OCT to resolve *in-vivo* cone photoreceptors as close as 1.5^o from the foveal center without using any optical aberration compensation other than prescribed eyeglasses. Moreover, the presented FF-OCT has the capacity to generate *en-face* retinal images with an enhanced axial resolution compared to confocal AO-SLO, $8\mu m$ for the former against $40\mu m$ for the latter [13]. Some studies have demonstrated that, for healthy subjects with good eye optics, individual cone photoreceptors could be resolved within SD-OCT or confocal SLO images without optically correcting for ocular aberrations [14,27]. However, most of these studies used illumination/detection scanning techniques, which present an inherent low frame rate, limited FOV and high sensitivity to eye motion, the latter leading to intraframe distortion. All these drawbacks are minimized when using a full-field technique [3,28].

4.3. Limitations

The presented FF-OCT/SD-OCT imaging system still faces some limitations. Firstly, to favor the FF-OCT system, the capacity of the SD-OCT imaging was diminished by not-conjugating the galvanometer scanners to the eye's pupil, affecting its signal level and increasing its sensitivity to the subject alignment. Secondly, even if FF-OCT presents a low sensitivity to low-order ocular aberrations in terms of resolution, the latter still affects the FF-OCT signal level [10]. Ocular aberrations and the variation of the subject pupil diameter might explain the fact that single-frame images obtained in Visualization 2 (when axial motion correction is activated) present a higher signal than Fig. 5(A). Finally, because ocular aberrations affect the SNR of the current FF-OCT, imaging other retinal layers, such as ganglion cells, possible with AO-OCT systems [29], becomes challenging. As discussed in [10], now that FF-OCT images can be acquired with high consistency, a compact implementation of AO could be used, consisting of a wavefront sensorless approach, and a multi-actuator adaptive lens [30] positioned just in front of the eye, like regular glasses (*i.e.* without strict conjugation). As ocular aberrations are dominated by low-order aberrations [4], we expect to significantly improve the FF-OCT SNR, and therefore hope to be able to image less reflective retinal layers.

4.4. Towards dynamic FF-OCT in the living human eye

One interesting way to obtain a high image contrast using FF-OCT is by exploring temporal fluctuations of the backscattered light, revealing subcellular structures and transparent tissues [18,31]. So far, this technique, when applied to retinal imaging, has only been shown for *ex-vivo* retinal imaging. To be able to achieve dynamic *in-vivo* retinal imaging an axial motion correction better than the axial resolution of the FF-OCT system is necessary [32]. Our proposed method achieves this performance 60% of the time, and it might be sufficient. Otherwise, a higher performance would only be possible with a faster reaction of the voice-coil translation stage or with an SD-OCT with a higher acquisition rate (here we are limited to 36 000 A-scans per second).

5. Conclusion

One of the biggest challenges of time-domain FF-OCT when applied for *in-vivo* human retinal imaging is the presence of continuous involuntary head and eye axial motion. We presented a method to optically compensate for axial motion in real-time for time-domain FF-OCT. This was possible by introducing an SD-OCT and a voice-coil translation stage in the system, the former to generate retinal cross-section images, where retinal axial motion could be measured,

and the latter to correct the FF-OCT reference arm position. The closed-loop optical stabilization reduced the RMS error by a factor of 7, significantly increasing the FF-OCT image acquisition efficiency. By these means, we demonstrated the capacity of the FF-OCT to resolve cone mosaic as close as 1.5^o from the fovea center with high consistency and repeatability, without the need for AO. The good precision and efficiency achieved in the FF-OCT system, by virtue of the real-time axial motion optical stabilization, together with its relative simplicity and low-cost compared to the other high-resolution techniques which use conventional AO, may pave the way towards the adoption of FF-OCT as a routine clinical imaging system.

Funding

Acknowledgments

Disclosures

The authors declare no conflicts of interest.

References

1. D. Huang, E. Swanson, C. Lin, J. Schuman, W. Stinson, W. Chang, M. Hee, T. Flotte, K. Gregory, C. Puliafito, and J. G. Fujimoto, "Optical coherence tomography," Science **254**(5035), 1178–1181 (1991).
2. W. Drexler and J. G. Fujimoto eds., *Optical Coherence Tomography: Technology and Applications* (Springer, 2015), 2nd ed.
3. E. Gofas-Salas, P. Mecê, C. Petit, J. Jarosz, L. M. Mugnier, A. M. Bonnefois, K. Grieve, J. Sahel, M. Paques, and S. Meimon, "High loop rate adaptive optics flood illumination ophthalmoscope with structured illumination capability," Appl. Opt. **57**(20), 5635–5642 (2018).
4. J. Jarosz, P. Mecê, J.-M. Conan, C. Petit, M. Paques, and S. Meimon, "High temporal resolution aberrometry in a 50-eye population and implications for adaptive optics error budget," Biomed. Opt. Express **8**(4), 2088–2105 (2017).
5. P. Mecê, E. Gofas-Salas, C. Petit, F. Cassaing, J. Sahel, M. Paques, K. Grieve, and S. Meimon, "Higher adaptive optics loop rate enhances axial resolution in nonconfocal ophthalmoscopes," Opt. Lett. **44**(9), 2208–2211 (2019).
6. R. S. Jonnal, O. P. Kocaoglu, R. J. Zawadzki, Z. Liu, D. T. Miller, and J. S. Werner, "A review of adaptive optics optical coherence tomography: technical advances, scientific applications, and the future," Invest. Ophthalmol. Visual Sci. **57**(9), OCT51–OCT68 (2016).
7. M. Pircher and R. J. Zawadzki, "Review of adaptive optics oct (AO-OCT): principles and applications for retinal imaging," Biomed. Opt. Express **8**(5), 2536–2562 (2017).
8. A. Dubois, K. Grieve, G. Moneron, R. Lecaque, L. Vabre, and C. Boccara, "Ultrahigh-resolution full-field optical coherence tomography," Appl. Opt. **43**(14), 2874–2883 (2004).
9. O. Thouvenin, K. Grieve, P. Xiao, C. Apelian, and A. C. Boccara, "En face coherence microscopy," Biomed. Opt. Express **8**(2), 622–639 (2017).
10. P. Mecê, P. Xiao, V. Mazlin, J. Scholler, K. Grieve, J.-A. Sahel, M. Fink, and C. Boccara, "Towards lens-based wavefront sensorless adaptive optics full-field oct for in-vivo retinal imaging (conference presentation)," in *Optical Coherence Tomography and Coherence Domain Optical Methods in Biomedicine XXIII*, vol. 10867 (International Society for Optics and Photonics, 2019), p. 1086722.
11. P. Xiao, V. Mazlin, K. Grieve, J.-A. Sahel, M. Fink, and A. C. Boccara, "In vivo high-resolution human retinal imaging with wavefront-correctionless full-field oct," Optica **5**(4), 409–412 (2018).
12. L. Ginner, A. Kumar, D. Fechtig, L. M. Wurster, M. Salas, M. Pircher, and R. A. Leitgeb, "Noniterative digital aberration correction for cellular resolution retinal optical coherence tomography in vivo," Optica **4**(8), 924–931 (2017).
13. D. T. Miller, J. Qu, R. S. Jonnal, and K. E. Thorn, "Coherence gating and adaptive optics in the eye," in *Coherence Domain Optical Methods and Optical Coherence Tomography in Biomedicine VII*, vol. 4956 (International Society for Optics and Photonics, 2003), pp. 65–72.
14. M. Pircher, E. Götzinger, H. Sattmann, R. A. Leitgeb, and C. K. Hitzenberger, "In vivo investigation of human cone photoreceptors with slo/oct in combination with 3d motion correction on a cellular level," Opt. Express **18**(13), 13935–13944 (2010).
15. P. Mecê, J. Jarosz, J.-M. Conan, C. Petit, K. Grieve, M. Paques, and S. Meimon, "Fixational eye movement: a negligible source of dynamic aberration," Biomed. Opt. Express **9**(2), 717–727 (2018).

16. E. Auksorius and A. C. Boccara, "Dark-field full-field optical coherence tomography," Opt. Lett. **40**(14), 3272–3275 (2015).

17. J. Scholler, "FFOCT control and acquisition software," (2019). https://doi.org/10.5281/zenodo.3137245.

18. J. Scholler, V. Mazlin, O. Thouvenin, K. Groux, P. Xiao, J.-A. Sahel, M. Fink, C. Boccara, and K. Grieve, "Probing dynamic processes in the eye at multiple spatial and temporal scales with multimodal full field oct," Biomed. Opt. Express **10**(2), 731–746 (2019).

19. F. Roddier, *Adaptive Optics in Astronomy* (Cambridge University Press, 1999).

20. S. Meimon, C. Petit, T. Fusco, and C. Kulcsar, "Tip–tilt disturbance model identification for kalman-based control scheme: application to xao and elt systems," J. Opt. Soc. Am. A **27**(11), A122–A132 (2010).

21. S. Duke-Elder, "The anatomy of the visual system," A System of Ophthalmology **2**, 363–382 (1961).

22. R. F. Cooper, C. S. Langlo, A. Dubra, and J. Carroll, "Automatic detection of modal spacing (yellott's ring) in adaptive optics scanning light ophthalmoscope images," Ophthalmic Physiol. Opt. **33**(4), 540–549 (2013).

23. L. Sawides, A. de Castro, and S. A. Burns, "The organization of the cone photoreceptor mosaic measured in the living human retina," Vision Res. **132**, 34–44 (2017).

24. M. Pircher, B. Baumann, E. Götzinger, H. Sattmann, and C. K. Hitzenberger, "Simultaneous slo/oct imaging of the human retina with axial eye motion correction," Opt. Express **15**(25), 16922–16932 (2007).

25. R. J. Zawadzki, S. M. Jones, S. Pilli, S. Balderas-Mata, D. Y. Kim, S. S. Olivier, and J. S. Werner, "Integrated adaptive optics optical coherence tomography and adaptive optics scanning laser ophthalmoscope system for simultaneous cellular resolution in vivo retinal imaging," Biomed. Opt. Express **2**(6), 1674–1686 (2011).

26. Z. Liu, J. Tam, O. Saeedi, and D. X. Hammer, "Trans-retinal cellular imaging with multimodal adaptive optics," Biomed. Opt. Express **9**(9), 4246–4262 (2018).

27. N. D. Shemonski, F. A. South, Y.-Z. Liu, S. G. Adie, P. S. Carney, and S. A. Boppart, "Computational high-resolution optical imaging of the living human retina," Nat. Photonics **9**(7), 440–443 (2015).

28. P. Bedggood and A. Metha, "De-warping of images and improved eye tracking for the scanning laser ophthalmoscope," PLoS One **12**(4), e0174617 (2017).

29. Z. Liu, K. Kurokawa, F. Zhang, J. J. Lee, and D. T. Miller, "Imaging and quantifying ganglion cells and other transparent neurons in the living human retina," Proc. Natl. Acad. Sci. **114**(48), 12803–12808 (2017).

30. S. Bonora, Y. Jian, P. Zhang, A. Zam, E. N. Pugh, R. J. Zawadzki, and M. V. Sarunic, "Wavefront correction and high-resolution in vivo oct imaging with an objective integrated multi-actuator adaptive lens," Opt. Express **23**(17), 21931–21941 (2015).

31. C. Apelian, F. Harms, O. Thouvenin, and A. C. Boccara, "Dynamic full field optical coherence tomography: subcellular metabolic contrast revealed in tissues by interferometric signals temporal analysis," Biomed. Opt. Express **7**(4), 1511–1524 (2016).

32. J. Scholler, "Motion artifact removal and signal enhancement to achieve in vivo dynamic full field OCT," Opt. Express **27**(14), 19562–19572 (2019).

C.2 Correction of the curvature of the coherence gate in an asymmetric FFOCT

Coherence gate shaping for wide field high-resolution in vivo retinal imaging with full-field OCT

PEDRO MECÊ,[1,*] (ID) KASSANDRA GROUX,[1] JULES SCHOLLER,[1] OLIVIER THOUVENIN,[1] (ID) MATHIAS FINK,[1] KATE GRIEVE,[2,3] AND CLAUDE BOCCARA[1]

[1]*Institut Langevin, ESPCI Paris, CNRS, PSL University, 1 rue Jussieu, 75005 Paris, France*
[2]*Institut de la Vision, Sorbonne Université, INSERM, CNRS, F-75012, Paris, France*
[3]*Quinze-Vingts National Eye Hospital, 28 Rue de Charenton, Paris, 75012, France*
[*]pedro.mece@espci.fr

Abstract: Allying high-resolution with a large field-of-view (FOV) is of great importance in the fields of biology and medicine, but it is particularly challenging when imaging non-flat living samples such as the human retina. Indeed, high-resolution is normally achieved with adaptive optics (AO) and scanning methods, which considerably reduce the useful FOV and increase the system complexity. An alternative technique is time-domain full-field optical coherence tomography (FF-OCT), which has already shown its potential for *in-vivo* high-resolution retinal imaging. Here, we introduce coherence gate shaping for FF-OCT, to optically shape the coherence gate geometry to match the sample curvature, thus achieving a larger FOV than previously possible. Using this instrument, we obtained high-resolution images of living human photoreceptors close to the foveal center without AO and with a $1\,mm \times 1\,mm$ FOV in a single shot. This novel advance enables the extraction of photoreceptor-based biomarkers with ease and spatiotemporal monitoring of individual photoreceptors. We compare our findings with AO-assisted ophthalmoscopes, highlighting the potential of FF-OCT, as a compact system, to become a routine clinical imaging technique.

1. Introduction

Owing to the optical properties of the eye, the retina is the only part of the central nervous system that can be visualized non-invasively *in-vivo* with micrometer resolution, a crucial aspect for studying neuronal activity [1,2]. Due to their capacity to correct for static and dynamic ocular aberrations [3,4], AO ophthalmoscopes have become the primary technique to image individual retinal neurons such as cone and rod photoreceptors in the living human retina [5–8]. Imaging individual retinal neurons *in-vivo* with AO ophthalmoscopes has enabled new insights into retinal function [2] and a better understanding of progression of retinal diseases such as age-related macular degeneration [9]. However, AO systems require quite complex, expensive and cumbersome hardware, limiting their clinical and commercial deployment [10,11]. Moreover, the eye's isoplanatic patch (around 0.6 mm) limits the useful field-of-view (FOV) where high-resolution retinal imaging can be achieved when using AO [12]. Although multi-conjugate AO was demonstrated in order to achieve a larger useful FOV, increasing the eye's isoplanatic patch, this solution adds complexity, as two deformable mirrors are necessary [13]. Thus, achieving cellular resolution in a large portion of the living human retina without using AO is of great interest.

Recent studies have achieved high-resolution retinal imaging without using AO by implementing computational ocular aberration correction [11,14–17]. Although promising, these approaches only presented results in far foveal eccentricities (3° or more), where photoreceptors are most

easily resolved. Moreover, they require heavy post-processing steps hence providing limited feedback during imaging sessions, and, in some cases, expensive hardware was also necessary (*e.g.* a very fast camera and/or swept source laser). The use of a super-resolution optical-reassignment technique was also proposed as a tool to achieve cellular resolution in in-vivo retina without AO [18]. Nevertheless, a scanning illumination/detection is used, presenting an inherently low frame rate, limited FOV (lower than 0.3 *mm* × 0.3 *mm*) and high sensitivity to fixational eye motion [19] leading to intraframe distortion.

An alternative modality to achieve high-cellular resolution without using AO is FF-OCT, which uses a spatially incoherent light source, a high-speed megapixel camera and time-domain phase modulation to acquire *en-face* sections of the sample at a given depth [20]. One attractive point of this technique for retinal imaging is the fact that the optical resolution of FF-OCT has a weak sensitivity to predominant ocular aberrations (*i.e.* defocus and astigmatism) [21–23]. This interesting feature was recently highlighted in [24], where *in-vivo* human cone mosaic at eccentricities close to the fovea was resolved. Although FF-OCT's FOV is theoretically only limited by the spatial sampling of the imaging camera, retinal curvature causes current images to have a limited useful FOV of about 0.4 *mm* × 0.4 *mm* [24,25].

Typically, FF-OCT uses a Linnik interferometer, where identical microscope objectives are placed in both reference and sample arms in a symmetric optical path configuration. When applied to retinal imaging, the FF-OCT symmetry is broken, as the sample arm no longer contains a microscope objective (Fig. 2), but rather contains the anterior segment optics of the human eye. Here, we theoretically and experimentally demonstrate that when the symmetry is broken a curved coherence gate is generated, provoking a mismatch with the retinal curvature, and consequently limiting the useful FOV. The useful FOV can be defined as the FOV over which a structure from a given depth of the sample can be visualized. We present novel advances in FF-OCT allowing for optical shaping of the geometry of the coherence gate, adapting it to the retinal geometry, enabling the generation of single-shot, high-resolution, wide FOV images (1 *mm* × 1 *mm*) of the photoreceptor mosaic as close as 1° from the foveal center. The 1 *mm* × 1 *mm* useful FOV is 6.25 times larger in this new configuration compared to our previous results [24]. Then, we show that useful tools to diagnose retinal disorders at the early stage such as photoreceptor-based biomarkers and spatiotemporal monitoring of individual photoreceptors can be achieved without the need for AO.

2. Methods

2.1. Theory

The optical path length (OPL) when light propagates in a material x of thickness e_x, refractive index n_x for a given angle θ_x can be expressed as:

$$OPL(\lambda) = \sum_{x=1}^{N} n_x(\lambda) \frac{e_x}{cos\theta_x}. \tag{1}$$

Where $n_x(\lambda)$ is given by the Sellmeier equation [26]. The incidence angle in a material x, θ_x, can be expressed as a function of the incidence angle in air θ_1, as follows:

$$\theta_x = sin^{-1}\left(\frac{sin\theta_1}{n_x(\lambda)}\right). \tag{2}$$

Through Eqs. (1) and (2), one can notice the dependency of the OPL on the wavelength (λ) and the incidence angle in air (θ_1):

$$OPL(\lambda, \theta_1) = \sum_{x=1}^{N} n_x(\lambda) \frac{e_x}{cos\left(sin^{-1}\left(\frac{sin\theta_1}{n_x(\lambda)}\right)\right)}. \tag{3}$$

The depth position of the *en-face* image generated by the FF-OCT, *i.e.* the coherence gate, is given by the the optical path difference (OPD) between the reference and sample arms:

$$OPD(\lambda, \theta_1) = OPL_{reference}(\lambda, \theta_1) - OPL_{sample}(\lambda, \theta_1). \tag{4}$$

If the OPL of both arms is symmetric, as is the case when a microscope objective is placed in each arm, the OPD is null for all values of θ_1, *i.e.* in the FOV. On the other hand, an asymmetry between the reference and sample OPLs creates a dependency on the the wavelength (λ) and the incident angle in the air (θ_1). In this case, OPD would only be null for a given incident angle, and it would increase as this angle is increased. This is the origin of the curvature of the coherence gate.

To shape the coherence gate geometry, we propose the use of optical windows. To better understand how optical windows can shape the coherence gate geometry, we can consider a typical FF-OCT set-up composed of identical microscopic objectives positioned in each arm, with an optical window of thickness e_b and refractive index n_b positioned in the sample arm (Fig. 1). For simplicity, we assume that both arms are illuminated with monochromatic light.
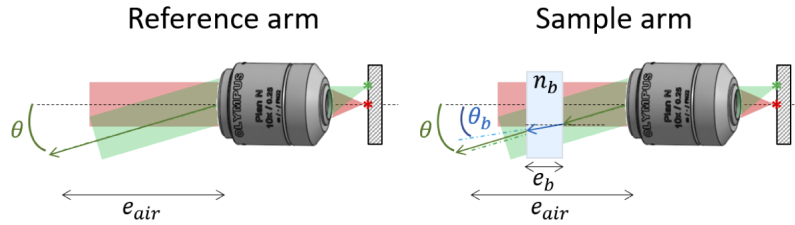
Fig. 1. Schematic of the reference and sample arms introducing notations for the OPD model.

Their respective OPLs will be given as follows (only considering the path between the microscope objective and the beam splitter):

$$OPL_{ref}(\theta) = \frac{e_{air}}{cos(\theta)} \tag{5}$$

$$OPL_{sample}(\theta) = \frac{e_{air} - e_b}{cos(\theta)} + \frac{e_b n_b}{cos(\theta_b(\theta))} \tag{6}$$

where θ_b is given as a function of the incident angle in the air θ according to Eq. (2). In this case, the OPD would be:

$$OPD(\theta) = e_b \left(\frac{n_b}{cos(\theta_b(\theta))} - \frac{1}{cos(\theta)} \right). \tag{7}$$

To image at a depth of interest of the sample, one has to move the reference arm. We can move the reference arm in order to match both OPLs for a given angle, for example at a central point in the FOV, i.e. $\theta = 0$, which gives:

$$OPD(0) = e_b(n_b - 1). \tag{8}$$

Now, the OPD for all the other angles θ will be given by:

$$OPD(\theta) = e_b \left(\frac{n_b}{cos(\theta_b(\theta))} - \frac{1}{cos(\theta)} \right) - e_b(n_b - 1) \tag{9}$$

which can be simplified as follows:

$$OPD(\theta) = e_b \left(n_b \frac{1 - cos(\theta_b(\theta))}{cos(\theta_b(\theta))} - \frac{1 - cos(\theta)}{cos(\theta)} \right). \tag{10}$$

Note that the introduction of an optical window induces a variation of the OPD as a function of the FOV, generating a curved coherence gate.

126

2.2. Experimental setup

To investigate the impact of the asymmetric Linnik interferometer configuration on coherence gate curvature, three samples were imaged: 1) a standard USAF resolution target; 2) an OEMI-7 model eye (Ocular Instruments, Inc) which takes into account the eye geometry, optical power and dispersion properties (henceforth, named model eye); and 3) *in-vivo* human retina. Figure 2 presents the schematic of the custom-built FF-OCT system coupled through a dichroic mirror with a Thorlabs Ganymede-II SD-OCT system. The FF-OCT comprises a light-emitting diode (LED) with $\lambda = 850$ nm center wavelength and 30 nm bandwidth (M850L3, Thorlabs), used as a spatially incoherent illumination source, giving a theoretical axial resolution of approximately 8 μm in water. The LED is focused by a condenser lens 20 *mm* in front of the eye's pupil. A physical diaphragm is positioned in front of the LED, conjugate to the retina and the FF-OCT reference mirror. The illumination beam is split into reference and sample arms by a 50:50 cubic beam splitter (BS). For the reference arm, an Olympus 10X/0.25 NA Plan Achromat objective is used with a silicon mirror placed at the focal plane of the objective. The whole reference arm (microscope objective and silicon mirror) is mounted on a fast voice-coil translation stage (X-DMQ12P-DE52, Zaber Technologies Inc.), enabling adjustment of the coherence gate position. For the sample arm, two configurations were used. In the case of the USAF target imaging, a microscope objective, identical to the one used in the reference arm, is used leading to a symmetric Linnik configuration (not shown in Fig. 2). In the case of the model eye and *in-vivo* retinal imaging, both were aligned along the optical axis, without the use of a microscope objective, leading to an asymmetric Linnik configuration (shown in Fig. 2). The FF-OCT light beam arrives with an 8 mm diameter in the eye's pupil. The back-scattered photons from both arms are recombined by the same BS and focused onto a high-speed (up to 720 Hz at 1440×1440 pixel) CMOS camera (Q-2A750-Hm/CXP-6, Adimec) for FF-OCT imaging. The FF-OCT system aperture was limited by the eye's pupil. In the case of *in-vivo* retinal imaging, the SD-OCT and the voice-coil translation stage were used to measure and correct for involuntary axial eye movements during the imaging acquisition in a closed-loop fashion [24]. The SD-OCT light beam was filtered out from the FF-OCT reference and detection arms by using a short-pass filter (FESH0850 25mm aperture, Thorlabs).
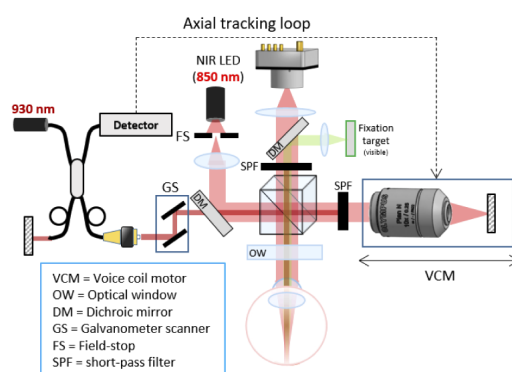
Fig. 2. Schematic drawing of the custom-built FF-OCT system coupled with an SD-OCT for real-time axial motion correction and FF-OCT coherence gate positioning guidance. In the case of the USAF target imaging, a microscope objective, identical to the one used in the reference arm, is used leading to a symmetric Linnik configuration (not shown in the schematic). In the case of the model eye and *in-vivo* retinal imaging, no microscope objective is placed in the sample arm, leading to an asymmetric Linnik configuration (shown in the schematic).

2.3.   Image acquisition

In the case of the USAF target and the model eye imaging, a total of 200 images from different depths were acquired at 10 Hz, by moving the voice-coil translation stage of the reference arm at a constant speed of 5 μm/s. This procedure allowed us to acquire *en-face* images from different depths, forming Z-stacks. This procedure was repeated after adding optical windows of N-BK7 of different thicknesses in the reference or sample arms in order to change the geometry of the coherence gate.

In the case of in vivo retinal imaging, the image acquisition was performed on two healthy subjects S1 and S2 aged 25 and 30 respectively. S1 presents a refractive error of $1.5D \times 0.5D \times 160^o$ (spherical $\times$ cylindrical $\times$ axis of cylindrical errors), S2 does not wear prescribed eyeglasses and had had LASIK refractive surgery several years ago. Research procedures followed the tenets of the Declaration of Helsinki. Informed consent was obtained from subjects after the nature and possible outcomes of the study were explained. The study was authorized by the appropriate ethics review boards (CPP and ANSM (IDRCB number: 2019-A00942-55)). Subjects were seated in front of the system and stabilized with a chin and forehead rest and asked to fixate a target placed at an infinite focal conjugate. During the imaging session, the subject S1 was wearing her prescription glasses to increase the signal level of FF-OCT [23]. Image acquisition was realized in a dark room, maximizing the pupil dilation. Phase modulation was performed by the residual axial motion after optical stabilization [24]. Image sequences were composed of 150 frames acquired at 300 Hz using custom-built software. The FF-OCT camera worked close to saturation to use the whole full well capacity, decreasing relative importance of shot noise [27]. During image acquisition, the total power entering the eye from the FF-OCT illumination source and the SD-OCT scanning source were respectively 1.3 mW (for the 0.5 s of image acquisition) and 0.25 mW (continuous scanning), which are below the ocular safety limits established by the ISO standards for group 1 devices.

2.4.   Image processing

In the case of the USAF target and the model eye imaging, each Z-stack was digitally converted into axial sections, *i.e.* a cross-sectional view of the sample. This step was possible by taking into account only the pixels of a central row of each image. Next, image segmentation was applied using an intensity-based thresholding algorithm and a least square parabola fitting algorithm, enabling measurement of the degree of curvature of converted cross-sections.

For *in-vivo* retinal imaging, each image was normalized by dividing itself by its mean value. Since the phase was randomly modulated by the residual tracking error, and to eliminate the incoherent terms, we adopted a 2-phase demodulation [24]. The 2-phase demodulation consists of subtracting one image I_N from the next I_{N+1} and taking the absolute value. Next, images with a very low or absent useful signal, mainly due to an insufficient phase shift between consecutive images, were automatically detected using an intensity-based threshold algorithm, and then excluded from the image sequence. Finally, useful images were registered using a custom-built normalized cross-correlation algorithm, where the image presenting the highest signal level was chosen as the reference. Retinal images of subject S1 were also acquired using the rtx-1 adaptive optics flood-illumination ophthalmoscope (AO-FIO - Imagine Eyes, France) and the MAORI confocal adaptive optics scanning-laser ophthalmoscope (AO-SLO - Physical Sciences, Inc, Andover, MA, USA). Retinal fundus images of both subjects were also acquired with Spectralis scanning-laser ophtalmoscope (SLO) (Heidelberg Engineering, Germany). All images were acquired in the same conditions as previously described, *i.e.* in a dark room, maximizing the pupil dilation and with subject S1 wearing her prescribed eyeglasses. To generate a pointwise density map, we divided the cone mosaic image into an overlapping grid of 300×300 pixels (corresponding to 200 $\mu m \times 200$ μm) regions of interest (ROIs), where each ROI was displaced from the previous by 30 pixels (corresponding to $20\mu m$). These values were chosen empirically

to provide a good trade-off between pointwise accuracy and map smoothness. Then, cone density and spacing were computed for each ROI using a fully automated algorithm based on modal spacing as described in [28]. Bicubic image interpolation was used to increase the size of the cone density map in order to match the cone mosaic image.

3. Results

3.1.   *Optical shaping of the coherence gate geometry*

Figure 3 shows how the coherence gate geometry can be optically shaped by adding optical windows in one of the interferometer arms. When imaging the USAF target (Fig. 3(a)) in a symmetric configuration the cross-section looks completely flat. The addition of an optical window in one of the arms breaks this symmetry, consequently, the flat sample presents an apparent curved cross-section. This apparent curvature happens because of a non-constant optical path difference along the FOV, generating a curved coherence gate.
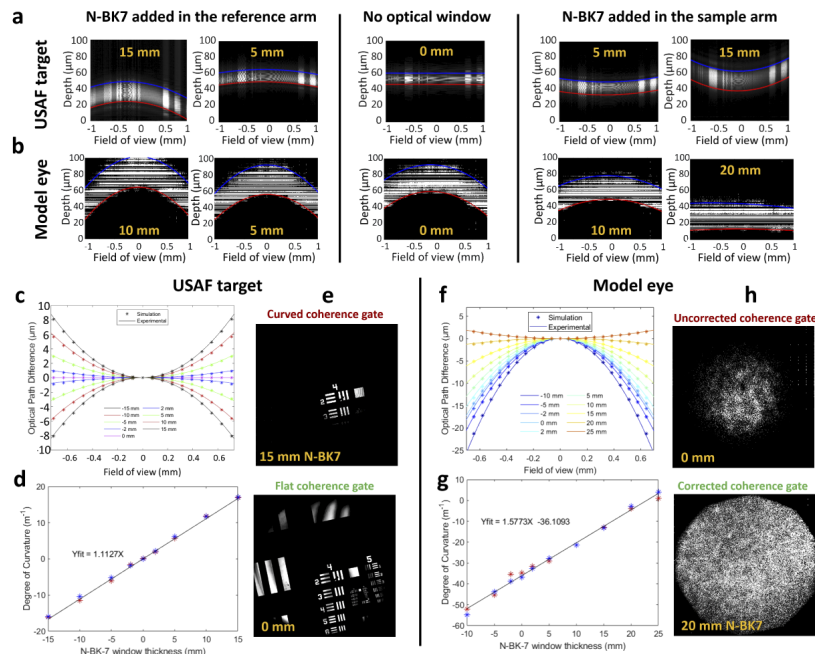
Fig. 3. a-b, Cross-sections after introducing N-BK7 optical windows with various thicknesses (in yellow) in the reference or sample arms when imaging, respectively, the USAF target and the model eye. **c,d,f,g,** Measured and theoretical optical path differences as a function of the FOV for different optical window thicknesses, as well as their respective degree of curvature, for respectively the USAF target and the model eye. When the optical window was introduced in the reference arm, the N-BK7 optical window thickness was represented in negative value. **e,h,** The effect of the coherence gate geometry over the FF-OCT useful FOV.

Figure 3(c) presents the measured and the theoretical (see Sect. 2.1) OPDs as a function of the FOV. Depending on which arm the optical window is introduced in, the coherence gate curvature can present a concave or a convex shape. One can notice that the curvature increases as a function of the thickness of the optical window introduced in one of the arms (Fig. 3(d)). The induced curvature of the coherence gate directly impacts the useful FOV of an FF-OCT system, since it acquires *en-face* curved sections of a flat sample at a given depth (Fig. 3(e)).

The same experiment can be done now using the model eye, which presents similar geometry and dispersion of the eye, in an asymmetric configuration (Fig. 3(b)). In this case, already when no optical window is introduced, the coherence gate presents a significant curvature. Figures 3(f,g) give the measured and theoretical curvature as a function of the FOV and the optical window thickness. The introduction of an 20 mm thick N-BK7 optical window in the sample arm enables compensation for the initial apparent curvature, increasing the useful FOV (Fig. 3(h)). Visualization 1, Visualization 2, Visualization 3, and Visualization 4 show acquired Z-stacks for curved and flat coherence gate when imaging the USAF target and the model eye.

3.2. Living human retinal cone mosaic imaging

Figures 4(a,b) presents *in-vivo* retinal images from the inner/outer segment junction (IS/OS) of subject S1 before and after compensation of the coherence gate curvature respectively. The yellow square in the retinal fundus image (Fig. 4(c)) indicates the location of acquired images, *i.e.* as close as 1° from the foveal center. According to Fig. 3(g), by adding an N-BK7 optical window with 20mm thickness, the coherence gate curvature would be strongly minimized. With this configuration, we obtained a high-resolution foveal cone mosaic imaging with a useful FOV of $1\,mm \times 1\,mm$, larger than the previous FOV ($0.4\,mm \times 0.4\,mm$) [24] by a factor of 6.25, only correcting ocular aberrations with prescribed eyeglasses. Zoomed areas and their respective power spectral densities (PSD) are also presented. All PSDs presented Yellot's ring, the spectral signature of the photoreceptor mosaic image [29].
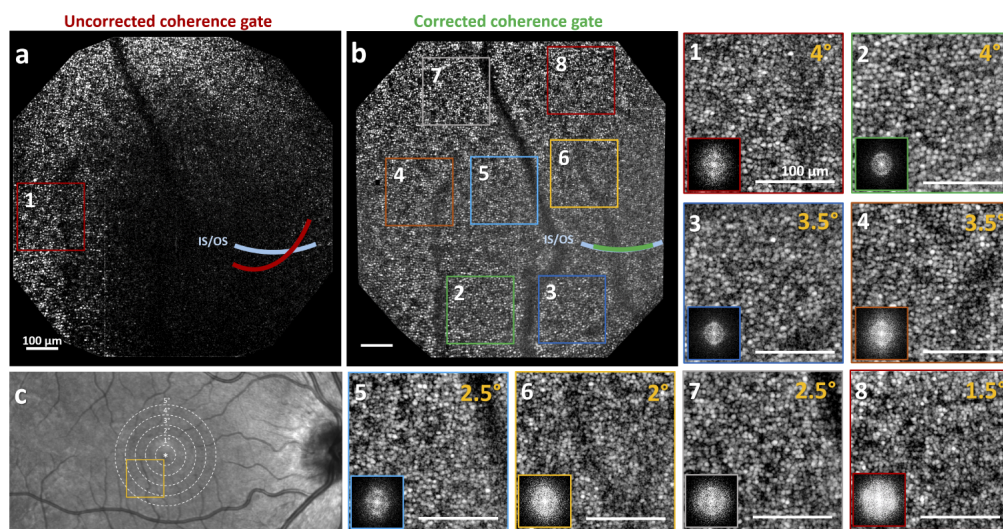
Fig. 4. Foveal cone mosaic images of subject S1 as close as 1° from the foveal center (yellow square of the retinal fundus image). **a,b,** Respectively, acquired images from the IS/OS junction before and after correcting for the coherence gate curvature. Zoomed areas, and their respective eccentricity (in yellow) and PSD are also presented. All PSDs present the Yellot's ring [29]. Scale bar, $100\mu m$.

Figure 5 presents cone mosaic images obtained for subject S2 at 3° eccentricity temporal to the fovea after correcting the coherence gate curvature. Cone photoreceptors can also be resolved in the whole $1\,mm \times 1\,mm$ FOV. Note that the same 20 mm thick N-BK7 optical window used for S1 is also suitable to correct the coherence gate curvature for S2.
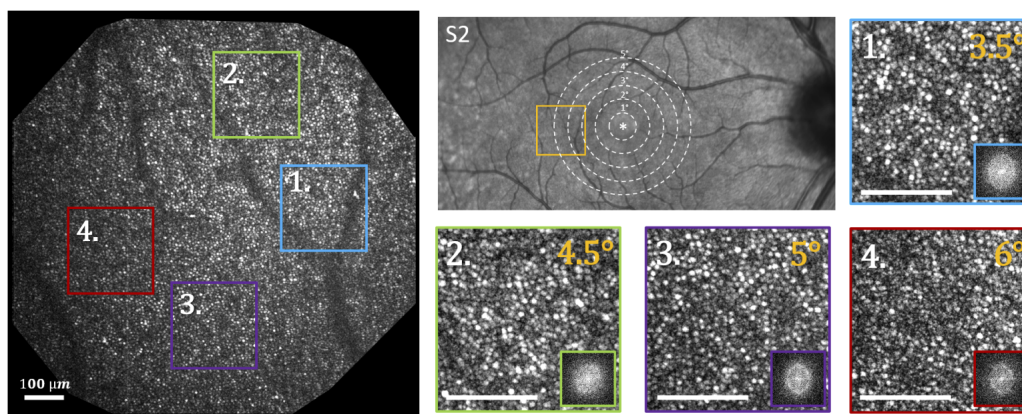
Fig. 5. Foveal cone images of subject S2 after correcting the coherence gate curvature. Zoomed areas, and their respective eccentricity (in yellow) and PSD are also presented. Scale bar, 100μm.

3.3. Photoreceptor-based biomarkers and 4D monitoring of individual photoreceptors

The compensation of the coherence gate curvature enables the visualization of photoreceptors in the whole FOV. Consequently, we can obtain important information on photoreceptor-based biomarkers such as distribution, density, and spacing within a few seconds in a single-shot (no image montaging is necessary) with ease (Fig. 6). All measurements are consistent with histology and AO-assisted cone density measurement [30,31].
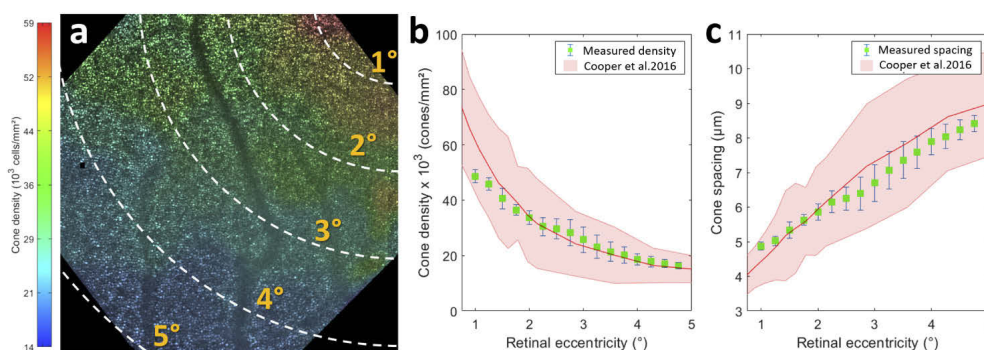
Fig. 6. a, Cone density distribution color coded for the image acquired from subject S1. **b-c,** Respectively, mean (green squares) and standard deviation (blue lines) of the measured cone density and spacing as a function of the retinal eccentricity. The red line is the mean computed density and the shaded region is 95% prediction interval obtained from a dataset of a 20-eye healthy population using an AO scanning-laser ophthalmoscope [31].

Minimizing the effect of the coherence gate curvature also helps to increase the repeatability of the imaging, allowing for spatiotemporal monitoring of individual photoreceptors. Visualization 5 presents four image sequences acquired in the same region with a 10 *min* interval between acquisitions. Note in zoomed areas that individual photoreceptors can be tracked frame-by-frame (3 *ms* interval) and video-by-video (10 *min* interval). Green boxes highlight cones that are visible in all four videos, while yellow boxes highlight those visible for only some of the videos, which might indicate a long-term change of reflectivity [32]. Red hexagons highlight the typical pattern found in cone mosaic close to the fovea [30]. Figure 7(a-d) presents the averaged image obtained from zoomed areas of Visualization 5. Figures 7(e-h) and Visualization 6 and

131

Visualization 7 show a cone-to-cone comparison of FF-OCT image with images generated by two AO ophthalmoscope modalities for subject S1 at same location. FF-OCT allows visualization of most, if not all, photoreceptors identified in AO-assisted images. Note in Fig. 7(i) that PSDs from all FF-OCT images present a clear and well-defined cone mosaic spatial frequency (vertical pale red bar) at 120 cycles/mm, as is the case for both AO-assisted imaging modalities. On the other hand, when using a scanning laser ophthalmoscope without closing the AO-loop, an erroneous spatial frequency is measured, leading to an error in cone density computation.
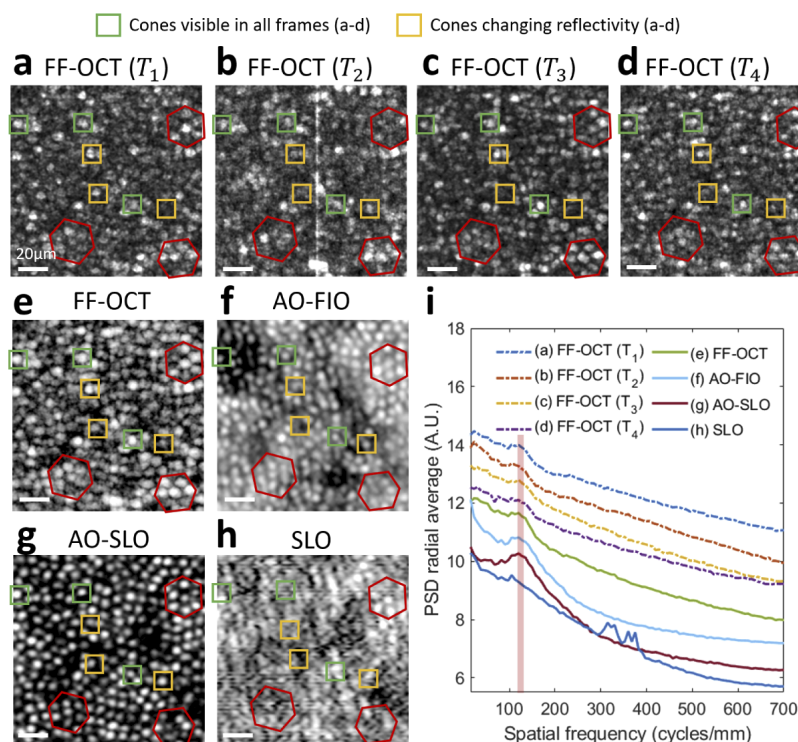
Fig. 7. a-d, Cone mosaic images acquired at the same region (4.5^o eccentricity) for different time points $T_{1,2,3,4}$, with 10 minutes interval between acquisitions, for subject S1, highlighting the capacity of FF-OCT with coherence gate shaping to track individual cones in space and time. Green boxes: cones visible for all four acquisitions. Yellow boxes: cones changing reflectivity. Red hexagons: pattern found in cone mosaic close to the fovea [30]. **e,** Cone mosaic image obtained after averaging images from **a-d**. **f-h,** Cone mosaic image at the same region acquired using AO-ophthalmoscopes. **f,** FIO: Flood-illumination ophthalmoscope. **g,** SLO: confocal scanning-laser ophthalmoscope. **h,** Acquisition made without closing the AO-loop. **i,** PSD radial average for images **a-h**, where the vertical pale red bar outlines the expected cone mosaic spatial frequency. PSDs were vertically displaced for better visualization. Scale bar, 20 μm.

4. Discussion

In this paper, we saw that the Linnik symmetry plays an important role in obtaining a flat coherence gate. Although this symmetry is broken in the case of retinal imaging, inducing an intrinsically curved coherence gate, we showed that the coherence gate geometry can be corrected by introducing a simple optical element such as an optical window into one of the interferometer arms. We used this technique to compensate the intrinsic curved coherence gate in the asymmetric configuration of FF-OCT for retinal imaging, obtaining an useful FOV of

1 *mm* × 1 *mm*, limited only by the size and the spatial sampling of the imaging camera. To the best of our knowledge, this is the first OCT system allying a FOV as large as 1 *mm* × 1 *mm*, high spatial resolution in all three dimensions and high acquisition rate of a given retinal plane (up to 300 Hz), without using any optical or digital aberration compensation other than prescribed eyeglasses, considerably simplifying the hardware and software complexity. The coherence gate curvature was previously reported for scanning-like OCT, mainly linked to the scanning-induced path length variation in non telecentric optical systems [33]. Therefore, the described method to optically shape the coherence gate can also be applied in OCT and Optical Coherence Microscopy imaging techniques to avoid curvature artefacts and to compensate for optical components that are only positioned in one of the arms, inducing an asymmetry.

Another expected effect brought by the asymmetry of the Linnik interferometry is dispersion, affecting the axial resolution of the FF-OCT (*i.e.* axial sectioning capacity). This phenomenon can be noted in cross-sections of Figs. 3(a,b) as an increase of the coherence gate thickness (distance between the blue and red curves). Figure 8 shows the FWHM of the coherence gate thickness (FF-OCT axial resolution) as a function of the optical window thickness in the case of the USAF target imaging (in red) and the model eye imaging (in blue). Note that for the USAF target imaging, a flat coherence gate coincides with the best axial sectioning capability, both happening when no optical window is added (symmetric configuration). In the case of the model eye imaging, not surprisingly, the optimum correction of dispersion does not coincide with the optimum correction of coherence gate curvature, since these two phenomena have different physical origins.
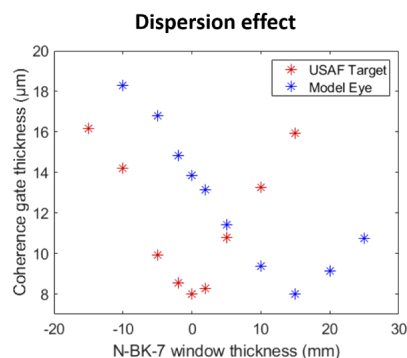
Fig. 8. Experimental data from Fig. 3 showing how dispersion evolves for different thicknesses of optical windows. The FWHM of the coherence gate thickness (FF-OCT axial resolution) as a function of the optical window thickness in the case of the USAF target (red points) and model eye (blue points) imaging respectively.

An optimum compensation of the coherence gate curvature would be possible with a 22 mm N-BK7 optical window (Fig. 3(g)). Figure 8 shows, for the model eye imaging, that an optimum dispersion compensation would be possible with a 15 mm of N-BK7 optical window. In this study, in order to compromise and minimize the effects of both curvature of the coherence gate and dispersion for *in-vivo* retinal imaging, we used a N-BK7 optical window with 20 mm thickness. According to Fig. 3(g) and Fig. 8, a good trade-off could be found in this case: the axial resolution would be around 9μm, instead of 8μm, and the degree of curvature would be lower than 5, meaning an edge-center difference of 1μm.

We presented results in two different subjects presenting different refractive errors at two different retinal eccentricities. In both cases, a 20-mm thick N-BK7 optical window was suitable to achieve a 1 *mm* × 1 *mm* FOV. Indeed, since the axial resolution is around 9μm, a mismatch between the coherence gate geometry and the retina curvature inferior to the optical sectioning (given by the FF-OCT axial resolution) would not be seen (Fig. 9(a-c)). Figure 9(d) shows

theoretical degree of curvature values, validated by our previous model (Sect. 2.1 and Fig. 3(c,f)), for different eye lengths. One can see that a 20-mm thick N-BK7 optical window would be suitable (edge-center distance inferior to 1μm) to achieve a $1\,mm \times 1\,mm$ FOV for eye lengths varying from 20 mm to 28 mm, which covers the majority of cases in the population [34]. It is therefore not necessary to swap optical window for each subject: the 20mm thick window covers the whole range of eye lengths that one would typically see in the clinic.
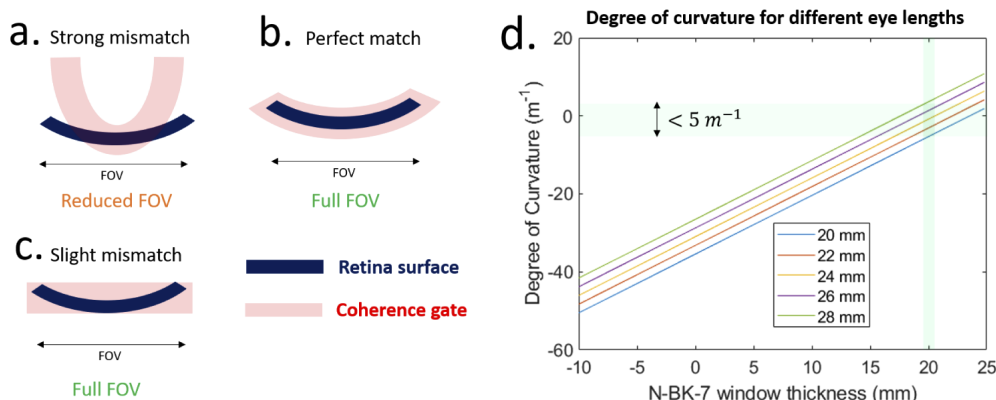
Fig. 9. **(a-c)** Schematic showing different degrees of curvature for the coherence gate and their consequence on the FOV of the FF-OCT image. Although the coherence gate curvature does not perfectly match the retinal curvature in the case of **(c)**, a full FOV is still generated, as the coherence gate has a given thickness defined by the axial resolution. **(d)** Expected theoretical value of degree of curvature (computed using Eq. (1)) as a function of the thickness of the N-BK7 introduced to compensate for coherence gate curvature for different eye lengths. Green shaded area highlights that a N-BK7 of 20 mm thickness covers the majority of eye lengths in the population (from 20 mm to 28 mm) [34].

In this study, we only considered N-BK7 optical windows to minimize effects of both coherence gate curvature and dispersion. Another solution to optically shape the geometry of the coherence gate is the introduction of a deformable reference mirror in the reference arm. This solution would decouple the correction of the coherence gate curvature and dispersion, since a suitable optical window in the sample arm could compensate for dispersion effect and the deformable reference arm would correct the residual curvature of the coherence gate, without affecting dispersion, improving signal level, axial resolution and possibly achieving even larger FOV. Moreover, this solution might extend the coherence gate shaping to samples with an irregular surface, more complex than a curvature, such as deformed retina due to degeneration, detachment, etc. In the case of imaging a deformed retina, a deformable reference would enable imaging an irregular retinal layer over a large FOV in a single shot instead of acquiring *en-face* images for different coherent plane positions. Nevertheless, the main drawback of this solution is the considerable increase of the system complexity and cost, making clinical transfer challenging. A solution considering only a 20 mm thick N-BK7 optical window, as presented in this paper, seems suitable to minimize both curvature of the coherence gate and dispersion for a large population.

The direct visualization of individual photoreceptors together with photoreceptor-based biomarkers, such as distribution, density and spacing, could be useful tools to diagnose retinal disorders at the early stages, in order to monitor retinal disease progression as well as the effect of potential therapeutic interventions [32]. The presented FF-OCT system with coherence gate shaping enables 4D monitoring of individual photoreceptors and photoreceptor-based biomarkers with good accuracy and repeatability in a wide FOV, without image distortion (due to eye motion) and long, fastidious acquisition sessions to cover the retinal area of interest, as is the case with

lab-built scanning systems with limited FOV such as AO-SLO and AO-OCT. While AO-FIO can achieve 1 *mm* × 1 *mm* FOV at a high-frame rate [8], high-resolution brought by ocular aberration correction using AO is limited by the eye's field aberrations, commonly known as the isoplanatic patch [12], affecting the accuracy of the resultant photoreceptor-based biomarkers. This issue can be tackle by limiting the system aperture (around 5 mm in the eye's pupil plane), provoking a decrease of resolution and signal-to-noise ratio (SNR), as rtx-1 (Imagine Eyes, France) and [8]; or by using multi-conjugated AO, with an increased system complexity as a second deformable mirror is necessary [13]. The present FF-OCT with coherence gate shaping can resolve photoreceptor and extract photoreceptor-based biomarkers in the whole FOV without AO, considerably decreasing the system complexity and footprint, which may help clinical deployment. Additionally, FF-OCT has the capacity to generate en-face retinal images with an enhanced axial resolution (9 *μm*) compared to confocal AO-SLO (around 40 *μm* [35]) and AO-FIO (no inherent optical sectioning). This advantage can be observed in Fig. 7, especially in comparison with AO-FIO, where a structured background can be observed in the latter, probably coming from the choroid positioned beneath the photoreceptor layer, which is completely filtered out by the FF-OCT thanks to its high axial resolution. Although FF-OCT axial resolution may be slightly poorer than AO-OCT [10], it has advantages of larger FOV, higher-frame rate and lower complexity and size, and is still able to resolve the photoreceptor interfaces such as IS/OS junction and cone outer segment tips. Moreover, the high temporal resolution of FF-OCT may play an important role to characterize the temporal behavior of retinal capillaries from different plexus [36,37] and the temporal dynamics of subcellular structures [27]. Finally, although FF-OCT is only weakly sensitive to low-order ocular aberrations in terms of resolution, aberrations still reduce the FF-OCT signal level [38]. Ocular aberrations may explain why the SNR of FF-OCT images varies across the FOV (Figs. 4 and 5) and why the AO-SLO image has higher contrast than the FF-OCT image (Fig. 7). Although the presented imaging technique presents lower SNR compared to AO-SLO, photoreceptors can still be visualized in single unaveraged frames, as it was demonstrated in Visualization 5, and photoreceptor-based biomarkers can still be extracted with accuracy (Fig. 6).

5. Conclusion

In conclusion, we have developed coherence gate shaping for FF-OCT to adapt coherence gate geometry to the curvature of the sample being imaged, making large FOV imaging possible while keeping high-resolution in samples under constant motion, such as the living human eye. We applied this method to achieve, in a single shot, and without the use of AO, 1 *mm* × 1 *mm* FOV image of the living human cone mosaic as close as 1° from the foveal center. We showed that a large FOV allied with a high resolution in all three dimensions, brings a significant benefit for retinal imaging: the large FOV facilitates the localization of the region of interest, allows a global interpretation of the retinal condition over this area, such as cone density distribution, and drastically reduces the image session duration; the high resolution allows tracking of individual cones and computation of cellular information, such as cell density and spacing, that could be used as biomarkers to diagnose retinal disorders at early stages. FF-OCT with improved performance thanks to coherence gate shaping may pave the way towards its adoption as a routine clinical imaging system, helping to understand retinal structure and disease.

Acknowledgments

Disclosures

P. Mecê: PSL University (P), C. Boccara: PSL University (P), others: none.

References

1. A. London, I. Benhar, and M. Schwartz, "The retina as a window to the brain - from eye research to cns disorders," Nat. Rev. Neurol. **9**(1), 44–53 (2013).
2. J. J. Hunter, W. H. Merigan, and J. B. Schallek, "Imaging retinal activity in the living eye," Annu. Rev. Vis. Sci. **5**(1), 15–45 (2019).
3. J. Jarosz, P. Mecê, J.-M. Conan, C. Petit, M. Paques, and S. Meimon, "High temporal resolution aberrometry in a 50-eye population and implications for adaptive optics error budget," Biomed. Opt. Express **8**(4), 2088–2105 (2017).
4. P. Mecê, E. Gofas-Salas, C. Petit, F. Cassaing, J. Sahel, M. Paques, K. Grieve, and S. Meimon, "Higher adaptive optics loop rate enhances axial resolution in nonconfocal ophthalmoscopes," Opt. Lett. **44**(9), 2208–2211 (2019).
5. J. Liang, D. R. Williams, and D. T. Miller, "Supernormal vision and high-resolution retinal imaging through adaptive optics," J. Opt. Soc. Am. A **14**(11), 2884–2892 (1997).
6. A. Roorda, F. Romero-Borja, W. J. Donnelly III, H. Queener, T. J. Hebert, and M. C. Campbell, "Adaptive optics scanning laser ophthalmoscopy," Opt. Express **10**(9), 405–412 (2002).
7. M. Zacharria, B. Lamory, and N. Chateau, "Biomedical imaging: New view of the eye," Nat. Photonics **5**(1), 24–26 (2011).
8. E. Gofas-Salas, P. Mecê, C. Petit, J. Jarosz, L. M. Mugnier, A. M. Bonnefois, K. Grieve, J. Sahel, M. Paques, and S. Meimon, "High loop rate adaptive optics flood illumination ophthalmoscope with structured illumination capability," Appl. Opt. **57**(20), 5635–5642 (2018).
9. M. Paques, S. Meimon, F. Rossant, D. Rosenbaum, S. Mrejen, F. Sennlaub, and K. Grieve, "Adaptive optics ophthalmoscopy: Application to age-related macular degeneration and vascular diseases," Prog. Retinal Eye Res. **66**, 1–16 (2018).
10. R. S. Jonnal, O. P. Kocaoglu, R. J. Zawadzki, Z. Liu, D. T. Miller, and J. S. Werner, "A review of adaptive optics optical coherence tomography: technical advances, scientific applications, and the future," Invest. Ophthalmol. Visual Sci. **57**(9), OCT51–OCT68 (2016).
11. N. D. Shemonski, F. A. South, Y.-Z. Liu, S. G. Adie, P. S. Carney, and S. A. Boppart, "Computational high-resolution optical imaging of the living human retina," Nat. Photonics **9**(7), 440–443 (2015).
12. P. Bedggood, M. Daaboul, R. A. Ashman, G. G. Smith, and A. Metha, "Characteristics of the human isoplanatic patch and implications for adaptive optics retinal imaging," J. Biomed. Opt. **13**(2), 024008 (2008).
13. M. Laslandes, M. Salas, C. K. Hitzenberger, and M. Pircher, "Increasing the field of view of adaptive optics scanning laser ophthalmoscopy," Biomed. Opt. Express **8**(11), 4811–4826 (2017).
14. D. Hillmann, H. Spahr, C. Hain, H. Sudkamp, G. Franke, C. Pfäffle, C. Winter, and G. Hüttmann, "Aberration-free volumetric high-speed imaging of in vivo retina," Sci. Rep. **6**(1), 35209 (2016).
15. D. Borycki, E. Auksorius, P. Węgrzyn, and M. Wojtkowski, "Computational aberration correction in spatiotemporal optical coherence (stoc) imaging," Opt. Lett. **45**(6), 1293–1296 (2020).
16. L. Ginner, A. Kumar, D. Fechtig, L. M. Wurster, M. Salas, M. Pircher, and R. A. Leitgeb, "Noniterative digital aberration correction for cellular resolution retinal optical coherence tomography in vivo," Optica **4**(8), 924–931 (2017).
17. H. Sudkamp, D. Hillmann, P. Koch, M. vom Endt, H. Spahr, M. Münst, C. Pfäffle, R. Birngruber, and G. Hüttmann, "Simple approach for aberration-corrected oct imaging of the human retina," Opt. Lett. **43**(17), 4224–4227 (2018).
18. T. B. DuBose, F. LaRocca, S. Farsiu, and J. A. Izatt, "Super-resolution retinal imaging using optically reassigned scanning laser ophthalmoscopy," Nat. Photonics **13**(4), 257–262 (2019).
19. P. Mecê, J. Jarosz, J.-M. Conan, C. Petit, K. Grieve, M. Paques, and S. Meimon, "Fixational eye movement: a negligible source of dynamic aberration," Biomed. Opt. Express **9**(2), 717–727 (2018).
20. A. Dubois, K. Grieve, G. Moneron, R. Lecaque, L. Vabre, and C. Boccara, "Ultrahigh-resolution full-field optical coherence tomography," Appl. Opt. **43**(14), 2874–2883 (2004).
21. O. Thouvenin, K. Grieve, P. Xiao, C. Apelian, and A. C. Boccara, "En face coherence microscopy," Biomed. Opt. Express **8**(2), 622–639 (2017).
22. P. Xiao, M. Fink, and A. C. Boccara, "Full-field spatially incoherent illumination interferometry: a spatial resolution almost insensitive to aberrations," Opt. Lett. **41**(17), 3920–3923 (2016).
23. P. Mecê, P. Xiao, V. Mazlin, J. Scholler, K. Grieve, J.-A. Sahel, M. Fink, and C. Boccara, "Towards lens-based wavefront sensorless adaptive optics full-field oct for in-vivo retinal imaging (conference presentation)," in *Optical Coherence Tomography and Coherence Domain Optical Methods in Biomedicine XXIII*, vol. 10867 (International Society for Optics and Photonics, 2019), p. 1086722.

Biomedical Optics EXPRESS

24. P. Mecê, J. Scholler, K. Groux, and C. Boccara, "High-resolution in-vivo human retinal imaging using full-field oct with optical stabilization of axial motion," Biomed. Opt. Express **11**(1), 492–504 (2020).

25. P. Xiao, V. Mazlin, K. Grieve, J.-A. Sahel, M. Fink, and A. C. Boccara, "In vivo high-resolution human retinal imaging with wavefront-correctionless full-field oct," Optica **5**(4), 409–412 (2018).

26. W. Sellmeier, "Zur erkarung der abnormen farbenfolge im spectrum einiger. substanzen," Ann. Phys. **219**(6), 272–282 (1871).

27. J. Scholler, V. Mazlin, O. Thouvenin, K. Groux, P. Xiao, J.-A. Sahel, M. Fink, C. Boccara, and K. Grieve, "Probing dynamic processes in the eye at multiple spatial and temporal scales with multimodal full field oct," Biomed. Opt. Express **10**(2), 731–746 (2019).

28. R. F. Cooper, G. K. Aguirre, and J. I. Morgan, "Fully automated estimation of spacing and density for retinal mosaics," Trans. Vis. Sci. Tech. **8**(5), 26 (2019).

29. J. I. Yellott Jr, "Spectral analysis of spatial sampling by photoreceptors: topological disorder prevents aliasing," Vision Res. **22**(9), 1205–1210 (1982).

30. C. A. Curcio, K. R. Sloan, R. E. Kalina, and A. E. Hendrickson, "Human photoreceptor topography," J. Comp. Neurol. **292**(4), 497–523 (1990).

31. R. F. Cooper, M. A. Wilk, S. Tarima, and J. Carroll, "Evaluating descriptive metrics of the human cone mosaic," Invest. Ophthalmol. Visual Sci. **57**(7), 2992–3001 (2016).

32. K. M. Litts, R. F. Cooper, J. L. Duncan, and J. Carroll, "Photoreceptor-based biomarkers in aoslo retinal imaging," Invest. Ophthalmol. Visual Sci. **58**(6), BIO255 (2017).

33. A. Podoleanu, M. Seeger, G. Dobre, D. Webb, D. Jackson, and F. Fitzke, "Transversal and longitudinal images from the retina of the living eye using low coherence reflectometry," J. Biomed. Opt. **3**(1), 12 (1998).

34. H. Kolb, "Gross anatomy of the eye," in *Webvision: The Organization of the Retina and Visual System [Internet]*, (University of Utah Health Sciences Center, 2007).

35. D. T. Miller, J. Qu, R. S. Jonnal, and K. E. Thorn, "Coherence gating and adaptive optics in the eye," in *Coherence Domain Optical Methods and Optical Coherence Tomography in Biomedicine VII*, vol. 4956 (International Society for Optics and Photonics, 2003), pp. 65–72.

36. E. Gofas-Salas, P. Mecê, L. Mugnier, A. M. Bonnefois, C. Petit, K. Grieve, J. Sahel, M. Paques, and S. Meimon, "Near infrared adaptive optics flood illumination retinal angiography," Biomed. Opt. Express **10**(6), 2730–2743 (2019).

37. C. Lavia, P. Mecê, M. Nassisi, S. Bonnin, J. Marie-Louise, A. Couturier, A. Erginay, R. Tadayoni, and A. Gaudric, "Retinal capillary plexus pattern and density from fovea to periphery measured in healthy eyes with swept-source optical coherence tomography angiography," Sci. Rep. **10**(1), 1474 (2020).

38. J. Scholler, K. Groux, K. Grieve, C. Boccara, and P. Mecê, "Adaptive-glasses wavefront sensorless full-field oct for high-resolution retinal imaging over a wide field-of-view," arXiv preprint arXiv:2007.04986 (2020).

137

Appendix D

Scientific contributions

Publications

Jules Scholler, Viacheslav Mazlin, Olivier Thouvenin, **Kassandra Groux**, Peng Xiao, José-Alain Sahel, Mathias Fink, Claude Boccara, and Kate Grieve. *Probing dynamic processes in the eye at multiple spatial and temporal scales with multimodal full field OCT.* Biomedical Optics Express, 10(2):731-746, February 2019

Pedro Mecê, Jules Scholler, **Kassandra Groux**, and Claude Boccara. *High-resolution in-vivo human retinal imaging using full-field OCT with optical stabilization of axial motion.* Biomedical Optics Express, 11(1):492, January 2020.

Jules Scholler*, **Kassandra Groux***, Olivier Goureau, José-Alain Sahel, Mathias Fink, Sacha Reichman, Claude Boccara, and Kate Grieve. *Dynamic full-field optical coherence tomography: 3D live-imaging of retinal organoids.* Light: Science & Applications, 9(1):140, August 2020. * equal contribution

Pedro Mecê, **Kassandra Groux**, Jules Scholler, Olivier Thouvenin, Mathias Fink, Kate Grieve, and Claude Boccara. *Coherence gate shaping for wide field high-resolution in vivo retinal imaging with full-field OCT.* Biomedical Optics Express, 11(9):4928–4941, September 2020.

Jules Scholler, **Kassandra Groux**, Kate Grieve, Claude Boccara, and Pedro Mecê. *Adaptive-glasses time-domain FFOCT for wide-field high-resolution retinal imaging with increased SNR.* Optics Letters, 45(21):5901–5904, November 2020.

Victor Barolle, Jules Scholler, Pedro Mecê, Jean-Marie Chassot, **Kassandra Groux**, Mathias Fink, A. Claude Boccara, and Alexandre Aubry. *Manifestation of aberrations in full-field optical coherence tomography.* Optics Express, 29(14):22044–22065, July 2021.

Kassandra Groux, Anna Verschueren, Céline Nanteau, Marilou Clémençon, Mathias Fink, José-Alain Sahel, Claude Boccara, Michel Paques, Sacha Reichman, and Kate Grieve. *Non invasive live imaging of a novel retinal pigment epithelium stress model with Dynamic Full-Field Optical Coherence Tomography.* arXiv:2106.10531 [physics], June 2021. Under review Communications Biology.

Conferences

2019

Kassandra Groux, Jules Scholler, Kate Grieve, and Claude Boccara. *Probing cells dynamics with quantitative Dynamic Full-Field OCT.* In QBI Poster session, QBI conference, Rennes, France, January 2019.

Jules Scholler, **Kassandra Groux**, Kate Grieve, and Claude Boccara. *Methods and applications of quantitative dynamic full-field OCT.* In QBI Optical Methods Developments session, QBI conference, Rennes, France, January 2019.

Kassandra Groux, Jules Scholler, Kate Grieve, and Claude Boccara. *Dynamic full-field optical coherence tomography in label-free live/dead imaging of cells cultures for disease modeling.* In Photonics West 2019 Label-free Biomedical Imaging and Sensing 2019, San Francisco, USA, February 2019. International Society for Optics and Photonics.

Emilie Benoit a la Guillaume, **Kassandra Groux**, Jules Scholler, Diana Mandache, Houpu Yang, Shu Wang, Vannary Meas-Yedid, and Claude Boccara. *Intracellular dynamics as a biomarker in tumor assessment using full-field optical coherence tomography.* In Photonics West 2019 Molecular-Guided Surgery: Molecules, Devices, and Applications V, volume 10862, page 1086204, San Francisco, USA, February 2019. International Society for Optics and Photonics.

Kassandra Groux, Jules Scholler, Kate Grieve, and Claude Boccara. *Optimized setup for sub-cellular live imaging in 2D and 3D cell cultures and tissues with dynamic full-field OCT.* In Photonics West 2019 Imaging, Manipulation, and Analysis of Biomolecules, Cells, and Tissues XVII, San Francisco, USA, February 2019. International Society for Optics and Photonics.

Jules Scholler, **Kassandra Groux**, Sacha Reichman, Michel Paques, Olivier Goureau, José Sahel, Mathias Fink, Claude Boccara, and Kate Grieve. *Subcellular quantitative dynamic imaging: from metabolic activity to cell tracking of retinal and corneal structure.* In Photonics West 2019 Optical Coherence Tomography and Coherence Domain Optical Methods in Biomedicine XXIII, volume 10867, page 108670E, San Francisco, USA, March 2019. International Society for Optics and Photonics.

Kassandra Groux, Jules Scholler, Sacha Reichman, Michel Paques, Olivier Goureau, Jose Alain Sahel, Mathias Fink, Claude Boccara, and Kate Grieve. *Imaging retinal organoid subcellular dynamics non invasively with Full-Field OCT.* ARVO 2019. Investigative Ophthalmology & Visual Science, 60(9):3337–3337, July 2019. Publisher: The Association for Research in Vision and Ophthalmology.

Jules Scholler, **Kassandra Groux**, Jose Alain Sahel, Mathias Fink, Claude Boccara, and Kate Grieve. *Real time dynamic imaging of retinal samples with full field OCT.* ARVO 2019. Investigative Ophthalmology & Visual Science, 60(9):1265–1265, July 2019. Publisher: The Association for Research in Vision and Ophthalmology.

Jules Scholler, **Kassandra Groux**, Mathias Fink, Claude Boccara, and Kate Grieve. *Label free retinal cell imaging with dynamic full-field OCT.* ARVO Imaging in the eye 2019. Investigative Ophthalmology & Visual Science, 60(11):009–009, August 2019. Publisher: The Association for Research in Vision and Ophthalmology.

Kassandra Groux, Jules Scholler, Sacha Reichman, Michel Paques, Olivier Goureau, Jose-Alain Sahel, Mathias Fink, Claude Boccara, and Kate Grieve. *Following retinal organoid developmental stages with Dynamic Full-Field OCT imaging.* In Imaging organoids, spheroids & 3D cultures symposium, Paris, France, October 2019.

Kassandra Groux, Jules Scholler, Michel Paques, José-Alain Sahel, Mathias Fink, Olivier Goureau, Claude Boccara, Sacha Reichman, and Kate Grieve. *2D & 3D retinal cell culture imaging with Dynamic Full-Field OCT.* In Vision Restoration: Emerging Therapies, Joint French-Japanese Scientific Seminar Institut de la Vision and RIKEN, Paris, France, November 2019.

2020

Kassandra Groux, Jules Scholler, Pedro Mecê, Sacha Reichman, Valerie Fradot, Michel Paques, Claude Boccara, and Kate Grieve. *Stress and repair in retinal pigmented epithelium cell culture imaged with dynamic full-field OCT.* In Photonics West 2020 Dynamics and Fluctuations in Biomedical Photonics XVII, volume 11239, page 112390O, San Francisco, USA, February 2020. International Society for Optics and Photonics.

Pedro Mecê, Jules Scholler, **Kassandra Groux**, Mathias Fink, Kate Grieve, and Claude Boccara. *Adaptive glasses-assisted Full-Field OCT for SNR enhanced 3D high-resolution retinal imaging.* In Photonics West 2020 Optical Coherence Tomography and Coherence Domain Optical Methods in Biomedicine XXIV, volume 11228, page 112281O, San Francisco, USA, February 2020. International Society for Optics and Photonics.

Pedro Mecê, **Kassandra Groux**, Jules Scholler, Mathias Fink, Kate Grieve, and Claude Boccara. *Increased fieldof- view full-field OCT for 3D high-resolution retinal imaging.* In Photonics West 2020 Ophthalmic Technologies XXX, volume 11218, page 112180S, San Francisco, USA, February 2020. International Society for Optics and Photonics.

Jules Scholler, Pedro Mecê, **Kassandra Groux**, Viacheslav Mazlin, Claude Boccara, and Kate Grieve. *Motion artifact removal and signal enhancement to achieve in vivo dynamic full field OCT.* In Photonics West 2020 Optical Coherence Tomography and Coherence Domain Optical Methods in Biomedicine XXIV, volume 11228, page 112281N, San Francisco, USA, February 2020. International Society for Optics and Photonics.

Pedro Mecê, Jules Scholler, **Kassandra Groux**, Olivier Thouvenin, Mathias Fink, Kate Grieve, and Claude Boccara. *1-mm field-of-view imaging of living human foveal cone mosaic with Full-Field OCT.* ARVO 2020. Investigative Ophthalmology & Visual Science, 61(7):216–216, Online, June 2020. Publisher: The Association for Research in Vision and Ophthalmology.

Kassandra Groux, Jules Scholler, Anna Verschueren, Marie Darche, Olivier Goureau, Jose Alain Sahel, Mathias Fink, Michel Paques, Claude Boccara, Olivier Thouvenin, Sacha Reichman, and Kate Grieve. *Dynamic Full- Field OCT to image RPE cell cultures.* ARVO 2020. Investigative Ophthalmology & Visual Science, 61(7):1867–1867, Online, June 2020. Publisher: The Association for Research in Vision and Ophthalmology. **Travel Grant**.

Kassandra Groux, Jules Scholler, Pedro Mecê, Mathias Fink, Claude Boccara, Olivier Thouvenin, and Kate Grieve. *Dynamic full-field OCT imaging for regenerative medicine.* ARVO Imaging in the eye 2020. Investigative Ophthalmology & Visual Science, 61(9):PP008–PP008,

Online, July 2020. Publisher: The Association for Research in Vision and Ophthalmology.

Pedro Mecê, Jules Scholler, **Kassandra Groux**, Kate Grieve, and Claude Boccara. *Compact, adaptive-glasses Full-Field OCT for high-resolution in-vivo human retinal imaging over a large field-of-view.* ARVO Imaging in the eye 2020. Investigative Ophthalmology & Visual Science, 61(9):PP0025–PP0025, Online, July 2020. Publisher: The Association for Research in Vision and Ophthalmology.

Jules Scholler, Pedro Mece, **Kassandra Groux**, Mathias Fink, Claude Boccara, Kate Grieve, and Kate Grieve. *Adaptive Glasses Full-Field OCT with axial tracking for 3D high-resolution retinal imaging.* In Imaging and Applied Optics Congress (2020), paper IF2E.3, page IF2E.3, Online, June 2020. Optical Society of America.

Kassandra Groux, Jules Scholler, Anna Verschueren, Marie Darche, Leyna Boucherit, Mathias Fink, Sacha Reichman, Michel Paques, Claude Boccara, Olivier Thouvenin, and Kate Grieve. *Stress and repair on RPE cell cultures imaged with Dynamic Full-Field OCT.* i2Eye meeting, Online, October 2020.

2021

Pedro Mecê, **Kassandra Groux**, Jules Scholler, Kate Grieve, and Claude Boccara. *Retinal curvature correction with coherence gate shaping for full-field OCT high-resolution retinal imaging over a wide field-of-view.* In Photonics West 2021 Optical Coherence Tomography and Coherence Domain Optical Methods in Biomedicine XXV, volume 11630, page 116300C, Online, March 2021. International Society for Optics and Photonics.

Kassandra Groux, Jules Scholler, Anna Verschueren, Marie Darche, Leyna Boucherit, Pedro Mecê, Valérie Fradot, Jean-Marie Chassot, Mathias Fink, Sacha Reichman, Michel Paques, Claude Boccara, Olivier Thouvenin, and Kate Grieve. *Dynamic full-field optical coherence tomography of retinal pigment epithelium cell cultures to model degenerative diseases.* In Photonics West 2021 Optical Coherence Tomography and Coherence Domain Optical Methods in Biomedicine XXV, volume 11630, page 1163014, Online, March 2021. International Society for Optics and Photonics.

Pedro Mecê, Jules Scholler, **Kassandra Groux**, Kate Grieve, and Claude Boccara. *Adaptive glasses wavefront sensorless full-field OCT for high-resolution retinal imaging over a wide field-of-view.* In Photonics West 2021 Ophthalmic Technologies XXXI, volume 11623, page 1162306, Online, March 2021. International Society for Optics and Photonics.

Viacheslav Mazlin, Peng Xiao, Kristina Irsch, Jules Scholler, **Kassandra Groux**, Kate Grieve, Mathias Fink, and Claude Boccara. *Optical phase modulation by natural eye movements: application to time-domain FF-OCT image retrieval.* In Photonics West 2021 Optical Coherence Tomography and Coherence Domain Optical Methods in Biomedicine XXV, volume 11630, page 116300G, Online, March 2021. International Society for Optics and Photonics.

Pedro Mecê, Jules Scholler, **Kassandra Groux**, Yao Cai, Michel Paques, Kate Grieve, and Claude Boccara. *Adaptive-glasses Full-Field OCT for high-resolution retinal imaging over a large field-of-view.* ARVO 2021. Investigative Ophthalmology & Visual Science, 62(8):9-9, Online, June 2021. Publisher: The Association for Research in Vision and

Ophthalmology.

Kassandra Groux, Anna Verschueren, Mathias Fink, Claude Boccara, Sacha Reichman, and Kate Grieve. *Detecting subcellular dynamic behaviours with Dynamic Full-Field OCT on stressed Retinal Pigment Epithelium cell cultures.* In ECBO 2021 Advances in Eye Imaging, Online, June 2021. Optical Society of America.

Yao Cai, Jules Scholler, **Kassandra Groux**, Olivier Thouvenin, Claude Boccara, Kate Grieve, and Pedro Mecê. *Adaptive glasses wavefront sensorless Full-Field OCT for high-resolution in vivo retinal imaging over a wide field-of-view.* In ECBO 2021 Advances in Eye Imaging, Online, June 2021. Optical Society of America.

Appendix E

Résumé en Français

E.1 Introduction

L'œil est un échantillon facilement accessible du corps humain grâce à sa transparence. Ces dernières années, de nombreuses techniques ont été développées pour étudier l'œil humain de différentes manières.

La façon la plus simple est d'étudier des yeux *ex vivo*, provenant de différentes espèces telles que humain, porc, singe, souris, etc. De nos jours, les études sur les yeux humains réalisées à l'Institut de la Vision utilisent des yeux prélevés aux Etats-Unis. Certains échantillons arrivent fixés afin de résister au transport. Afin d'étudier des échantillons vivants, les autres espèces sont utilisées.

Les échantillons *in vitro* (i.e. les cultures cellulaires) sont une autre possibilité. La première méthode de culture cellulaire a été développée au XIXme siècle par Wilhelm Roux [1]. La culture cellulaire a évolué au fil des siècles et est maintenant inhérente à la biologie. Aujourd'hui, il est possible de cultiver des cellules en 2D afin d'étudier certains types cellulaires comme une couche spécifique de la rétine (par exemple l'épithelium pigmentaire rétinien). Cependant, les cultures cellulaires 2D ne reflètent pas vraiment la réalité observable *in vivo* [2, 3], par exemple pour la compréhension de structures spécifiques comme les tumeurs: les sphéroïdes [4] (cultures 3D) permettent d'y remédier. Les biologistes avaient toujours besoin de cultures cellulaires capables de mimer des organes, c'est-à-dire avec une fonction et une structure similaires [5] appelé organoïde. Pour cela, il faut utiliser des cellules souches capables de se différencier en l'organe d'intérêt, mais cela pose des problèmes éthiques. Takahashi et al. ont donc trouvé une alternative: l'utilisation de cellules reprogrammées en cellules souches pluripotentes [6, 7], qui ne peuvent se différencier qu'en certains organes. Différents protocoles ont été développés pour générer ces cellules [8, 9]. L'utilisation des cellules pluripotentes est une technique facile [10] et très prometteuse pour générer des échantillons *in vitro* [11, 12], par exemple pour la modélisation de maladies ou la recherche de traitements. Ce genre d'échantillons peut être cultivé pour créer des organoïdes de rétine à l'Institut de la Vision [13, 14].

La dernière possibilité est d'imager l'œil *in vivo*. La rétine peut être imagée grâce à la transparence de la cornée et du cristallin. Cependant, la rétine étant elle-même transparente, son imagerie n'est pas directe et facile. Pour cela, de nombreuses techniques d'imagerie non invasives ont été développées, en voici quelques exemples. La première technique était le fond d'œil, mais cela ne révèle que le flux sanguin. Il a fallu attendre les années 1980 pour obtenir une meilleure résolution et un meilleur contraste grâce au Ophtalmoscope Laser à balayage [15] qui permet d'imager les couches de la rétine grâce au sectionnement optique. On peut aussi penser à la Tomographie en Cohérence Optique [17, 53], une technique qui permet de scanner la rétine afin d'imager les différentes couches en sections verticales. En 1994, Liang et al. [18] a importé l'optique adaptative

depuis l'astronomie pour corriger les aberrations de l'œil afin d'imager des cellules individuelles en Ophtalmoscopie à illumination plein champ (Flood illumination en anglais) [19]. En 2002, Roorda et al. ont amélioré l'Ophtalmoscope Laser à balayage qui pâtit des aberrations optiques venant de la cornée et du cristallin pour l'imagerie de la rétine. En ajoutant de l'optique adaptative à l'Ophtalmoscope Laser à balayage [20], ils ont corrigé les aberrations optiques pour obtenir une meilleure résolution lors de l'imagerie de la rétine. Plus récemment, une Caméra rétinienne à illumination plein champ (Flood-illumination Retinal Camera) utilisant l'optique adaptative [21] a été développée par une entreprise française, permettant de détecter et surveiller des photorecepteurs individuellement.

Habituellement, les techniques microscopiques permettent d'étudier les échantillons *ex vivo* et *in vitro*. Afin d'imager des structures spécifiques, des organelles ou des protéines, les échantillons sont fixés et labelisés en immunohistochimie, qui est une technique invasive. Il est donc devenu impératif de trouver une technique permettant de caractériser les échantillons de manière non invasive, afin de suivre des processus biologiques. La Tomographie en Cohérence Optique a été conçue initialement pour l'imagerie 3D *in vivo*. A la fin des années 1990, une version *en face* de cette technique a été développée par l'équipe de Claude Boccara: la Tomographie en Cohérence Optique plein champ. L'avantage de cette technique est son utilisation possible à la fois pour la microscopie (*ex vivo* et *in vitro*), et pour l'imagerie de l'œil *in vivo*.

Ce manuscrit est divisé en cinq chapitres. Le premier chapitre présente les intérêts d'étudier l'œil humain. Les différentes parties de l'œil sont décrites afin de comprendre son fonctionnement et les différentes interactions entre les structures. Ensuite, le rôle de l'épithelium pigmentaire rétinien, la dernière couche de la rétine qui est étudiée dans le quatrième chapitre, est présenté en détails. Quelques maladies rétiniennes sont présentées, que ce soit des maladies dégénératives ou venant du nerf optique. Finalement, je décris les cultures cellulaires utilisées dans cette thèse pour mimer l'œil.

Le deuxième chapitre introduit l'imagerie 3D d'échantillons biologiques avec différentes techniques. L'implémentation de la Tomographie en Cohérence Optique est ensuite présentée ainsi que l'origine de sa conception. Les trois différentes formes de cette technique (domaine temporel, domaine spectral, source accordable) sont décrites avec leurs caractéristiques. J'introduis ensuite la version *en face*: la Tomographie en Cohérence Optique plein champ. L'évolution du montage est montrée à travers les différentes modalités d'imagerie et leurs caractéristiques. Je présente finalement l'imagerie dynamique qui acquiert les mouvements intracellulaires. Ce chapitre est basé sur l'article de Scholler et al., 2019 [22].

Le troisième chapitre décrit les résultats obtenus sur des organoïdes de rétines, travail réalisé en collaboration avec Jules Scholler doctorant à l'Institut Langevin. J'y présente les améliorations apportées aux acquisitions. La stabilisation des acquisitions temporelles afin d'imager toujours le même plan, ainsi que le codage des images en HSV pour une meilleure interprétation des images dynamique sont décrits dans les deux premières parties. Enfin, j'expose l'évolution de la preuve de concept de l'imagerie dynamique. Ces résultats s'appuient sur la publication Scholler, Groux et al., 2020 [23].

Le quatrième chapitre démontre l'utilisation de l'OCT plein champ dynamique pour la détection du stress cellulaire sur des cultures de cellules. Je présente la réalisation de stress sur les cultures cellulaires dont la dynamique est ensuite étudiée à l'aide d'un code Matlab que j'ai développé [24]: SAVE (Scratch Assay Velocity Evolution) Profiler. Je décris ensuite mes dernières avancées sur la compréhension et la validation du signal dynamique (inhibiteurs et immunohistochimie). Afin de créer un stress plus répétable et contrôlé sur les cultures cellulaires, j'ai conçu un nouveau montage combiné à un laser

afin de créer un courpure dans la couche cellulaire. Finalement, je présente l'imagerie de microvillosités sur l'épithelium pigmentaire rétinien (présentes à la surface apicale des cellules), à l'aide d'une imagerie temps-réel implémentée auparavant sur les organoïdes de rétine.

Le dernier chapitre s'attache à l'imagerie *in vivo* de la rétine, un travail réalisé en collaboration avec Pedro Mecê, post-doctorant à l'Institut Langevin. Je décris les différentes améliorations du montage, avec l'espoir de pouvoir faire de l'imagerie dynamique un jour. Les mouvements physiologiques de l'œil sont stabilisés par l'utilisation d'un SD-OCT. Nous avons aussi corrigé la courbure de la fenêtre de cohérence de l'OCT plein champ pour coïncider avec la courbure de la rétine. Le signal a été amélioré en plaçant une lentille adaptative devant l'œil du patient. Enfin, je montre l'intérêt que pourrait avoir l'imagerie dynamique *in vivo* pour les maladies rétiniennes.

En annexe se trouvent d'autres articles expliquant les améliorations faites au montage OCT plein champ pour l'imagerie *in vivo*. La conception pas à pas d'un OCT plein champ est décrite en annexe également.

E.2   Chapitre 1: structure et maladies de l'œil

L'œil est composé de trois parties le segment antérieur, l'humeur vitreuse et le segment postérieur.

Le segment antérieur (Fig.1.1 a.) permet de focaliser la lumière sur la rétine [25, 26]. Il est composé de la cornée, l'humeur aqueuse et le cristallin. La cornée est soumise à l'environnement extérieur et sert donc de barrière au reste de l'œil. Elle doit être entièrement transparente afin de laisser passer la lumière. La cornée possède deux courbures, participant ainsi à la focalisation de la lumière sur la rétine. L'humeur aqueuse quant à elle, permet de maintenir la forme de l'œil grâce à la pression oculaire. Elle apporte les nutriments nécessaires à la cornée et le cristallin. Le cristallin focalise la lumière sur la rétine. en changeant de forme, elle change la distance focale de l'œil, ce phénomène est connu sous le nom d'accomodation. La cataracte et la presbytie sont des maladies du cristallin.

L'humeur vitreuse constitue 80% de l'œil. [25, 26]. Elle est entièrement transparente et maintient la forme sphérique de l'œil. En vieillissant, l'humeur vitreuse peut changer et entraîner des troubles de la vision, voire même des détachements de la rétine dans les cas les plus extrêmes.

Le segment postérieur est constitué de la rétine et de la choroïde [26–28]. On peut différencier la rétine en deux parties. La rétine neurale (Fig.1.1 b.) est composée de sept couches allant de la couche de fibres nerveuses aux segments externes des photorecepteurs, qui sont connectés à l'épithélium pigmentaire rétinien. L'épithélium pigmentaire rétinien (RPE) est une monocouche de cellules hexagonales séparant la rétine neurale (sensible à la lumière) de l'apport sanguin, composé de la membrane de Bruch et de la choroïde [29, 30]. Les cellules de RPE ont un noyau basal, de nombreuses organelles et des granules de mélanine. La surface basale étant connectée à la membrane de Bruch, elle permet l'absorption des nutriments nécessaires à l'approvisionnement du RPE et de la rétine neurale. La surface apicale des cellules est composée de microvillosités [31] permettant à la fois de maintenir une connection avec les segments externes et d'effectuer le transport trans-épithélial. Le RPE joue plusieurs rôles [29, 32]. Il permet de protéger la rétine neurale de la lumière (absorption grâce à la mélanine) et des radicaux libres qui peuvent l'endommager par oxydation. Le RPE phagocyte les segments externes trop vieux (> 10 jours) pour renouveler la rétine. Il sert également de transporteur, aen apportant les nutriments de la choroïde vers la rétine neurale, et en évacuant les déchets de la rétine

vers le sang.

Le segment postérieur de l'œil peut être touché par de nombreuses maladies rétiniennes et neuropathies optiques, telles que la Dégénérescence Maculaire Liée à l'Âge [33], la rétinite pigmentaire [39], la rétinopathie diabétique [40] ou encore le glaucome [42] ou les névrites optiques [43].

E.3 Chapitre 2: imagerie 3D d'échantillons biologiques, de la structure à l'activité intracellulaire

Depuis la création de la microscopie, il y a un besoin crucial de pouvoir imager les échantillons biologiques en 3D [47].

La technique classique pour étudier un échantillon biologique en 3D est l'histopathologie. Cette technique invasive et exogène ne permet pas d'étudier d'échantillons vivants. La résolution est limitée par les caractéristiques du microscope. Avec l'invention de la microscopie confocale [49], l'imagerie 3D a été simplifiée en éliminant l'étape de découpe de l'échantillon, mais reste une technique invasive car utilisant la fluorescence. Par ailleurs l'imagerie par ultrasons [51] est utilisée *in vivo* car non invasive. Une onde est envoyée et le signal renvoyé par les différentes structures de l'échantillon est enregistré avec une résolution de 10 à 100 μm sur une profondeur de quelques centimètres. De la combinaison entre ces deux techniques est né l'OCT, alliant l'aspect non invasif des ultrasons et la résolution de la microscopie (Fig.2.1).

La Tomographie en Cohérence Optique (OCT) consiste à envoyer une onde lumineuse et enregistré la lumière rétro-diffusée par l'échantillon [52]. L'OCT allie haute résolution et imagerie 3D pour révéler la structure d'un échantillon à une échelle microscopique. La technique a été démontrée pour la première fois en 1988 par Fercher et al. [53], et son utilisation en imagerie sur des échantillons *ex vivo* en 1991 par Huang et al. [54]. Son utilisation *in vivo* sur la rétine a été présentée en 1993 par deux groupes indépendants [16,17]. Cette technique est basée sur l'interférométrie de Michelson, plusieurs modalités d'imageries sont possibles (1 scans, B scans et C scans) pour reconstruire des volumes (Fig.2.2). Il existe deux types d'OCT: le "Time Domain OCT", basé sur l'étude temporelle du signal en modifiant la longueur du bras de référence pour scanner l'échantillon en profondeur, et le "Fourier Domain OCT", qui permet d'imager l'échantillon à différentes profondeurs en utilisant différentes longueurs d'ondes (i.e. une étude fréquentielle du signal).

En 1998, une variante de l'OCT a été développée par l'équipe de Claude Boccara: l'OCT plein champ, qui est une version *en face* de l'OCT "Time domain", permettant d'acquérir une image *en face* à une profondeur donnée sans scanner l'échantillon latéralement [55]. Ceci est rendu possible par une configuration interféromètre de Linnik (avec des objectifs de microcsope dans chaque bras) et une caméra 2D. Au fil des années [56,57], le système a évolué pour atteindre de meilleures résolutions axiales dont l'équation générale est donnée par l'équation E.1a (eq.E.1 pour une petite ouverture numérique et une haute ouverture numérique respectivement) et transverse (eq.E.2).

$$\Delta z = \frac{1}{\sqrt{\left(\frac{n\pi}{2ln2l_c}\right)^2 + \left(\frac{NA^2}{n\lambda}\right)^2}} \tag{E.1a}$$

$$\Delta z = \frac{l_c}{2n\sqrt{(2)}} \tag{E.1b}$$

$$\Delta z = \frac{0,44\lambda}{n(1-cos(\theta_{max}))} \sim \frac{0,44\lambda}{n(1-cos(arcsin(\frac{NA}{n})))} \tag{E.1c}$$

$$\Delta r = 0,61 \times \frac{\lambda}{NA} \qquad \text{(E.2)}$$

L'OCT plein champ est une technique interférométrique, chaque image comportant une partie de signal cohérent et une partie incohérente. Pour isoler lapartie cohérente du signal, on peut utiliser de l'imagerie 2 phases (où amplitude et phase sont mélangées) et l'imagerie 4 phases (où l'on peut dissocier amplitude et phase). L'OCT plein champ se révèle être une technique appropriée pour l'imagerie d'échantillons biologiques (e.g. yeux *ex vivo* et *in vivo*) [62–66].

Plus récemment, un nouveau contraste a été découvert en utilisant l'OCT plein champ, révélant des variations temporelles causées par le mouvement des organelles contenues dans les cellules de l'échantillon biologique [67]. Cette technique est appelée OCT plein champ dynamique. Pour obtenir une image dynamique, plusieurs centaines d'images sont enregistrées à 100Hz dans le même plan de l'échantillon. Une analyse de Fourier est ensuite effectuée et les différentes fréquences obtenues sont codées en RGB (de 0.1 à 0.5 Hz pour le bleu, de 0.5 à 5 Hz pour le vert et supérieur à 5 Hz pour le rouge) pour obtenir une image dynamique en couleurs [68,69]. Pour plus de stabilité, j'ai conçu deux systèmes: un système pour les échantillons *ex vivo* et un système pour les échantillons *in vitro* (Fig.2.6).

Cette partie s'appuie sur l'article présenté dans la partie 2.5 [22].

E.4 Chapitre 3: une imagerie 3D et temporelle robuste, application aux organoïdes de rétine

L'OCT plein champ étant une technique interférométrique, il est possible d'imager des échantillons en 3D grâce au sectionnement optique. Il est possible d'acquérir des images dans des plans de l'échantillon (découpe virtuelle de l'échantillon). Plus le plan d'acquisition est profond, plus le signal rétrodiffusé est atténué par les plans situés au-dessus. Nous avons évalué la profondeur maximale d'imagerie en OCT plein champ dynamique pour des échantillons transparents à $200\mu m$ (e.g. cultures de cellules 3D) et $80\mu m$ pour des échantillons non transparents (e.g. échantillons *ex vivo* de foie). Les acquisitions 3D sont effectués à l'aide d'un moteur Zaber avec une précision sub-micrométrique. Pendant des acquisitions sur plusieurs heures, il est possible que l'échantillon dérive légèrement, par exemple à cause de l'évaporation du milieu d'imagerie ou un échantillon avec des différences de densité. Pour éviter ces dérives, nous avons développé un code de stabilisation, basé sur l'autocorrélation entre deux images d'OCT plein champ statique, l'une prise au début de l'acquisition, l'autre quelques minutes plus tard. Si le facteur d'autocorrélation est élevé, l'acquisition continue, sinon un stack 3D est effectué afin de trouver le plan le plus ressemblant à celui de départ.

Pour obtenir une meilleure continuité dans les images dynamiques tout au long des acquisitions, nous avons changé la manière de coder les images. Les images sont à présent codées en HSV: Hue (couleur), Saturation, Value (intensité). Ce code couleur est orthogonal (chaque canal est indépendant), permettant ainsi d'implémenter différents paramètres physiques dans chaque canal. Pour cela, 512 images sont acquises dans le même plan et une analyse du spectre de puissance est réalisée. La fréquence moyenne code pour la couleur (Hue): bleu pour une faible fréquence et rouge pour une haute fréquence, en passant par le vert. La saturation est représentée par l'inverse de la bande de fréquences: une fine bande de fréquences donnera une couleur vive, contre une couleur grisâtre pour une large bande de fréquences. Finalement, la Value est codée par une déviation standard calculée sur des piles de 50 images en utilisant une fenêtre glissante de 16 images, ce qui permet un bon compromis entre temps de calcul et le contraste visuel de l'image.

L'OCT plein champ est une nouvelle technique d'imagerie 3D non invasive permettant de distinguer des cellules par leur comportement intracellulaire. Elle ne requiert aucune préparation de l'échantillon (pas de découpe de l'échantillon, pas d'agents fluorescents) contrairement aux autres techniques utilisées habituellement pour des échantillons 3D biologiques [70]. Par exemple, l'imagerie à contraste de phase est non invasive mais ne possède pas de sectionnement optique. Quant aux imageries de fluorescence, elles nécessitent souvent des marquages exogènes. Pour prouver l'utilité du contraste dynamique, nous avons comparé nos images à la technique de référence en biologie: l'imagerie de fluorescence. En 2017, Thouvenin et al. [71, 72] ont présenté un OCT plein champ couplé à une fluorescence plein champ: en testant des échantillons biologiques vivants labelisés avec des molécules fluorescentes, il a été démontré que l'OCT plein champ dynamique montre des processus biologiques. En 2019 [22], nous avons démontré que l'OCT plein champ dynamique permet de distinguer cellules vivantes, mourantes ou mortes. En 2020 [23], nous avons été plus loin dans le compréhension de l'OCT plein champ dynamique: une cellule mourante apparaît avec une sur-activation des organelles, montrant un profil dynamique rouge et intense. Nous avons également montré que dans les organoïdes de rétine, il est possible de distinguer les photorécepteurs uniquement par leur profil dynamique.

L'OCT plein champ dynamique présente donc un contraste totalement non invasif, permettant de différencier les types cellulaires, ce qui se révèle très utile en biologie.

E.5   Chapitre 4: détection de stress cellulaire par OCT plein champ dynamique

La rétine est touchée par de nombreuses maladies dégénératives, dont certaines commençant dans le RPE. Afin de modéliser une maladie dégénérative, nous voulions créer un stress dans une couche de RPE. J'ai créé un trou dans la couche cellulaire d'une culture de RPE à l'aide d'un scalpel, afin d'étudier le comportement des cellules à la suite d'un stress. Grâce à ce stress "physique", nous pouvons différencier les cellules "normales" (loin de la blessure) et les cellules "stressées" (proche de la blessure). Habituellement, deux paramètres sont étudiés: la taille et l'aire de la blessure. En calculant la taille de la blessure, on peut déterminer la vitesse de fermeture. L'évolution de l'aire permet de calculer le pourcentage de fermeture de la blessure tout au long de l'acquisition. J'ai développé un code Matlab afin d'analyser ces résultats, appelé SAVE Profiler (scratch Assay Velocity Evolution), réalisant une segmentation semi-automatique de la blessure. La pile d'images en niveaux de gris est transformée en images binaires (blessure (0), cellules (1)) à l'aide d'un seuil d'intensité déterminé par l'utilisateur. La direction de la blessure est localisée par l'utilisateur afin que le logiciel pivote les images pour placer la blessure verticalement sur les images. L'utilisateur dessine approximativement le contour de la blessure, sur la première image si la blessure se referme, sur la dernière image sinon. Ceci permet d'éviter le bruit venant des interstices entre les cellules loin de la blessure. Finalement, le logiciel calcule les paramètres décrits ci-dessus. Pour valider le calcul de la vitesse, nous avons utilisé la méthode de flux optique de Matlab [22]: les résultats obtenus étaient très similaires. Pour les calculs du pourcentage de fermeture de la blessure, nous avons utilisé le logiciel Cell Profiler [73]. Ce logiciel est plus lent que notre code et moins efficace: le logiciel ne parvient pas à gérer les fluctuations d'intensité parfois visibles dans les images dynamiques (Fig.4.1). Enfin, j'ai évalué la segmentation de notre code à l'aide d'une segmentation manuelle et le reste des calculs a été effectué avec notre code. Le processus s'est révélé lent pour obtenir des résultats similaires (Fig.4.3). Le SAVE Profiler permettra d'étudier des modèles de maladies dégénératives en analysant des images dynamiques pour une meilleure compréhension des maladies et tester de nouveaux médicaments.

L'utilité de l'OCT plein champ dynamique a été démontrée plusieurs fois depuis

2016 [67], grâce notamment à des validations par fluorescence [22, 23, 71]. Cependant, l'origine du signal dynamique n'avait encore jamais été démontrée. Les images dynamiques permettent de visualiser des mouvements intracellulaires que nous appelons profil dynamique. Dans une cellule, de multiples organelles contribuent à la survie de la cellule. Notre première approche était d'inhiber différentes organelles sur des cultures de cellules afin d'évaluer leur participation dans le profil dynamique. Deux organelles principales ont été ciblées: les mitochondries et les vésicules, pour lesquelles la CCCP et la Bréfeldine A sont respectivement des inhibiteurs. Habituellement, ces molécules sont utilisées sur des fibroblastes. Malheureusement, ces cellules étant très plates, elles créent des artefacts (franges) comme un miroir. Nous avons donc essayé sur des cultures de RPE, mais les résultats n'ont pas été concluants. La façon la plus simple de valider notre technique est de la comparer à l'imagerie par fluorescence. Cependant, combiner OCT plein champ et fluorescence n'est pas chose aisée. Nous avons donc décidé d'utiliser à la fois un OCT plein champ et un microscope confocal en fluorescence pour comparer les images obtenues [24]. Les supports de culture étant différents pour les deux techniques, nous avons utilisé des cultures parallèles. Afin de distinguer des variations dans le mouvement des organelles, le stress induit par le scalpel permet de différencier aisément deux comportements cellulaires normal ou stressé (phénotype), comme nous l'avons observé sur les images dynamiques. Le phénotype étant gouverné par les organelles, plusieurs organelles et phénotypes ont été testés:

- les mitochondries, en utilisant deux molécules fluorescentes: mCoxIV et ATP synthase

- les noyaux avec le DAPI

- les filaments d'actine avec la phalloidine

- les lysosomes: LAMP1 et CATSD

- l'appareil de Golgi: TGN46

- les cellules mourantes, labellisées avec l'iodure de propidium

L'appareil de Golgi semble contribuer équitablement au signal dynamique entre cellules stressées et normales. Les lysosomes contribuent au signal pour les cellules mourantes. Finalement, l'organisation des mitochondries est clairement différente entre cellules stressées et normales, passant d'un réseau à des mitochondries individuelles. Les mitochondries semblent donc être le contributeur principal du profil dynamique des cellules.

Afin de générer un modèle de maladie dégénérative plus précis et répétable, j'ai imaginé un montage combinant OCT plein champ et un laser pour découper la culture cellulaire. Pour cela, nous avons utilisé un laser créé pour l'enseignement des Travaux Pratiques de l'ESPCI centré à 805nm, ainsi que des miroirs galvanométriques Thorlabs (GVS102) conjugués avec le plan focal arrière des objectifs de microscope (immersion à eau UMPLFLN10XW, Olympus) de l'OCT plein champ (voir annexe A pour la construction de la partie OCT plein champ). Malheureusement, plusieurs problèmes se sont posés. Le faisceau du laser étant trop divergent (montage du laser non optimisé), j'ai essayé de le collimater, sans véritable succès. Les objectifs de microscope utilisés donnent une résolution axiale trop grande pour l'imagerie d'une culture de cellules. Nous avons donc essayé des objectifs sans milieu d'immersion, mais ils ne convenaient pas au support de culture. Les pistes d'amélioration consitent en l'utilisation d'un meilleur laser ainsi que des objectifs de microscope similaires à ceux de notre montage pour les cultures cellulaires.

Nous avons aussi montré la possibilité d'imager en temps réel grâce à Holovibes, un logiciel pour l'holographie créé dans notre laboratoire par l'équipe de Michael Atlan [78].

Habituellement, les microvillosités des RPE sont imagés en contraste de phase, immuno-histochimie et microscopie électronique, ce qui ne permet pas de l'imagerie en temps réel [25, 30, 31, 79]. A notre connaissance, c'est la première fois dans la littérature que le mouvement des microvillosités est imagé en temps réel. Les perspectives d'utilisation sont multiples: ajout de macrophages ou de segments externes de photorécepteurs sur les microvillosités par exemple.

E.6 Chapitre 5: vers une imagerie dynamique *in vivo* de la rétine par OCT plein champ

L'œil est soumis à de multiples mouvements physiologiques: la respiration, la pulsation cardiaque, les saccades oculaires dues à la fixation. Les deux premières causes décrivent des mouvements sinusoïdaux à basse fréquence [82, 83]. Au contraire, les saccades de l'œil sont plus difficiles à prédire: elles dépendent de la personne et du temps [84], créant des aberrations et des pertes de signal. Même si l'OCT plein champ est peu sensible aux aberrations [85, 86], la cohérence se perd entre l'œil et le miroir de référence. Il est donc nécessaire de pouvoir garder le plan d'intérêt dans la fenêtre de cohérence pendant l'imagerie: c'est possible en réalisant une stabilisation axiale à l'aide d'un SD-OCT. Ce dernier permet de traquer la rétine afin d'ajuster la longueur du bras de référence en temps réel [87] (système également implémenté pour l'imagerie de la cornée [88]).

L'œil est un organe sphérique présentant différentes courbures pour la cornée [89] et la rétine. Récemment, un OCT plein champ courbé a été développé par Mazlin et al. [90], permettant de courber le miroir de référence à l'aide de lentilles pour le faire coïncider avec la cornée (obtenant ainsi des images plein champ de chaque couche). Contrairement à la cornée, la rétine possède la même courbure pour toutes ses couches. Pour l'imagerie de la rétine, la symétrie de l'OCT plein champ n'existe plus: l'objectif de microscope dans le bras de référence est légèrement différent de l'œil [81, 87], introduisant une différence de courbure entre la rétine et la fenêtre de cohérence (Fig.5.1). Afin de compenser cette différence, nous avons introduit une lame de verre N-BK7 de 20mm d'épaisseur dans le bras échantillon [91].

La rétine est conçue pour transmettre la lumière et non la réfléchir, rendant le signal rétrodiffusé très faible. Il était donc important de maximiser ce signal. Habituellement, de l'optique adaptative est utilisée, rendant le système complexe et difficile à aligner et utiliser. Nous avons donc proposé l'utilisation d'une lentille adaptative positionnée juste devant l'œil du patient (Fig.5.2). Celle-ci permet d'augmenter le signal et le contraste en réduisant les aberrations de premier ordre [92]. Elle permet également de mieux traquer la rétine lors des acquisitions.

Nous avons récemment montré l'utilité de l'OCT plein champ dynamique pour l'imagerie d'échantillons *in vitro*. Les cultures de cellules montrent des signaux dynamiques très intenses et diverses, dépendant du type cellulaire mais aussi de leur phénotype [23, 24], très prometteur pour les maladies de l'œil *in vivo*. Grâce à notre montage adapté aux échantillons *ex vivo*, nous avons pu imager des rétines *ex vivo* de différentes espèces (souris, singe, humain) (Fig.5.3). La prochaine étape est donc d'implémenter l'imagerie OCT plein champ dynamique *in vivo*, mais il reste des limitations. On pense notamment aux aberrations de l'œil [85, 86] ou aux mouvements physiologiques de l'œil [94] qui peuvent créer de forts changements de phase pour les acquisitions de 1ms. Des corrections peuvent être appliquées après acquisitions comme la Décomposition en Valeurs singulières [95], mais qui ne fonctionne que si toutes les images sont acquises dans le même plan. Nous réfléchissons encore à la meilleure stratégie à adopter pour atteindre l'imagerie dynamique *in vivo*.

E.7   Conclusion et perspectives

Dans cette thèse, j'ai démontré les possibilités offertes par l'OCT plein champ pour l'imagerie de la rétine, qu'il s'agisse de l'étude de maladies dégénératives dans le cadre de la modélisation de maladies, ou encore pour l'investigation de ces maladies directement *in vivo*. L'œil est un organe complexe facilement accessible par imagerie, affecté par de nombreuses maladies qui nécessitent encore d'être étudiées. J'ai montré que l'OCT plein champ est utile pour la microscopie (*in vitro* et *ex vivo*) ainsi que pour l'imagerie *in vivo*, offrant de nombreuses possibilités pour l'étude de l'œil.

En donnant une information sur la structure des échantillons, l'OCT plein champ peut être un outil intéressant en biologie. Cette technique est non invasive: elle ne nécessite pas de contact, ni de labélisation ni de préparation de l'échantillon, permettant d'étudier des échantillons vivants potentiellement sur plusieurs jours. L'OCT plein champ dynamique présente un contraste intrinsèque innovant révélant l'activité cellulaire, différente selon le type cellulaire ou le phénotype. Nous avons stabilisé les acquisitions et amélioré l'interprétation des images dynamiques en codant les variations en HSV, en appliquant la technique à l'imagerie d'organoïdes de rétine et de RPE. J'ai également développé un code Matlab permettant d'étudier des maladies telles que la DMLA. Tout ceci me conforte dans l'utilité de cette technique pour la modélisation de maladies rétiniennes dégénératives. J'ai également apporté des éléments de réponse sur la compréhension du signal dynamique: les mitochondries semblent être le contributeur principal du signal alors que l'appareil de Golgi semble participer équitablement au signal dans les différents phénotypes. J'ai également montré le développement du montage *in vivo* dans l'optique de faire de l'imagerie dynamique *in vivo* de maladies dégénératives, qui pourront être étudiées auparavant *in vitro*.

Plusieurs perspectives se dessinent pour l'utilisation de l'OCT plein champ. Le suivi d'organoïdes de rétine fait partie du projet OREO grâce à un OCT plein champ combiné à un microscope confocal en fluorescence placé dans un laboratoire de niveau L2 à l'Institut de la Vision pour contrôler l'environnement. L'étude de maladies de l'épithélium pigmentaire rétinien en améliorant le montage avec le laser, en étudiant la phagocytose des segments externes de photorécepteurs par les microvillosités, ou encore l'étude de traitements. On peut aussi envisager l'utilisation de l'apprentissage automatique pour détecter automatiquement les changements de signal dynamique et les interpréter.

List of Figures

List of Tables

Bibliography

[1] Jedrzejczak-Silicka, M. History of Cell Culture. In *New Insights into Cell Culture Technology* (IntechOpen, 2017). URL `https://www.intechopen.com/books/new-insights-into-cell-culture-technology/history-of-cell-culture`.

[2] Cukierman, E., Pankov, R. & Yamada, K. M. Cell interactions with three-dimensional matrices. *Current Opinion in Cell Biology* **14**, 633–640 (2002). URL `https://www.sciencedirect.com/science/article/pii/S0955067402003642`.

[3] Dhaliwal, A. Three Dimensional Cell Culture : A Review. *Materials and Methods* **2** (2012). URL `http://www.labome.com/method/Three-Dimensional-Cell-Culture-A-Review.html`.

[4] Acker, H., Carlsson, J., Durand, R. & Sutherland, R. M. (eds.) *Spheroids in Cancer Research: Methods and Perspectives.* Recent Results in Cancer Research (Springer-Verlag, Berlin Heidelberg, 1984). URL `https://www.springer.com/gp/book/9783642823428`.

[5] Abbott, A. Biology's new dimension. *Nature* **424**, 870–872 (2003). URL `https://www.nature.com/articles/424870a`. Bandiera_abtest: a Cg_type: Nature Research Journals Number: 6951 Primary_atype: News Publisher: Nature Publishing Group.

[6] Takahashi, K. & Yamanaka, S. Induction of Pluripotent Stem Cells from Mouse Embryonic and Adult Fibroblast Cultures by Defined Factors. *Cell* **126**, 663–676 (2006). URL `https://www.sciencedirect.com/science/article/pii/S0092867406009767`.

[7] Takahashi, K. *et al.* Induction of Pluripotent Stem Cells from Adult Human Fibroblasts by Defined Factors. *Cell* **131**, 861–872 (2007). URL `https://www.sciencedirect.com/science/article/pii/S0092867407014717`.

[8] Maherali, N. & Hochedlinger, K. Guidelines and Techniques for the Generation of Induced Pluripotent Stem Cells. *Cell Stem Cell* **3**, 595–605 (2008). URL `https://www.sciencedirect.com/science/article/pii/S1934590908005791`.

[9] Park, I.-H., Lerou, P. H., Zhao, R., Huo, H. & Daley, G. Q. Generation of human-induced pluripotent stem cells. *Nature Protocols* **3**, 1180–1186 (2008). URL `https://www.nature.com/articles/nprot.2008.92`. Bandiera_abtest: a Cg_type: Nature Research Journals Number: 7 Primary_atype: Protocols Publisher: Nature Publishing Group.

[10] Foty, R. A Simple Hanging Drop Cell Culture Protocol for Generation of 3D Spheroids. *Journal of Visualized Experiments : JoVE* 2720 (2011). URL `https://www.ncbi.nlm.nih.gov/pmc/articles/PMC3197119/`.

[11] Robinton, D. A. & Daley, G. Q. The promise of induced pluripotent stem cells in research and therapy. *Nature* **481**, 295–305 (2012). URL `https://www.nature.com/articles/nature10761`. Bandiera_abtest: a Cg_type: Nature Research Journals Number: 7381 Primary_atype: Reviews Publisher: Nature Publishing Group Subject_term: Induced pluripotent stem cells;Pluripotency;Reprogramming;Stem-cell therapies Subject_term_id: induced-pluripotent-stem-cells;pluripotency;reprogramming;stem-cell-therapies.

[12] Yamanaka, S. Induced Pluripotent Stem Cells: Past, Present, and Future. *Cell Stem Cell* **10**, 678–684 (2012). URL `https://www.sciencedirect.com/science/article/pii/S1934590912002378`.

[13] Reichman, S. *et al.* From confluent human iPS cells to self-forming neural retina and retinal pigmented epithelium. *Proceedings of the National Academy of Sciences* **111**, 8518–8523 (2014).

[14] Reichman, S. *et al.* Generation of Storable Retinal Organoids and Retinal Pigmented Epithelium from Adherent Human iPS Cells in Xeno-Free and Feeder-Free Conditions. *Stem Cells* **35**, 1176–1188 (2017). URL `https://hal.sorbonne-universite.fr/hal-01480587`.

[15] Webb, R. H. & Hughes, G. W. Scanning Laser Ophthalmoscope. *IEEE Transactions on Biomedical Engineering* **BME-28**, 488–492 (1981).

[16] Fercher, A. F. In vivo optical coherence tomography in ophthalmology. In *Medical Optical Tomography: Functional Imaging and Monitoring*, vol. 10311, 103110L (International Society for Optics and Photonics, 1993). URL `https://www.spiedigitallibrary.org/conference-proceedings-of-spie/10311/103110L/In-vivo-optical-coherence-tomography-in-ophthalmology/10.1117/12.2283766.short`.

[17] Swanson, E. A. *et al.* In vivo retinal imaging by optical coherence tomography. *Optics Letters* **18**, 1864–1866 (1993). URL `https://www.osapublishing.org/ol/abstract.cfm?uri=ol-18-21-1864`. Publisher: Optical Society of America.

[18] Liang, J., Grimm, B., Goelz, S. & Bille, J. F. Objective measurement of wave aberrations of the human eye with the use of a Hartmann–Shack wave-front sensor. *JOSA A* **11**, 1949–1957 (1994). URL `https://www.osapublishing.org/josaa/abstract.cfm?uri=josaa-11-7-1949`. Publisher: Optical Society of America.

[19] Liang, J., Williams, D. R. & Miller, D. T. Supernormal vision and high-resolution retinal imaging through adaptive optics. *JOSA A* **14**, 2884–2892 (1997). URL `https://www.osapublishing.org/josaa/abstract.cfm?uri=josaa-14-11-2884`. Publisher: Optical Society of America.

[20] Roorda, A. *et al.* Adaptive optics scanning laser ophthalmoscopy. *Optics Express* **10**, 405–412 (2002). URL `https://www.osapublishing.org/oe/abstract.cfm?uri=oe-10-9-405`. Publisher: Optical Society of America.

[21] Viard, C. *et al.* Imaging microscopic structures in pathological retinas using flood-illumination adaptive optics retinal camera. In *Ophthalmic Technologies XXI*, vol. 11630, 788509 (International Society for Optics and Photonics, 2011). URL `https://www.spiedigitallibrary.org/conference-proceedings-of-spie/7885/788509/Imaging-microscopic-structures-in-pathological-retinas-using-a-flood-illumination/10.1117/12.874766.short`.

[22] Scholler, J. *et al.* Probing dynamic processes in the eye at multiple spatial and temporal scales with multimodal full field OCT. *Biomedical Optics Express* **10**, 731–746 (2019). URL `https://www.osapublishing.org/boe/fulltext.cfm?uri=boe-10-2-731&id=404178`.

[23] Scholler, J. *et al.* Dynamic full-field optical coherence tomography: 3D live-imaging of retinal organoids. *Light: Science & Applications* **9**, 140 (2020). URL `https://www.nature.com/articles/s41377-020-00375-8`. Number: 1 Publisher: Nature Publishing Group.

[24] Groux, K. *et al.* Non invasive live imaging of a novel retinal pigment epithelium stress model with Dynamic Full-Field Optical Coherence Tomography. *arXiv:2106.10531 [physics]* (2021). URL `http://arxiv.org/abs/2106.10531`. ArXiv: 2106.10531.

[25] Forrester, J. V., Dick, A. D., McMenamin, P. G., Roberts, F. & Pearlman, E. Chapter 1 - Anatomy of the eye and orbit. In Forrester, J. V., Dick, A. D., McMenamin, P. G., Roberts, F. & Pearlman, E. (eds.) *The Eye (Fourth Edition)*, 1–102.e2 (W.B. Saunders, 2016). URL `http://www.sciencedirect.com/science/article/pii/B9780702055546000010`.

[26] Kolb, H., Nelson, R., Fernandez, E. & Jones, B. (eds.) *Webvision – The Organization of the Retina and Visual System* (2013), webvision edn. URL `https://webvision.med.utah.edu/`.

[27] Webvision: Simple Anatomy of the Retina. URL `http://webvision.umh.es/webvision/sretina.html`.

[28] Carlson, B. M. Chapter 7 - Special Senses—Vision and Hearing. In Carlson, B. M. (ed.) *The Human Body*, 177–207 (Academic Press, 2019). URL `https://www.sciencedirect.com/science/article/pii/B9780128042540000077`.

[29] Boulton, M. & Dayhaw-Barker, P. The role of the retinal pigment epithelium: Topographical variation and ageing changes. *Eye* **15**, 384–389 (2001). URL `http://www.nature.com/articles/eye2001141`.

[30] Strauss, O. The retinal pigment epithelium by Olaf Strauss – Webvision. In *Webvision – The Organization of the Retina and Visual System* (2013), webvision edn. URL `https://webvision.med.utah.edu/book/part-ii-anatomy-and-physiology-of-the-retina/the-retinal-pigment-epithelium/`. Library Catalog: webvision.med.utah.edu.

[31] Bonilha, V. L. *et al.* The Retinal Pigment Epithelium apical microvilli and retinal function. *Advances in experimental medicine and biology* **572**, 519–524 (2006). URL `https://www.ncbi.nlm.nih.gov/pmc/articles/PMC2748829/`.

[32] Sparrow, J., Hicks, D. & Hamel, C. The Retinal Pigment Epithelium in Health and Disease. *Current molecular medicine* **10**, 802–823 (2010). URL `https://www.ncbi.nlm.nih.gov/pmc/articles/PMC4120883/`.

[33] Boyd, K. What Is Macular Degeneration? (2021). URL `https://www.aao.org/eye-health/diseases/amd-macular-degeneration`.

[34] Boyd, K. Detached Retina (2020). URL `https://www.aao.org/eye-health/diseases/detached-torn-retina`.

[35] Gupta, O. P., Shah, V. A., Tripathy, K. & Bhagat, N. Epiretinal Membrane - EyeWiki. URL `https://eyewiki.aao.org/Epiretinal_Membrane`.

[36] Boyd, K. What Is a Macular Hole? What Causes a Macular Hole? (2020). URL `https://www.aao.org/eye-health/diseases/what-is-macular-hole`.

[37] Porter, D. What Is Macular Edema? (2020). URL `https://www.aao.org/eye-health/diseases/what-is-macular-edema`.

[38] Boyd, K. What Is Retinoblastoma? (2020). URL `https://www.aao.org/eye-health/diseases/what-is-retinoblastoma`.

[39] Boyd, K. What Is Retinitis Pigmentosa? (2020). URL `https://www.aao.org/eye-health/diseases/what-is-retinitis-pigmentosa`.

[40] Boyd, K. What Is Diabetic Retinopathy? (2021). URL `https://www.aao.org/eye-health/diseases/what-is-diabetic-retinopathy`.

[41] Porter, D. What Is Usher Syndrome? (2020). URL `https://www.aao.org/eye-health/diseases/what-is-usher-syndrome`.

[42] Boyd, K. What Is Glaucoma? (2021). URL `https://www.aao.org/eye-health/diseases/what-is-glaucoma`.

[43] Boyd, K. What Is Optic Neuritis? (2021). URL `https://www.aao.org/eye-health/diseases/what-is-optic-neuritis`.

[44] Slembrouck-Brec, A., Nanteau, C., Sahel, J.-A., Goureau, O. & Reichman, S. Defined Xeno-free and Feeder-free Culture Conditions for the Generation of Human iPSC-derived Retinal Cell Models. *Journal of Visual Experiments* **139** (2018).

[45] Gagliardi, G. *et al.* Characterization and Transplantation of CD73-Positive Photoreceptors Isolated from Human iPSC-Derived Retinal Organoids. *Stem Cell Reports* **11**, 665–680 (2018). URL `http://www.sciencedirect.com/science/article/pii/S2213671118303102`.

[46] Gagliardi, G., M'Barek, K. B. & Goureau, O. Photoreceptor cell replacement in macular degeneration and retinitis pigmentosa: A pluripotent stem cell-based approach. *Progress in Retinal and Eye Research* **71**, 1 – 25 (2019). URL `http://www.sciencedirect.com/science/article/pii/S1350946218300910`.

[47] Kherlopian, A. R. *et al.* A review of imaging techniques for systems biology. *BMC Systems Biology* **2**, 74 (2008).

[48] Hajdu, S. I. The First Use of the Microscope in Medicine. *Annals of Clinical & Laboratory Science* **32**, 309–310 (2002). URL `http://www.annclinlabsci.org/content/32/3/309`.

[49] Pawley, J. B. *Handbook of biological confocal microscopy* (Springer, 2010), third edition edn. URL `https://books.google.fr/books?id=IKcPnaNPrhoC&printsec=frontcover&hl=fr#v=onepage&q&f=false`.

[50] Yuste, R. Fluorescence microscopy today. *Nature Methods* **2**, 902–904 (2005). URL `https://www.nature.com/articles/nmeth1205-902`.

[51] Fenster, A., Downey, D. B. & Cardinal, H. N. Three-dimensional ultrasound imaging. *Physics in Medicine and Biology* **46**, R67–R99 (2001).

[52] Drexler, W. & Fujimoto, J. G. (eds.) *Optical coherence tomography: technology and applications* (Springer, Cham, 2015), 2. ed edn. OCLC: 919429452.

[53] Fercher, A. F., Mengedoht, K. & Werner, W. Eye-length measurement by interferometry with partially coherent light. *Optics Letters* **13**, 186–188 (1988). URL `https://www.osapublishing.org/ol/abstract.cfm?uri=ol-13-3-186`. Publisher: Optical Society of America.

[54] Huang, D. *et al.* Optical coherence tomography. *Science* **254**, 1178–1181 (1991). URL `https://science.sciencemag.org/content/254/5035/1178`.

[55] Beaurepaire, E., Boccara, A. C., Lebec, M., Blanchot, L. & Saint-Jalmes, H. Full-field optical coherence microscopy. *Optics Letters* **23**, 244–246 (1998). URL `https://www.osapublishing.org/ol/abstract.cfm?uri=ol-23-4-244`.

[56] Dubois, A., Vabre, L., Boccara, A.-C. & Beaurepaire, E. High-resolution full-field optical coherence tomography with a Linnik microscope. *Applied Optics* **41**, 805–812 (2002).

[57] Dubois, A. *et al.* Ultrahigh-resolution full-field optical coherence tomography. *Applied Optics* **43**, 2874–2883 (2004).

[58] Moneron, G., Boccara, C. & Dubois, A. Polarization-sensitive full-field optical coherence tomography. *Optics Letters* **32**, 2058 (2007). URL `https://hal.archives-ouvertes.fr/hal-00520535`.

[59] Federici, A., Costa, H. S. G. d., Ogien, J., Ellerbee, A. K. & Dubois, A. Wide-field, full-field optical coherence microscopy for high-axial-resolution phase and amplitude imaging. *Applied Optics* **54**, 8212–8220 (2015). URL `https://www.osapublishing.org/ao/abstract.cfm?uri=ao-54-27-8212`. Publisher: Optical Society of America.

[60] Auksorius, E., Borycki, D. & Wojtkowski, M. Crosstalk-free volumetric in vivo imaging of a human retina with Fourier-domain full-field optical coherence tomography. *Biomedical Optics Express* **10**, 6390–6407 (2019). URL `https://www.osapublishing.org/boe/abstract.cfm?uri=boe-10-12-6390`. Publisher: Optical Society of America.

[61] Stremplewski, P. *et al.* In vivo volumetric imaging by crosstalk-free full-field OCT. *Optica* **6**, 608–617 (2019). URL `https://www.osapublishing.org/optica/abstract.cfm?uri=optica-6-5-608`. Publisher: Optical Society of America.

[62] Dubois, A., Moneron, G., Grieve, K. & Boccara, A. C. Three-dimensional cellular-level imaging using full-field optical coherence tomography. *Physics in Medicine and Biology* **49**, 1227–1234 (2004). URL `https://doi.org/10.1088/0031-9155/49/7/010`. Publisher: IOP Publishing.

[63] Grieve, K. *et al.* Ocular Tissue Imaging Using Ultrahigh-Resolution, Full-Field Optical Coherence Tomography. *Investigative Ophthalmology & Visual Science* **45**, 4126–4131 (2004). URL `https://iovs.arvojournals.org/article.aspx?articleid=2124464`. Publisher: The Association for Research in Vision and Ophthalmology.

[64] Grieve, K., Moneron, G., Dubois, A., Gargasson, J.-F. L. & Boccara, C. Ultrahigh resolutionex vivoocular imaging using ultrashort acquisition timeen faceoptical coherence tomography. *Journal of Optics A: Pure and Applied Optics* **7**, 368–373 (2005). URL `https://doi.org/10.1088/1464-4258/7/8/003`. Publisher: IOP Publishing.

[65] Grieve, K. *et al.* In vivo anterior segment imaging in the rat eye with high speed white light full-field optical coherence tomography. *Optics Express* **13**, 6286–6295 (2005). URL `https://www.osapublishing.org/oe/abstract.cfm?uri=oe-13-16-6286`. Publisher: Optical Society of America.

[66] Thouvenin, O., Grieve, K., Xiao, P., Apelian, C. & Boccara, C. En face coherence microscopy. *Biomedical Optics Express* **8**, 622 (2017).

[67] Apelian, C., Harms, F., Thouvenin, O. & Boccara, C. Dynamic full field optical coherence tomography: subcellular metabolic contrast revealed in tissues by interferometric signals temporal analysis. *Biomedical Optics Express* **7**, 1511 (2016).

[68] Apelian, C., Gastaud, C. & Boccara, A. C. Extracting relevant information for cancer diagnosis from dynamic full field OCT through image processing and learning. In *Optical Coherence Tomography and Coherence Domain Optical Methods in Biomedicine XXI*, vol. 10053, 100531H (International Society for Optics and Photonics, 2017). URL `https://www.spiedigitallibrary.org/conference-proceedings-of-spie/10053/100531H/Extracting-relevant-information-for-cancer-diagnosis-from-dynamic-full-field/10.1117/12.2254824.short`.

[69] Thouvenin, O. *et al.* Cell motility as contrast agent in retinal explant imaging with full-field optical coherence tomography. *Investigative Ophtalmology & Visual Science* **58**, 4605 (2017).

[70] Browne, A. W. *et al.* Structural and Functional Characterization of Human Stem-Cell-Derived Retinal Organoids by Live Imaging. *Investigative Ophthalmology & Visual Science* **58**, 3311–3318 (2017). URL `https://iovs.arvojournals.org/article.aspx?articleid=2642891`.

[71] Thouvenin, O., Fink, M. & Boccara, A. C. Dynamic multimodal full-field optical coherence tomography and fluorescence structured illumination microscopy. *Journal of Biomedical Optics* **22**, 026004 (2017). URL `https://www.spiedigitallibrary.org/journals/Journal-of-Biomedical-Optics/volume-22/issue-2/026004/Dynamic-multimodal-full-field-optical-coherence-tomography-and-fluorescence-structu/10.1117/1.JBO.22.2.026004.short`.

[72] Thouvenin, O., Apelian, C., Nahas, A., Fink, M. & Boccara, C. Full-Field Optical Coherence Tomography as a Diagnosis Tool: Recent Progress with Multimodal Imaging. *Applied Sciences* **7**, 236 (2017). URL `https://www.mdpi.com/2076-3417/7/3/236`.

[73] Lamprecht, M. R., Sabatini, D. M. & Carpenter, A. E. CellProfiler™: free, versatile software for automated biological image analysis. *BioTechniques* **42**, 71–75 (2007). URL `https://www.future-science.com/doi/10.2144/000112257`. Publisher: Future Science.

[74] Arnoult, D. Mitochondrial fragmentation in apoptosis. *Trends in Cell Biology* **17**, 6–12 (2007). URL `http://www.sciencedirect.com/science/article/pii/S0962892406003072`.

[75] Ahmad, T. *et al.* Computational classification of mitochondrial shapes reflects stress and redox state. *Cell Death & Disease* **4**, e461–e461 (2013). URL `https://www.nature.com/articles/cddis2012213`. Number: 1 Publisher: Nature Publishing Group.

[76] Miyazono, Y. *et al.* Uncoupled mitochondria quickly shorten along their long axis to form indented spheroids, instead of rings, in a fission-independent manner. *Scientific Reports* **8**, 350 (2018). URL https://www.nature.com/articles/s41598-017-18582-6.

[77] AQUYRE Biosciences - LLTech developing biopsy evaluation in two minutes. URL http://www.lltech.co/.

[78] Atlan, M. Holovibes: hologram rendering made easy (2014). URL http://holovibes.com/.

[79] Themes, U. F. O. Cell Biology of the Retinal Pigment Epithelium (2017). URL https://entokey.com/cell-biology-of-the-retinal-pigment-epithelium/.

[80] Mazlin, V. *et al.* In vivo high resolution human corneal imaging using full-field optical coherence tomography. *Biomedical Optics Express* **9**, 557–568 (2018). URL https://www.osapublishing.org/boe/abstract.cfm?uri=boe-9-2-557. Publisher: Optical Society of America.

[81] Xiao, P. *et al.* In vivo high-resolution human retinal imaging with wavefront-correctionless full-field OCT. *Optica* **5**, 409 (2018). URL https://www.osapublishing.org/abstract.cfm?URI=optica-5-4-409.

[82] Kinkelder, R. d. *et al.* Heartbeat-Induced Axial Motion Artifacts in Optical Coherence Tomography Measurements of the Retina. *Investigative Ophthalmology & Visual Science* **52**, 3908–3913 (2011). URL https://iovs.arvojournals.org/article.aspx?articleid=2166200. Publisher: The Association for Research in Vision and Ophthalmology.

[83] Hedley, M. & Yan, H. Motion artifact suppression: A review of post-processing techniques. *Magnetic Resonance Imaging* **10**, 627–635 (1992). URL https://www.sciencedirect.com/science/article/pii/0730725X9290014Q.

[84] Mecê, P. *et al.* Fixational eye movement: a negligible source of dynamic aberration. *Biomedical Optics Express* **9**, 717–727 (2018). URL https://www.osapublishing.org/boe/abstract.cfm?uri=boe-9-2-717. Publisher: Optical Society of America.

[85] Xiao, P., Fink, M. & Boccara, A. C. Full-field spatially incoherent illumination interferometry: a spatial resolution almost insensitive to aberrations. *Optics Letters* **41**, 3920–3923 (2016). URL https://www.osapublishing.org/ol/abstract.cfm?uri=ol-41-17-3920. Publisher: Optical Society of America.

[86] Barolle, V. *et al.* Manifestation of aberrations in full-field optical coherence tomography. *Optics Express* **29**, 22044–22065 (2021). URL https://www.osapublishing.org/oe/abstract.cfm?uri=oe-29-14-22044. Publisher: Optical Society of America.

[87] Mecê, P., Scholler, J., Groux, K. & Boccara, C. High-resolution in-vivo human retinal imaging using full-field OCT with optical stabilization of axial motion. *Biomedical Optics Express* **11**, 492 (2020). URL https://www.osapublishing.org/abstract.cfm?URI=boe-11-1-492.

[88] Mazlin, V. *et al.* Real-time non-contact cellular imaging and angiography of human cornea and limbus with common-path full-field/SD OCT. *Nature Communications* **11**, 1868 (2020). URL https://www.nature.com/articles/s41467-020-15792-x. Bandiera_abtest: a Cc_license_type: cc_by Cg_type:

Nature Research Journals Number: 1 Primary_atype: Research Publisher: Nature Publishing Group Subject_term: Biomedical engineering;Microscopy;Optical imaging;Translational research Subject_term_id: biomedical-engineering;microscopy;optical-imaging;translational-research.

[89] Dubbelman, M., Sicam, V. A. D. P. & Van der Heijde, G. L. The shape of the anterior and posterior surface of the aging human cornea. *Vision Research* **46**, 993–1001 (2006). URL `https://www.sciencedirect.com/science/article/pii/S0042698905004906`.

[90] Mazlin, V. *et al.* Curved-field optical coherence tomography: large-field imaging of human corneal cells and nerves. *Optica* **7**, 872–880 (2020). URL `https://www.osapublishing.org/optica/abstract.cfm?uri=optica-7-8-872`. Publisher: Optical Society of America.

[91] Mecê, P. *et al.* Coherence gate shaping for wide field high-resolution in vivo retinal imaging with full-field OCT. *Biomedical Optics Express* **11**, 4928–4941 (2020). URL `https://www.osapublishing.org/boe/abstract.cfm?uri=boe-11-9-4928`. Publisher: Optical Society of America.

[92] Scholler, J., Groux, K., Grieve, K., Boccara, C. & Mecê, P. Adaptive-glasses time-domain FFOCT for wide-field high-resolution retinal imaging with increased SNR. *Optics Letters* **45**, 5901–5904 (2020). URL `https://www.osapublishing.org/ol/abstract.cfm?uri=ol-45-21-5901`. Publisher: Optical Society of America.

[93] Thouvenin, O. *et al.* Automatic diagnosis and biopsy classification with dynamic full-field oct and machine learning. *Research Square* (2021).

[94] Mazlin, V. *et al.* Optical phase modulation by natural eye movements: application to time-domain FF-OCT image retrieval. In *Optical Coherence Tomography and Coherence Domain Optical Methods in Biomedicine XXV*, vol. 11630, 116300G (International Society for Optics and Photonics, Online, 2021). URL `https://www.spiedigitallibrary.org/conference-proceedings-of-spie/11630/116300G/Optical-phase-modulation-by-natural-eye-movements--application-to/10.1117/12.2583413.short`.

[95] Scholler, J. Motion artifact removal and signal enhancement to achieve in vivo dynamic full field OCT. *Optics Express* **27**, 19562 (2019). URL `https://www.osapublishing.org/abstract.cfm?URI=oe-27-14-19562`.

[96] Croze, R. H., Thi, W. J. & Clegg, D. O. ROCK Inhibition Promotes Attachment, Proliferation, and Wound Closure in Human Embryonic Stem Cell–Derived Retinal Pigmented Epithelium. *Translational Vision Science & Technology* **5**, 7–7 (2016). URL `https://tvst.arvojournals.org/article.aspx?articleid=2587769`. Publisher: The Association for Research in Vision and Ophthalmology.

[97] Qiu, S. *et al.* Migration of retinal pigment epithelium cells is regulated by protein Kinase C-alpha in vitro. *Investigative Ophthalmology & Visual Science* **54**, 7082–7090 (2013).

[98] Miura, Y. *et al.* Hepatocyte Growth Factor Stimulates Proliferation and Migration During Wound Healing of Retinal Pigment Epithelial Cells In Vitro. *Japanese Journal of Ophthalmology* **47**, 268–275 (2003). URL `https://www.sciencedirect.com/science/article/pii/S0021515503000030`.

[99] Mazzoni, F., Safa, H. & Finnemann, S. C. Understanding photoreceptor outer segment phagocytosis: Use and utility of RPE cells in culture. *Experimental eye research* **0**, 51–60 (2014). URL `https://www.ncbi.nlm.nih.gov/pmc/articles/PMC4145030/`.

[100] Scholler, J. FFOCT control and acquisition software (2019). URL `https://zenodo.org/record/3137246`.

RÉSUMÉ

Cette thèse cherche à démontrer l'utilité de la Tomographie en Cohérence Optique (OCT) plein champ statique et dynamique pour l'imagerie de la rétine, qu'il s'agisse d'échantillons *in vitro* (cultures cellulaires 2D ou 3D), *ex vivo* (rétines extraites de différentes espèces) ou *in vivo* (imagerie direct de l'œil du patient). La stabilisation des acquisitions dy-

namiques, à la fois 3D et temporelle, permet un meilleur suivi et une meilleure interprétation de l'évolution d'échantillons *in vitro*, tels que les organoïdes de rétine (produits à partir de cellules souches pluripotentes humaines) ou les cultures cellulaires d'épithélium pigmentaire rétinien (à partir de cellules souches humaines et de cellules primaires de porc). Les signaux dynamiques obtenus diffèrent selon le type cellulaire (photorécepteurs, épithélium pigmentaire rétinien, etc.), mais également selon les phénotypes exprimés (mort cellulaire, division cellulaire, etc.), permettant une imagerie totalement non invasive en biologie. Ces signaux, représentant l'activité cellulaire, proviennent des organelles présentes dans les cellules, et notamment des mitochondries, et aide à l'interprétation de l'état des cellules. Ce contraste innovant per-

mettra d'étudier des maladies dégénératives de la rétine *in vitro*, telles que la Dégénérescence Maculaire Liée à l'Age ou la Rétinite Pigmentaire. La modélisation de maladies peut être facilement étudier en évaluant la réponse des cellules au cours du temps, par exemple après un stress induit à la culture cellulaire. La recherche de traitements adéquats pour ces maladies sera aussi facilitée par le suivi de l'évolution du signal dynamique des cellules, après traitement. Enfin l'appli-

cation de l'OCT plein champ à l'imagerie *in vivo* de la rétine permet une étude non invasive des différentes couches de la rétine (des nerfs jusqu'à l'épithélium pigmentaire rétinien). Elle est aussi moins complexe que les techniques d'optique adaptative habituellement utilisées. Les améliorations de stabilisation et de signal justifient l'idée d'implémenter l'OCT plein champ dynamique *in vivo* dans le futur pour une détection précoce des maladies, telles que la Dégénérescence Maculaire Liée à l'Age ou le Glaucome.

MOTS CLÉS

Tomographie en cohérence optique plein champ - Imagerie dynamique - Activité cellulaire - Microscopie - Cultures cellulaires - Rétine

ABSTRACT

This thesis aims to demonstrate the usefulness of static and dynamic Full-Field Optical Coherence Tomography (FFOCT) for retinal imaging, with *in vitro* (cell cultures in 2D or 3D), *ex vivo* (retinas dissected from different species) and *in vivo* (direct imaging of the eye of the patient) samples. By stabilising the three dimensional and timelapse dynamic acquisitions,

it allows a better following and interpretation of the evolution of *in vitro* samples, such as retinal organoids (produced from human pluripotent stem cells) or retinal pigment epithelium cell cultures (from pluripotent stem cells and primary porcine cells). The recorded dynamic signals can be differentiated by the cell type (photoreceptors, retinal pigment epithelium, etc.) or the expressed phenotypes (for example dying cell, cell division, etc.), allowing a totally non invasive imaging in biology. These signals, representing the cellular activity, come from organelles present in the cells, especially mitochondria, and help to an easy interpretation of the condition of the cells. This innovative contrast allows to study retinal degenerative

diseases *in vitro*, such as Age-related Macular Degeneration or Retinitis Pigmentosa. Disease modeling can easily be studied by evaluating the cell response over time, for example after an induced stress on the cell culture (scratch assays). Drug screening for these diseases will also be eased by following the evolution of the dynamic signal produced by the cells after treatment. Finally, the application of Full-Field Optical Coherence Tomography to *in vivo* retinal imaging permit

a non invasive study of the different layers of the retina (from the nerves to the retinal pigment epithelium). It is a technique less complex than those with adaptive optics usually used for *in vivo* imaging. The stabilisation and signal improvement justify the idea of the future *in vivo* implementation of dynamic FFOCT for the detection of diseases at early stages, such as Age-related Macular Degeneration or Glaucoma.

KEYWORDS

Full Field Optical coherence tomography - Dynamic imaging - Cellular activity - Microscopy - Cell cultures - Retina